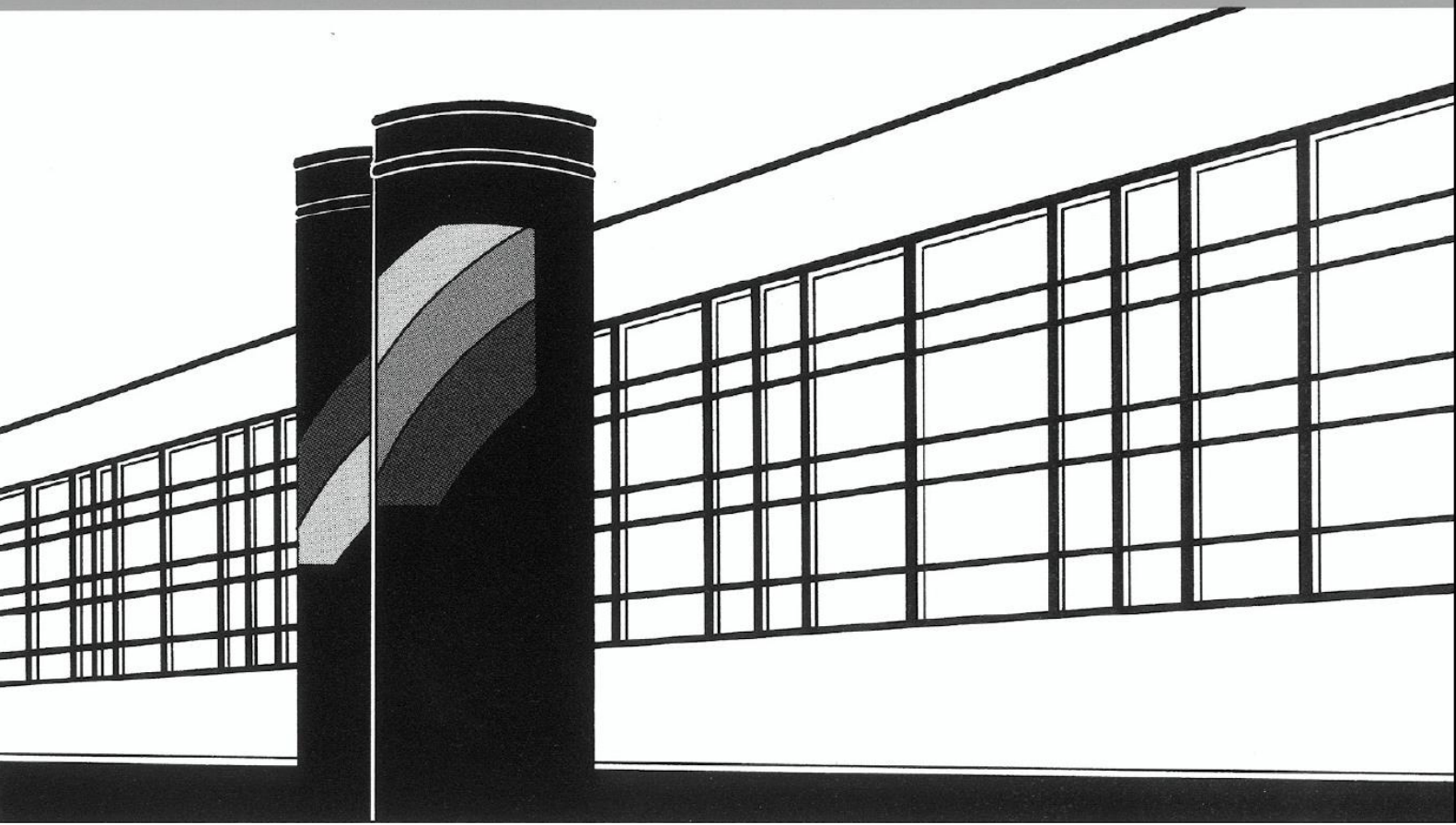


Universität Stuttgart



Institut für Wasser- und Umweltsystemmodellierung

Mitteilungen



Heft 275 Dennis Gläser

Discrete fracture modeling of multi-phase flow
and deformation in fractured poroelastic media

Discrete fracture modeling of multi-phase flow and deformation in fractured poroelastic media

von der Fakultät Bau- und Umweltingenieurwissenschaften
und dem Stuttgart Research Centre for Simulation Technology der
Universität Stuttgart zur Erlangung der Würde eines
Doktor-Ingenieurs (Dr.-Ing.) genehmigte Abhandlung

vorgelegt von

Dennis Gläser

aus Ludwigsburg, Deutschland

Hauptberichter: apl. Prof. Dr. rer. nat. Bernd Flemisch
Mitberichter: Prof. Dr.-Ing. Rainer Helmig
Prof. Hadi Hajibeygi, Ph.D.

Tag der mündlichen Prüfung: 23. März 2020

Institut für Wasser- und Umweltsystemmodellierung
der Universität Stuttgart
2020

Heft 275 **Discrete fracture modeling of
multi-phase flow and
deformation in fractured
poroelastic media**

von
Dr.-Ing.
Dennis Gläser

Eigenverlag des Instituts für Wasser- und Umweltsystemmodellierung
der Universität Stuttgart

D93 Discrete fracture modeling of multi-phase flow and deformation in fractured poroelastic media

Bibliografische Information der Deutschen Nationalbibliothek

Die Deutsche Nationalbibliothek verzeichnet diese Publikation in der Deutschen Nationalbibliografie; detaillierte bibliografische Daten sind im Internet über <http://www.d-nb.de> abrufbar

Gläser, Dennis:

Discrete fracture modeling of multi-phase flow and deformation in fractured poroelastic media, Universität Stuttgart. - Stuttgart: Institut für Wasser- und Umweltsystemmodellierung, 2020

(Mitteilungen Institut für Wasser- und Umweltsystemmodellierung, Universität Stuttgart: H. 275)

Zugl.: Stuttgart, Univ., Diss., 2020

ISBN 978-3-942036-79-5

NE: Institut für Wasser- und Umweltsystemmodellierung <Stuttgart>: Mitteilungen

Gegen Vervielfältigung und Übersetzung bestehen keine Einwände, es wird lediglich um Quellenangabe gebeten.

Herausgegeben 2020 vom Eigenverlag des Instituts für Wasser- und Umweltsystemmodellierung

Druck: DCC Kästl e.K., Ostfildern

Danksagung

Im Folgenden möchte ich mich bei all denjenigen bedanken, durch deren Unterstützung die Entstehung dieser Arbeit möglich wurde. Besonderen Dank möchte ich dabei an Rainer Helmig, Bernd Flemisch und Holger Class richten, die mir die Möglichkeit gegeben haben, als wissenschaftlicher Mitarbeiter am Lehrstuhl für Hydromechanik und Hydrosystemmodellierung zu arbeiten, und in diesem Rahmen die hier vorgestellte Arbeit zu verfassen. Die große Unterstützung in fachlichen und auch persönlichen Belangen, die ich erfahren durfte, halte ich für außergewöhnlich und bin dafür sehr dankbar. An dieser Stelle möchte ich mich auch bei der Deutschen Forschungsgemeinschaft (DFG) bedanken, die die Finanzierung dieses Projektes im Rahmen des Exzellenzclusters Simulation Technology und des Sonderforschungsbereichs 1313 ermöglicht haben.

Außerdem danke ich meinen Kollegen am Lehrstuhl für die harmonische Arbeitsatmosphäre, sowie für die vielen interessanten und philosophischen Diskussionen beim Mittagessen, beim Kaffee oder jeder sonstigen Gelegenheit. Besonderen Dank möchte ich an Timo, Martin und Kilian richten, mit denen ich ausgiebig über viele verschiedene fachliche Fragen diskutieren, und viel dabei lernen durfte. Pru und Steffi danke ich für die große Hilfe bei administrativen Fragen, und Michelle und David für die Lösung technischer Probleme. I would also like to thank Hadi Hajibeygi for the review of this work, as well as for the many interesting discussions we had during the time of his visit to the University of Stuttgart. I very much appreciate his ability to ask the right (often philosophical) questions that helped me to see my work within the bigger picture, and to motivate further steps of investigation.

Schließlich möchte ich mich noch bei meinen Freunden und meiner Familie bedanken, insbesondere bei meinen Eltern und bei Stefanie, Philipp, Anna, Monique und Moritz. Danke für die mentale Unterstützung und die motivierenden Worte, vor allem in Zeiten, in denen es nicht so gut lief.

Contents

<i>List of Figures</i>	<i>XIII</i>
<i>List of Tables</i>	<i>XVII</i>
<i>Nomenclature</i>	<i>XIX</i>
<i>Abstract</i>	<i>XXV</i>
<i>Zusammenfassung</i>	<i>XXVII</i>
1 Introduction	1
1.1 Objectives of this research	3
1.2 Structure of the thesis	4
2 Mathematical models for flow and deformation in porous media	5
2.1 Macroscopic description of flow in porous media	5
2.2 Rock Mechanics	12
2.2.1 Rock as a material	12
2.2.2 Stress and strain measures	13
2.2.3 Linear elasticity	15
2.2.4 Poroelasticity	16
2.3 Balance equations	17
2.3.1 Mass balance equations	20
2.3.2 Momentum balance equations	21
3 Mathematical models for flow and deformation in fractured porous media	23
3.1 Fracture geology	23
3.2 Modeling flow in fractured porous media	24
3.2.1 Equi-dimensional model	26

3.2.2	Mixed-dimensional model	29
3.2.3	Adaptations for open fractures	37
3.3	Modeling flow and deformation in fractured poroelastic media	40
3.3.1	Contact conditions	42
3.3.2	Mixed-dimensional formulation	44
4	<i>Numerical schemes</i>	49
4.1	Finite-volume discretizations of the flow equations	49
4.1.1	Cell-centered finite volume schemes	52
4.1.2	Box scheme	59
4.2	Discretization schemes for the mechanical equations	63
4.2.1	Box scheme	64
4.2.2	Standard Galerkin finite element scheme	65
4.3	Evaluation of the coupling terms	69
4.4	Solution strategy	73
5	<i>Numerical experiments</i>	75
5.1	Single-phase flow in rigid fractured porous media	76
5.1.1	Test case 1: convergence test	76
5.1.2	Test case 2: anisotropic matrix permeability	81
5.1.3	Test case 3: complex two-dimensional fracture network	87
5.1.4	Test case 4: complex three-dimensional fracture network	91
5.1.5	Test case 5: determination of effective permeabilities	95
5.1.6	Conclusions from the test cases	102
5.2	Two-phase flow in rigid fractured porous media	103
5.2.1	Test case 6: crossing fractures	103
5.2.2	Test case 7: two-phase flow in a synthetic core sample	112
5.2.3	Conclusions from the test cases	122
5.3	Single-phase flow in deformable fractured poroelastic media	123
5.3.1	Test case 8: convergence study	123
5.3.2	Test case 9: closing fractures	127
5.3.3	Test case 10: consolidation	136
5.3.4	Conclusions from the test cases	140
5.4	Two-phase flow in deformable fractured poroelastic media	140
5.4.1	Test case 11: dynamically closing and re-opening fractures	141

5.4.2	Test case 12: dilating fractures	145
5.4.3	Conclusions from the test cases	149
6	<i>Summary and Outlook</i>	151
6.1	Outlook	154
A	<i>Effective Porosity</i>	155
B	<i>Time step control</i>	157
	<i>Bibliography</i>	159

List of Figures

2.1	Averaging process over an REV in a porous medium	6
2.2	Porosity of a porous medium as function of the averaging volume size	7
2.3	Configuration inside an idealized pore with two present fluid phases .	8
2.4	Motion functions of constituents in a multiphasic continuum	11
2.5	Internal forces acting on an arbitrary body \mathcal{B}	15
3.1	Model concept for flow in fractured porous media	25
3.2	Equi-dimensional domain decomposition of a fractured porous medium	27
3.3	Mixed-dimensional domain decomposition of a fractured porous medium	29
3.4	Conceptual model domain for the contact problem	40
4.1	Exemplary grid configuration around a fracture for the TPFA scheme .	53
4.2	Exemplary grid configuration around a fracture for the MPFA scheme	55
4.3	Exemplary grid configuration around a fracture for the BOX scheme .	60
4.4	Distribution of degrees of freedom for CG1, BOX and CG2	69
4.5	Distribution of degrees of freedom around a fracture in the full poromechanical problem considering two-phase flow	70
5.1	Test case 1: convergence plots for pressure and interface fluxes	77
5.2	Test case 1: convergence plots using the volume-corrected source term	80
5.3	Test case 2: domain and boundary conditions	81
5.4	Test case 2: convergence plots for pressure ($k = 1 \cdot 10^4$)	82
5.5	Test case 2: matrix-fracture transfer fluxes for $k = 1 \cdot 10^4$ and $\Phi = \pi/4$	83
5.6	Test case 2: convergence plots for pressure ($k = 1 \cdot 10^{-4}$)	84
5.7	Test case 2: exemplary pressure profile for $k = 1 \cdot 10^{-4}$	85
5.8	Test case 2: relative pressure errors for different values of k	86
5.9	Test case 3: domain, boundary conditions and pressure solution . . .	87
5.10	Test case 3: pressure profiles along $y = 500$ m and $x = 625$ m	90

5.11	Test case 4: fracture network, boundary conditions and pressure solution	91
5.12	Test case 4: pressure profiles obtained with the different schemes . . .	94
5.13	Test case 4: Δp for considering/neglecting intersection flow	94
5.14	Test case 5: synthetic core samples with artificial fracture networks .	97
5.15	Test case 5: influence of grid refinement on k_{eff}	98
5.16	Test case 5: effective permeability versus hydraulic fracture aperture .	100
5.17	Test case 5: velocity distributions for the networks \mathcal{F}_{21} and \mathcal{F}_{23} . . .	101
5.18	Test case 5: pressure plot along the z -axis for the networks \mathcal{F}_{21} and \mathcal{F}_{23}	102
5.19	Test case 6: domain, boundary conditions and exemplary grid	103
5.20	Test case 6.1: saturation distributions and errors	106
5.21	Test case 6.1: saturation plots through the domain	107
5.22	Test case 6.2: saturation distributions and errors	109
5.23	Test case 6.2: saturation plots through the domain	110
5.24	Test case 6.2: MPFA vs coarse equi-dimensional and reference saturation	111
5.25	Test case 7: domain, fracture network and boundary conditions . . .	113
5.26	Test case 7.1: saturation and velocity distributions	115
5.27	Test case 7.1: hydrogen production curves	116
5.28	Test case 7.1: presure along the z -axis	117
5.29	Test case 7.1: influence of gravity on saturation and velocity	117
5.30	Test case 7.1: results considering flow along intersections	119
5.31	Test case 7.1: saturation and velocity with flow along intersections . .	119
5.32	Test case 7.2: results for blocking fractures	121
5.33	Test case 7.2: saturation and velocity distributions	121
5.34	Test case 8: domain and fracture configuration	124
5.35	Test case 8: discretization used for the Lagrange multiplier	125
5.36	Test case 8: convergence rates for $\llbracket u \rrbracket^{\parallel}$	126
5.37	Test case 8: plots of $\llbracket u \rrbracket^{\parallel}$ and τ^{\perp}	127
5.38	Test case 9: domain and boundary conditions	128
5.39	Test case 9.1/9.2: pressure and velocity distributions	130
5.40	Test case 9.1: $\llbracket u \rrbracket^{\parallel}$ and τ^{\perp} along fractures 1 and 2	131
5.41	Test case 9.1: $\llbracket u \rrbracket^{\parallel}$ and τ^{\parallel} along fracture 1	132
5.42	Test case 9.3/9.4/9.5: ϱ and τ^{\parallel} along fracture 1	133
5.43	Test case 9.6: three-dimensional results for $F = 0.5$	135
5.44	Test case 9.7: three-dimensional results for $F = 0.001$	136
5.45	Test case 10: displacement, slip and contact tractions	138

5.46	Test case 10: subsidence profiles at $t = 4900$ s	139
5.47	Test case 10: subsidence over time	139
5.48	Test case 11: S_{TCE} and \mathbf{q}_{TCE} for $E = 1$ GPa	142
5.49	Test case 11: S_{TCE} , \mathbf{q}_{TCE} and $\boldsymbol{\tau}$ for $E = 0.1$ GPa	143
5.50	Test case 11: mass of TCE in the domain over time	144
5.51	Test case 12: mass of TCE in the domain over time	146
5.52	Test case 12: S_{TCE} , \mathbf{q}_{TCE} and \mathbf{u} for three different time steps	147
5.53	Test case 12: fracture volume change over time	148

List of Tables

5.1	Test case 3: matrix specifications, solver times and condition numbers	88
5.2	Test case 4.1: matrix specifications, solver times and condition numbers	93
5.3	Test case 4.2: matrix specifications, solver times and condition numbers	93
5.4	Test case 6: number of cells of the used grids.	104
5.5	Test case 7.1: parameter choices for the subdomains	114
5.6	Test case 7.2: parameter choices for the subdomains	120
5.7	Test case 9: parameter choices for ρ_0 , a_0 and E	129
5.8	Test case 9: k_{eff} computed with various scheme combinations	130
5.9	Test case 9: computational cost of various scheme combinations	134

Nomenclature

Selected Acronyms

BOX vertex-centered finite volume scheme (box scheme)

CG1 acronym for standard galerkin finite element scheme using linear elements

CG2 acronym for standard galerkin finite element scheme using quadratic elements

MPFA multi-point flux approximation scheme

REV representative elementary volume

TPFA two-point flux approximation scheme

Calligraphic Letters

\mathcal{B} some arbitrary body

\mathcal{CV} control volume

\mathcal{E} the set of faces of a computational mesh

\mathcal{I} mapping of points from the master to the slave side of a fracture

\mathcal{K} a subset of some arbitrary body

\mathcal{M} computational mesh

\mathcal{P} a material point on some arbitrary body

\mathcal{S}	the set of faces of a finite-volume discretization	
\mathcal{T}	the set of control volumes of a finite-volume discretization	
\mathcal{V}	the set of vertices of a discretization	

Greek Letters

α	index of a phase	
α_B	biot coefficient	[-]
α^{VG}	parameter of the van-Genuchten relationship	[1/Pa]
β	index of a fluid phase	
ϵ_d	cross-section of a d -dimensional domain in n -dimensional space	[m ^{n-d}]
ϵ_s	infinitesimal strain tensor of the solid skeleton	[-]
Γ_d	surface of some d -dimensional domain	[m ^{d-1}]
γ_d	interface between Ω_d and Ω_{d+1} in mixed-dimensional setting	[m ^d]
λ	first lamé parameter (of the linear-elastic stress-strain relationship)	[Pa]
μ	dynamic viscosity of a phase	[Pa·s]
G	second lamé parameter (of the linear-elastic stress-strain relationship)	[Pa]
ν	Poisson's ratio	[-]
Ω_n	computational (n -dimensional) domain	[m ⁿ]
$\omega_{K,\sigma}$	transmissibility associated with a face σ of a control volume K	[m ³]
ϕ	porosity	[-]
φ	basis function of function space of scalar functions	[-]

φ	basis function of a function space of vector-valued functions	[-]
ϕ_{eff}	effective porosity	[-]
Ψ	some extensive thermodynamic quantity	[-]
ψ	some intensive, volume-specific thermodynamic quantity	[1/m ³]
ρ	density of a phase	[kg/m ³]
ϱ	gap between two fracture surfaces	[m]
σ_s	linear stress tensor of the solid skeleton	[Pa]
σ	total stress tensor of the porous medium	[Pa]
ϑ	flux of some scalar thermodynamic quantity	[1/s]
Θ	flux of some vectorial thermodynamic quantity	[1/s]
τ	mortar variable (contact traction) in an n -dimensional setting	[N/m ^{$n-1$}]
χ	motion function of material points	[-]
ξ_i	basis vector of the fracture-local coordinate system	[-]

Roman Letters

a	acceleration vector	[m/s ²]
<i>a</i>	hydraulic fracture aperture	[m]
b	body force	[N/m ³]
C	right Cauchy-Green deformation tensor	[-]
E	Green-Lagrangean strain tensor	[-]
<i>E</i>	element of a d -dimensional computational mesh, i.e. $E \in \mathcal{M}_d$	[m ^{d}]

E	Young's modulus	[Pa]
\mathbf{F}	deformation gradient	[-]
$F_\beta^{K,\sigma}$	discrete flux of phase β across face σ , seen from control volume $K \in \mathcal{T}_d$	[kg/s]
$\mathbf{F}^{K,\sigma}$	discrete force exerted on the face σ , seen from control volume $K \in \mathcal{T}_d$	[N]
\mathbf{f}	force vector	[N]
g	gravitational acceleration	[m/s ²]
\mathbf{g}	gravitational acceleration vector $\mathbf{g} = [0, 0, -g]^T$	[m/s ²]
\mathbf{H}	Displacement gradient	[-]
\mathbf{K}_f	hydraulic conductivity	[m/s]
\mathbf{K}	intrinsic permeability	[m ²]
$\kappa_{r\alpha}$	relative permeability of a phase α	[-]
m	mass	[kg]
\mathbf{n}	outer unit normal vector	[m]
n^{VG}	parameter of the van-Genuchten capillary pressure-saturation relationship	[-]
n_α	volume fraction of a phase α	[-]
\mathbf{p}	momentum vector	[N s]
p_c	capillary pressure	[Pa]
p_β	macroscopic pressure of a fluid phase β	[Pa]
\mathbf{q}	Darcy velocity	[m/s]
\mathbf{q}_α	Darcy velocity of a phase α	[m/s]

$\mathbf{q}_{\alpha,d}$	Average darcy velocity of phase α on domain with dimension d	[m/s]
S_α	saturation of a phase α	[-]
$S_{\alpha,e}$	effective saturation of a phase α	[-]
$S_{\alpha,r}$	residual saturation of a phase α	[-]
t	time	[s]
\mathbf{t}	traction vector	[N/m ²]
\mathbf{u}	displacement vector	[m]
\mathbf{v}	velocity	[m/s]
v	vertex of a computational mesh, i.e. $v \in \mathcal{M}$	[-]
V	volume	[m ³]
V_p	pore volume	[m ³]
\mathbf{x}	spatial coordinate vector	[m]
\mathbf{X}	spatial coordinate vector in a reference configuration	[m]

Abstract

Numerical models play an important role in many geotechnical engineering applications, for instance, in the process of designing the operating conditions of a specific project. Moreover, numerical simulations help to improve the process understanding and to identify the most relevant mechanisms or parameters that govern a certain geological system. Geological applications typically involve flow processes through porous rock, which can be a complex material composed of many rock-forming minerals. Moreover, most rocks are broken up by fractures that may substantially alter the hydraulic and mechanical behavior of a rock mass. As a consequence, understanding the complex flow patterns that arise in fractured rock might be crucial for successful project designs. However, numerical modeling of flow and deformation processes of fractured porous rock is challenging due to the complex geometries involved in arbitrary networks of fractures, and the typically very small fracture apertures in comparison with the spatial scales of interest in most applications. Due to this difference in scales, a widely-used approach in the literature is to describe the fractures as lower-dimensional objects, which circumvents the need to discretize the interior of the fractures. We adopt such an approach in this work and present hybrid-dimensional models for single- and two-phase flow in rigid fractured porous media as well as fractured poroelastic media.

Hybrid-dimensional model for flow in rigid fractured porous media We consider a hybrid-dimensional decomposition of a domain of interest into a bulk medium as well as lower-dimensional fractures (codimension 1) and intersections (codimension 2). On fractures and their intersections, cross-section integrated balance equations are derived and coupling conditions between domains of codimension one are formulated. The latter account for mass transfer between the bulk medium and the fractures as well as between fractures and their intersections. Moreover, we present different numerical approaches, based on well-established finite volume discretization schemes, that solve

the hybrid-dimensional system of equations. Convergence of the schemes is tested on the basis of numerical experiments for single-phase flow using analytical and numerical reference solutions, which consider both isotropic and anisotropic permeabilities in the bulk medium. Furthermore, we apply the schemes to a benchmark case from the literature and find good agreement with the results reported in the original study. We then perform numerical core sample experiments to determine the effective permeabilities of synthetic core samples in which different types of fracture networks are embedded. Physically meaningful dependencies of the effective permeabilities on the fracture apertures and network topologies can be identified in the numerical results. In the context of two-phase flow, we compare the hybrid-dimensional schemes against an equi-dimensional reference solution on a simple geometric setting involving two intersecting fractures. While significant deviations in saturation are observed locally for the case of blocking fractures, a good agreement with the reference is observed for conductive fractures. We then apply the hybrid-dimensional schemes to a synthetic gas injection experiment into a water saturated cylindrical core sample and investigate the influence of gravity and flow along intersections of fractures on the experimental results.

Hybrid-dimensional model for flow in fractured poroelastic media In this part of the work, the hybrid-dimensional flow model is extended to account for poroelastic bulk media containing open fractures, while flow along intersections is not considered. Mechanical interactions between the bulk medium and the fractures are incorporated by means of deformation-dependent fracture apertures, compressive stresses on the medium caused by the fluid pressure inside the fractures, as well as the transition to a contact mechanical problem in the case of closing fractures. We first test the convergence of the numerical schemes for a purely mechanical problem considering frictional contact on a single fracture for which an analytical solution exists, and find a good agreement of the numerical results with the analytical solution. In the subsequent numerical examples, we apply the schemes to both single- and two-phase flow experiments to investigate the effects of closing and opening fractures on the flow field. The results are discussed in terms of the physical relevance of the observed phenomena as a quantitative assessment would require detailed experimental data.

Zusammenfassung

Numerische Modelle können einen wichtigen Beitrag während der Auslegungsphase eines geotechnischen Projekts leisten. Abgesehen davon können numerische Simulationen dabei helfen, ein verbessertes Prozessverständnis zu gewinnen, sowie die einflussreichsten Parameter auf ein bestimmtes geologisches System zu bestimmen. Geologische Anwendungen beinhalten in der Regel Strömungsprozesse durch poröses Gestein, welches oft ein komplexes Konglomerat bestehend aus diversen Mineralen ist. Darüber hinaus sind die meisten Gesteinsformationen dadurch gekennzeichnet, dass sie Klüfte aufweisen, welche einen großen Einfluss auf die hydraulischen und mechanischen Eigenschaften der Formation haben können. Aus diesem Grund ist ein Verständnis für die komplexen Strömungs- und Deformationsprozesse in geklüfteten porösen Medien sehr wichtig für die erfolgreiche Auslegung geotechnischer Projekte. Aufgrund der komplexen Geometrien von Kluftnetzwerken, sowie der äußerst kleinen Öffnungsweiten der Klüfte im Vergleich zu der Skala der geotechnischen Anwendung, stellt die numerische Modellierung dieser Prozesse in geklüfteten porösen Medien eine Herausforderung dar. Wegen der kleinen Öffnungsweiten nutzen viele Ansätze aus der Literatur dimensionsreduzierte Beschreibungen für die Klüfte, was verhindert, dass das Innere der Klüfte diskretisiert werden muss. In dieser Arbeit übernehmen wir einen solchen Ansatz und präsentieren hybrid-dimensionale Modelle zur Beschreibung von Ein- und Mehrphasenströmungsvorgängen in starren geklüfteten porösen Medien sowie geklüfteten poroelastischen Medien.

Hybrid-dimensionales Modell für Strömungsvorgänge in starren geklüfteten porösen Medien

Wir präsentieren ein hybrid-dimensionales Modell, das eine poröse Matrix und darin eingebettete nieder-dimensionale Klüfte (Kodimension 1) und deren Überschneidungen (Kodimension 2) beinhaltet. Auf den Klüften und Überschneidungsregionen werden integrale Bilanzgleichungen formuliert, welche durch Integration über die Querschnitte

erhalten werden. Des Weiteren werden Kopplungsbedingungen formuliert, auf deren Basis der Massenaustausch zwischen der Matrix und den Klüften, sowie den Klüften und deren Überschneidungsregionen, dargestellt wird. Darüber hinaus präsentieren wir verschiedene numerische Ansätze zur Lösung des hybrid-dimensionalen Gleichungssystems, welche auf etablierten finite Volumen Methoden basieren. Diese werden in numerischen Simulationen hinsichtlich ihres Konvergenzverhaltens, für sowohl isotrope als auch anisotrope Permeabilitäten in der porösen Matrix, getestet. Außerdem werden die Modelle auf einen Benchmark-Test aus der Literatur angewendet, für den eine sehr gute Übereinstimmung mit den Resultaten aus dem Originalbericht gefunden wird. Anschließend werden numerische Experimente mit synthetisch erstellten Bohrkernen durchgeführt, um die Abhängigkeit der effektiven Permeabilitäten der Kerne von darin eingebetteten Kluftnetzwerken verschiedener Topologien zu bestimmen. Die Ergebnisse der hybrid-dimensionalen Modelle werden dann mit einer equi-dimensionalen Referenzlösung für den Fall einer Zweiphasen-Strömung durch ein Medium mit zwei sich überschneidenden Klüften verglichen. Für schwach durchlässige Klüfte waren lokal deutliche Abweichungen in den Sättigungsprofilen zu sehen, während für stark durchlässige Klüfte eine gute Übereinstimmung festgestellt wurde. Schließlich wird ein Gas-Injektionsszenario in einen synthetischen Bohrkern simuliert, durch welches der Einfluss der Gravitation, sowie der Strömungsprozesse entlang von Überschneidungen von Klüften auf die experimentellen Ergebnisse untersucht wird.

Hybrid-dimensionales Modell für Strömungsvorgänge in geklüfteten poroelastischen Medien

In diesem Teil der Arbeit wird das Strömungsmodell erweitert, sodass poroelastische Medien berücksichtigt werden können. Das Modell beschränkt sich auf Strömungsprozesse in der Matrix und offenen Klüften, während die Überschneidungsregionen der Klüfte vernachlässigt werden. Die Mechanische Interaktion zwischen der Matrix und den Klüften wird berücksichtigt, indem der Druck in den Klüften auf die Matrix aufgetragen wird und die Öffnungsweiten der Klüfte abhängig vom Verschiebungsfeld der Matrix sind. Des Weiteren wird ein Kontaktproblem gelöst, wenn die Klüfte sich schließen. Zunächst werden die Modelle für ein rein mechanisches Problem mit einer Kluft, die sich in reibungsbehaftetem Kontakt befindet, getestet. Eine gute Übereinstimmung der numerischen mit der analytischen Lösung lässt sich für diesen Fall beobachten. In den anschließenden Beispielen werden die Modelle auf verschiedene Ein- und Zweiphasensysteme angewendet, um den Einfluss sich schließender und öffnender Klüfte zu untersuchen.

1 Introduction

Numerical simulations are an important tool in the planning process of many geotechnical engineering applications. For example, they can be used to identify the most relevant mechanisms and parameters that govern a geological system. Moreover, the efficiency and the environmental impact of an application can be studied under varying operating conditions. Geological applications typically involve flow processes through porous rock, however, due to the omnipresence of fractures in nature, they have to be accounted for in most applications. Examples range from groundwater management [Qian et al., 2014] over enhanced oil recovery techniques [Torabi et al., 2012] to geothermal energy production [McFarland and Murphy, 1976, Shaik et al., 2011]. Another prominent application in which fractures are an essential ingredient are unconventional natural gas production techniques [Sovacool, 2014]. In such, preexisting natural fractures are opened and new fractures are created by means of hydraulic fracturing prior to production. This provides the flow paths and surface areas across which gas exchange can occur for the application to run properly. Furthermore, significant experimental and numerical efforts have been made to study the influence of fractures in the context of underground radioactive waste disposal sites *. The construction of the storage facility can cause fractures to be generated in the vicinity of the storage caverns, in which the anaerobic corrosion of the metal containers leads to a production of hydrogen gas. This leads to a pressure increase in the cavern accompanied by a large temperature increase caused by the radioactive decay processes. Research questions are, for example, how the presence of fractures influences the evolution of pressures in the caverns, if fracture propagation occurs, and if these effects endanger the integrity of a waste disposal site.

Fractures are ruptures in the rock mass, that can either be open space or filled with matter and which are typically very thin in comparison to the sizes of interest of an

*See, for example, the technical reports of the Swiss National Cooperative for the Disposal of Radioactive Waste (*nagra.ch*)

application. The hydraulic properties of the space between the fracture surfaces can be orders of magnitude different from those of the surrounding rock and can have a strong impact on the overall hydraulic behavior of a rock mass. Thus, numerical methods that are to be used for the modeling of the processes occurring in fractured rock need to be capable of describing its strongly heterogeneous nature. Various different modeling techniques have been developed over the years which can be classified into *continuum fracture models* and *discrete fracture-matrix* (dfm) models. In the first class of models, the geometry of the fractures is not explicitly captured. Instead, the fractured medium is described by means of averaged properties in so-called *single-continuum* models [Pruess et al., 1990, Royer et al., 2002], or, the fractures are accounted for by an individual overlapping continuum in *dual-continuum* models [Warren and Root, 1963, Kazemi et al., 1976, Zimmerman et al., 1993, 1996]. In the latter, the mutual interaction between the fractures and the bulk medium is incorporated via transfer functions. An extension to multiple continua is also possible [Pruess, 1992, Tatomir, 2013]. In dfm models, the fracture geometries are discretely captured either by an equi-dimensional discretization of the fractures [Matthai et al., 2007], or by means of lower-dimensional discretizations with adequate aperture distributions. The latter, i.e. mixed-dimensional (or hybrid-dimensional) dfm models, can be realized in a conforming way by constraining the element faces of the discretization used for the bulk domain to the fracture geometries. This type of models has been realized for single-phase flow e.g. using mixed finite elements [Martin et al., 2005, Boon et al., 2018], mixed virtual element methods [Nordbotten et al., 2019], mimetic finite differences [Antonietti et al., 2016], or cell-centered finite volume techniques [Karimi-Fard et al., 2004, Sandve et al., 2012, Ahmed et al., 2015, Nordbotten et al., 2019]. A python-based open-source software package including several of the above-mentioned approaches is presented in Keilegavlen et al. [2017]. For two-phase flow, Reichenberger et al. [2006] and Brenner et al. [2014] present models on the basis of a node-centered finite volume scheme and the vertex approximate gradient scheme, respectively. A big advantage of non-conforming approaches is the ability to use independent discretizations which substantially facilitates the grid creation, especially for highly fractured systems. Examples for this type of models for single-phase flow using finite elements and Lagrange multipliers can be found in Köppel et al. [2018, 2019], Schädle et al. [2019]. An approach using an extended finite element formulation can be found e.g. in Schwenck [2015] for single-phase and in Fumagalli and Scotti [2013] for two-phase flow. Finite-volume based non-conforming approaches are presented e.g. in Tene et al. [2016, 2017].

1.1 Objectives of this research

In this work, conforming mixed-dimensional dfm models for two-phase flow in fractured porous media are developed. We follow the ideas presented in Karimi-Fard et al. [2004], Sandve et al. [2012], Ahmed et al. [2015] and develop numerical approaches, based on cell-centered finite volume techniques, that require conformity of the discretization of the bulk domain to the fracture geometries. However, in this work we extend them to the case of two-phase flow. Moreover, we enhance the vertex-centered finite volume scheme presented in Reichenberger et al. [2006] such that additional balance equations are solved on the fractures and that the possible discontinuities across the fractures can be captured. One objective of this work is to compare these different approaches in terms of accuracy and computational efficiency. Apart from that, the models are applied to more complex geometrical and physical configurations in order to investigate if they are capable of capturing the involved phenomena, and if physically meaningful results and relationships can be identified. The second main objective of this work is the extension of the flow models to account for deformable poroelastic media. This substantially increases the complexity of the model as the fractures are no longer static but can dilate or close. In the case of the latter, a contact mechanical problem has to be solved in order to prevent the unphysical mutual penetration of the fracture surfaces and to model the traction due to friction that arise in the case of contact. We present several numerical approaches to the modeling of this problem, which we again want to compare in terms of accuracy and computational cost. Moreover, we apply the models to several test cases, each of which is dedicated to identify the capability of the models to capture designated physical processes.

All models presented in this work have been implemented in the open-source simulator DuMu^x [Flemisch et al., 2011, Koch et al., 2018a]. Furthermore, some of the modeling capabilities implemented in the scope of this work have been presented in Gläser et al. [2017], Gläser et al. [2019], and have been used by other researchers in Andrianov and Nick [2019].

1.2 Structure of the thesis

The thesis is structured as follows: In Chapter 2 we present the basic ideas, concepts and equations that are used to describe flow and deformation in porous media. In particular, the concept of volume-averaged quantities is introduced, on the basis of which the processes are described on the scale of a representative elementary volume (REV). Moreover, we present the concepts of linear elasticity and poroelasticity which constitute the foundation of the mechanical model developed in this work. Finally, we conclude the chapter with the derivation of the balance equations relevant for this work. Chapter 3 is devoted to the derivation of the mixed-dimensional problem formulations for flow and deformation in fractured porous media. After providing some background on geologic characteristics of fractures, the mixed-dimensional flow model is presented. Subsequently, the conditions for the mechanical contact of fracture surfaces are outlined, on the basis of which the mixed-dimensional model for flow and deformation in fractured poroelastic media is stated. In Chapter 4 we present the derivation of the numerical schemes that were developed in this work for the solution of the mixed-dimensional problem formulations. Since the underlying numerical schemes are well known, the presentation focuses on the extensions necessary to incorporate the coupling terms appearing in the mixed-dimensional formulations. All numerical examples targeting at investigating the above-mentioned objectives are presented in Chapter 5, before the results are summarized and an outlook is given in Chapter 6.

2 *Mathematical models for flow and deformation in porous media*

In this chapter we want to present the basic ideas and concepts for the mathematical description of porous media. In Section 2.1 the concepts and quantities that are used for the description of flow processes through the void space of porous media are introduced, while Section 2.2 focuses on the description of the mechanical deformations of poroelastic materials. Finally, in Section 2.3, the balance equations on the basis of which the above-mentioned processes are described are introduced.

2.1 *Macroscopic description of flow in porous media*

”Initially, we may attempt to describe a porous medium as a solid with holes” [Bear, 2013]. This citation is taken from the well-known book *Dynamics of Fluids in Porous Media* by Jacob Bear, in which the subsequent passage discusses comprehensively why this definition is far from being sufficiently accurate. It then follows an extensive definition of a porous medium, which shows that the task of finding a proper definition is harder than expected at first. To keep it short, we try to summarize the basic ideas as follows: A porous medium is a portion of space that consists of solid and fluid phases, and where the solid phase is distributed such that there is an interconnected pore space throughout the domain, in which fluids can flow. Modeling these flow processes on the pore-scale is often not possible as the geometry of the pore space is extremely complex and often unknown or difficult to determine. In any case, on the scales of interest of most applications, a pore-scale modeling approach quickly becomes unfeasible.

In this work, we adopt a macroscopic description of flow processes in porous media. On the macroscopic scale, volume-averaged quantities are introduced (see Figure 2.1)

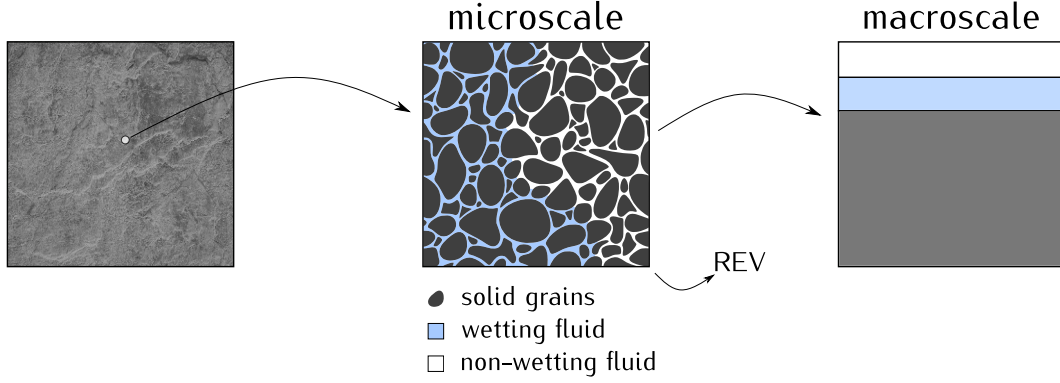


Figure 2.1 – From microscale to macroscale. Illustration of the averaging process over a representative elementary volume, leading to a macroscopic description of the porous medium.

that are obtained by homogenization over a *representative elementary volume* (REV). For example, the exact geometrical distribution of the pore space is substituted by a single scalar quantity, the porosity, which is defined as the ratio of the pore space volume V_p divided by the entire volume of the REV, V_{REV} :

$$\phi = \frac{V_p}{V_{\text{REV}}}. \quad (2.1)$$

Note that below the REV scale the porosity cannot be properly defined as it is subject to strong fluctuations depending on the size of the volume over which the averaging process is carried out. Thus, the REV scale is the scale over which the porosity stays (more or less) constant (see Figure 2.2). Analogously, the exact geometrical distributions of the phases α on the microscale can be translated into the fractions of space occupied by them within the REV:

$$n_\alpha = \frac{V_\alpha}{V_{\text{REV}}}. \quad (2.2)$$

Here, n_α denotes the volume fraction. In this work we use the notion of saturations for the fluid phases, which relate the volume occupied by a fluid phase β to the available pore volume:

$$S_\beta = \frac{V_\beta}{V_p}. \quad (2.3)$$

A natural consequence of these definitions is that

$$\sum_{\beta} S_\beta = 1, \quad 0 \leq S_\beta \leq 1, \quad \sum_{\alpha} n_\alpha = 1, \quad 0 \leq n_\alpha \leq 1, \quad (2.4)$$

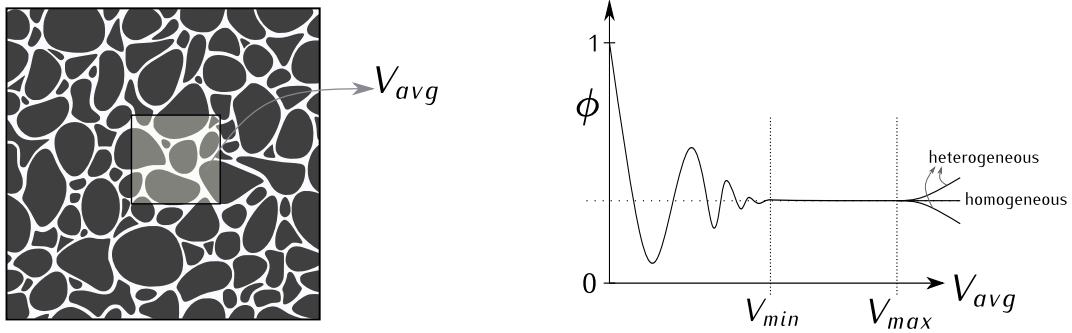


Figure 2.2 – Choosing the REV size. Illustration of the choice of the averaging volume (left) and the porosity as a function of its size (right) (modified after Bear [2013]).

and that the saturation of a fluid phase is related to its volume fraction by:

$$S_\beta = \frac{n_\beta}{\phi}. \quad (2.5)$$

When multiple fluid phases (e.g. water, oil, air) share the pore space, surface tension causes a pressure difference at the interfaces between them. As a result, contact angles develop, here denoted with θ_α , at the interface between two fluid phases and the solid matrix (see Figure 2.3). In this setting, the fluid phase that develops an acute angle at the interface is referred to as the wetting phase, whereas the fluid with the obtuse interface angle is called the non-wetting phase [Helmig, 1997]. While the fluids move through the pore space, the interfaces are displaced as well and eventually one fluid phase might completely vanish within a part of the domain. However, the above mentioned pressure differences can get very large, especially in smaller pores, and can lead to clusters of immobile fluid phases which cannot be displaced. A number of further trapping mechanisms, e.g. the presence of dead-end pores, might lead to the same effect, i.e. a residual amount of trapped fluid phase. These mechanisms are incorporated on the macroscale via the concept of residual saturations $S_{\alpha,r}$ and correspondingly the concept of effective saturations:

$$S_{\beta,e} = \frac{S_\beta - S_{\beta,r}}{1 - S_{w,r} - S_{n,r}}. \quad (2.6)$$

Note that here we have introduced the effective saturations for the case of two present fluid phases. Conceptually, $S_{\beta,e}$ quantifies the amount of mobile fluid phase available in the pore space. With the residual and effective saturations we have introduced quantities related to the possible effects (partly) caused by the above-mentioned pressure

differences at the fluid-fluid interfaces, while the cause itself has not yet been transferred to the macroscopic scale. Assuming a tube-shaped pore throat in which the fluids touch, the emerging pressure difference could be computed locally using the well-known Young-Laplace equation. However, on the REV scale we need to describe this on the basis of averaged quantities. A widely-used approach in the context of two-phase flow is the definition of the macroscopic capillary pressure as a function of the effective wetting phase saturation $S_{w,e}$:

$$p_c(S_{w,e}) = p_n - p_w, \quad (2.7)$$

where p_n and p_w refer to the macroscopic non-wetting and wetting phase pressures, respectively. A number of empirical relationships are available in the literature, of which the most commonly used are the Brooks-Corey [Brooks and Corey, 1964] and the Van-Genuchten model [Van Genuchten, 1980]. The latter is used in this work and reads:

$$p_c(S_{w,e}) = \frac{1}{\alpha^{\text{VG}}} \left(S_{w,e}^{-1/(1-\frac{1}{n^{\text{VG}}})} - 1 \right)^{1/n^{\text{VG}}}. \quad (2.8)$$

Note that the parameters α^{VG} and n^{VG} have to be determined experimentally for a given porous medium and fluid configuration. With the capillary pressure we have introduced the notion of a macroscopic pressure, and it should be noted that the wetting and non-wetting phase pressures in equation (2.7) are to be understood as macroscopic, i.e. averaged pressures, as well. While pressure gradients drive fluid flow on the microscale, it is the macroscopic pressure gradients that lead to a discharge of fluid phases out of or into an REV.

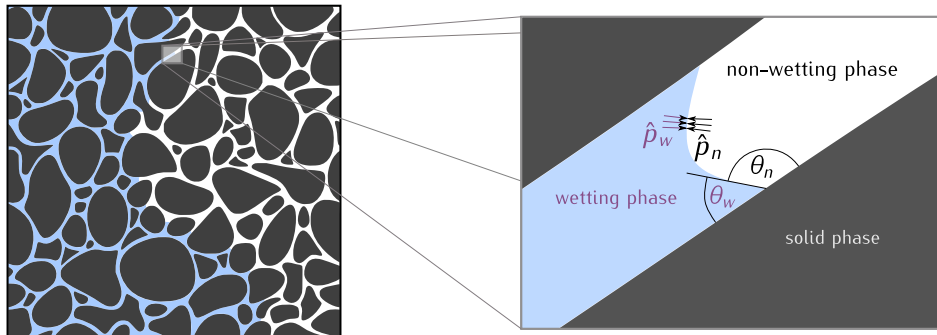


Figure 2.3 – Contact angles. Illustration of an idealized individual pore throat and the angles developing at the fluid-fluid-solid interface. Here, \hat{p}_w and \hat{p}_n denote the wetting and non-wetting phase pressures on the pore-scale, respectively.

Darcy's Law The first one to describe fluid flow through porous media in a macroscopic sense was the french engineer Henry Darcy (★June 10th 1803 in Dijon, France, †January 3rd 1858 in Paris). From experiments on sand columns he deduced that the discharge of water was proportional to the differences in water head between the inlet and the outlet divided by the length of the column. The corresponding proportionality factor is called the hydraulic conductivity \mathbf{K}_f and describes the resistance of the porous medium to fluid flow for a specific fluid. Making use of its relation

$$\mathbf{K}_f = \mathbf{K} \frac{\rho g}{\mu} \quad (2.9)$$

to the intrinsic permeability \mathbf{K} , which is a property of the porous medium only, one can write *Darcy's Law* in the following way:

$$\mathbf{q} = -\frac{1}{\mu} \mathbf{K} (\nabla p - \rho \mathbf{g}). \quad (2.10)$$

Note that in the above equations we have used the density ρ and dynamic viscosity μ of the fluid, as well as the gravitational acceleration g and the corresponding gravity vector \mathbf{g} . Equation (2.10) provides a relation of the macroscopic fluid velocity \mathbf{q} , also called Darcy velocity or specific discharge (unit: [m³/s/m²]), to pressure gradients and gravitational acceleration, i.e. it can be used as a constitutive relationship to deduce the flow field from a pressure field and a given permeability distribution. Please also note the following relation

$$\phi (\mathbf{v}_f - \mathbf{v}_s) = \mathbf{q}, \quad (2.11)$$

i.e. the specific discharge results from the difference between the fluid velocity \mathbf{v}_f and the velocity of the solid matrix \mathbf{v}_s , scaled with the porosity ϕ to account for the reduced space that is available for flow. The velocity \mathbf{v}_s results from a mechanical deformation of the solid matrix and vanishes if it is assumed to be rigid (see Section 2.3). The extension of equation (2.10) to multiphase-flow systems can be formulated as [Helmig, 1997, Bear, 2013]

$$\mathbf{q}_\beta = -\frac{\kappa_{r\beta}}{\mu_\beta} \mathbf{K} (\nabla p_\beta - \rho_\beta \mathbf{g}), \quad (2.12)$$

where we again have an analogous relation between the Darcy velocity and the phase velocity of a fluid phase β :

$$\phi S_\beta (\mathbf{v}_\beta - \mathbf{v}_s) = \mathbf{q}_\beta. \quad (2.13)$$

In (2.12) the relative permeability $\kappa_{r\beta}$ of a fluid phase β has been introduced, which is a macroscopic quantity that accounts for the mutual interaction between the phases and the effect of the presence of a phase on the flow of another phase. The presence of another phase can never increase the macroscopic velocity, i.e. $0 \leq \kappa_{r\beta} \leq 1$, and furthermore $\kappa_{r\beta} = 1$ for $S_\beta = 1.0$. With the latter condition it is ensured that equation (2.12) reduces to the single-phase formulation (2.10) when a phase occupies the entire pore space. Accordingly, $\kappa_{r\beta} = 0$ for $S_{\beta,e} = 0$ must hold. In this work, we use the Van-Genuchten-Mualem model [Van Genuchten, 1980, Mualem, 1976, Luckner et al., 1989] for the relative permeability as a function of the effective wetting phase saturation:

$$\kappa_{r\beta}(S_{w,e}) = \sqrt{S_{w,e}} \left[1 - (1 - S_{w,e}^{1/m_{VG}})^{m_{VG}} \right]^2. \quad (2.14)$$

Here, $m_{VG} = 1 - \frac{1}{n_{VG}}$ has been used for the sake of readability.

Kinematic relations Throughout this section we have described the processes that occur in a porous medium related to fluid flow and have presented their description on a macroscopic scale together with the involved macroscopic quantities. For example, in the definitions of the Darcy velocities (2.11) and (2.13) we have introduced the fluid phase velocities \mathbf{v}_β and the solid phase velocity \mathbf{v}_s , with respect to which the fluid flow is described in Darcy's Law. In the remainder of this section, we want to introduce the quantities necessary to describe the individual movement of the phases, following the ideas presented in Ehlers [2002]. To this end, let us consider an arbitrary body \mathcal{B} , representing a porous medium, in some initial state at a time t_0 . We refer to this initial state as the reference configuration of \mathcal{B} and denote with \mathbf{X}_α the corresponding coordinates of the material points \mathcal{P}_α of phase α at the time $t = t_0$. Note that the subscript α stems from the fact that due to the overlapping continua, there exist material points \mathcal{P}_α for all considered phases in each spatial coordinate. Let us now introduce the motion functions χ_α , which map the material points of phase α from the reference configuration to coordinates on the current configuration of \mathcal{B} at time $t > t_0$:

$$\mathbf{x} = \chi_\alpha(\mathbf{X}_\alpha, t). \quad (2.15)$$

Here, \mathbf{x} denotes the coordinates of the material points in the current configuration. An illustration of this is given in Figure 2.4. We further assume that the χ_α at time $t > t_0$

have a unique reference position \mathbf{X} at t_0 , i.e.

$$\det \mathbf{F}_\alpha = \det \left(\frac{\partial \chi_\alpha(\mathbf{X}_\alpha, t)}{\partial \mathbf{X}_\alpha} \right) \neq 0, \quad (2.16)$$

where the deformation gradient $\mathbf{F}_\alpha = \frac{\partial \chi_\alpha}{\partial \mathbf{X}_\alpha}$ has been introduced. The fulfillment of condition (2.16) enables us to define the inverse mapping $\mathbf{X}_\alpha = \chi_\alpha^{-1}(\mathbf{x}_\alpha, t)$ and guarantees that the material points of a phase do not overlap. We can now state the relation of the phase velocities to the respective motion functions:

$$\mathbf{v}_\alpha = \frac{\partial \chi_\alpha(\mathbf{X}_\alpha, t)}{\partial t}. \quad (2.17)$$

Furthermore, we define the displacement of the solid phase:

$$\mathbf{u} = \mathbf{x} - \mathbf{X}_s = \chi_s - \mathbf{X}_s. \quad (2.18)$$

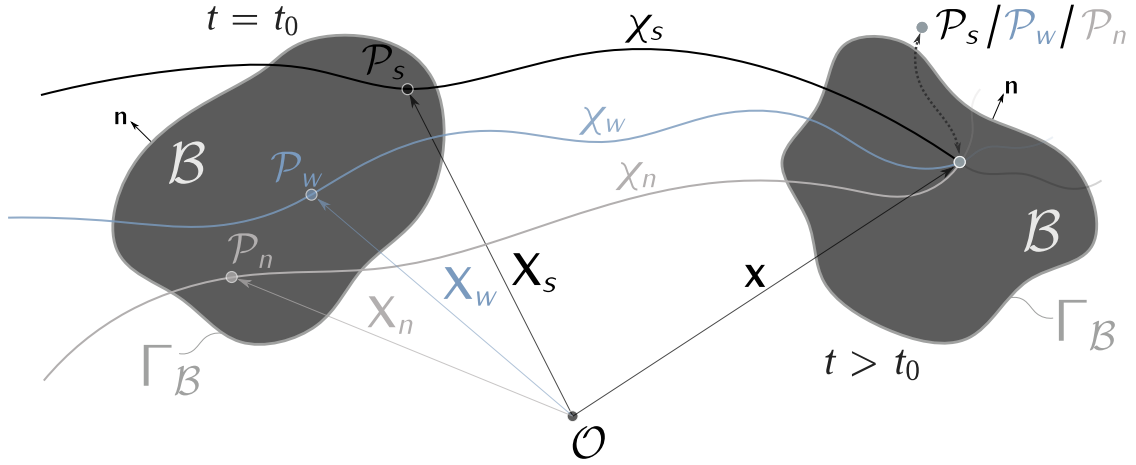


Figure 2.4 – Kinematic relations. Illustration of the individual motion functions χ_α in the presence of a solid phase s and two fluid phases w and n. Shown are the material points \mathcal{P}_α with coordinates \mathbf{x} in the current configuration and the corresponding coordinates \mathbf{X}_α on the reference configuration at $t = t_0$.

2.2 *Rock Mechanics*

It was mentioned in the previous section that the solid skeleton of a porous medium might be subject to transformations due to mechanical deformations. These deformations are strongly coupled with the fluid flow processes occurring within the pore space and vice versa. In this work, we choose a poroelastic description of the mechanical behavior of the porous medium, i.e. we assume the solid skeleton of the porous medium to be composed of a linear elastic material. After a brief classification of different types of rocks encountered in nature, we will introduce the concepts of stress and strain, which are essential for the mathematical description of linear elastic materials. Finally, the concept of poroelasticity is presented at the end of this section.

2.2.1 *Rock as a material*

Typically, it is distinguished between three types of rock that are classified according to the processes involved in their genesis. *Igneous* or *magmatic* rocks form from solidified lava that was transported to the Earth's surface or crust due to volcanic activity. Once at the surface, both chemical and mechanical processes cause the degradation of rock, and the eroded material is transported by winds, rivers, oceans, glaciers, etc., eventually accumulating in sedimentary basins. Continuous deposition in such basins can cause the compaction of the accumulated material and lead to the formation of *Sedimentary rock* [Beck, 2018]. Due to their genesis out of particles and grains of several other rocks, sedimentary rocks typically exhibit significant porosities [Jaeger et al., 2007], while the porosity in magmatic rocks is usually very low. Finally, *Metamorphic rocks* form deep inside the Earth when heat and/or stress causes mineralogical, chemical or textural changes on either sedimentary, magmatic or other metamorphic rocks. Both the mineralogical composition of rocks as well as the processes that were involved in their creation have major impacts on their mechanical properties. In the following sections we will introduce the properties and quantities that are used in this work to describe the mechanical response of rocks to both external forces as well as hydraulic forces exerted on the solid skeleton by the fluid phases within the pore volume.

2.2.2 Stress and strain measures

The mechanical behavior of a material, manifested in a material law, is often described mathematically by relating deformations to the stresses acting on a material. In this section we will present the basic quantities used in this work to quantify both deformations and stresses, on the basis of which we will state the linear elastic material law in the subsequent section.

Strain The strain measures the deformation, i.e. the displacement, between material points on a body relative to a reference distance. With the kinematic relations introduced at the end of Section 2.1, we can state the relationship between the squared length of infinitesimal line elements on the reference and the current configuration within the solid phase:

$$|d\mathbf{x}|^2 = d\mathbf{x}^T d\mathbf{x} = (\mathbf{F}_s d\mathbf{X}_s)^T (\mathbf{F}_s d\mathbf{X}_s) = d\mathbf{X}_s^T (\mathbf{F}_s^T \mathbf{F}_s) d\mathbf{X}_s = d\mathbf{X}_s^T \mathbf{C}_s d\mathbf{X}_s. \quad (2.19)$$

Here, we introduced the right *Cauchy-Green* deformation tensor $\mathbf{C}_s = \mathbf{F}_s^T \mathbf{F}_s$ for the solid phase. Let us now look at the difference of the squared lengths of these line elements:

$$|d\mathbf{x}|^2 - |d\mathbf{X}_s|^2 = d\mathbf{x}^T d\mathbf{x} - d\mathbf{X}_s^T d\mathbf{X}_s = d\mathbf{X}_s^T (\mathbf{C}_s - \mathbf{I}) d\mathbf{X}_s = 2 d\mathbf{X}_s^T \mathbf{E}_s d\mathbf{X}_s. \quad (2.20)$$

Note that in this derivation we have used (2.19) and have introduced the *Green-Lagrangian* strain tensor $\mathbf{E}_s = \frac{1}{2} (\mathbf{C}_s - \mathbf{I})$. Let us now introduce the displacement gradient

$$\mathbf{H}_s = \frac{\partial \mathbf{u}}{\partial \mathbf{X}_s} = \frac{\partial (\mathbf{x}_s - \mathbf{X}_s)}{\partial \mathbf{X}_s} = \mathbf{F}_s - \mathbf{I}, \quad (2.21)$$

for which we can identify its relationship with the *Green-Lagrangian* strain tensor:

$$\begin{aligned}
\mathbf{E}_s &= \frac{1}{2} (\mathbf{C}_s - \mathbf{I}) \\
&= \frac{1}{2} (\mathbf{F}_s^T \mathbf{F}_s - \mathbf{I}) \\
&= \frac{1}{2} \left((\mathbf{I} + \mathbf{H}_s)^T (\mathbf{I} + \mathbf{H}_s) - \mathbf{I} \right) \\
&= \frac{1}{2} (\mathbf{H}_s + \mathbf{H}_s^T + \mathbf{H}_s^T \mathbf{H}_s) \\
&= \frac{1}{2} \left(\frac{\partial \mathbf{u}}{\partial \mathbf{X}_s} + \left(\frac{\partial \mathbf{u}}{\partial \mathbf{X}_s} \right)^T + \left(\frac{\partial \mathbf{u}}{\partial \mathbf{X}_s} \right)^T \frac{\partial \mathbf{u}}{\partial \mathbf{X}_s} \right).
\end{aligned} \tag{2.22}$$

This means the *Green-Lagrangian* strain tensor is a nonlinear function of the displacement. However, a widely used assumption is that the displacements are much smaller than the dimensions of the domain of interest (*infinitesimal strain theory*). The assumption implies that there is little difference between the reference coordinates \mathbf{X}_α and the current coordinates \mathbf{x} of a material point, that is $\mathbf{X}_\alpha \approx \mathbf{x}$. From this follows that $\frac{\partial \mathbf{u}}{\partial \mathbf{X}_s} \approx \frac{\partial \mathbf{u}}{\partial \mathbf{x}} = \nabla \mathbf{u}$, where $\nabla (\cdot)$ is the gradient operator. On the basis of this assumption we linearize (2.22) and drop the quadratic term, which leads us to the definition of the *infinitesimal strain tensor* used in this work:

$$\boldsymbol{\epsilon}_s = \frac{1}{2} (\nabla \mathbf{u} + \nabla^T \mathbf{u}). \tag{2.23}$$

Stress Let us go back to the arbitrary body \mathcal{B} introduced at the end of Section 2.1. Its movement and/or deformation is caused by forces acting on it, for which we can generally distinguish contact forces (per surface area) acting on its surface and body forces (per volume) acting on the volume of \mathcal{B} (e.g. gravity). Let us now consider a subset $\mathcal{K} \subset \mathcal{B}$ with boundary $\Gamma_{\mathcal{K}}$ and outer unit normal vector \mathbf{n} , for which we furthermore require that $\Gamma_{\mathcal{K}} \cap \Gamma_{\mathcal{B}} = \emptyset$, i.e. \mathcal{K} has no direct contact with forces imposed on the boundary of \mathcal{B} . Let us assume \mathcal{B} to be composed of a single solid phase (subscript s). The internal contact force \mathbf{t}_s , acting on the infinitesimal surface element $d\Gamma_{\mathcal{K}}$, represents the force that is exerted on \mathcal{K} by the surrounding material on \mathcal{B} , while \mathbf{b}_s denotes the body force (see Figure 2.5 for an illustration). The internal contact force \mathbf{t}_s depends on the position, the time and also on the normal vector \mathbf{n} of the surface element $d\Gamma_{\mathcal{K}}$, i.e. it depends on how \mathcal{K} is cut out of \mathcal{B} . In order to find a measure that is independent of the orientation, we apply *Cauchy's theorem*, which states that there

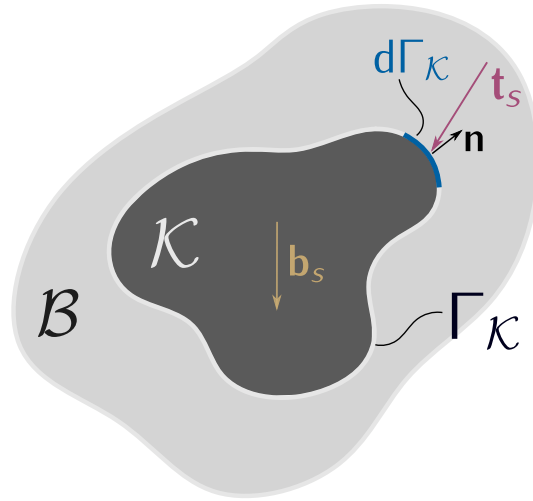


Figure 2.5 – Forces acting on \mathcal{K} . Illustration of the forces acting on a subset $\mathcal{K} \in \mathcal{B}$ of some arbitrary body \mathcal{B} . The subscript s indicates the quantities specific to the solid phase, however, corresponding quantities can be identified for the other phases as well.

exists a tensorial quantity \mathbf{T}_s such that:

$$\mathbf{t}_s(\mathbf{x}, t, \mathbf{n}) = [\mathbf{T}_s(\mathbf{x}, t)] \mathbf{n}. \quad (2.24)$$

The tensor \mathbf{T}_s is called the *Cauchy* stress tensor of the solid phase and is a measure that lives on the current configuration. However, as mentioned earlier, in this work the assumption of small deformations is made. In this case we assume $\mathbf{T}_s \approx \boldsymbol{\sigma}_s$, where $\boldsymbol{\sigma}_s$ is the linear stress tensor (see below). Please note that one can show (using the conservation equation for the angular momentum) that $\boldsymbol{\sigma}_s$ has to be symmetric [Häberle, 2017]. This fact has to be taken into account when deriving thermodynamically consistent material laws.

2.2.3 Linear elasticity

The characteristic behavior of a linear elastic material can be summarized in two phenomena. On one hand, the deformation of a linear elastic body is linearly related to the forces acting on it. Furthermore, when these forces are released, the body deforms back into its original state. A mathematical description of such behavior is attributed to the British physicist Robert Hooke (★July 18th 1635 in Freshwater, UK, †March 3rd 1702 in London) and is consequently often called *Hooke's Law*. In its general form, it

can be stated as follows:

$$\boldsymbol{\sigma}_s = \underline{\underline{\mathbf{C}}} : \boldsymbol{\epsilon}_s, \quad (2.25)$$

where we have used the infinitesimal strain tensor and the linear stress tensor from Section 2.2.2, i.e. we assume small-strain conditions. Furthermore, $\underline{\underline{\mathbf{C}}}$ is the fourth-order elasticity tensor. It has 81 independent entries, however, when applying the above-mentioned constraint on the symmetry of the stress tensor, only 21 remain. Furthermore, we only consider isotropic materials in this work, in which case the number of parameters can be reduced to two and the stress-strain relationship can be stated as follows:

$$\boldsymbol{\sigma}_s = \lambda \text{tr}(\boldsymbol{\epsilon}_s) \mathbf{I} + 2G \boldsymbol{\epsilon}_s, \quad (2.26)$$

with λ and G being the first and second *Lamé* parameters and $\text{tr}(\boldsymbol{\epsilon}_s)$ the trace of the strain tensor $\boldsymbol{\epsilon}_s$. While λ has no obvious physical interpretation, G describes the ratio of shear stress and shear strain. The parameters λ and G are only two of several so-called *elastic moduli*. The linear stress-strain relationship (2.26) can be expressed by means of a pair of any of the elastic moduli, and in the examples presented in Chapter 5 we use *Young's modulus* E and *Poisson's ratio* ν to characterize the stiffness of a material. Young's modulus measures the relationship between uniaxial stress and strain in the direction of the stress, for instance, the elongation of a material under tensile stress. Correspondingly, Poisson's ratio describes the deformation orthogonal to the applied uniaxial stress. Being given two elastic moduli, any other can be calculated, and we use the relationships

$$\lambda = \frac{E\nu}{(1+\nu)(1-2\nu)} \quad (2.27)$$

and

$$G = \frac{E}{2(1+\nu)} \quad (2.28)$$

to determine the Lamé parameters on the basis of Young's modulus E and Poisson's ratio ν .

2.2.4 Poroelasticity

The material law presented in the previous paragraph is only valid for single phase materials, or, for the purely mechanical stresses within the solid matrix of a porous medium. However, the overall stress in the latter also contains contributions from the

mechanical interaction with the pore fluids. In 1925, Karl von Terzaghi postulated that the *effective stress* $\boldsymbol{\sigma}_{\text{eff}}$ acting on the solid skeleton in a porous medium is the total stress reduced by the pore pressure [Terzaghi et al., 1925]:

$$\boldsymbol{\sigma} = \boldsymbol{\sigma}_{\text{eff}} - p\mathbf{I}, \quad (2.29)$$

where the minus sign arises from compressive stresses being indicated as negative. This has been reformulated in 1941 by Maurice Anthony Biot [Biot, 1941] to

$$\boldsymbol{\sigma} = \boldsymbol{\sigma}_{\text{eff}} - \alpha_{\text{B}} p\mathbf{I}, \quad (2.30)$$

where α_{B} is the so-called Biot coefficient. In the context of two-phase flow, we use the concept of the effective pressure (see e.g. Beck [2018], Darcis [2013])

$$p_{\text{eff}} = \sum_{\beta} S_{\beta} p_{\beta}, \quad (2.31)$$

and define the effective stress via

$$\boldsymbol{\sigma} = \boldsymbol{\sigma}_{\text{eff}} - \alpha_{\text{B}} p_{\text{eff}}\mathbf{I}. \quad (2.32)$$

We note that this reduces to (2.30) for the case of a single fluid phase. In this work, we relate the stress acting on the solid skeleton to the displacements via equation (2.26), i.e. it is $\boldsymbol{\sigma}_{\text{eff}} = \boldsymbol{\sigma}_{\text{s}}$.

2.3 Balance equations

Physical systems are often described on the basis of fundamental axioms regarding the conservation of thermodynamic quantities as e.g. the system's mass, momentum or energy. Let us again consider an arbitrary body \mathcal{B} with boundary $\Gamma_{\mathcal{B}}$, representing a physical system, and thereon an arbitrary part $\mathcal{K} \subset \mathcal{B}$ with boundary $\Gamma_{\mathcal{K}}$ and outer unit normal vector \mathbf{n} (see Figure 2.5). We again require that $\Gamma_{\mathcal{K}} \cap \Gamma_{\mathcal{B}} = \emptyset$, i.e. \mathcal{K} has no direct contact with boundary conditions imposed on the system. Let us further consider some scalar extensive thermodynamic property Ψ , for which we state its conservation

equation over \mathcal{K} as follows:

$$\frac{d}{dt} \int_{\mathcal{K}} \psi \, dV = \int_{\Gamma_{\mathcal{K}}} \boldsymbol{\vartheta} \cdot \mathbf{n} \, d\Gamma + \int_{\mathcal{K}} q \, dV. \quad (2.33)$$

Here, we introduced the corresponding intensive, volume-specific thermodynamic property $\psi = \frac{d\Psi}{dV}$. While the left-hand side of the equation represents the amount of Ψ within \mathcal{K} , the right-hand side states the type of processes that can lead to a change of this amount. In accordance to the possible forces acting on the body in Section 2.2.4, here we identify two possible general actions on \mathcal{K} that provoke a change of Ψ : the flux or action $\boldsymbol{\vartheta}$ as an interaction with the surrounding medium (i.e. the remainder of \mathcal{B}) that acts on the surface of \mathcal{K} and q as a source or sink term that acts inside \mathcal{K} . For a vectorial quantity $\boldsymbol{\Psi}$, we can state the conservation equation correspondingly:

$$\frac{d}{dt} \int_{\mathcal{K}} \boldsymbol{\psi} \, dV = \int_{\Gamma_{\mathcal{K}}} \boldsymbol{\Theta} \mathbf{n} \, d\Gamma + \int_{\mathcal{K}} \mathbf{q} \, dV. \quad (2.34)$$

Moreover, during the process to be described, \mathcal{K} might undergo some deformation and/or translation and is thus time-dependent. In the following we will discuss the Lagrangian and the Eulerian approach to deriving a local form of equation (2.33), of which the first is more often used in the context of solid mechanics, whereas the latter is more prominent in the field of fluid mechanics. Note that we restrict the presentation to the case of a scalar quantity, however, for a vectorial quantity the process can be realized analogously. Besides that, we omit phase indices in this section and refer to a single continuum.

Lagrangian approach Given a motion function $\mathbf{x} = \boldsymbol{\chi}(\mathbf{X}, t)$ that describes the trajectories of the material points on \mathcal{B} from a reference to the current configuration (see Figure 2.4), one can show that

$$\frac{d}{dt} \int_{\mathcal{K}} \psi \, dV = \int_{\mathcal{K}} \frac{\partial \psi}{\partial t} \, dV + \int_{\Gamma_{\mathcal{K}}} \psi (\mathbf{v} \cdot \mathbf{n}) \, d\Gamma. \quad (2.35)$$

This equation is known as the Reynolds transport theorem, which states that the temporal change of ψ in the time-dependent region \mathcal{K} has a contribution due to temporal changes in the field itself as well as a contribution due to the change in volume of \mathcal{K} resulting from its dynamic boundary $\Gamma_{\mathcal{K}}$. Insertion of (2.35) into equation (2.33) lets

us state the conservation equation in a Lagrangian perspective:

$$\int_{\mathcal{K}} \frac{\partial \psi}{\partial t} dV + \int_{\Gamma_{\mathcal{K}}} \psi (\mathbf{v} \cdot \mathbf{n}) d\Gamma = \int_{\Gamma_{\mathcal{K}}} \boldsymbol{\vartheta} \cdot \mathbf{n} d\Gamma + \int_{\mathcal{K}} q dV. \quad (2.36)$$

Further utilizing the localization theorem $|\mathcal{K}| \rightarrow 0$ under the assumption that all integrands are sufficiently smooth, we can write the corresponding local form of a general master balance law:

$$\frac{\partial \psi}{\partial t} + \nabla \cdot (\psi \mathbf{v}) = \nabla \cdot \boldsymbol{\vartheta} + q, \quad (2.37)$$

and correspondingly for tensorial quantities:

$$\frac{\partial \boldsymbol{\psi}}{\partial t} + \nabla \cdot (\boldsymbol{\psi} \otimes \mathbf{v}) = \nabla \cdot \boldsymbol{\Theta} + \mathbf{q}, \quad (2.38)$$

Eulerian approach Another approach, mostly used in the field of fluid mechanics, is the choice of a static, time-independent region $\mathcal{CV} \subset \mathcal{K}$, also called control volume, over which the conservation equation is enforced:

$$\frac{d}{dt} \int_{\mathcal{CV}} \psi dV = \int_{\Gamma_{\mathcal{CV}}} \boldsymbol{\vartheta}^e \cdot \mathbf{n} d\Gamma + \int_{\mathcal{CV}} q dV. \quad (2.39)$$

Note that since in this approach the boundary of the integration domain does not coincide with the boundaries of \mathcal{K} , we introduced the flux $\boldsymbol{\vartheta}^e$ to distinguish it from the one introduced in (2.33). In the case of a static control volume the equality

$$\frac{d}{dt} \int_{\mathcal{CV}} \psi dV = \int_{\mathcal{CV}} \frac{\partial \psi}{\partial t} dV \quad (2.40)$$

holds, and after insertion into (2.39) and again utilizing the localization theorem, we obtain:

$$\frac{\partial \psi}{\partial t} = \nabla \cdot \boldsymbol{\vartheta}^e + q. \quad (2.41)$$

Since, after localization, the resulting local partial differential equations must be the same, we can find the relation between $\boldsymbol{\vartheta}$ and $\boldsymbol{\vartheta}^e$ by comparison of (2.41) and (2.37):

$$\boldsymbol{\vartheta}^e = \boldsymbol{\vartheta} - \psi \mathbf{v}. \quad (2.42)$$

Thus, when balancing over a static control volume, one has to take into account the transport of Ψ across its boundaries due to the movement of \mathcal{K} .

2.3.1 Mass balance equations

The fundamental axiom of mass conservation says that mass can neither be created nor destroyed. On the basis of this axiom we want to derive the mass balance equations for the constituents in a porous medium, which in this work comprise a single solid phase and one or two fluid phases. Furthermore, we assume immiscibility between the phases such that we can formulate the mass balance equations for each phase without accounting for mass exchange between the phases. Resuming to the notion of the body \mathcal{B} and subset $\mathcal{K} \subset \mathcal{B}$, we can state the mass of a phase α contained in \mathcal{K} as

$$m_\alpha = \int_{\mathcal{K}} n_\alpha \rho_\alpha \, dV. \quad (2.43)$$

After comparison with (2.33) we identify $\psi = n_\alpha \rho_\alpha$. Furthermore, we have used the domain of consideration \mathcal{K} as integration domain, i.e. it follows the motion of phase α . For this reason we set $\vartheta = 0$, which means that we do not consider any mass transfer of phase α between \mathcal{K} and the surrounding material on \mathcal{B} . As a side remark, when balancing the mass of a dissolved component, one could substitute ϑ by a model for diffusive transport which accounts for mass transfer relative to the motion of \mathcal{K} . The resulting local form of the mass balance reads:

$$\frac{\partial (n_\alpha \rho_\alpha)}{\partial t} + \nabla \cdot (n_\alpha \rho_\alpha \mathbf{v}_\alpha) = q_\alpha. \quad (2.44)$$

The source term on the right-hand side of the above equation seems contradictory to the axiom that mass cannot be created or destroyed at first. But, in the context of e.g. geological porous media, the source term can be used to describe an injection of mass by an injection well whose geometry is not taken into account in the definition of the body \mathcal{B} .

Solid matrix The volume fraction of solid can be written in terms of the porosity of the porous medium, i.e. $n_s = 1 - \phi$. We furthermore assume incompressible solid grains ($\rho_s = \text{const}$) and that there is no source of solid material ($q_s = 0$). Under these assumptions the mass balance equation (2.44), for the solid matrix, turns into an

evolution equation for the porosity:

$$\frac{\partial \phi}{\partial t} = \nabla \cdot ((1 - \phi) \mathbf{v}_s). \quad (2.45)$$

Fluid phases For the fluid phases β , we reformulate the mass balance equation (2.44) using the relations (2.5) and (2.13):

$$\frac{\partial (\phi \rho_\beta S_\beta)}{\partial t} + \nabla \cdot (\rho_\beta \mathbf{q}_\beta + \phi \rho_\beta S_\beta \mathbf{v}_s) = q_\beta. \quad (2.46)$$

However, in this work we neglect the advective transport component with the velocity of the solid. This leads us to the form of the fluid mass balance equation used in this work:

$$\frac{\partial (\phi \rho_\beta S_\beta)}{\partial t} + \nabla \cdot (\rho_\beta \mathbf{q}_\beta) = q_\beta. \quad (2.47)$$

2.3.2 Momentum balance equations

Newton's second law states a relationship between an object's mass m , its acceleration \mathbf{a} and the sum of forces acting on it:

$$\mathbf{f} = m\mathbf{a}. \quad (2.48)$$

This can be rewritten into a conservation equation for the momentum $\mathbf{p} = m\mathbf{v}$:

$$\frac{d\mathbf{p}}{dt} = \mathbf{f}, \quad (2.49)$$

which states that a change in momentum of an object can only be caused by forces acting on it. It should be mentioned that *Darcy's Law* in the form of (2.10) and (2.12) can be derived from the momentum balance equation under the assumption of creeping flow and immiscibility between the fluid phases and the solid [Häberle, 2017]. As we have seen in the presentation of the mass balance equations for the fluid phases (2.47), in this work we use *Darcy's Law* as a constitutive relationship and omit the presentation of the fluid phase momentum balance equations at this point. Instead, we want to formulate the momentum balance equation for the porous medium, i.e. the overall aggregate, for which we will use the subscript "b". Let us again consider the

body \mathcal{B} with $\mathcal{K} \subset \mathcal{B}$, for which we write the momentum of the aggregate as

$$\mathbf{p}_b = \int_{\mathcal{K}} \rho_b \mathbf{v}_b dV, \quad (2.50)$$

where we have introduced the density of the aggregate $\rho_b = \sum_{\alpha} n_{\alpha} \rho_{\alpha}$ and its velocity $\mathbf{v}_b = \frac{1}{\rho_b} \sum_{\alpha} n_{\alpha} \rho_{\alpha} \mathbf{v}_{\alpha}$. From a comparison of (2.49) with (2.38) we see that in this case $\boldsymbol{\psi} = \rho_b \mathbf{v}_b$, and we furthermore set $\boldsymbol{\Theta} = \mathbf{T}_b$ and $\mathbf{q} = \rho_b \mathbf{g}$, i.e. the stress acts on the surface of \mathcal{K} and gravity as a body force inside it. This leads to the local form of the momentum balance equation:

$$\frac{\partial (\rho_b \mathbf{v}_b)}{\partial t} + \nabla \cdot (\rho_b \mathbf{v}_b \otimes \mathbf{v}_b) = \nabla \cdot \mathbf{T}_b + \rho_b \mathbf{g}, \quad (2.51)$$

where the left-hand side of this equation can be expanded to

$$\begin{aligned} & \frac{\partial (\rho_b \mathbf{v}_b)}{\partial t} + \nabla \cdot (\rho_b \mathbf{v}_b \otimes \mathbf{v}_b) \\ &= \rho_b \frac{\partial \mathbf{v}_b}{\partial t} + \rho_b \mathbf{v}_b^T \nabla \mathbf{v}_b + \mathbf{v}_b \left(\frac{\partial \rho_b}{\partial t} + \nabla \cdot (\rho_b \mathbf{v}_b) \right). \end{aligned} \quad (2.52)$$

In this equation, considering the above-mentioned definitions of \mathbf{v}_b and ρ_b , we recognize the mass balance equation of the overall aggregate in the last term in brackets, i.e. the sum of (2.44) over all phases. This allows us to reformulate the momentum balance equation to:

$$\rho_b \dot{\mathbf{v}}_b = \nabla \cdot \mathbf{T}_b + \rho_b \mathbf{g} - \mathbf{v}_b \sum_{\alpha} q_{\alpha}^m, \quad (2.53)$$

where we have used the notation $\dot{\mathbf{v}}_b$ for the material or total time derivative of the velocity of the aggregate, that is $\dot{\mathbf{v}}_b = \frac{d\mathbf{v}_b}{dt} = \frac{\partial \mathbf{v}_b}{\partial t} + \mathbf{v}_b^T \nabla \mathbf{v}_b$. The last term on the right-hand side of the equation (2.53) accounts for the change in momentum due to sources or sinks of mass. We assume this contribution to be negligible in comparison to the stresses and gravitational forces. Furthermore, we assume quasi-static conditions, i.e. we neglect the acceleration term ($\rho_b \dot{\mathbf{v}}_b \approx 0$), we use $\mathbf{T}_b = \boldsymbol{\sigma}$ (see equation (2.32)) and insert the definition of ρ_b to arrive at the formulation used in this work:

$$0 = \nabla \cdot (\boldsymbol{\sigma}_s - \alpha_B p_{\text{eff}} \mathbf{I}) + \left((1 - \phi) \rho_s + \phi \sum_{\beta} S_{\beta} \rho_{\beta} \right) \mathbf{g}. \quad (2.54)$$

Note that here the subscript β again refers to the fluid phases.

3 *Mathematical models for flow and deformation in fractured porous media*

This chapter is devoted to extending the concepts of the previous chapter to fractured porous media. To this end, we will first give an overview over different types of fractures encountered in nature, and discuss the processes that lead to their creation in Section 3.1. After that, in Section 3.2, we will present the mathematical model used in this work for the description of flow in fractured porous media, before we extend it to the case of deformable fractured poroelastic media in Section 3.3.

3.1 *Fracture geology*

Most rocks exhibit fractures on a variety of scales, possibly ranging from microscopic to continental [National Research Council and others, 1996]. Fractures are mechanical breaks in rocks that are created in response to lithostatic, tectonic or thermal stresses, or due to high fluid pressures within the pore space. They are typically classified into *joints* and *faults*, where the first class of fractures is characterized by a discontinuity in normal displacement but little to no transversal displacement, that is, the fracture surfaces have moved away from each other. The space between the fracture surfaces can be "open" and therefore might provide channels for rapid fluid flow and transport [Jaeger et al., 2007]. On the other hand, they might also be filled with minerals that precipitated from the fluids flowing in the fractures, in which case they are usually referred to as *veins* [National Research Council and others, 1996]. The hydraulic properties of *veins* can be substantially different to open fractures, in fact, they can range from channels for fluid flow to such acting as hydraulic barriers. *Faults* are characterized by significant relative shear displacement, and can occur in large numbers within so-called *fault zones*.

Since the fracture surfaces are typically rough, the shear displacement might cause the abrasion of material, for which reason faults are often filled with matter to some extent. Apart from that, mineral precipitation from fluids can also take place in faults, forming the above-mentioned *veins*.

Matthai et al. [2007] estimate that in-situ fracture apertures in rocks are likely to range between 5 mm and 1 cm, which is very small in comparison to the domain sizes of interest in many geological applications. Nevertheless, the presence of fractures might substantially affect the hydraulic behavior of rock due to the large contrast in hydraulic properties in comparison with the surrounding rock matrix. Furthermore, fractures provide surfaces along which sliding can occur, and thus, the mechanical behavior of rock might also be significantly altered by the presence of fractures.

3.2 Modeling flow in fractured porous media

Many approaches to the numerical modeling of flow in fractured porous media have been developed, which, as mentioned in the introduction of this document, can generally be classified into *continuum fracture models* and *discrete fracture models*. For the first class of models, early works presented the concept of Dual-continuum models [Warren and Root, 1963, Kazemi et al., 1976], in which the fractures are not resolved geometrically but are accounted for by a second overlapping continuum with transfer functions describing the mutual interactions. This approach is widely used in the literature and many works focus on deriving improved transfer functions (see e.g. Zimmerman et al. [1993, 1996], Penuela et al. [2002]). Dual-continuum models can be further sub-classified into models that take into account storage and transport capacity in both continua, or neglect any of these processes in one of them. Moreover, this class of models has been extended to account for multiple continua [Pruess, 1992, Tatomir, 2013]. Apart from that, *effective continuum models* have been developed, e.g. in Pruess et al. [1990]. In such models, a fractured porous medium is modeled as a single continuum, but with effective properties that are derived taking into account the individual material properties (i.e. capillary pressure and relative permeability-saturation relationships) of both fractures and matrix. For example, Matthai et al. [2007] numerically derive such effective properties for a number of different fracture networks. The model they use to compute the effective properties falls into the class of *discrete fracture models*, in which

the larger fractures are captured explicitly as heterogeneities within the computational domain. The model presented in this work also falls into the class of *discrete fracture models* and will be presented in detail in the following sections.

As we have seen in Section 3.1, fractures can occur on many different scales and in a variety of different shapes. Most importantly, they range from being open channels for flow to highly sealed barriers that force the fluid to flow around them. In this work, we assume that the very small fractures that are much smaller than the domain size of interest can be upscaled and the effects of their presence can be accounted for in macroscopic quantities such as the permeability tensor \mathbf{K} or the residual saturations $S_{\alpha,r}$. In contrast to that, we want to explicitly capture the large fractures whose extensions are in the order of the size of the domain. For this, a favorable characteristic of fractures is that they are usually very "thin", which means that they exhibit a direction in which they are much less extended than in the other two space directions. Nevertheless, they often significantly influence the hydraulic behavior of rock, as the hydraulic conductivity in the fractures may differ substantially from that of the surrounding porous medium.

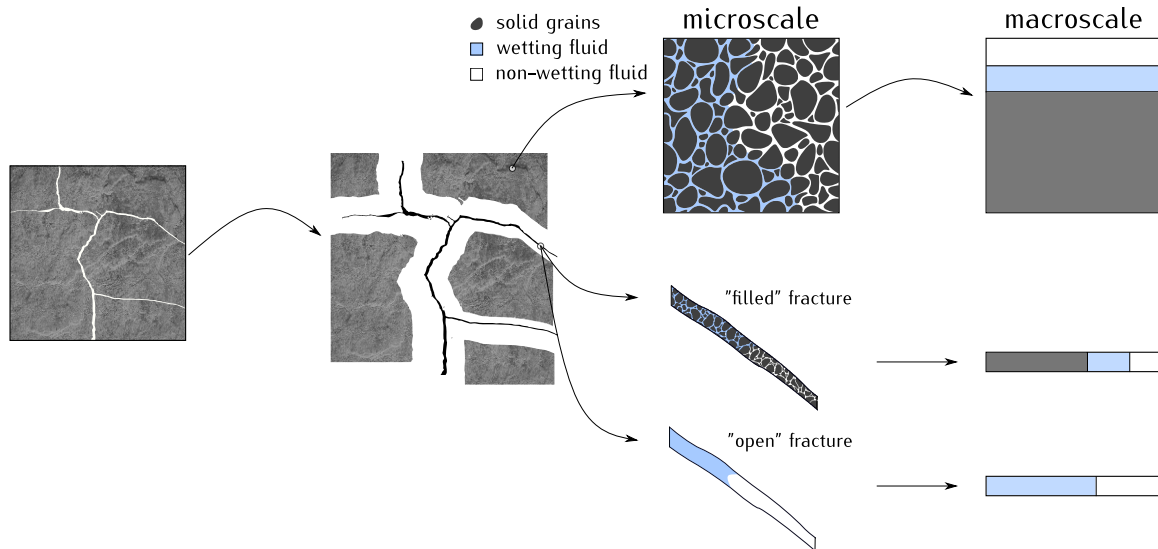


Figure 3.1 – Model concept for flow in fractured porous media. The fracture network splits the domain into separate blocks, each of which is described as a porous medium. Between these blocks, the flow through the fracture network is described on a separate, lower-dimensional continuum. Adequate interface conditions are required that describe the interaction between the network and the surrounding porous medium.

Due to the thin nature of fractures, a very common approach is the treatment of fractures as geometrical objects of co-dimension one with a dimension-reduced system of equations describing the flow along them. Such approaches have been reported, among many others, in Martin et al. [2005], Frih et al. [2012], Sandve et al. [2012], Antonietti et al. [2016], Ahmed et al. [2015, 2017], Nordbotten et al. [2019], Keilegavlen et al. [2017] for single-phase flow and in Reichenberger et al. [2006], Jaffré et al. [2011], Fumagalli and Scotti [2013], Brenner et al. [2014], Tene et al. [2017] for two-phase flow in fractured porous media. Figure 3.1 depicts the basic idea behind the models presented in this work. The large-scale fractures effectively split the domain into separate sub-domains, each of which is described as a porous medium following the ideas presented in Section 2.1. Between these sub-domains, the flow through the fracture network is described on a separate, lower-dimensional continuum. Thus, the fractures are treated as interfaces and adequate interface conditions need to be derived that describe the interaction between the fractures and the surrounding porous medium. In a first step we want to state the equi-dimensional formulation of the problem, in which we see the fractures as heterogeneities with varying parameters but assume that the mass balance in the fractures can be expressed with an equation of the form (2.47), which was derived for a porous medium. In the case of the fractures being filled with matter, one can argue that the fractures themselves behave like a porous medium. The case of open fractures will be discussed in Section 3.2.3. In Section 3.2.2, we state the mixed-dimensional flow problem that is used in this work. The notation follows some of the ideas presented in Berre et al. [2018], Nordbotten et al. [2019], where mixed-dimensional formulations for single-phase flow in fractured porous media are presented.

3.2.1 *Equi-dimensional model*

Let us consider a domain $\Omega \subset \mathbb{R}^3$ with boundary $\partial\Omega$. Furthermore, let Ω_b , Ω_f , Ω_{is} and Ω_j be disjoint partitions of Ω representing the bulk porous medium, the fractures, the intersections of fractures and the intersections of intersections, respectively. For the sake of readability, we will use the term junctions to refer to the intersections of intersections. The external subdomain boundaries are denoted with $\Gamma_b := \partial\Omega_b \cap \partial\Omega$, $\Gamma_f := \partial\Omega_f \cap \partial\Omega$ and $\Gamma_{is} := \partial\Omega_{is} \cap \partial\Omega$. For simplicity, we assume that junctions do not occur on the boundary of Ω , i.e. it is $\Gamma_j = \emptyset$. The interfaces between subdomains are defined as $\gamma_{k,l} = \partial\Omega_k \cap \partial\Omega_l$, where $k \neq l$ and $k, l \in \{b, f, is, j\}$. We furthermore define

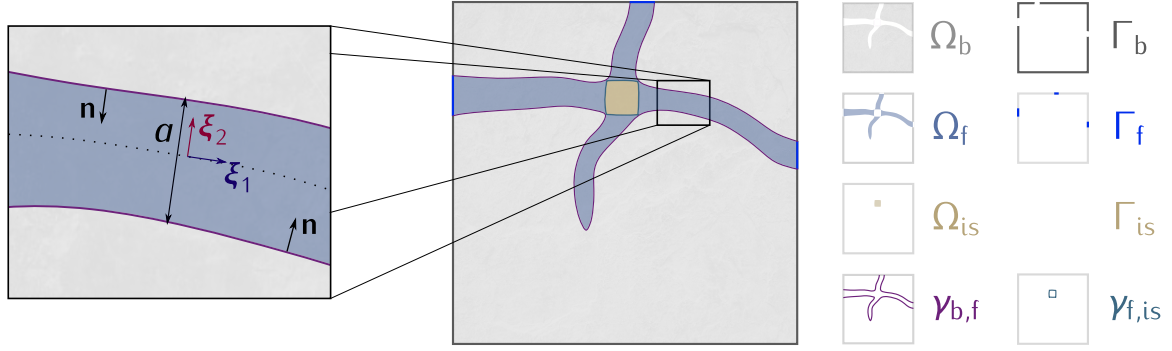


Figure 3.2 – Equi-dimensional domain decomposition. The domain Ω is decomposed into the disjoint partitions Ω_f for the fractures, Ω_{is} for the fracture intersections and Ω_b for the surrounding bulk porous medium. The interfaces between the domains are denoted with γ_f and γ_{is} while the external boundaries of the sub-domains are denoted with Γ_b , Γ_f and Γ_{is} , respectively. Furthermore, the close-up on the left side illustrates the fracture aperture a as well as the basis vectors ξ_1 and ξ_2 of the local coordinate system in the fracture. In a two-dimensional setting, junctions of fracture intersections do not occur and are not visualized here. Please also note that the thickness of the fractures is exaggerated in this figure for illustrative purposes.

the normal vectors on the interfaces $\gamma_{k,l}$ to be pointing outwards of the domains Ω_k . A two-dimensional illustration of this decomposition is depicted in Figure 3.2.

Let us further decompose the external sub-domain boundaries $\Gamma_b = \Gamma_b^D \cup \Gamma_b^N$, $\Gamma_f = \Gamma_f^D \cup \Gamma_f^N$ and $\Gamma_{is} = \Gamma_{is}^D \cup \Gamma_{is}^N$ to indicate whether Dirichlet (superscript D) or Neumann (superscript N) boundary conditions are imposed. We require $|\Gamma_l^D| > 0$ for at least one subdomain $l \in \{b, f, is\}$. The subdivision of the domain as described above and illustrated in Figure 3.2 might lead to the subdomains being disconnected sets. For instance, in the situation illustrated in Figure 3.2, the bulk domain is partitioned into three and the fracture domain into four subsets, which are themselves connected. We make this apparent in the notation by equipping the subdomains with the superscript i indicating the index within the partition of a subdomain, i.e. it is $\Omega_k = \bigcup_{i \in I_k} \Omega_k^i$, where $I_k = \{0, 1, \dots, n_{\Omega_k}\}$ and $k \in \{b, f, is, j\}$. Consequently, let us introduce the interfaces between subsets $\gamma_{k,l}^{i,j} = \partial\Omega_k^i \cap \partial\Omega_l^j$, $k \neq l$, $i \in I_k$ and $j \in I_l$, where we note that $\gamma_{k,l} = \bigcup_{\substack{i \in I_k \\ j \in I_l}} \gamma_{k,l}^{i,j}$. On this setting, we derive the equi-dimensional formulation for two-phase flow by enforcing the mass balance equations (2.47) within each subdomain

Ω_k^i , $i \in I_k$ and $k \in \{\text{b, f, is, j}\}$:

$$\mathbf{q}_{\beta,k}^i + \frac{K_{\text{r}\beta,k}^i}{\mu_\beta} \mathbf{K}_k^i (\nabla p_{\beta,k}^i - \rho_\beta \mathbf{g}) = 0, \quad (3.1a)$$

$$\frac{\partial (\phi_k^i \rho_\beta S_{\beta,k}^i)}{\partial t} + \nabla \cdot (\rho_\beta \mathbf{q}_{\beta,k}^i) = q_{\beta,k}^i, \quad \text{in } \Omega_k^i, \quad (3.1b)$$

$$p_{\text{w},k}^i = p_{\text{w},k}^{\text{D}}, \quad (3.1c)$$

$$S_{\text{n},k}^i = S_{\text{n},k}^{\text{D}}, \quad \text{on } \Gamma_k^{\text{D}} \cap \partial \Omega_k^i, \quad (3.1d)$$

$$\rho_\beta (\mathbf{q}_{\beta,k}^i \cdot \mathbf{n}) = f_{\beta,k}^i, \quad \text{on } \Gamma_k^{\text{N}} \cap \partial \Omega_k^i, \quad (3.1e)$$

$$p_{\beta,k}^i = p_{\beta,l}^j, \quad (3.1f)$$

$$\mathbf{q}_{\beta,k}^i \cdot \mathbf{n} = \mathbf{q}_{\beta,l}^j \cdot \mathbf{n}, \quad \text{on } \gamma_{k,l}^{i,j}, \quad (3.1g)$$

where $l \in \{\text{b, f, is, j}\}$ and $j \in I_l$. Note that $\beta \in \{\text{w, n}\}$ i.e. the equations must hold for both the wetting and the non-wetting phase in all subdomains. Even though the numerical schemes used in this work to discretize the equations (3.1a) are based on the primal formulation (see Section 4.1), the problem is presented here in its mixed form for the sake of readability. We have added the subscript k and superscript i to data, fluxes and unknowns to indicate that they might vary among the subdomains Ω_k^i , $k \in \{\text{b, f, is, j}\}$, $i \in I_k$, on which they live on. Equation (3.1a) states that *Darcy's Law* is valid in the entire partition and (3.1b) is the corresponding mass balance equation. The equations (3.1c)-(3.1e) are the Dirichlet and Neumann boundary conditions on the external subdomain boundaries and (3.1f) - (3.1g) define the interface conditions, which consist of pressure and flux continuity for both phases over the interfaces between two subdomains. Note that in this work we assume the fluid densities to be either constant or functions of pressure, thus the density is continuous on the interfaces between subdomains, due to (3.1f). This means that (3.1g) implicitly enforces mass conservation across the interface. We choose the wetting phase pressures $p_{\text{w},k}^i$ and the non-wetting phase saturation $S_{\text{n},k}^i$ as primary variables and close the system with the closure relationship (2.4) for the saturations and the definition of the capillary pressure (2.7). The formulation is completed by stating the initial conditions

$$p_{\text{w},k}^i = p_{\text{w},k}^{0,i}, \quad \text{for } t = t_0, \quad (3.2a)$$

$$S_{\text{n},k}^i = S_{\text{n},k}^{0,i}, \quad \text{for } t = t_0, \quad (3.2b)$$

for $i \in I_k$ and $k \in \{\text{b, f, is}\}$.

3.2.2 Mixed-dimensional model

We now want to approximate the subdomains of the equi-dimensional setting for the fractures, fracture intersections and junctions of intersections, i.e. Ω_f , Ω_{is} and Ω_j , by lower-dimensional geometries. More precisely, the fractures are approximated by 2-dimensional entities that are constructed such that they follow the planes that describe the center of the fractures. Correspondingly, the intersections of fractures are approximated by 1-dimensional segments that describe center lines of the intersection regions between fractures and the junctions are approximated by 0-dimensional points located at their center. In this mixed-dimensional setting, we will from now on refer to the sub-domains with the subscript d indicating the dimension, i.e. the original domain Ω is split into a 3-dimensional bulk domain Ω_3 , as well as the lower-dimensional domains Ω_2 , Ω_1 and Ω_0 for the fractures, their intersections and junctions of intersections, respectively.

A first simplification with respect to the equi-dimensional setting is that we only consider interfaces between subdomains of codimension one, which we denote by $\gamma_d = \partial\Omega_{d+1} \cap \Omega_d$, $0 \leq d < 3$, i.e. γ_2 , γ_1 and γ_0 denote the interface between the bulk domain and the fractures, the interface between the fractures and their intersections and the interface between intersections and junctions. The normal vectors are defined such that they point outwards of the higher-dimensional domains. The external boundaries of the subdomains are denoted with $\Gamma_d = \partial\Omega_d \cap \partial\Omega$, where we note that $\partial\Omega_0 = \Gamma_0 = \emptyset$.

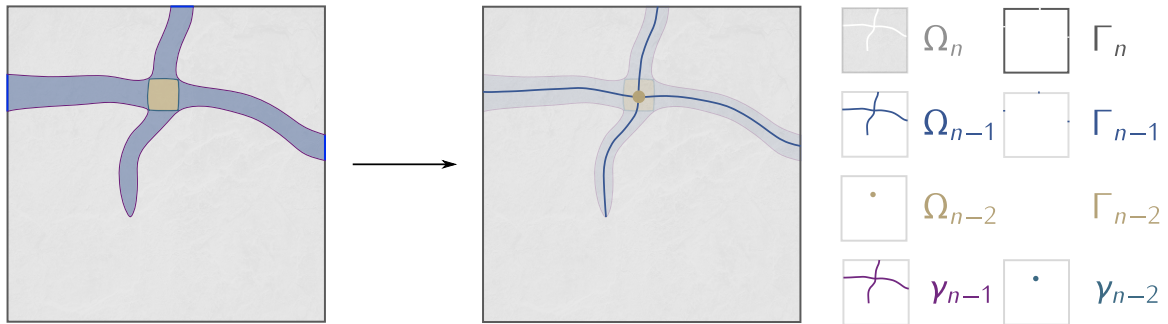


Figure 3.3 – Mixed-dimensional domain decomposition. The n -dimensional domain Ω is decomposed into the n -dimensional subdomain Ω_n for the bulk porous medium and the lower-dimensional subdomains Ω_{n-1} for the fractures and Ω_{n-2} for the intersections of fractures. The interfaces between d - and $(d - 1)$ -dimensional subdomains are denoted with γ_{d-1} , while the external boundaries of the sub-domains are denoted with Γ_d , with d again indicating the dimension of the subdomain. Note that in two-dimensional settings, junctions of intersections do not occur which is why they are not visualized here.

A two-dimensional illustration of this decomposition of Ω is given in Figure 3.3. Please note that in this mixed-dimensional setting, there can also occur immersed boundaries $\hat{\Gamma}_2 = \partial\Omega_2 \setminus \Gamma_2$ and $\hat{\Gamma}_1 = \partial\Omega_1 \setminus \Gamma_1$, and we extend the notation to the highest-dimensional domain by defining $\hat{\Gamma}_3 = \emptyset$.

As for the equi-dimensional case, the subdomains Ω_d might be disconnected sets. We denote with Ω_d^i , $i \in I_d$, a connected subset of a subdomain Ω_d and by $\gamma_d^{ij} = \partial\Omega_{d+1}^i \cap \Omega_d^j$, $i \in I_{d+1}$, $j \in I_d$, an interface between two such subsets. Let us furthermore introduce for each Ω_d^i , $0 \leq d \leq 3$, the set of neighbors on the subdomain Ω_{d+1} , $\mathcal{N}_d^{i,\uparrow}$, and the set of neighbors on Ω_{d-1} , $\mathcal{N}_d^{i,\downarrow}$. These are given by

$$\mathcal{N}_d^{i,\uparrow} = \{\Omega_{d+1}^j, j \in I_{d+1} : \gamma_d^{ji} \neq \emptyset\}, \quad (3.3a)$$

$$\mathcal{N}_d^{i,\downarrow} = \{\Omega_{d-1}^j, j \in I_{d-1} : \gamma_d^{ij} \neq \emptyset\}, \quad (3.3b)$$

where we note that $\mathcal{N}_3^{i,\uparrow} = \emptyset$ and $\mathcal{N}_0^{i,\downarrow} = \emptyset$.

Following the illustration given in Figure 3.2, we denote by $\boldsymbol{\xi}_d = (\boldsymbol{\xi}_{d,1}^i, \boldsymbol{\xi}_{d,2}^i, \boldsymbol{\xi}_{d,3}^i)$ an orthonormal basis of the local coordinate system that can be defined in each point on the lower-dimensional domains, i.e. for all $\mathbf{x} \in \Omega_d^i$, $0 \leq d < 3$. These basis vectors are constructed such that $\boldsymbol{\xi}_{d,k}^i$, for $1 < k \leq d$, are parallel to Ω_d^i in \mathbf{x} , while $\boldsymbol{\xi}_{d,l}^i$, for $d < l \leq 3$, are normal to it. This means that for the lower-dimensional fracture domain, $\boldsymbol{\xi}_{2,3}^i$ is a normal vector on Ω_2^i , while the vectors $\boldsymbol{\xi}_{1,2}^i$ and $\boldsymbol{\xi}_{1,3}^i$ are two vectors normal to Ω_1^i , i.e. to the one-dimensional approximation of a fracture intersection. The basis vectors normal to the lower-dimensional domains are in turn bases for cross-sections of the original equi-dimensional domains Ω_f^i and Ω_{is}^i . Let us denote these cross-sections with $\epsilon_d^i = \epsilon_d^i(\mathbf{x})$, where we notice that $|\epsilon_2^i|$ is the aperture $a^i \geq 0$ in [m] of a fracture, and $|\epsilon_1^i|$ is the cross-sectional area of an intersection of fractures in [m²]. For the sake of compatibility in the notation, we also introduce the non-dimensional measure $|\epsilon_3^i|^i = 1$.

Integrated balance equations In order to arrive at a lower-dimensional description of the flow processes on the domains Ω_2 and Ω_1 , we need to integrate the mass balance equations (3.1b) and *Darcy's Law* (3.1a) over the cross-sections ϵ_2^i and ϵ_1^i , i.e. along the dimensions that were reduced in order to construct the sub-domains Ω_2 and Ω_1 . First, let us split the permeability tensors of the equi-dimensional domains \mathbf{K}_k^i , $k \in \{f, \text{is}\}$, $i \in I_k$, into parts that are tangential (denoted with $\mathbf{K}_k^{i,\parallel}$) and normal (denoted with

$\mathbf{K}_k^{i,\perp}$) to their lower-dimensional counterparts Ω_d^i , $d \in \{1, 2\}$:

$$\mathbf{K}_k^i = \mathbf{K}_k^{i,\parallel} + \mathbf{K}_k^{i,\perp}. \quad (3.4)$$

Recalling the construction of the local basis vectors $\boldsymbol{\xi}_{d,l}^i$ on Ω_d^i , we find the following relations:

$$\mathbf{K}_k^{i,\perp} \boldsymbol{\xi}_{d,l}^i = 0, \quad \text{for } 1 < l \leq d, \quad (3.5a)$$

$$\mathbf{K}_k^{i,\parallel} \boldsymbol{\xi}_{d,l}^i = 0, \quad \text{for } d < l \leq 3. \quad (3.5b)$$

Analogously, we split the Darcy fluxes

$$\mathbf{q}_{\beta,k}^i = \mathbf{q}_{\beta,k}^{i,\parallel} + \mathbf{q}_{\beta,k}^{i,\perp}, \quad (3.6)$$

and define the tangential and normal contributions to be:

$$\mathbf{q}_{\beta,k}^{i,\parallel} = -\frac{\kappa_{r\beta,k}^i}{\mu_\beta} \mathbf{K}_k^{i,\parallel} \left(\nabla_d^{i,\parallel} p_{\beta,k}^i - \rho_\beta \mathbf{g} \right), \quad (3.7a)$$

$$\mathbf{q}_{\beta,k}^{i,\perp} = -\frac{\kappa_{r\beta,k}^i}{\mu_\beta} \mathbf{K}_k^{i,\perp} \left(\nabla_d^{i,\perp} p_{\beta,k}^i - \rho_\beta \mathbf{g} \right). \quad (3.7b)$$

Here, we have introduced the gradient operators $\nabla_d^{i,\parallel}$ and $\nabla_d^{i,\perp}$ in tangential and normal direction with respect to Ω_d^i . With the corresponding tangential and normal divergence operators $\nabla_d^{i,\parallel} \cdot$ and $\nabla_d^{i,\perp} \cdot$ we can reformulate (3.1b) to

$$\frac{\partial (\phi_k^i \rho_\beta S_{\beta,k}^i)}{\partial t} + \nabla_d^{i,\parallel} \cdot (\rho_\beta \mathbf{q}_{\beta,k}^{i,\parallel}) + \nabla_d^{i,\perp} \cdot (\rho_\beta \mathbf{q}_{\beta,k}^{i,\perp}) = q_{\beta,k}^i. \quad (3.8)$$

Let us now introduce cross-section averaged variables, e.g. for the fluid phase pressure:

$$p_{\beta,d}^i = \frac{1}{|\epsilon_d^i|} \int_{\epsilon_d^i} p_{\beta,k}^i \, dx, \quad (3.9)$$

where $p_{\beta,k}^i$ refers to the equi-dimensional pressure in the fracture or intersection of fractures (see Section 3.2.1). Using the same averaging procedure, we can further define the average saturations $S_{\beta,d}^i$, porosity ϕ_d^i and sources $q_{\beta,d}^i$. Another simplification that we make at this point is that we define the fluid density ρ_β and viscosity μ_β to be functions of the cross-section averaged pressure (in case they are not taken as constant)

such that these quantities are now invariant over ϵ_d^i . Correspondingly, we define the relative permeability $\kappa_{r\beta,k}^i = \kappa_{r\beta,k}^i(S_{w,k}^i)$ on a lower-dimensional domain to be expressed in terms of the cross-section averaged wetting phase saturation, and we make this apparent in the notation again by using the subscript d related to the dimension, i.e. $\kappa_{r\beta,d}^i = \kappa_{r\beta,d}^i(S_{w,d}^i)$. On the basis of these assumptions we can define the average of the tangential fluxes (3.7a):

$$\begin{aligned}
 \mathbf{q}_{\beta,d}^i &= \frac{1}{|\epsilon_d^i|} \int_{\epsilon_d^i} \mathbf{q}_{\beta,k}^{i,\parallel} dx \\
 &= \frac{1}{|\epsilon_d^i|} \int_{\epsilon_d^i} -\frac{\kappa_{r\beta,k}^i}{\mu_\beta} \mathbf{K}_k^{i,\parallel} \left(\nabla_d^{i,\parallel} p_{\beta,k}^i - \rho_\beta \mathbf{g} \right) dx \\
 &\approx -\frac{\kappa_{r\beta,d}^i}{\mu_\beta} \mathbf{K}_k^{i,\parallel} \left(\nabla_d^{i,\parallel} \left[\frac{1}{|\epsilon_d^i|} \int_{\epsilon_d^i} p_{\beta,k}^i dx \right] - \rho_\beta \mathbf{g} \right) \\
 &= -\frac{\kappa_{r\beta,d}^i}{\mu_\beta} \mathbf{K}_k^{i,\parallel} \left(\nabla_d^{i,\parallel} p_{\beta,d}^i - \rho_\beta \mathbf{g} \right).
 \end{aligned} \tag{3.10}$$

Here we have used the definition of the cross-section averaged pressure (3.9) and have assumed that $\mathbf{K}_k^{i,\parallel}$ is constant over ϵ_d^i . We furthermore assume $\mathbf{K}_k^{i,\perp}$ to be invariant over cross-sections and apply the mixed-dimensional notation also on the permeabilities, i.e. we introduce $\mathbf{K}_d^i := \mathbf{K}_k^{i,\parallel}$ and $\mathbf{K}_d^{i,\perp} := \mathbf{K}_k^{i,\perp}$. We extend this notation to the highest-dimensional domain ($d = 3$) by introducing $p_{\beta,3}^i := p_{\beta,b}^i$, $S_{\beta,3}^i := S_{\beta,b}^i$, $\mathbf{q}_{\beta,3}^i := \mathbf{q}_{\beta,b}^i$, $q_{\beta,3}^i := q_{\beta,b}^i$, $\phi_3^i := \phi_b^i$ and $\mathbf{K}_3^i := \mathbf{K}_b^i$ (as well as $\mathbf{K}_3^{i,\perp} = 0$). Let us now integrate equation (3.8) over the cross sections ϵ_d^i . On the basis of the averaged variables we approximate the integral over the first term of (3.8) with

$$\int_{\epsilon_d^i} \frac{\partial (\phi_k^i \rho_\beta S_{\beta,k}^i)}{\partial t} dx \approx \frac{\partial (|\epsilon_d^i| \phi_d^i \rho_\beta S_{\beta,d}^i)}{\partial t} \tag{3.11}$$

and the second term using the cross-section averaged tangential flux (3.10):

$$\int_{\epsilon_d^i} \nabla_d^{i,\parallel} \cdot \left(\rho_\beta \mathbf{q}_{\beta,k}^{i,\parallel} \right) dx \approx \nabla_d^{i,\parallel} \cdot \left(|\epsilon_d^i| \rho_\beta \mathbf{q}_{\beta,d}^i \right). \tag{3.12}$$

For the third term, we make use of divergence theorem

$$\int_{\epsilon_d^i} \nabla_d^{i,\perp} \cdot \left(\rho_\beta \mathbf{q}_{\beta,k}^{i,\perp} \right) dx = \int_{\partial\epsilon_d^i} \rho_\beta \left(\mathbf{q}_{\beta,k}^{i,\perp} \cdot \tilde{\mathbf{n}} \right) d\Gamma, \tag{3.13}$$

where $\tilde{\mathbf{n}}$ denotes the normal vector on the boundary of the cross-section. Recall the definition of interfaces between two subdomains Ω_k^i and Ω_l^j in the equi-dimensional setting presented in Section 3.2.1, i.e. $\gamma_{k,l}^{i,j} = \partial\Omega_k^i \cap \partial\Omega_l^j$, $k \neq l$, $i \in I_k$ and $j \in I_l$. In the case of $d = 2$, the cross-section boundary $\partial\epsilon_2^i$ at a specific location \mathbf{x} consists of two points located on two interfaces between the equi-dimensional bulk porous medium and fracture domain, while for the intersections, $\partial\epsilon_1^i$ describes a curve that possibly overlaps with interfaces to both the fracture and the bulk porous medium domain (for example at t-junctions of fractures). As mentioned above, we only consider mass transfer between subdomains of codimension one and thus neglect any direct mass transfer between fracture intersections and the bulk domain. This can be cast into

$$\int_{\partial\epsilon_2^i} \rho_\beta \left(\mathbf{q}_{\beta,f}^{i,\perp} \cdot \tilde{\mathbf{n}} \right) d\Gamma \approx \sum_{j \in I_b} \int_{\partial\epsilon_2^i \cap \gamma_{b,f}^{j,i}} \rho_\beta \left(\mathbf{q}_{\beta,b}^j \cdot \tilde{\mathbf{n}} \right) d\Gamma, \quad (3.14a)$$

$$\int_{\partial\epsilon_1^i} \rho_\beta \left(\mathbf{q}_{\beta,is}^{i,\perp} \cdot \tilde{\mathbf{n}} \right) d\Gamma \approx \sum_{j \in I_f} \int_{\partial\epsilon_1^i \cap \gamma_{f,is}^{j,i}} \rho_\beta \left(\mathbf{q}_{\beta,f}^j \cdot \tilde{\mathbf{n}} \right) d\Gamma, \quad (3.14b)$$

where we have used the interface condition (3.1g) of the equi-dimensional formulation. With the definitions of the neighbor sets (3.3b) and (3.3a) we now approximate the right-hand sides of (3.14a) and (3.14b) using the fluxes of the mixed-dimensional setting:

$$\sum_{j \in I_b} \int_{\partial\epsilon_2^i \cap \gamma_{b,f}^{j,i}} \rho_\beta \left(\mathbf{q}_{\beta,b}^j \cdot \tilde{\mathbf{n}} \right) d\Gamma \approx - \sum_{j \in \mathcal{N}_2^{i,\uparrow}} \rho_\beta \left(\mathbf{q}_{\beta,3}^j \cdot \mathbf{n} \right) |_{\Omega_2^i}, \quad (3.15a)$$

$$\sum_{j \in I_f} \int_{\partial\epsilon_1^i \cap \gamma_{f,is}^{j,i}} \rho_\beta \left(\mathbf{q}_{\beta,f}^j \cdot \tilde{\mathbf{n}} \right) d\Gamma \approx - \sum_{j \in \mathcal{N}_1^{i,\uparrow}} |\epsilon_2^j| \rho_\beta \left(\mathbf{q}_{\beta,2}^j \cdot \mathbf{n} \right) |_{\Omega_1^i}. \quad (3.15b)$$

The minus signs on the right-hand side of (3.15a) and (3.15b) appear as we define the normal vectors to be pointing outwards of the higher-dimensional domains. The notation $(\mathbf{q}_{\beta,d+1}^j \cdot \mathbf{n})|_{\Omega_d^i}$ means that for each neighbor Ω_{d+1}^j , $j \in \mathcal{N}_d^{i,\uparrow}$, the fluxes are evaluated at the location on Ω_d^i at which the cross-section ϵ_d^i was constructed. Making use of the above-mentioned definition $|\epsilon_3|^i = 1$, we can now state the integrated mass balance along the lower-dimensional subdomains Ω_d^i , $1 \leq d < 3$:

$$\frac{\partial \left(|\epsilon_d^i| \phi_d^i \rho_\beta S_{\beta,d}^i \right)}{\partial t} + \nabla_d^{i,\parallel} \cdot \left(|\epsilon_d^i| \rho_\beta \mathbf{q}_{\beta,d}^i \right) = |\epsilon_d^i| q_{\beta,d}^i + \sum_{j \in \mathcal{N}_d^{i,\uparrow}} |\epsilon_{d+1}^j| \rho_\beta \left(\mathbf{q}_{\beta,d+1}^j \cdot \mathbf{n} \right) |_{\Omega_d^i}. \quad (3.16)$$

The last term in (3.16) describes the transfer fluxes with the adjacent next higher-dimensional subdomains Ω_{d+1}^j in each location $\mathbf{x} \in \Omega_d$, $1 \leq d < 3$. During the derivation of the above equation, we have used the gradient and divergence operators in normal and tangential direction with respect to Ω_d^i . Since we will not need the normal gradient and divergence operators $\nabla_d^{i,\perp}$ and $\nabla_d^{i,\perp} \cdot$ throughout the remainder of this document, we will from now on denote with $\nabla_d^i := \nabla_d^{i,\parallel}$ and $\nabla_d^i \cdot := \nabla_d^{i,\parallel} \cdot$ the tangential gradient and divergence operators for the sake of readability. We also note that the respective operators ∇_3^i and $\nabla_3^i \cdot$ for the highest-dimensional domain are equivalent to the standard gradient/divergence operators.

Junctions of fracture intersections The mixed-dimensional model presented in this work does not account for storage capacity within zero-dimensional junctions of fractures. Instead, we enforce mass flux and pressure continuity over all adjacent branches of fracture intersections:

$$p_{\beta,1}^i = p_{\beta,1}^j, \quad \text{on } \Omega_0^k, \quad k \in I_0, \quad i, j \in \mathcal{N}_0^{k,\uparrow}, \quad (3.17a)$$

$$0 = \sum_{i \in \mathcal{N}_0^{k,\uparrow}} \rho_\beta (\mathbf{q}_{\beta,1}^i \cdot \mathbf{n}), \quad \text{on } \Omega_0^k, \quad k \in I_0. \quad (3.17b)$$

Interface conditions In order for the notation to be more compact we follow the notation used in Berre et al. [2018] and define the jump operator

$$\llbracket \rho_\beta (\mathbf{q}_{\beta,d+1} \cdot \mathbf{n}) \rrbracket_d^i = \sum_{j \in \mathcal{N}_d^{i,\uparrow}} |\epsilon_{d+1}^j| \rho_\beta (\mathbf{q}_{\beta,d+1}^j \cdot \mathbf{n})|_{\Omega_d^i}, \quad (3.18)$$

where $1 \leq d \leq 3$, with its extension to the highest-dimensional $\llbracket \rho_\beta (\mathbf{q}_{\beta,n+1} \cdot \mathbf{n}) \rrbracket_n^i = 0$. Finally, we have to formulate interface conditions for the fluxes $\mathbf{q}_{\beta,d+1}^j$ appearing therein. In the equi-dimensional formulation (3.1) both pressure and flux continuity are prescribed at the interfaces in order to guarantee mechanical equilibrium and mass conservation (see (3.1f) and (3.1g)). Since the higher-dimensional fluxes appear as source terms in the integrated lower-dimensional mass balance equations (3.16), mass conservation is guaranteed in the mixed-dimensional setting. However, this only holds for the sum of all flux contributions from the next higher-dimensional subdomain, as

can be seen from the equations (3.15a) and (3.15b). We use the interface conditions

$$\mathbf{q}_{\beta,d+1}^j \cdot \mathbf{n} = -\frac{\kappa_{r\beta,d}^i}{\mu_\beta} \mathbf{n}^T \mathbf{K}_d^{i,\perp} \left(\frac{p_{\beta,d}^i - p_{\beta,d+1}^j}{L_d^{i,\perp}} \mathbf{n} - \rho_\beta \mathbf{g} \right), \quad \text{on } \gamma_d^{ji}, \quad (3.19)$$

to achieve flux continuity for each of the contributions, where we have approximated the normal flux in the lower-dimensional domain with a finite difference. The pressure at the interface, evaluated in the next higher-dimensional domain, enters this finite difference such that pressure continuity is implicitly enforced. Please note that $L_d^{i,\perp}$ denotes a characteristic length scale in normal direction of Ω_d^i that represents the distance from the original equi-dimensional interface to the dimension-reduced domain. For the fracture domain, this is half the aperture, i.e. $L_2^{i,\perp} = a^i/2 = |\epsilon_2|^i/2$. However, fracture intersections can have complex geometries and the distance to the center of Ω_{is}^i can be different for each adjacent fracture branch. In this work, we approximate the length scale by taking the square root of the cross-sectional area defined for an intersection, i.e. $L_1^{i,\perp} = \frac{\sqrt{|\epsilon_1|}}{2}$, but more complex approaches can be used if information on the intersection geometry is available (see e.g. Walton et al. [2017]).

Let us denote with $L_d^{i,\parallel}$ a characteristic length scale in tangential direction of Ω_d^i , which for $1 \leq d < n$ represents the tangential extent of the fracture Ω_2^i or intersection Ω_1^i . We furthermore note that $L_3^{i,\perp} = L_3^{i,\parallel}$ is a characteristic length scale of Ω_3^i . This enables us to classify the interfaces γ_d^{ij} depending on the normal permeability ratio of the neighboring subdomains, i.e. we introduce with

$$\mathcal{Y}_d = \{ \gamma_d^{ij} : \mathbf{n}^T \mathbf{K}_{d+1}^i \mathbf{n} / L_{d+1}^{i,\parallel} \ll \mathbf{n}^T \mathbf{K}_d^j \mathbf{n} / L_d^{j,\perp} \} \quad (3.20)$$

the set of interfaces for which normal resistance to flow in the lower-dimensional domain is much smaller than in the higher-dimensional domain. The remaining interfaces are given by

$$\mathcal{X}_d = \{ \gamma_d^{ij} : \gamma_d^{ij} \notin \mathcal{Y}_d \}. \quad (3.21)$$

On the interfaces $\gamma_d^{ij} \in \mathcal{Y}_d$, the difference between $p_{\beta,d}^i$ and $p_{\beta,d+1}^j$ in the condition (3.19) are expected to be negligibly small. The interface condition can then be simplified to enforcing pressure continuity:

$$p_{\beta,d+1}^j = p_{\beta,d}^i, \quad \text{on } \gamma_d^{ji} \in \mathcal{Y}_d. \quad (3.22)$$

Mixed-dimensional problem formulation Until now the derivations of the equations have been presented in a three-dimensional setting. However, we want to state a mixed-dimensional formulation for both two- and three-dimensional systems. Furthermore, in three-dimensional settings we want to allow for the possibility to neglect the flow processes along intersections of fractures and to replace them by continuity conditions in the manner of (3.17). Let $n \in \{2, 3\}$ be the dimension of the domain $\Omega \subset \mathbb{R}^n$ under consideration and δ the dimension of the domain Ω_δ with the lowest dimension on which flow processes are taken into account. We note that $\delta = 1$ for $n = 2$ and $\delta \in \{1, 2\}$ for $n = 3$. The mixed-dimensional problem formulation is now obtained by enforcing mass conservation in each subdomain Ω_d^i , $\delta \leq d \leq n$, $i \in I_d$:

$$\mathbf{q}_{\beta,d}^i + \frac{\kappa_{r\beta,d}^i}{\mu_\beta} \mathbf{K}_d^i (\nabla_d p_{\beta,d}^i - \rho_\beta \mathbf{g}) = 0, \quad (3.23a)$$

$$\frac{\partial (|\epsilon_d^i| \phi_d^i \rho_\beta S_{\beta,d}^i)}{\partial t} + \nabla_d \cdot (|\epsilon_d^i| \rho_\beta \mathbf{q}_{\beta,d}^i) = |\epsilon_d^i| q_{\beta,d}^i + \llbracket \rho_\beta (\mathbf{q}_{\beta,d+1} \cdot \mathbf{n}) \rrbracket_d^i, \quad \text{in } \Omega_d^i, \quad (3.23b)$$

together with the boundary conditions

$$p_{w,d}^i = p_{w,d}^D, \quad (3.24a)$$

$$S_{n,d}^i = S_{n,d}^D, \quad \text{on } \Gamma_d^D \cap \partial\Omega_d^i, \quad (3.24b)$$

$$\rho_\beta (\mathbf{q}_{\beta,d}^i \cdot \mathbf{n}) = f_{\beta,d}, \quad \text{on } \Gamma_d^N \cap \partial\Omega_d^i, \quad (3.24c)$$

$$\rho_\beta (\mathbf{q}_{\beta,d}^i \cdot \mathbf{n}) = 0, \quad \text{on } \hat{\Gamma}_d \cap \partial\Omega_d^i, \quad (3.24d)$$

the initial conditions

$$p_{w,d}^i = p_{w,d}^{0,i}, \quad (3.25a)$$

$$S_{n,d}^i = S_{n,d}^{0,i} \quad \text{in } \Omega_d^i, \quad \text{for } t = t_0, \quad (3.25b)$$

the interface conditions

$$-\frac{\kappa_{r\beta,\bar{d}}^j}{\mu_\beta} \mathbf{n}^T \mathbf{K}_{\bar{d}}^{j,\perp} \left(\frac{p_{\beta,\bar{d}}^j - p_{\beta,\bar{d}+1}^i}{L_{\bar{d}}^{j,\perp}} \mathbf{n} - \rho_\beta \mathbf{g} \right) = \mathbf{q}_{\beta,\bar{d}+1}^i \cdot \mathbf{n}, \quad \text{on } \gamma_{\bar{d}}^{ij} \in \mathcal{X}_{\bar{d}}, \quad (3.26a)$$

$$p_{\beta,\bar{d}}^j = p_{\beta,\bar{d}+1}^i, \quad \text{on } \gamma_{\bar{d}}^{ij} \in \mathcal{Y}_{\bar{d}}, \quad (3.26b)$$

on the interfaces γ_d^{ij} with $\delta < \tilde{d} \leq n$, $i \in I_{\tilde{d}+1}$, $j \in I_{\tilde{d}}$ as well as mass flux and pressure continuity conditions at junctions of the lowest-dimensional domain:

$$p_{\beta,\delta}^i = p_{\beta,\delta}^j, \quad (3.27a)$$

$$0 = \sum_{i \in \mathcal{N}_{\delta-1}^{k,\uparrow}} \rho_\beta (\mathbf{q}_{\beta,\delta}^i \cdot \mathbf{n}), \quad \text{on } \Omega_{\delta-1}^k, \quad (3.27b)$$

where $k \in I_{\delta-1}$ and $i, j \in \mathcal{N}_{\delta-1}^{k,\uparrow}$. As can be seen from the equations (3.24), we use the bulk wetting phase pressures $p_{w,n}^i$ and non-wetting phase saturations $S_{n,n}^i$, as well as the lower-dimensional averaged wetting phase pressures and averaged non-wetting phase saturations $p_{w,d}^i$ and $S_{n,d}^i$, $\delta \leq d < n$ as primary variables. As in the equi-dimensional case, the system is closed with the closure relationship (2.4) for the saturations and the definition of the capillary pressure (2.7), for which we use the constitutive relationship (2.8). The relative permeabilities are model after (2.14).

Please note that equations (3.23a) are n -dimensional also for the lower-dimensional domains Ω_d , $d < n$. Thus, the permeability tensors \mathbf{K}_d^i are of size $n \times n$ and must be given in the basis used for the coordinate space \mathbb{R}^n .

3.2.3 Adaptations for open fractures

The derivation of the mixed-dimensional problem formulation (3.23)-(3.27) was carried out assuming that the fractures and their intersections behave as porous media themselves. As discussed in Section 3.1, different processes can result in fractures being filled with material, in which case it can be justified to treat them with concepts for porous media. However, fractures are not necessarily filled with matter, but could also be open or closed gaps between two rough surfaces. Closed in this context can mean mechanically closed but still hydraulically open, when relative shear displacements of the irregular fracture surfaces cause them to be in contact only locally at asperities, leaving space for the fluid to flow through. It is therefore often distinguished between the mechanical and the hydraulic aperture, see e.g. Ucar et al. [2018]. In this section we want to discuss dimension-reduced approaches for open fractures and how they fit into the mixed-dimensional model presented in the previous section.

Single-phase flow A widely-used approach in the literature is to use the cubic law to define the tangential fracture permeability as a function of the hydraulic fracture aperture:

$$k_{n-1}^{\parallel} = \frac{a^2}{12}. \quad (3.28)$$

If inserted into equation (3.23b), we can see that the flux term scales with a^3 , thus the name "cubic law". It can be formally derived from the Navier-Stokes equations for the case of laminar flow between smooth, parallel surfaces. Its applicability to rough fracture surfaces is extensively discussed in, for example, Zimmerman and Bodvarsson [1996], Jaeger et al. [2007], where approaches to define the hydraulic aperture dependent on the properties of the fracture surfaces are presented. These require assumptions or knowledge on the asperities of the fracture surfaces and are not considered in this work, where only qualitative investigations, focusing on the performance and applicability of numerical methods, are presented. Several authors have used this relationship or at least the proportionality $k_{n-1}^{\parallel} \propto a^2$ in their models (see e.g. Ucar et al. [2018], Monteagudo et al. [2011], Karimi-Fard and Firoozabadi [2003], Matthai et al. [2007]). In Garipov et al. [2016], a modified version of (3.28) is used:

$$k_{n-1}^{\parallel} = \frac{a^2}{12} + k_0, \quad (3.29)$$

where k_0 represents the tangential conductivity in the case of the two irregular fracture surfaces being in contact. Making assumptions on the cross-section geometry, one can consider similar relationships for the tangential permeability k_{n-2}^{\parallel} depending on the cross-sectional area.

In open fractures, resistivity to flow in normal direction is only given by the viscosity of the fluid due to the absence of a porous matrix. Thus, the resistivity is negligibly low in comparison to that of the surrounding rock matrix. In this case the pressure jump across the fracture can also be neglected and the pressure continuity conditions (3.26b) can be used in the mixed-dimensional formulation at the matrix-fracture interfaces.

Two-phase flow Numerous efforts reported in the literature address the task of finding average properties on the basis of which two-phase flow through open fractures with rough surfaces can be described. Of particular interest are dependencies of fluid phase relative permeabilities and capillary pressures on saturation. Early experimental studies on two-phase flow through artificial parallel-plate fractures of water and

kerosene have been carried out in Romm [1966], which reported a linear dependency of the relative permeabilities on saturation. Later numerical studies were targeted at finding more representative relationships for capillary pressures and relative permeabilities as functions of the saturation [Pruess and Tsang, 1990, Pyrak-Nolte et al., 1992, Mendoza, 1992]. They found that power-law functions of the wetting or non-wetting phase saturation can be used to describe relative permeabilities, while Mendoza [1992] further reports that both the Brooks-Corey [Brooks and Corey, 1964] as well as the Van-Genuchten model [Van Genuchten, 1980] provide adequate relationships to describe capillary pressures as functions of the saturations. Further experimental evidence that relative permeabilities non-linearly depend on saturation was reported in Fourar et al. [1993], where artificially roughened parallel glass plates were used in the experiments. Persoff and Pruess [1995] conducted experiments on natural rough-walled fractures, and observed strong phase interference and very small relative permeabilities already at intermediate saturations for both phases. More recently, Hughes and Blunt [2001] developed a pore network model to describe wetting in a single fracture, and performed numerical investigations on both artificially created networks and on a network created on the basis of aperture measurements from computed tomography (CT) scans.

The investigations performed in the above-mentioned references suggest that it could be possible to find aperture-averaged capillary pressure- and relative permeability-saturation relationships that are able to capture the most relevant phenomena of two-phase flow through open, rough-walled fractures. Therefore, we apply the mixed-dimensional description, as presented in the previous section, also to the case of open fractures and rely on suitable constitutive relationships for the relative permeabilities and capillary pressures at this point. However, it might be possible that the wetting phase preferentially resides or flows along the fracture walls while the non-wetting phase prefers the central regions of fractures. In such configurations, the presence of the wetting phase at the fracture walls could lead to an increased resistance for the non-wetting phase to flow from the bulk porous matrix into the fractures or vice versa, and it is questionable whether this effect can be incorporated into the constitutive relationships. Please note that this issue is not addressed in the numerical and experimental investigations mentioned above, which focused on determining averaged properties of single fractures in tangential direction. It should be mentioned that several works in the literature have used such averaged properties for hybrid-dimensional numerical modeling of two-phase flow through open, rough-walled fractures. For instance, Walton et al. [2017] use the data provided in Mendoza [1992] to perform numerical experiments on

two-phase flow through intersecting fractures, studying in particular the importance of the intersection regions of fractures. Monteagudo et al. [2011] use a linear relative permeability-saturation and a logarithmic capillary pressure-saturation relationship for investigations of fracture dilation on oil recovery efficiency. In Matthai et al. [2007], a numerical approach is presented to determine upscaled properties of fractured rock, including hydraulic conductivities, relative permeabilities and residual saturations. They resolve the fractures equ-dimensionally and use the cubic law to describe the fracture permeability as function of the hydraulic aperture. For relative permeability- and capillary pressure-saturation relationships they use a Brooks-Corey model for the smaller fractures with a hydraulic aperture of less than 0.5 mm, while they use a linear model for the wider fractures. They refer to the experiments performed in Romm [1966], which were conducted on parallel plates, as argument for this choice of model for fractures with larger apertures, where the effects of the wall roughness on the flow behavior are expected to be less prominent.

3.3 Modeling flow and deformation in fractured poroelastic media

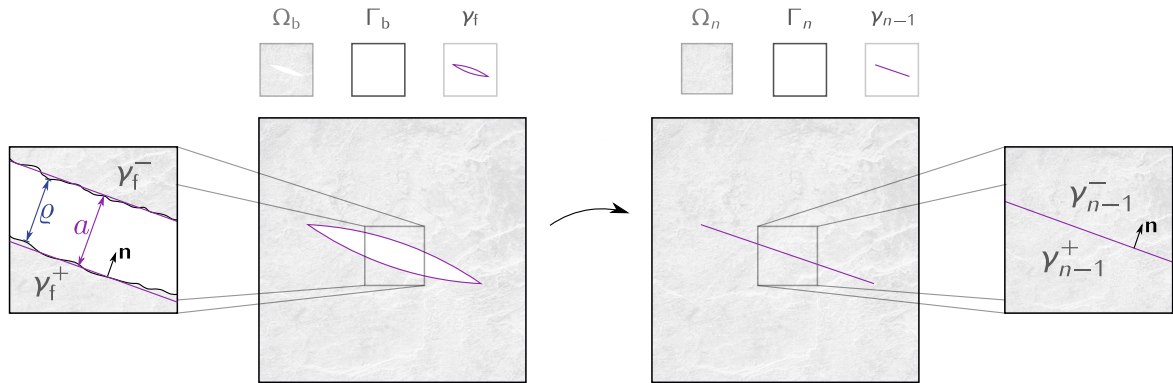


Figure 3.4 – Contact interface. Conceptual equ-dimensional model domain and the corresponding abstraction for the mixed-dimensional setting in the context of the contact mechanical problem. On the left side both the hydraulic aperture a and the gap or mechanical aperture ρ are illustrated. Furthermore, the definitions of the master (superscript $+$) and slave (superscript $-$) sides of the fracture interface are depicted in both the equ-dimensional and the mixed-dimensional representation. Please note that in contrast to the Figures 3.2 and 3.3, we omit the illustration of the outer boundary of the fracture domain Γ_f (which is empty in this case) as well as the lower-dimensional counterpart Γ_{n-1} .

In the previous Section 3.2 we have discussed the mixed-dimensional flow model used in this work. Therein, we have assumed the permeability, porosity and fracture aperture to be a given and static distribution. In this chapter we want to take into account changes in the pore structure due to mechanical deformations, which could be induced both mechanically or hydraulically. As we have seen in Section 2.3, for incompressible solid grains ($\rho_s = \text{const}$) the mass balance equation can be turned into an evolution equation for the porosity (see equation (2.45)). Therein, the velocity \mathbf{v}_s of the solid occurs, for which we note that with (2.18) it is $\mathbf{v}_s = \dot{\mathbf{u}}$. Using this relationship, the evolution equation for porosity can be cast into the constitutive relationship (see e.g. Beck [2018], Darcis [2013]):

$$\phi_{\text{eff}} = \frac{\phi_0 + \nabla \cdot \mathbf{u}}{1 + \nabla \cdot \mathbf{u}}, \quad (3.30)$$

which describes the change in available pore volume to the mechanical displacement \mathbf{u} (for details on the derivation see Appendix A). The additional introduced unknowns are the components of \mathbf{u} , which we solve for using the momentum balance equation (2.54) of the porous medium. Note that several empirical relationships exist that relate the changes in porosity to changes in permeability [Kozeny, 1927, Carman, 1937]. However, in this work we focus on the impact of fractures and their deformations on the hydraulic behavior of rock and do not consider such relationships. Instead, we assume the rock permeability to be constant. In the context of fractures, the mechanical behavior of rock can change significantly, for example when sliding occurs along the fracture surfaces. In turn, the mechanical deformations can lead to a closing or opening up of fractures, which can strongly affect the hydraulic response of the rock and can cause a redistribution of the flow field. Following the ideas presented in the previous section, we want to derive a mixed-dimensional formulation of flow and deformation in fractured porous media, where the fractures are treated as interfaces of codimension one. The flow model presented in the previous section possibly considers flow along the intersections of fractures and is applicable to both open fractures as well as fractures acting as porous media. In the case of the latter, mechanical deformations inside the porous fracture would have to be considered and a dimension-reduced formulation of the momentum balance equation (2.54) would have to be derived together with adequate interface conditions to the surrounding matrix. We will not consider this case in the model including mechanical deformations, but will restrict ourselves to the case of open fractures. Furthermore, the intersections of fractures will not be considered. To this end, let us resume to the equi-dimensional domain introduced in Section 3.2.1,

but omit the domain for the intersection, i.e. we set $\Omega_{\text{is}} = \emptyset$. We are thus left with the porous medium domain Ω_{b} and the fracture domain Ω_{f} , or in the mixed-dimensional setting with Ω_n and Ω_{n-1} . An illustration of this conceptual domain in both the equi-dimensional and mixed-dimensional representation, reusing the notation introduced in the previous section, is given in Figure 3.4.

As the porous medium undergoes deformations, fractures or fracture segments might close and develop regions of contact. Numerous studies in the literature deal with the contact between two bodies, where common approaches are the penalty method or the use of Lagrange multipliers (see e.g. Wohlmuth [2011]). A drawback of the penalty method is that for small values of the penalty parameter, one might obtain inaccurate and unphysical solutions [Wohlmuth, 2011], whereas for large values the condition number of the system becomes very large, which might significantly decrease the solver convergence. Literature is also available for the contact problem arising in fractured media. For example, Nejati et al. [2016] consider frictional contact at fracture surfaces in the context of elastic media containing fractures (not considering fluid flow), using an augmented Lagrangian method. Garipov et al. [2016] present a model for single-phase flow in both matrix and fractures, with frictional contact at fracture surfaces using the penalty method. Berge et al. [2019] use Lagrange multiplier techniques while flow inside the fractures is not considered and the fractures are additionally considered impermeable. Monteagudo et al. [2011] present a model that considers a deformable poroelastic medium in the context of two-phase flow in fractured porous media, however, they assume the fracture surfaces never to reach contact and only consider cases in which the fractures open. In the following we want to present the contact conditions used in this work, where we follow the ideas and parts of the notation used in Hüber and Wohlmuth [2005] and Berge et al. [2019].

3.3.1 Contact conditions

Resuming to the conceptual setup as illustrated in Figure 3.4, let us define a positive (or master) side γ_{f}^+ and a negative (or slave) side γ_{f}^- of the boundary γ_{f} such that $\gamma_{\text{f}} = \gamma_{\text{f}}^+ \cup \gamma_{\text{f}}^-$ (see Figure 3.4). Additionally, we define a unique normal vector on γ_{f} , which we set to be the one as seen from the positive side, that is $\mathbf{n} = \mathbf{n}(\mathbf{x}) = \mathbf{n}^+(\mathbf{x})$, and introduce a mapping that projects a point from the positive to its corresponding

point on the negative side:

$$\mathcal{I} : \gamma_f^+ \rightarrow \gamma_f^-. \quad (3.31)$$

This maps a point \mathbf{x} on γ_f^+ to the intersection of the normal on γ_f^+ in \mathbf{x} with γ_f^- [Hüeber and Wohlmuth, 2005]. With this we define the gap or mechanical aperture ϱ of a fracture at a position $\mathbf{x} \in \gamma_f^+$ as

$$\varrho = \varrho(\mathbf{x}) = \|\mathbf{x} - \mathcal{I}(\mathbf{x})\|. \quad (3.32)$$

The displacement jump in a position $\mathbf{x} \in \gamma_f^+$ is defined as $\llbracket \mathbf{u} \rrbracket = \llbracket \mathbf{u}(\mathbf{x}) \rrbracket = \mathbf{u}(\mathbf{x}) - \mathbf{u}(\mathcal{I}(\mathbf{x}))$ and can be further divided into a scalar normal and a vectorial tangential part, that is

$$\llbracket u \rrbracket^\perp = \llbracket \mathbf{u}(\mathbf{x}) \rrbracket^\perp = \llbracket \mathbf{u}(\mathbf{x}) \rrbracket \cdot \mathbf{n}(\mathbf{x}), \quad (3.33a)$$

$$\llbracket \mathbf{u} \rrbracket^\parallel = \llbracket \mathbf{u}(\mathbf{x}) \rrbracket^\parallel = \llbracket \mathbf{u}(\mathbf{x}) \rrbracket - \llbracket \mathbf{u}(\mathbf{x}) \rrbracket^\perp \mathbf{n}(\mathbf{x}). \quad (3.33b)$$

Here we follow the notation in the previous section and denote these parts with the superscripts $(\cdot)^\parallel$ and $(\cdot)^\perp$, respectively. Using the definitions (3.32) and (3.33a), we can relate the mechanical aperture to the displacement and an initial gap $\varrho_0 = \varrho_0(\mathbf{x})$, $\mathbf{x} \in \gamma_f^+$, of the undeformed state:

$$\varrho = \varrho_0 - \llbracket u \rrbracket^\perp. \quad (3.34)$$

Similarly to the displacement jump, we identify the normal and the tangential part of the surface contact traction $\mathbf{t} = \mathbf{t}(\mathbf{x})$ in a position $\mathbf{x} \in \gamma_f^+$:

$$t^\perp = t^\perp(\mathbf{x}) = \mathbf{t}(\mathbf{x}) \cdot \mathbf{n}(\mathbf{x}), \quad (3.35a)$$

$$\mathbf{t}^\parallel = \mathbf{t}^\parallel(\mathbf{x}) = \mathbf{t}(\mathbf{x}) - t^\perp(\mathbf{x}) \mathbf{n}(\mathbf{x}). \quad (3.35b)$$

According to *Newton's third law*, in the case of the fracture surfaces being in contact, the traction acting on the two sides must be equal in magnitude but in opposite direction. Apart from that, the contact forces exerted on the two sides must be compressive or must vanish if the surfaces are not in contact, respectively. Moreover, the two surfaces cannot penetrate each other. The above-mentioned can be cast into the following

conditions in normal direction of the fracture:

$$\left\{ \begin{array}{l} t^\perp(\mathbf{x}) = t^\perp(\mathcal{I}(\mathbf{x})) \\ \varrho(\mathbf{x}) \geq 0 \\ t^\perp(\mathbf{x}) \varrho(\mathbf{x}) = 0 \\ t^\perp(\mathbf{x}) \leq 0 \end{array} \right. , \quad \mathbf{x} \in \gamma_f^+, \quad (3.36)$$

where the first condition states Newton's third law in normal direction and the second condition avoids the unphysical penetration of the two fracture sides. The third condition enforces that the normal traction is zero for nonzero mechanical apertures (no contact) and the last condition ensures the normal traction to be compressive. For the tangential part of the contact traction, we apply a Coulomb friction law:

$$\left\{ \begin{array}{l} \mathbf{t}^\parallel(\mathbf{x}) = -\mathbf{t}^\parallel(\mathcal{I}(\mathbf{x})) \\ \|\mathbf{t}^\parallel(\mathbf{x})\| \leq F \|t^\perp(\mathbf{x})\| \\ \|\mathbf{t}^\parallel(\mathbf{x})\| < F \|t^\perp(\mathbf{x})\| \quad \rightarrow \llbracket \dot{\mathbf{u}}(\mathbf{x}) \rrbracket^\parallel = 0 \\ \|\mathbf{t}^\parallel(\mathbf{x})\| = F \|t^\perp(\mathbf{x})\| \quad \rightarrow \mathbf{t}^\parallel(\mathbf{x}) = -\eta \llbracket \dot{\mathbf{u}}(\mathbf{x}) \rrbracket^\parallel, \quad \eta > 0 \end{array} \right. , \quad \mathbf{x} \in \gamma_f^+. \quad (3.37)$$

Therein, the first equation is Newton's third law in tangential direction, the second condition states that the tangential traction is bounded by the normal traction multiplied with the friction coefficient F , the third condition ensures that the fracture surfaces are not sliding as long as the friction bound is not reached and the last condition states that when the friction bound is reached, the sliding velocity $\llbracket \dot{\mathbf{u}}(\mathbf{x}) \rrbracket^\parallel$ is parallel to the tangential traction. Note that in the static case, the sliding velocity $\llbracket \dot{\mathbf{u}}(\mathbf{x}) \rrbracket^\parallel$ is replaced by the tangential displacement jump $\llbracket \mathbf{u}(\mathbf{x}) \rrbracket^\parallel$.

3.3.2 Mixed-dimensional formulation

We now want to derive the mixed-dimensional formulation for the hydromechanical problem including fracture mechanics. Let $\Omega \subset \mathbb{R}^n$, $n \in \{2, 3\}$ be the domain under consideration and Ω_d , $d \in \{n-1, n\}$ its mixed-dimensional decomposition following the ideas presented in Section 3.2.2, where we consider an n -dimensional bulk domain Ω_n and an $(n-1)$ -dimensional domain Ω_{n-1} for the fractures. The equations for the flow problem were presented in (3.23)-(3.27) and will be inherited here, where we set

$\delta = n - 1$. The mechanical deformations of the bulk porous medium are modeled after the momentum balance equation (2.54) and the fracture mechanics are described using the contact conditions (3.36) and (3.37). To this end, let us introduce the mortar variable $\boldsymbol{\tau}$ on Ω_{n-1} , which represents the surface traction due to contact. This requires n additional equations, for which we use the contact conditions (3.36) and (3.37), recast into the nonlinear complementary functions presented in Hübner and Wohlmuth [2005], Berge et al. [2019]. For (3.36) this reads:

$$C^\perp = C^\perp([\![u]\!]^\perp, \boldsymbol{\tau}^\perp) = -\tau^\perp - \max\{0, -\tau^\perp - c\varrho\}, \quad (3.38)$$

where C^\perp is a function of $[\![u]\!]^\perp$ because of the dependency of the gap ϱ on the displacement as given in (3.34). The Coulomb friction law (3.37) is cast into

$$\begin{aligned} \mathbf{C}^\parallel = \mathbf{C}^\parallel([\![\mathbf{u}(\mathbf{x})]\!]^\parallel, \boldsymbol{\tau}^\parallel) &= \max\{F(-\tau^\parallel - c\varrho), \|c[\![\dot{\mathbf{u}}(\mathbf{x})]\!]^\parallel - \boldsymbol{\tau}^\parallel\|\} (-\boldsymbol{\tau}^\parallel) \\ &\quad - F \max\{0, -\tau^\parallel - c\varrho\} (c[\![\dot{\mathbf{u}}(\mathbf{x})]\!]^\parallel - \boldsymbol{\tau}^\parallel). \end{aligned} \quad (3.39)$$

Here, $\max\{\cdot, \cdot\}$ is the maximum function and c in [Pa/m] is a numerical parameter. Please note again that in static conditions, the sliding velocity $[\![\dot{\mathbf{u}}(\mathbf{x})]\!]^\parallel$ is substituted with the tangential displacement jump $[\![\mathbf{u}(\mathbf{x})]\!]^\parallel$ in (3.39). Moreover, we have used the tangential and normal parts of $\boldsymbol{\tau}$, $\boldsymbol{\tau}^\parallel$ and τ^\perp , which are defined in the same way as the tractions in (3.35).

Recall the mixed-dimensional decomposition of the domain Ω into d -dimensional subdomains Ω_d^i , $i \in I_d$, and interfaces γ_d^{ij} , $d < n$, $i \in I_{d+1}$, $j \in I_d$, between them. As mentioned above, here we consider $d \in \{n-1, n\}$, thus we only have the $(n-1)$ -dimensional interfaces γ_{n-1}^{ij} . As in the equi-dimensional considerations in the previous Section 3.3.1, master and slave sides $\gamma_{n-1}^{ij,+}$ and $\gamma_{n-1}^{ij,-}$ are defined for the interfaces, as well as a unique normal vector $\mathbf{n} = \mathbf{n}^+$. On this setting, we state the mixed-dimensional problem formulation by enforcing mass conservation (after equations (3.23a)) in each subdomain Ω_d^i , $d \in \{n-1, n\}$, $i \in I_d$:

$$\mathbf{q}_{\beta,d}^i + \frac{\kappa_{r\beta,d}^i}{\mu_\beta} \mathbf{K}_d^i (\nabla_d p_{\beta,d}^i - \rho_\beta \mathbf{g}) = 0, \quad (3.40a)$$

$$\frac{\partial (|\epsilon_d^i| \phi_d^i \rho_\beta S_{\beta,d}^i)}{\partial t} + \nabla_d \cdot (|\epsilon_d^i| \rho_\beta \mathbf{q}_{\beta,d}^i) = |\epsilon_d^i| q_{\beta,d}^i + [\![\rho_\beta (\mathbf{q}_{\beta,d+1} \cdot \mathbf{n})]\!]^i, \quad \text{in } \Omega_d^i, \quad (3.40b)$$

with the mass flux and pressure continuity conditions (3.27) at junctions of fractures:

$$p_{\beta,n-1}^i = p_{\beta,n-1}^j, \quad (3.41a)$$

$$0 = \sum_{i \in \mathcal{N}_{n-2}^{k,\uparrow}} \rho_{\beta} (\mathbf{q}_{\beta,n-1}^i \cdot \mathbf{n}), \quad \text{on } \Omega_{n-2}^k, \quad (3.41b)$$

where $k \in I_{n-2}$ and $i, j \in \mathcal{N}_{n-2}^{k,\uparrow}$. Furthermore, the momentum balance equations (2.54) are enforced in the bulk subdomains Ω_n^i , $i \in I_n$:

$$\boldsymbol{\epsilon}_s^i - \frac{1}{2} (\nabla \mathbf{u}^i + \nabla^T \mathbf{u}^i) = 0, \quad (3.42a)$$

$$\boldsymbol{\sigma}_s^i - \lambda^i \text{tr}(\boldsymbol{\epsilon}_s^i) \mathbf{I} - 2G^i \boldsymbol{\epsilon}_s^i = 0, \quad (3.42b)$$

$$\boldsymbol{\sigma}^i - \boldsymbol{\sigma}_s^i + \alpha_B \mathbf{I} \sum_{\beta} S_{\beta,n}^i p_{\beta,n}^i = 0, \quad (3.42c)$$

$$\nabla \cdot \boldsymbol{\sigma}^i + \left((1 - \phi_n^i) \rho_s + \phi_n^i \sum_{\beta} S_{\beta,n}^i \rho_{\beta,n}^i \right) \mathbf{g} = 0, \quad \text{in } \Omega_n^i, \quad (3.42d)$$

where in (3.42a)- (3.42c) we have used the definitions of the strain, stress and effective stress tensors given in (2.23), (2.26) and (2.32). Additionally, the interface conditions

$$C^{\perp} (\llbracket \mathbf{u}^i \rrbracket^{\perp}, \boldsymbol{\tau}^{j,\perp}) = 0, \quad (3.43a)$$

$$\mathbf{C}^{\parallel} (\llbracket \mathbf{u}^i \rrbracket^{\parallel}, \boldsymbol{\tau}^{j,\parallel}) = 0, \quad (3.43b)$$

$$p_{\beta,n}^i - p_{\beta,n-1}^j = 0, \quad \text{on } \gamma_{n-1}^{ij}, \quad (3.43c)$$

$$\boldsymbol{\sigma}^i \mathbf{n} - \boldsymbol{\tau}^j - \mathbf{n} \sum_{\beta} S_{\beta,n-1}^j p_{\beta,n-1}^j = 0, \quad \text{on } \gamma_{n-1}^{ij,+}, \quad (3.43d)$$

$$\boldsymbol{\sigma}^i \mathbf{n} + \boldsymbol{\tau}^j - \mathbf{n} \sum_{\beta} S_{\beta,n-1}^j p_{\beta,n-1}^j = 0, \quad \text{on } \gamma_{n-1}^{ij,-}, \quad (3.43e)$$

for $i \in I_n$ and $j \in I_{n-1}$, have to be fulfilled. The boundary conditions for flow, on external and immersed boundaries, are given by

$$p_{w,d}^i = p_{w,d}^D, \quad (3.44a)$$

$$S_{n,d}^i = S_{n,d}^D, \quad \text{on } \Gamma_d^{\text{D,ps}} \cap \partial \Omega_i, \quad (3.44b)$$

$$\rho_{\beta} (\mathbf{q}_{\beta,d}^i \cdot \mathbf{n}) = f_{\beta,d}, \quad \text{on } \Gamma_d^{\text{N,ps}} \cap \partial \Omega_d^i, \quad (3.44c)$$

$$\rho_{\beta} (\mathbf{q}_{\beta,d}^i \cdot \mathbf{n}) = 0, \quad \text{on } \hat{\Gamma}_d \cap \partial \Omega_d^i, \quad (3.44d)$$

and for the mechanical problem by

$$u_\chi^i = u_\chi^D, \quad \text{on } \Gamma_n^{D,u_\chi} \cap \partial\Omega_n^i, \quad (3.45a)$$

$$(\boldsymbol{\sigma}^i \mathbf{n})_\chi = t_\chi^N, \quad \text{on } \Gamma_n^{N,\sigma_\chi} \cap \partial\Omega_n^i, \quad (3.45b)$$

where $i \in I_n$ and $\chi \in \{1, \dots, n\}$ refers to a coordinate direction. From (3.44) and (3.45) it can be seen that here we further differentiate the boundary segments on which Dirichlet and Neumann boundaries are specified. In particular, $\Gamma_d^{D,ps}$ and $\Gamma_d^{N,ps}$ denote those boundary segments on which Dirichlet and Neumann boundary conditions are applied for all primary variables or all equations of the flow model, respectively. The superscript "ps" is chosen here to indicate that the primary variables of the flow model consist of a pressure ($p_{w,d}^i$) and a saturation ($S_{n,d}^i$). As in Section 3.2.2, $\Gamma_d^{D,ps}$ and $\Gamma_d^{N,ps}$ form a decomposition of Γ_d and we require $|\Gamma_d^{D,ps}| \neq 0$ for at least one subdomain $d \in \{n-1, n\}$. For the mechanical problem, we allow for different Neumann and Dirichlet boundary segments per primary variable or equation. This is included in the notation with superscripts indicating for which variable or equation a Dirichlet or Neumann boundary condition is specified. That is, Γ_n^{D,u_χ} and Γ_n^{N,σ_χ} refer to those parts of the boundary of the domain Ω_n on which the displacement or the traction in the coordinate direction $\chi \in \{1, \dots, n\}$ is specified. Here, Γ_n^{D,u_χ} and Γ_n^{N,σ_χ} must also form a decomposition of Γ_d and we require $|\Gamma_n^{D,u_\chi}| \neq 0$ for all coordinate directions χ . Finally, we complete the problem statement with the initial conditions:

$$p_{w,d}^i = p_{w,d}^{0,i}, \quad (3.46a)$$

$$S_{n,d}^i = S_{n,d}^{0,i}, \quad \text{in } \Omega_d^i, \quad \text{for } t = t_0, \quad (3.46b)$$

$$\mathbf{u}^i = \mathbf{u}^{0,i}, \quad \text{in } \Omega_n^i, \quad \text{for } t = t_0. \quad (3.46c)$$

Note that the porosities ϕ_n^i for the bulk domain appearing in (3.40) and (3.42) possibly refer to the effective porosities, modeled as functions of the displacement after (3.30). Recall that in the context of deformable fractured media we are only considering open fractures, for which reason we use the pressure continuity conditions (3.43c) and note that $\phi_{n-1}^i = 1$. The tangential fracture permeabilities \mathbf{K}_{n-1}^i are defined as functions of the hydraulic aperture $a = \epsilon_{n-1}$, which we relate to the mechanical displacements via (making use of (3.34)):

$$a = \epsilon_{n-1} = \varrho + a_0 = \varrho_0 - \llbracket u \rrbracket^\perp + a_0, \quad (3.47)$$

where a_0 is the hydraulic aperture in the case of contact, i.e. for $\varrho = 0$. We use (3.47) in conjunction with the cubic law (3.28), and thus, for $\varrho = 0$ the tangential permeability does not vanish, similar to the model given in (3.29). From (3.43d) and (3.43e) we see that both the contact tractions as well as compressive tractions due to the effective fluid pressure inside the fracture are exerted on the two sides of the porous medium adjacent to the interfaces γ_{n-1}^{ij} . The mortar variables for the contact tractions, $\boldsymbol{\tau}^j$, $j \in I_{n-1}$, are defined for the positive sides of the interface, $\gamma_{n-1}^{ij,+}$, which explains the inverted sign in the condition (3.43e) for the negative sides.

4 Numerical schemes

In this chapter we want to outline the spatial discretization schemes used in this work to discretize the mixed-dimensional formulations of flow, deformations and contact mechanics presented in the previous chapter. Different numerical schemes were developed and implemented in this work, and comparing them in terms of applicability, accuracy and efficiency will be one of the main goals of the numerical experiments presented in the subsequent chapter. In the sequel of this chapter, we will outline the finite-volume schemes used to discretize the mixed-dimensional flow equations (3.23)-(3.27) in Section 4.1, before we discuss the schemes used to discretize the mechanical equations (3.42) in Section 4.2. Section 4.3 describes how the coupling terms between the individual subdomains are computed, and the overall solution strategy is presented in Section 4.4.

Computational mesh To this end, let us introduce the primary discretizations \mathcal{M}_d , $1 \leq d \leq n$, with elements $E \in \mathcal{M}_d$ such that $\Omega_{d,h} = \bigcup_{E \in \mathcal{M}_d} E$ are discrete approximations of Ω_d . Correspondingly, let \mathcal{M}_d^i be the subset of \mathcal{M}_d associated with the discrete subdomain $\Omega_{d,h}^i \approx \Omega_d^i$. Moreover, let us denote with \mathcal{E}_d the set of faces of the primary discretization, where each face $\varsigma \in \mathcal{E}_d$ with measure $|\varsigma| > 0$ is part of a $(d - 1)$ -dimensional hyperplane. We define the subsets \mathcal{E}_E such that for each element $E \in \mathcal{M}_d$ it is $\partial E = \bigcup_{\varsigma \in \mathcal{E}_E} \varsigma$.

4.1 Finite-volume discretizations of the flow equations

Three well-established finite-volume schemes, the cell-centered two-point flux approximation scheme (TPFA), a multi-point flux approximation scheme (MPFA) [Aavatsmark,

2002], and the BOX scheme [Helmig, 1997] are considered in this work for the discretization of the mixed-dimensional flow equations. For all three, we require conformity between the primary discretizations of codimension one in the sense that the elements of a d -dimensional grid, $d < n$, must coincide with element faces of the $(d+1)$ -dimensional grid. That is, for each element $E \in \mathcal{M}_d$ there must be a face $\varsigma \in \mathcal{E}_{d+1}$ such that $E = \varsigma$. Please note that previous works have already reported such approaches for the case of both single- and two-phase flow. In particular, Karimi-Fard et al. [2004] presented a TPFA scheme for single-phase flow, while Sandve et al. [2012], Ahmed et al. [2015, 2017] developed similar models on the basis of multi-point flux approximations (MPFA). However, they did not consider flow along intersections of fractures. Nordbotten et al. [2019] present both TPFA and MPFA based models including flow along fracture intersections as well as storage capacity in junctions of intersections. Grillo et al. [2013] use the BOX scheme to study the importance of the Forchheimer correction in the context of density-driven flow in fractured porous media, where the results are restricted to two dimensions. For two-phase flow, a conforming discrete fracture model based on the BOX scheme has been presented in Reichenberger et al. [2006], while Brenner et al. [2014] developed a two-phase flow model using the Vertex Approximate Gradient (VAG) scheme. Apart from that, embedded approaches have been developed, in which the bulk and the fracture domains are discretized independently. This can be advantageous from the point of view of grid generation for complex fracture networks, however, they might struggle to capture the involved discontinuities, especially in the case of low-conductive fractures (see e.g. Köppel [2013]). Embedded discrete fracture models that are capable of capturing discontinuities on the basis of extended finite element methods are presented in e.g. Fumagalli and Scotti [2013], Schwenck [2015], and on the basis of finite volumes in e.g. Tene et al. [2017]. However, none of the above-mentioned approaches for two-phase flow consider flow along intersections of fractures. In this work, we consider a conforming approach which enables us to incorporate the conditions at interfaces between subdomains in a comparatively easy manner.

Finite-volume grid In addition to the primary grid, let us introduce the tessellations \mathcal{T}_d , composed of control volumes $K \in \mathcal{T}_d$ with measure $|K| > 0$ such that $\bigcup_{K \in \mathcal{T}_d} K = \Omega_{d,h}$. In general, the elements and control volumes do not have to coincide, but for cell-centered finite volume schemes we usually find $\mathcal{T}_d \equiv \mathcal{M}_d$. Furthermore, we denote by \mathcal{S}_d the sets of faces of the tessellations, where each face $\sigma \in \mathcal{S}_d$ is part of a $(d-1)$ -

dimensional hyperplane, and define the subset \mathcal{S}_K such that for a control volume $K \in \mathcal{T}_d$ it is $\partial K = \bigcup_{\sigma \in \mathcal{S}_K} \sigma$. The corresponding unit normal vector $\mathbf{n}_{K,\sigma}$ is defined to be pointing outwards of K . Let us further define the subsets $\mathcal{S}_{d,\text{coup}}$, $\mathcal{S}_{d,\text{int}}$ and $\mathcal{S}_{d,\text{ext}}$ of coupling faces that overlap with a $(d-1)$ -dimensional control volume $K \in \mathcal{T}_{d-1}$, internal faces and faces on the domain boundary, respectively. We now integrate (3.23b) over a control volume $K \in \mathcal{T}_d$ and apply the Gauss divergence theorem:

$$\begin{aligned} \int_K \frac{\partial (|\epsilon_d^i| \phi_d^i \rho_\beta S_{\beta,d}^i)}{\partial t} dV + \sum_{\sigma \in \mathcal{S}_K} \int_\sigma |\epsilon_d^i| \rho_\beta \mathbf{q}_{\beta,d}^i \cdot \mathbf{n}_{K,\sigma} d\Gamma \\ = \int_K |\epsilon_d^i| q_{\beta,d}^i + \llbracket \rho_\beta (\mathbf{q}_{\beta,d+1} \cdot \mathbf{n}) \rrbracket_d^i dV. \end{aligned} \quad (4.1)$$

From (3.23a) we see that $\mathbf{q}_{\beta,d}^i = -\frac{\kappa_{r\beta}^i}{\mu_\beta} \mathbf{K}_d^i (\nabla_d p_{\beta,d}^i - \rho_\beta \mathbf{g})$. Let us now introduce the discrete flux

$$F_\beta^{K,\sigma} \approx - \int_\sigma |\epsilon_d^i| \mathbf{n}_{K,\sigma}^T \mathbf{K}_d^i (\nabla_d p_{\beta,d}^i - \rho_\beta \mathbf{g}) d\Gamma, \quad (4.2)$$

which we do not equip with the sub- and superscripts d and i indicating the subdomain Ω_d^i for which it is evaluated, because the control volume K inherently carries the notion of its dimensionality and the subdomain it is embedded in. We will follow the same procedure in the following wherever a quantity receives a sub- or superscript referring to the discrete object on which it is evaluated, e.g. a cell or face. Using the discrete flux $F_\beta^{K,\sigma}$, we can approximate the face fluxes that appear in the second term of (4.1):

$$\begin{aligned} \int_K \frac{\partial (|\epsilon_d^i| \phi_d^i \rho_\beta S_{\beta,d}^i)}{\partial t} dV + \sum_{\sigma \in \mathcal{S}_K} \left(\rho_\beta \frac{\kappa_{r\beta}}{\mu_\beta} \right)^{\text{up}} F_\beta^{K,\sigma} \\ = \int_K |\epsilon_d^i| q_{\beta,d}^i + \llbracket \rho_\beta (\mathbf{q}_{\beta,d+1} \cdot \mathbf{n}) \rrbracket_d^i dV. \end{aligned} \quad (4.3)$$

Here, we have introduced with $(\cdot)^{\text{up}}$ the upwinding with respect to the sign of the flux $F_\beta^{K,\sigma}$. This means that for a face $\sigma \in \mathcal{S}_{d,\text{int}}$ between the two control volumes $K, L \in \mathcal{T}_d$ (i.e. $\sigma = \bar{K} \cap \bar{L}$), we evaluate the term $\left(\rho_\beta \frac{\kappa_{r\beta}}{\mu_\beta} \right)$ within control volume L if $F_\beta^{K,\sigma} < 0$ and within control volume K otherwise. Consequently, for coupling faces it is evaluated within the lower-dimensional control volume adjacent to K if $F_\beta^{K,\sigma} < 0$. The main difference between the various finite-volume schemes lies in the choice of the discrete fluxes $F_\beta^{K,\sigma}$. In the following we will present their construction for the schemes considered in this work, with a special focus on the fluxes across coupling faces.

4.1.1 Cell-centered finite volume schemes

In cell-centered schemes the primary grid elements are used as the control volumes and the degrees of freedom are associated with the cell centers. Accordingly, fluid properties as well as permeabilities are constant per cell. This allows us to simplify the volume integrals in equation (4.3) such that the mass conservation equation for a control volume $K \in \mathcal{T}_d$ now reads:

$$\begin{aligned} |K| \frac{\partial (|\epsilon_K| \phi_K \rho_{\beta,K} S_{\beta,K})}{\partial t} + \sum_{\sigma \in \mathcal{S}_K} \left(\rho_{\beta} \frac{\kappa_{r\beta}}{\mu_{\beta}} \right)^{\text{up}} F_{\beta}^{K,\sigma} \\ = |K| (|\epsilon_K| q_{\beta,K} + \llbracket \rho_{\beta} (\mathbf{q}_{\beta,d+1} \cdot \mathbf{n}) \rrbracket_K). \end{aligned} \quad (4.4)$$

As a reminder, the subscript K now indicates that the quantities are evaluated for the control volume. In this work we consider two cell-centered schemes, the two-point flux approximation scheme (TPFA) and a multi-point flux approximation scheme (MPFA), which mainly differ in the assembly of the discrete fluxes. For the construction of the discrete fluxes $F_{\beta}^{K,\sigma}$, in both of the schemes intermediate face pressures $\bar{p}_{\beta}^{K,\sigma}$ are introduced on all faces $\sigma \in \mathcal{S}_K$. On Dirichlet boundary faces the values of the face pressures are defined by the boundary conditions, and on coupling faces where the coupling conditions (3.26b) are used it is given by the pressure in the adjacent lower-dimensional control volume. On the other hand, on the remaining coupling faces they are eliminated using the interface condition (3.26a), while on interior faces both pressure and flux continuity are enforced. The pressure continuity condition essentially leads to the introduction of a single set of intermediate phase pressures $\bar{p}_{\beta}^{\sigma} = \bar{p}_{\beta}^{K,\sigma} = \bar{p}_{\beta}^{L,\sigma}$ for an internal face $\sigma \in \mathcal{S}_{d,\text{int}}$ between the two control volumes $K, L \in \mathcal{T}_d$, while the corresponding flux continuity condition can be reduced to

$$\begin{aligned} \left(\rho_{\beta} \frac{\kappa_{r\beta}}{\mu_{\beta}} \right)^{\text{up}} F_{\beta}^{K,\sigma} + \left(\rho_{\beta} \frac{\kappa_{r\beta}}{\mu_{\beta}} \right)^{\text{up}} F_{\beta}^{L,\sigma} = \left(\rho_{\beta} \frac{\kappa_{r\beta}}{\mu_{\beta}} \right)^{\text{up}} (F_{\beta}^{K,\sigma} + F_{\beta}^{L,\sigma}) = 0, \\ \rightarrow F_{\beta}^{K,\sigma} + F_{\beta}^{L,\sigma} = 0, \end{aligned} \quad (4.5)$$

due to the employed upwind scheme.

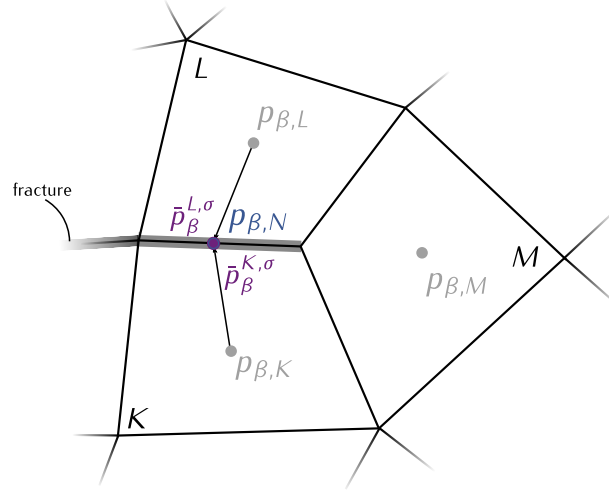


Figure 4.1 – Two-point flux approximation. Exemplary discrete configuration around a face σ which lies on a lower-dimensional fracture geometry for the TPFA scheme. The fracture is shown in gray and is depicted as a two-dimensional geometry for the sake of visibility. Depicted are three control volumes of the two-dimensional grid, $K, L, M \in \mathcal{T}_2$ ($n = 2$), and the face σ between K and L , which geometrically coincides with the control volume $N \in \mathcal{T}_1$ of the fracture discretization. Furthermore, the primary cell pressures as well as the two intermediate face pressures $\bar{p}_\beta^{K,\sigma}$ and $\bar{p}_\beta^{L,\sigma}$ are shown.

Two-point flux approximation

For the TPFA scheme, the discrete flux across a face σ of a control-volume K is defined as

$$F_\beta^{K,\sigma} = -|\sigma| |\epsilon_K| \mathbf{n}_{K,\sigma}^T \mathbf{K}_K \left(\frac{\bar{p}_\beta^{K,\sigma} - p_{\beta,K}}{\|\mathbf{d}_{K,\sigma}\|^2} \mathbf{d}_{K,\sigma} - \rho_{\beta,\sigma} \mathbf{g} \right). \quad (4.6)$$

where $\mathbf{d}_{K,\sigma}$ is the vector that connects the center of cell K with the center of the face σ and $\|\cdot\|$ is the euclidean norm. Furthermore, $|\epsilon_K|$ and \mathbf{K}_K are the measure of the cross-section and the permeability evaluated for cell K and $\rho_{\beta,\sigma}$ is the fluid density evaluated for the face σ . Introducing the half-transmissibilities

$$\omega_{K,\sigma} = -\frac{|\sigma| |\epsilon_K| \mathbf{n}_{K,\sigma}^T \mathbf{K}_K \mathbf{d}_{K,\sigma}}{\|\mathbf{d}_{K,\sigma}\|^2}, \quad (4.7)$$

this can be rewritten into

$$F_\beta^{K,\sigma} = \omega_{K,\sigma} \left(\bar{p}_\beta^{K,\sigma} - p_{\beta,K} \right) + |\sigma| |\epsilon_K| \rho_{\beta,\sigma} \mathbf{n}_{K,\sigma}^T \mathbf{K}_K \mathbf{g} = \omega_{K,\sigma} \left(\bar{p}_\beta^{K,\sigma} - p_{\beta,K} \right) + g_\beta^{K,\sigma}, \quad (4.8)$$

where $g_\beta^{K,\sigma} = |\sigma| |\epsilon_K| \rho_{\beta,\sigma} \mathbf{n}_{K,\sigma}^T \mathbf{K}_K \mathbf{g}$ has been introduced. With this, the condition (4.5) for internal faces $\sigma \in \mathcal{S}_{d,\text{int}}$ can be recast to an expression for the intermediate face pressure:

$$\bar{p}_\beta^{K,\sigma} = \bar{p}_\beta^{L,\sigma} = \bar{p}_\beta^\sigma = \frac{\omega_{K,\sigma} p_{\beta,K} + \omega_{L,\sigma} p_{\beta,L}}{\omega_{K,\sigma} + \omega_{L,\sigma}} - \frac{g_\beta^{K,\sigma} + g_\beta^{L,\sigma}}{\omega_{K,\sigma} + \omega_{L,\sigma}}, \quad (4.9)$$

and insertion of (4.9) into (4.8) leads to the final expression for the flux as a function of cell pressures only:

$$F_\beta^{K,\sigma} = -F_\beta^{L,\sigma} = \frac{\omega_{K,\sigma}}{\omega_{K,\sigma} + \omega_{L,\sigma}} \left(\omega_{L,\sigma} (p_{\beta,L} - p_{\beta,K}) - g_\beta^{K,\sigma} - g_\beta^{L,\sigma} \right) + g_\beta^{K,\sigma}. \quad (4.10)$$

The quotient $\frac{\omega_{K,\sigma} \omega_{L,\sigma}}{\omega_{K,\sigma} + \omega_{L,\sigma}}$, i.e. the harmonic mean of the two half-transmissibilities $\omega_{K,\sigma}$ and $\omega_{L,\sigma}$, is often referred to as the transmissibility. At this point it should also be mentioned that in this work we approximate the fluid density on the face with the arithmetic mean of the densities in the two neighboring cells, i.e. $\rho_{\beta,\sigma} = \frac{\rho_{\beta,K} + \rho_{\beta,L}}{2}$. Let us now consider a coupling face $\sigma \in \mathcal{S}_{d,\text{coup}}$, on which the conditions (3.26a) are used, and that is contained in a control volume $K \in \mathcal{T}_d$, i.e. $\sigma \in \mathcal{S}_K$, and which geometrically coincides with the $(d-1)$ -dimensional control volume $N \in \mathcal{T}_{d-1}$. Making use of the upwind scheme, analogously to (4.5), the interface condition can then be written as follows:

$$-|\sigma| |\epsilon_K| \mathbf{n}_{K,\sigma}^T \mathbf{K}_N^\perp \left(\frac{p_{\beta,N} - \bar{p}_\beta^{K,\sigma}}{L_N^\perp} \mathbf{n}_{K,\sigma} - \rho_{\beta,\sigma} \mathbf{g} \right) = F_\beta^{K,\sigma}. \quad (4.11)$$

For the situation depicted in Figure 4.1 ($n = 2$), where a face $\sigma \in \mathcal{S}_{2,\text{coup}}$ is located between the control volumes $K, L \in \mathcal{T}_2$, the conditions on the two sides of the depicted fracture read:

$$-|\sigma| |\epsilon_K| \mathbf{n}_{K,\sigma}^T \mathbf{K}_N^\perp \left(\frac{p_{\beta,N} - \bar{p}_\beta^{K,\sigma}}{L_N^\perp} \mathbf{n}_{K,\sigma} - \rho_{\beta,\sigma} \mathbf{g} \right) = F_\beta^{K,\sigma}, \quad (4.12a)$$

$$-|\sigma| |\epsilon_L| \mathbf{n}_{L,\sigma}^T \mathbf{K}_N^\perp \left(\frac{p_{\beta,N} - \bar{p}_\beta^{L,\sigma}}{L_N^\perp} \mathbf{n}_{L,\sigma} - \rho_{\beta,\sigma} \mathbf{g} \right) = F_\beta^{L,\sigma}. \quad (4.12b)$$

Let us now introduce the half-transmissibilities $\bar{\omega}_{K,\sigma} = -\frac{|\sigma| |\epsilon_K| \mathbf{n}_{K,\sigma}^T \mathbf{K}_N^\perp \mathbf{n}_{K,\sigma}}{L_N^\perp}$ for the coupling faces and accordingly $\bar{g}_\beta^{K,\sigma} = \frac{|\sigma| |\epsilon_K| \rho_{\beta,\sigma} \mathbf{n}_{K,\sigma}^T \mathbf{K}_N^\perp \mathbf{g}}{L_N^\perp}$. Following the derivation of

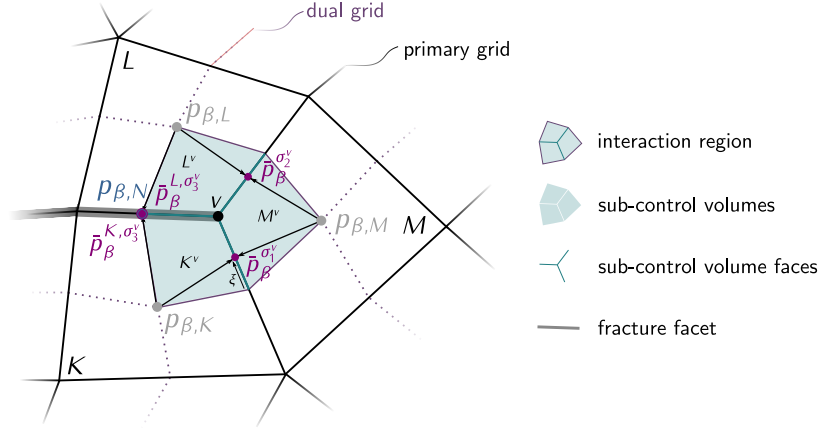


Figure 4.2 – Multi-point flux approximation. Exemplary interaction region in which the transmissibilities for the fluxes across sub-control volume faces are computed. The fracture is shown in gray and is depicted as a two-dimensional geometry for the sake of visibility. Depicted are three control volumes of the two-dimensional grid, $K, L, M \in \mathcal{T}_2$ ($n = 2$) together with the sub-control volumes K^v, L^v, M^v and sub-control volume faces σ_i^v , $i \in \{1, 2, 3\}$ that are contained within the interaction region constructed around the vertex v . Furthermore, The primary cell pressures $p_{\beta,i}$ as well as the intermediate face pressures $\bar{p}_{\beta}^{\sigma_i^v}$ are shown.

(4.10), the fluxes across coupling faces $\sigma \in \mathcal{S}_{d,\text{coup}}$ can be written analogously:

$$F_{\beta}^{K,\sigma} = \frac{\omega_{K,\sigma}}{\omega_{K,\sigma} + \bar{\omega}_{K,\sigma}} \left(\bar{\omega}_{K,\sigma} (p_{\beta,N} - p_{\beta,K}) - g_{\beta}^{K,\sigma} - \bar{g}_{\beta}^{K,\sigma} \right) + g_{\beta}^{K,\sigma}. \quad (4.13)$$

Multi-point flux approximation

While the two-point flux approximation method presented in the previous section provides a simple and robust scheme, it is well known that it is inconsistent on grids that are not \mathbf{K} -orthogonal (see e.g. Edwards and Rogers [1998]). Many efforts were made to develop schemes that do not have this limitation, many of which fall into the family of MPFA schemes (see e.g. Aavatsmark [2002], Aavatsmark et al. [2008], Agélas et al. [2010], Friis and Edwards [2011]), and more recently, non-linear finite volume schemes (see e.g. Le Potier [2009], Schneider et al. [2016]). The MPFA scheme used in this work is based on the so-called MPFA - O scheme [Aavatsmark, 2002] and the extension to account for discrete fractures follows the ideas presented in Sandve et al. [2012], Ahmed et al. [2015]. Please note that we will omit the suffix "-O" in this document, implicitly

referring to the MPFA - O scheme.

In contrast to the TPFA scheme, the faces of the control volumes do not fully coincide with the faces of the primary grid, but each primary grid face $\varsigma \in \mathcal{E}_d$ is sub-divided into a number of control volume faces that are constructed around its corners. In two-dimensional grids, this boils down to splitting each one-dimensional primary grid face at its center into two control volume faces (see Figure 4.2). In three-dimensional grids, construction occurs by connecting the primary grid face corners with the centers of the face edges and the face center. In each grid cell $K \in \mathcal{T}_d$, two ($d = 2$) or three ($d = 3$) faces meet at a corner, i.e. a grid vertex. Additionally connecting the primary grid face centers with the center of K , one can identify the subset $K^v \subset K$ associated with the vertex v , where the faces meeting at the vertex v describe a part of its boundary. Following this procedure for all cells and vertices of the grid, a dual grid as illustrated in Figure 4.2 becomes apparent. The discrete fluxes $F_\beta^{K,\sigma}$ are now constructed on the basis of constant discrete gradients $\nabla_{\mathcal{D}}^{K^v} p_{\beta,d}$ per subset K^v . Here, these are constructed such that the condition

$$\nabla_{\mathcal{D}}^{K^v} p_{\beta,d} \cdot (\mathbf{x}_{\sigma_i} - \mathbf{x}_K) = \bar{p}_\beta^{K,\sigma_i} - p_{\beta,K} \quad (4.14)$$

is fulfilled for all faces $\sigma_i \in \partial K^v$, $1 \leq i \leq d$, i.e. those faces that form a part of the boundary of K^v . A discrete gradient that fulfills these conditions is defined by

$$\nabla_{\mathcal{D}}^{K^v} p_{\beta,d} = \Xi_{K^v}^{-T} \begin{bmatrix} \bar{p}_\beta^{K,\sigma_1} - p_{\beta,K} \\ \vdots \\ \bar{p}_\beta^{K,\sigma_d} - p_{\beta,K} \end{bmatrix}, \quad \text{with } \Xi_{K^v} := \begin{bmatrix} \mathbf{x}_{\sigma_1} - \mathbf{x}_K, & \dots, & \mathbf{x}_{\sigma_d} - \mathbf{x}_K \end{bmatrix}. \quad (4.15)$$

This enables us to define the discrete flux across a face $\sigma \in \partial K^v$ for the MPFA scheme:

$$F_\beta^{K,\sigma} = -|\sigma| |\epsilon_K| \mathbf{n}_{K,\sigma}^T \mathbf{K}_K (\nabla_{\mathcal{D}}^{K^v} p_{\beta,d} - \rho_{\beta,\sigma} \mathbf{g}). \quad (4.16)$$

We note that this flux now depends not only on one face pressure (as it did for the TPFA scheme) but on the pressures of all faces $\sigma_i \in \partial K^v$, where $1 \leq i \leq d$. Furthermore, the position of the face pressure on a face can be chosen dependent on the parameter ξ , $0 \leq \xi < 1$, where $\xi = 0$ corresponds to the center point of the primary grid face and $\xi = 1$ would correspond to the position of the grid vertex (for an illustration see Figure 4.2). Please note that for coupling faces, we always use $\xi = 0$ in order for the face pressure to geometrically coincide with the cell pressure in the corresponding lower-

dimensional control volume. The elimination of the face pressures now occurs within so-called interaction regions, which contain all faces and subsets of control volumes that are connected to a common grid vertex (see again Figure 4.2). Introducing the MPFA half-transmissibilities

$$\omega_{K,\sigma}^i = -|\sigma| |\epsilon_K| \left(\mathbf{n}_{K,\sigma}^T \mathbf{K}_K \boldsymbol{\Xi}_{K^v}^{-T} \right)_i, \quad (4.17)$$

the discrete flux can be rewritten into:

$$F_{\beta}^{K,\sigma} = \sum_i \omega_{K,\sigma}^i \left(\bar{p}_{\beta,\sigma_i}^K - p_{\beta,K} \right) + g_{\beta}^{K,\sigma}. \quad (4.18)$$

Here, it is again $\sigma_i \in \partial K^v$, $1 \leq i \leq d$. Defining a unique normal vector for each face within the interaction region, the fluxes across them can be written in matrix form:

$$\mathbf{f}_{\beta}^d = \mathbf{C}^d \bar{\mathbf{p}}_{\beta}^d + \mathbf{D}^d \mathbf{p}_{\beta}^d + \mathbf{g}_{\beta}^d, \quad (4.19)$$

where the vectors \mathbf{f}_{β}^d and $\bar{\mathbf{p}}_{\beta}^d$ collect all fluxes $F_{\beta}^{K,\sigma}$ and all unknown face pressures $\bar{p}_{\beta}^{K,\sigma}$ within the interaction region, respectively. The emphasis on *unknown* face pressures is done here, as for interaction regions constructed around a boundary vertex, $\bar{\mathbf{p}}_{\beta}^d$ does not contain the known face pressures on Dirichlet boundaries. These are collected in the vector \mathbf{p}_{β}^d together with all cell pressures $p_{\beta,K}$ of the interaction region. Note that the size of $\bar{\mathbf{p}}_{\beta}^d$ is given by the sum of the number of interior faces, Neumann boundary faces and coupling faces on which the transmission conditions (3.26a) are used, within the interaction region. Each row of (4.19) corresponds to a discrete flux across one face of the interaction region. As mentioned above, within the interaction volume a unique normal vector is defined on each face, and the vector \mathbf{f}_{β}^d contains the fluxes $F_{\beta}^{K,\sigma}$ across the faces σ , as seen from the neighboring control volumes K which these normal vectors point out of. Consequently, the vector \mathbf{g}_{β}^d is composed of the coefficients $g_{\beta}^{K,\sigma}$ and the matrices \mathbf{C}^d and \mathbf{D}^d contain the half-transmissibilities $\omega_{K,\sigma}^i$ that appear in the flux expressions (4.18), evaluated for these control volumes. In order to eliminate the face pressures $\bar{\mathbf{p}}_{\beta}^d$, the flux continuity conditions (4.5) are imposed on interior, the transmission conditions (4.11) on coupling, and no-flow boundary conditions on Neumann boundary faces, respectively. This can be cast into the linear system:

$$\mathbf{A}_+^d \bar{\mathbf{p}}_{\beta}^d + \mathbf{B}_+^d \mathbf{p}_{\beta}^d + \mathbf{g}_{\beta,+}^d = \mathbf{A}_-^d \bar{\mathbf{p}}_{\beta}^d + \mathbf{B}_-^d \mathbf{p}_{\beta}^d + \mathbf{g}_{\beta,-}^d + \mathbf{E}^d \mathbf{p}_{\beta}^{d-1}, \quad (4.20)$$

where the left-hand side describes those fluxes of (4.19) that correspond to interior, coupling, and Neumann boundary faces. Thus, \mathbf{A}_+^d , \mathbf{B}_+^d and $\mathbf{g}_{\beta,+}^d$ contain the entries of \mathbf{C}^d , \mathbf{D}^d and \mathbf{g}_β^d from equation (4.19) of the respective rows. The matrices \mathbf{A}_-^d and \mathbf{B}_-^d contain the half-transmissibilities, that appear in (4.18), associated with the interior faces of the interaction region and evaluated for the adjacent control volumes that the normal vector points into. Similarly, $\mathbf{g}_{\beta,-}^d$ contains the coefficients $g_{\beta}^{K,\sigma}$ evaluated within the those control volumes. As mentioned above, we use no-flow boundary conditions on Neumann boundary faces, i.e. the right hand-side of (4.20) is zero in the respective rows. This is done because the Neumann boundary conditions are given in terms of mass fluxes, and for incompressible fluids the corresponding discrete flux cannot be computed straightforward. Moreover, the matrices \mathbf{A}_-^d , \mathbf{B}_-^d are zero in the rows associated with coupling faces, while the vector $\mathbf{g}_{\beta,-}^d$ contains the coefficients $\bar{g}_{\beta}^{K,\sigma}$ in these rows. Furthermore, the matrix \mathbf{E}^d holds the coefficients $\bar{\omega}_{K,\sigma}$ in those rows that are associated with coupling faces $\sigma \in \mathcal{S}_{d,\text{coup}}$ on which the conditions (4.11) are used, and is zero in all other rows. Apart from that, the vector \mathbf{p}_β^{d-1} was introduced, which contains the pressures of the control volumes of the $(d-1)$ -dimensional domain that appear in the interaction region. Rearrangement of (4.20) yields

$$\mathbf{A}^d \bar{\mathbf{p}}_\beta^d = \mathbf{B}^d \mathbf{p}_\beta^d + \Delta \mathbf{g}_\beta^d + \mathbf{E}^d \mathbf{p}_\beta^{d-1}, \quad (4.21)$$

where $\mathbf{A}^d = \mathbf{A}_+^d - \mathbf{A}_-^d$, $\mathbf{B}^d = \mathbf{B}_-^d - \mathbf{B}_+^d$ and $\Delta \mathbf{g}_\beta^d = \mathbf{g}_{\beta,-}^d - \mathbf{g}_{\beta,+}^d$. Thus, the face pressures can be expressed by

$$\bar{\mathbf{p}}_\beta^d = \mathbf{A}^{-d} (\mathbf{B}^d \mathbf{p}_\beta^d + \Delta \mathbf{g}_\beta^d + \mathbf{E}^d \mathbf{p}_\beta^{d-1}), \quad (4.22)$$

where $\mathbf{A}^{-d} = (\mathbf{A}^d)^{-1}$ refers to the inverse of \mathbf{A}^d . Insertion of (4.22) into (4.19) leads to the final expressions for the face fluxes:

$$\mathbf{f}_\beta^d = \underbrace{(\mathbf{C}^d \mathbf{A}^{-d} \mathbf{B}^d + \mathbf{D}^d)}_{:=\mathbf{T}} \mathbf{p}_\beta^d + (\mathbf{C}^d \mathbf{A}^{-d}) \Delta \mathbf{g}_\beta^d + (\mathbf{C}^d \mathbf{A}^{-d} \mathbf{E}^d) \mathbf{p}_\beta^{d-1} + \mathbf{g}_\beta^d. \quad (4.23)$$

The matrix \mathbf{T} is often referred to as the transmissibility matrix. From (4.23) we can see that each face flux possibly depends on the pressure values within all cells of the corresponding interaction region. This leads to much larger cell stencils as for the TPFA scheme, especially on unstructured simplex grids, where many cells might share a common vertex. Please note that on Neumann boundary faces, the fluxes are not com-

puted based on (4.23) together with the employed upwind scheme, but the entire term $\left(\rho_\beta \frac{\kappa_{r\beta}}{\mu_\beta}\right)^{\text{up}} F_\beta^{K,\sigma}$ in (4.4) is substituted by the specified Neumann boundary condition.

Fluxes at junctions In cell-centered schemes, the fluxes are computed on grid faces, which needs special treatment at junctions of fractures ($n = 2$) or junctions of intersections of fractures ($n = 3$). The conditions enforced at junctions are stated in (3.27), which consist of pressure and mass flux continuity across the junctions. Let us consider a face $\sigma \in \mathcal{S}_d$ on a junction and denote with \mathcal{N}_σ the set of control volumes of \mathcal{T}_d that contain σ . In contrast to the faces considered in the previous paragraphs, arbitrary many control volumes might be contained in \mathcal{N}_σ . The pressure continuity is enforced by introducing a single intermediate face pressure \bar{p}_β^σ on the face σ , while mass conservation can be expressed by

$$0 = \sum_{K \in \mathcal{N}_\sigma} \left(\rho_\beta \frac{\kappa_{r\beta}}{\mu_\beta}\right)^* F_\beta^{K,\sigma}, \quad (4.24)$$

where

$$\left(\rho_\beta \frac{\kappa_{r\beta}}{\mu_\beta}\right)^* = \begin{cases} \left(\rho_\beta \frac{\kappa_{r\beta}}{\mu_\beta}\right)^{\text{up}} & \text{if } F_\beta^{K,\sigma} > 0 \\ \left(\rho_\beta \frac{\kappa_{r\beta}}{\mu_\beta}\right)^\times & \text{if } F_\beta^{K,\sigma} < 0 \end{cases}, \quad (4.25)$$

with

$$\left(\rho_\beta \frac{\kappa_{r\beta}}{\mu_\beta}\right)^\times = \frac{\sum_{K \in \mathcal{N}_\sigma: F_\beta^{K,\sigma} > 0} \left(\rho_\beta \frac{\kappa_{r\beta}}{\mu_\beta}\right)^{\text{up}} F_\beta^{K,\sigma}}{\sum_{K \in \mathcal{N}_\sigma: F_\beta^{K,\sigma} < 0} F_\beta^{K,\sigma}} \quad (4.26)$$

being the upwind term associated with branches that receive inflow from the junction and which is constructed such that mass conservation across the junction is guaranteed.

4.1.2 Box scheme

In contrast to the cell-centered schemes presented in the previous section, the BOX scheme defines the control volumes around the grid vertices. For their construction, a dual grid is introduced, which is identical to the one that became apparent in the MPFA scheme. In fact, the interaction regions that were used to define the expressions for the discrete fluxes in the MPFA scheme, are geometrically identical to the control volumes in the BOX scheme. For the construction of the dual grid and the control volumes, we

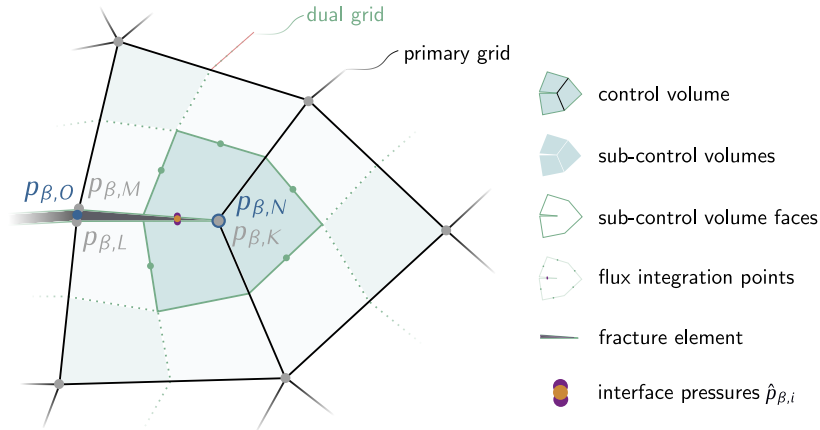


Figure 4.3 – Box scheme. Exemplary configuration of control volumes around a grid vertex. The central control volume R is constructed around a grid vertex lying on an immersed boundary of a fracture. The different colors around the remaining grid vertices illustrate the visible parts of the control volumes associated to them. On vertices that are not on immersed boundaries of the fracture domain, separate control volumes and degrees of freedom are constructed on each side of the fracture. This is illustrated on the left side with the control volumes T and S . Furthermore, the degrees of freedom associated with the lower-dimensional control volumes U and V are depicted.

therefore refer to Section 4.1.1. An illustration of the geometric setting and distribution of degrees of freedom is given in Figure 4.3. With the dual grid defined around the grid vertices, the control-volume boundaries lie within the grid cells. Thus, in contrast to the cell-centered schemes, fluxes are not computed at material discontinuities if the material properties are distributed over the grid cells. On the other hand, the degrees of freedom are then placed at material discontinuities which can be a major drawback if the solution of a primary variable is expected to be discontinuous there. This is the case for two-phase flow, where the saturations are generally discontinuous at material interfaces. This fact has led to the development of a modified BOX scheme for two-phase flow in which the saturations within the sub-control volumes around a grid vertex are reconstructed based on capillary pressure continuity [Reichenberger et al., 2006]. In this work, we will not consider heterogeneities within the individual subdomains and therefore do not include this approach.

However, according to the mixed-dimensional flow equations (3.23)-(3.27), pressures are allowed to be discontinuous across lower-dimensional interfaces. It thus not suffices to associate a single set of primary variables and a single control volume to each grid vertex, but each side of the interface has to be equipped with individual degrees of freedom. At junctions, multiple sets of primary variables are associated to a grid

vertex. An illustration of the degrees of freedom can be seen in the figures 4.3 and 4.4. The first depicts two control volumes and degrees of freedom, namely $p_{\beta,T}$ and $p_{\beta,S}$, for the left grid vertex. The illustration furthermore shows that a single set of primary variables is used on immersed boundaries. We note that a unique control volume exists for each set of primary variables.

Constructing the control volumes around the degrees of freedom in the way described above, we see that they overlap with several primary grid elements. We denote with κ a sub-control volume of the control volume K , where each κ can be associated to a primary grid element E such that $\kappa = K \cap E$. Let \mathcal{C} be the set of sub-control volumes of the discretization together with the subset \mathcal{C}_K such that $K = \bigcup_{\kappa \in \mathcal{C}_K} \kappa$. This lets us split the volume integrals in equation (4.3) into a sum over the sub-control volumes:

$$\begin{aligned} \sum_{\kappa \in \mathcal{C}_K} \int_{\kappa} \frac{\partial (|\epsilon_d^i| \phi_d^i \rho_{\beta} S_{\beta,d}^i)}{\partial t} dV + \sum_{\sigma \in \mathcal{S}_K} \left(\rho_{\beta} \frac{\kappa_{\tau\beta}}{\mu_{\beta}} \right)^{\text{up}} F_{\beta}^{K,\sigma} \\ = \sum_{\kappa \in \mathcal{C}_K} \int_{\kappa} |\epsilon_d^i| q_{\beta,d}^i + \llbracket \rho_{\beta} (\mathbf{q}_{\beta,d+1} \cdot \mathbf{n}) \rrbracket_d^i dV. \end{aligned} \quad (4.27)$$

As for the cell-centered schemes, where the quantities were taken to be constant over the control volumes, we now assume the quantities to be constant per sub-control volume for the storage and source terms:

$$\begin{aligned} \sum_{\kappa \in \mathcal{C}_K} |\kappa| \frac{\partial (|\epsilon_{\kappa}| \phi_{\kappa} \rho_{\beta,\kappa} S_{\beta,\kappa})}{\partial t} + \sum_{\sigma \in \mathcal{S}_K} \left(\rho_{\beta} \frac{\kappa_{\tau\beta}}{\mu_{\beta}} \right)^{\text{up}} F_{\beta}^{K,\sigma} \\ = \sum_{\kappa \in \mathcal{C}_K} |\kappa| (|\epsilon_{\kappa}| q_{\beta,\kappa} + \llbracket \rho_{\beta} (\mathbf{q}_{\beta,d+1} \cdot \mathbf{n}) \rrbracket_{\kappa}). \end{aligned} \quad (4.28)$$

Note that, as in the previous section, we omit the sub- and superscripts indicating the domain on which a quantity is evaluated, as the sub-control volume κ inherently carries this information. It should be mentioned that the material parameters of a sub-control volume, as e.g. ϕ_{κ} , are inherited from the grid cell it is embedded in.

Flux assembly The fluxes are assembled at the centers of the faces that describe the boundaries of the control volumes (see Figure 4.3), thus within primary grid elements. The BOX scheme uses piecewise (per primary grid element) linear basis functions to approximate variables and gradients within the primary grid cells, i.e. it is exemplarily

for the discrete fluid phase pressures at a position $\mathbf{x} \in \Omega_{d,h}^i$:

$$\tilde{p}_{\beta,d}(\mathbf{x}) = \sum_{K=1}^{N_d} p_{\beta,K} \varphi_K(\mathbf{x}), \quad (4.29)$$

where N_d is the number of control volumes. Recall that this is equal to the number of locations of degrees of freedom of the discretization. φ_K refers to the basis function that corresponds to the degrees of freedom associated with control volume K and $p_{\beta,K}$ are the corresponding pressures. The basis functions are defined such that $\varphi_K(\mathbf{x}_K) = 1$, where \mathbf{x}_K is the position of the degrees of freedom associated with control volume K (which is the position of the associated grid vertex), and $\varphi_K(\mathbf{x}_L) = 0$, with $K, L \in \mathcal{T}_d$, $K \neq L$. Furthermore, the basis functions φ_K are only non-zero within primary grid elements that the control volume K overlaps with. Let us collect the indices of the locations at which the degrees of freedom of the discretization \mathcal{T}_d are defined in $\mathcal{J}_d = \{1, \dots, N_d\}$, and denote with \mathcal{J}_E the restriction to those locations that are embedded in the primary grid element $E \in \mathcal{M}_d$. With this, the gradient of a variable, here exemplarily given for the discrete fluid phase pressure $\tilde{p}_{\beta,d}$, at a position $\mathbf{x} \in E$ inside an element $E \in \mathcal{M}_d$ can be expressed as:

$$\nabla \tilde{p}_{\beta,d}(\mathbf{x}) = \sum_{K \in \mathcal{J}_E} p_{\beta,K} \nabla \varphi_K(\mathbf{x}), \quad (4.30)$$

Consequently, we can define the discrete flux $F_\beta^{K,\sigma}$ across a face σ embedded in the grid element E for the BOX scheme with:

$$F_\beta^{K,\sigma} = -|\sigma| \epsilon_K |\mathbf{n}_{K,\sigma}^T| \mathbf{K}_d \left(\sum_{L \in \mathcal{J}_E} p_{\beta,L} \nabla \varphi_L(\mathbf{x}_\sigma) - \mathbf{g} \sum_{L \in \mathcal{J}_E} \rho_{\beta,L} \varphi_L(\mathbf{x}_\sigma) \right). \quad (4.31)$$

Here, \mathbf{x}_σ is the integration point on the face σ , which corresponds to the face center. Furthermore, secondary variables, in this case the fluid density ρ_β , are evaluated at the locations of the degrees of freedom and are then interpolated at the desired position, instead of evaluating the constitutive relationships at the integration point. The fluxes (4.31) are used on interior faces $\sigma \in \mathcal{S}_{d,\text{int}}$, while on Neumann boundary faces the boundary conditions (3.24c) are incorporated. The interface conditions (3.26a) on designated coupling faces $\sigma \in \mathcal{S}_{d,\text{coup}}$ are enforced via a Robin-type boundary condition,

which takes the following form:

$$F_{\beta}^{K,\sigma} = -|\sigma||\epsilon_{\kappa}|\mathbf{n}^T\mathbf{K}_F^{\perp}\left(\frac{\hat{p}_{\beta,F}-\hat{p}_{\beta,E}}{L_F^{\perp}}\mathbf{n}-\mathbf{g}\sum_{L\in\mathcal{J}_E}\rho_{\beta,L}\varphi_L(\mathbf{x}_{\sigma})\right). \quad (4.32)$$

Here, $\kappa \in \mathcal{C}_d$ refers to the sub-control volume of which the face σ describes a part of its boundary and E denotes the primary grid element in which both σ and κ are embedded in. Furthermore, we have denoted with F the primary grid element of the $(d-1)$ -dimensional grid with which the face σ overlaps. The pressures $\hat{p}_{\beta,F} = \sum_{L\in\mathcal{J}_F}p_{\beta,L}\varphi_L(\mathbf{x}_{\sigma})$ and $\hat{p}_{\beta,E} = \sum_{K\in\mathcal{J}_E}p_{\beta,K}\varphi_K(\mathbf{x}_{\sigma})$ refer to the $(d-1)$ - and d -dimensional pressures interpolated at the integration point. Note that the phase viscosity and relative permeabilities given in (3.26a) have dropped due to the definition of the discrete flux and the employed upwind scheme (see (4.2) and (4.5)). On coupling faces $\sigma \in \mathcal{S}_{d,\text{coup}}$, on which the conditions (3.26b) are enforced, the fluxes are computed according to (4.31).

Mass lumping In equation (4.28) we have defined the density and saturation in the storage term to be constant per sub-control volume. In fact, these are taken to be the values from the degrees of freedom that the sub-control volume is connected to, such that the storage term evaluation will have no contribution from other degrees of freedom of the element. This approach is called *mass lumping technique* and has been shown to improve the stability of the scheme [Huber and Helmig, 1999].

4.2 Discretization schemes for the mechanical equations

For the mechanical equations (3.42), we consider the BOX scheme as well as Standard Galerkin finite element schemes as spatial discretization methods, for which we want to outline the basic concepts in the sequel of this section. As presented in Section 3.3.2, in the context of mechanical deformations we only consider two subdomains, namely the subdomains of the bulk medium as well as the lower-dimensional fracture domain. Moreover, the mechanical equations (3.42) are only solved within the bulk domain. Recall the primary discretizations \mathcal{M}_d introduced in the beginning of this chapter, where we note that the highest-dimensional mesh \mathcal{M}_n is used for both the

discretization of the flow equations (see Section 4.1) as well as for the mechanical equations, which will be outlined in the sequel of this section. Please note that we will continue to omit sub- and superscripts on variables, related to the subdomain on which they are evaluated, whenever they are stated for a discrete object, e.g. a control volume or a face, as these objects inherently carry this information.

4.2.1 Box scheme

Following the same line of thought as in the derivation of the discrete equation (4.28) for the mass balance equation, the analogon for the momentum balance equation (3.42d) can be stated as

$$\sum_{\sigma \in \mathcal{S}_K} \mathbf{F}^{K,\sigma} = \sum_{\kappa \in \mathcal{C}_K} |\kappa| |\epsilon_\kappa| \left[(1 - \phi_\kappa) \rho_{s,\kappa} + \sum_{\beta} \phi_\kappa S_{\beta,\kappa} \rho_{\beta,\kappa} \right] \mathbf{g}. \quad (4.33)$$

Here, $\mathbf{F}^{K,\sigma}$ is the discrete force exerted on the face σ as seen from the sub-control volume κ . The variables appearing on the right-hand side of (4.33) are again evaluated for the sub-control volume κ , and we refer to Section 4.3 for details on how the fluid phase saturations and densities are evaluated. Let us denote with $\mathbf{u}_K = (u_{K,1}, \dots, u_{K,n})^T$ the displacement vector defined on the basis of the degrees of freedom associated with the control volume K , composed of the displacements in the individual coordinate directions $u_{K,\chi}$, $\chi \in \{1, \dots, n\}$. We can then express the gradient of the discrete displacement in the coordinate direction χ at the integration point \mathbf{x}_σ of the face σ , which is embedded in the primary grid element E , using (4.30):

$$\nabla \tilde{u}_{\sigma,\chi} = \sum_{K \in \mathcal{J}_E} u_{K,\chi} [\nabla \varphi_K(\mathbf{x}_\sigma)]_\chi. \quad (4.34)$$

The discrete displacement gradient is then given by:

$$\nabla \tilde{\mathbf{u}}_\sigma = (\nabla \tilde{u}_{\sigma,1}, \dots, \nabla \tilde{u}_{\sigma,n})^T. \quad (4.35)$$

This enables us to assemble the discrete strain and stress tensors from (3.42a) and (3.42b) at the integration point \mathbf{x}_σ on the face σ , which we denote with $\tilde{\epsilon}_{s,\sigma}$ and $\tilde{\boldsymbol{\sigma}}_{s,\sigma}$. Note that the Lamé parameters λ and G required for the construction of the discrete stress tensor are taken constant per primary grid element. For the assembly of the total

stress tensor after (3.42c) we furthermore need the effective pressure evaluated for the face σ . Let us denote with $S_{\beta,\sigma}$ and $p_{\beta,\sigma}$ the saturation and pressure of the fluid phase β evaluated at \mathbf{x}_σ (for details we again refer to Section 4.3). The discrete total stress tensor for the face σ is then given by

$$\tilde{\boldsymbol{\sigma}}_\sigma = \tilde{\boldsymbol{\sigma}}_{s,\sigma} - \alpha_B \mathbf{I} \sum_{\beta} S_{\beta,\sigma} p_{\beta,\sigma} \quad (4.36)$$

and the discrete force is $\mathbf{F}^{K,\sigma} = \tilde{\boldsymbol{\sigma}}_\sigma \mathbf{n}_{K,\sigma}$, which completes the discrete momentum balance equation (4.33). Please note that on Neumann boundaries, the discrete force is given by the boundary conditions (3.45b), and on coupling faces $\sigma \in \mathcal{S}_{d,\text{coup}}$ it is determined by the effective pressure in the fracture and the traction force due to contact after (3.43d) and (3.43e). For details on this it is referred to Section 4.3.

4.2.2 Standard Galerkin finite element scheme

The first step is to convert the mechanical problem on Ω_n^i and $\partial\Omega_n^i$, i.e. equations (3.42) with boundary and interface conditions (3.45), (3.43d) and (3.43e), into its weak formulations. To this end, let us consider the functional spaces

$$\mathbf{W}^i = \{\mathbf{w} \in (H^1(\Omega_n^i))^n : w_\chi = 0 \text{ on } \Gamma_n^{\text{D},u_\chi} \cap \partial\Omega_n^i\}, \quad (4.37a)$$

$$\mathbf{U}^i = \{\mathbf{u} \in (H^1(\Omega_n^i))^n : u_\chi = u_\chi^{\text{D}} \text{ on } \Gamma_n^{\text{D},u_\chi} \cap \partial\Omega_n^i\}, \quad (4.37b)$$

where we denoted with w_χ the element of test function \mathbf{w} associated with the coordinate direction $\chi \in \{1, \dots, n\}$, for which we require that it is zero on the boundary segments of Ω_n^i on which Dirichlet boundary conditions are set for the displacement u_χ^i , $\chi \in \{x_1, \dots, x_n\}$. Correspondingly, for the trial functions \mathbf{u} we require the fulfillment of the Dirichlet boundary conditions. Multiplication of (3.42d) with a test function $\mathbf{w} \in \mathbf{W}^i$ and integration over the domain Ω_n^i yields the variational formulation:

$$\begin{aligned} & \int_{\Omega_n^i} (\nabla \cdot \boldsymbol{\sigma}^i) \cdot \mathbf{w} \, dx \\ & + \int_{\Omega_n^i} \left((1 - \phi_n^i) \rho_s + \sum_{\beta} \phi_n^i S_{\beta,n}^i \rho_{\beta,n}^i \right) \mathbf{g} \cdot \mathbf{w} \, dx = 0, \quad \forall \mathbf{w} \in \mathbf{W}^i, \end{aligned} \quad (4.38)$$

and after integration by parts of the left term:

$$\begin{aligned}
& - \int_{\Omega_n^i} \nabla \mathbf{w} : \boldsymbol{\sigma}^i dx + \int_{\partial \Omega_n^i} \mathbf{w} \cdot (\boldsymbol{\sigma}^i \mathbf{n}) d\Gamma \\
& + \int_{\Omega_n^i} \left((1 - \phi_n^i) \rho_s + \sum_{\beta} \phi_n^i S_{\beta,n}^i \rho_{\beta,n}^i \right) \mathbf{g} \cdot \mathbf{w} dx = 0, \quad \forall \mathbf{w} \in \mathbf{W}^i.
\end{aligned} \tag{4.39}$$

Since the test functions vanish on Dirichlet boundaries (see (4.37a)), the second term in (4.39) can be substituted by the Neumann boundary conditions (3.45b) and the interface conditions (3.43d) and (3.43d) :

$$\begin{aligned}
& - \int_{\Omega_n^i} \nabla \mathbf{w} : \boldsymbol{\sigma}^i dx + \int_{\Gamma_n^{N,x}} \mathbf{w} \cdot \mathbf{t}_\chi^N d\Gamma \\
& + \int_{\partial \Omega_n^i \cap \Gamma_{n-1}^{i,j,+}} \mathbf{w} \cdot \left(\boldsymbol{\tau}^j + \mathbf{n} \sum_{\beta} S_{\beta,n-1}^j p_{\beta,n-1}^j \right) d\Gamma \\
& + \int_{\partial \Omega_n^i \cap \Gamma_{n-1}^{i,j,-}} \mathbf{w} \cdot \left(-\boldsymbol{\tau}^j + \mathbf{n} \sum_{\beta} S_{\beta,n-1}^j p_{\beta,n-1}^j \right) d\Gamma \\
& + \int_{\Omega_n^i} \left((1 - \phi_n^i) \rho_s + \mathbf{n} \sum_{\beta} \phi_n^i S_{\beta,n}^i \rho_{\beta,n}^i \right) \mathbf{g} \cdot \mathbf{w} dx = 0, \quad \forall \mathbf{w} \in \mathbf{W}^i,
\end{aligned} \tag{4.40}$$

for all $j \in \mathcal{N}_n^{i,\downarrow}$. Furthermore, with (3.42c) this can be recast into

$$\begin{aligned}
& - \int_{\Omega_n^i} \nabla \mathbf{w} : \boldsymbol{\sigma}_s^i dx + \int_{\Omega_n^i} \nabla \mathbf{w} : \left(\alpha_B \mathbf{I} \sum_{\beta} S_{\beta,n}^i \rho_{\beta,n}^i \right) dx + \int_{\Gamma_n^{N,x}} \mathbf{w} \cdot \mathbf{t}_\chi^N d\Gamma \\
& + \int_{\partial \Omega_n^i \cap \Gamma_{n-1}^{i,j,+}} \mathbf{w} \cdot \left(\boldsymbol{\tau}^j + \mathbf{n} \sum_{\beta} S_{\beta,n-1}^j p_{\beta,n-1}^j \right) d\Gamma \\
& + \int_{\partial \Omega_n^i \cap \Gamma_{n-1}^{i,j,-}} \mathbf{w} \cdot \left(-\boldsymbol{\tau}^j + \mathbf{n} \sum_{\beta} S_{\beta,n-1}^j p_{\beta,n-1}^j \right) d\Gamma \\
& + \int_{\Omega_n^i} \left((1 - \phi_n^i) \rho_s + \phi_n^i \sum_{\beta} S_{\beta,n}^i \rho_{\beta,n}^i \right) \mathbf{g} \cdot \mathbf{w} dx = 0, \quad \forall \mathbf{w} \in \mathbf{W}^i,
\end{aligned} \tag{4.41}$$

Let us now denote with $\tilde{\mathbf{W}}^i \subset \mathbf{W}^i$ and $\tilde{\mathbf{U}}^i \subset \mathbf{U}^i$ the finite element approximating spaces associated with the discretization \mathcal{M}_n^i , and let $\{\boldsymbol{\varphi}_1, \dots, \boldsymbol{\varphi}_N\}$ be a basis of them. On this basis we express both the discrete trial function $\tilde{\mathbf{u}} \in \mathbf{U}^i$ and test function

$\tilde{\mathbf{w}} \in \mathbf{W}^i$ with

$$\mathbf{u} \approx \tilde{\mathbf{u}} = (\tilde{u}_1, \dots, \tilde{u}_n)^T = \sum_{j=1}^N \boldsymbol{\varphi}_j \circ \hat{\mathbf{u}}_j, \quad (4.42a)$$

$$\mathbf{w} \approx \tilde{\mathbf{w}} = (\tilde{w}_1, \dots, \tilde{w}_n)^T = \sum_{j=1}^N \boldsymbol{\varphi}_j \circ \hat{\mathbf{w}}_j, \quad (4.42b)$$

where

$$\boldsymbol{\varphi}_j \circ \hat{\mathbf{u}}_j = (\varphi_{j,1}\hat{u}_{j,1}, \dots, \varphi_{j,n}\hat{u}_{j,n})^T, \quad (4.43a)$$

$$\boldsymbol{\varphi}_j \circ \hat{\mathbf{w}}_j = (\varphi_{j,1}\hat{w}_{j,1}, \dots, \varphi_{j,n}\hat{w}_{j,n})^T, \quad (4.43b)$$

with $\varphi_{j,\chi}$ denoting the j -th basis function in coordinate direction χ , $\chi \in \{1, \dots, n\}$, and $\hat{u}_{j,\chi}$ and $\hat{w}_{j,\chi}$ being the corresponding coefficients. Furthermore, $\hat{\mathbf{u}}_j = (\hat{u}_{j,1}, \dots, \hat{u}_{j,n})^T$ is the coefficient vector associated with the basis function $\boldsymbol{\varphi}_j$ and $\hat{\mathbf{w}}_j$ is defined accordingly. The expressions for the gradients follow from (4.42) and (4.43):

$$\nabla \mathbf{u} \approx \nabla \tilde{\mathbf{u}} = \begin{pmatrix} \partial \tilde{u}_1 / \partial x_1 & \dots & \partial \tilde{u}_1 / \partial x_n \\ \vdots & \ddots & \\ \partial \tilde{u}_n / \partial x_1 & \dots & \partial \tilde{u}_n / \partial x_n \end{pmatrix} = \sum_{j=1}^N \nabla \boldsymbol{\varphi}_j \odot \hat{\mathbf{u}}_j, \quad (4.44a)$$

$$\nabla \mathbf{w} \approx \nabla \tilde{\mathbf{w}} = \begin{pmatrix} \partial \tilde{w}_1 / \partial x_1 & \dots & \partial \tilde{w}_1 / \partial x_n \\ \vdots & \ddots & \\ \partial \tilde{w}_n / \partial x_1 & \dots & \partial \tilde{w}_n / \partial x_n \end{pmatrix} = \sum_{j=1}^N \nabla \boldsymbol{\varphi}_j \odot \hat{\mathbf{w}}_j, \quad (4.44b)$$

where

$$\nabla \boldsymbol{\varphi}_j \odot \hat{\mathbf{u}}_j = \begin{pmatrix} \hat{u}_{j,1} \partial \varphi_{j,1} / \partial x_1 & \dots & \hat{u}_{j,1} \partial \varphi_{j,1} / \partial x_n \\ \vdots & \ddots & \\ \hat{u}_{j,n} \partial \varphi_{j,n} / \partial x_1 & \dots & \hat{u}_{j,n} \partial \varphi_{j,n} / \partial x_n \end{pmatrix}, \quad (4.45a)$$

$$\nabla \boldsymbol{\varphi}_j \odot \hat{\mathbf{w}}_j = \begin{pmatrix} \hat{w}_{j,1} \partial \varphi_{j,1} / \partial x_1 & \dots & \hat{w}_{j,1} \partial \varphi_{j,1} / \partial x_n \\ \vdots & \ddots & \\ \hat{w}_{j,n} \partial \varphi_{j,n} / \partial x_1 & \dots & \hat{w}_{j,n} \partial \varphi_{j,n} / \partial x_n \end{pmatrix}. \quad (4.45b)$$

This lets us define the discrete strain and stress tensors, after (2.25) and (2.23):

$$\boldsymbol{\epsilon}_s^i \approx \tilde{\boldsymbol{\epsilon}}_s^i = \frac{1}{2} \sum_{j=1}^N \nabla \boldsymbol{\varphi}_j \odot \hat{\mathbf{u}}_j + (\nabla \boldsymbol{\varphi}_j \odot \hat{\mathbf{u}}_j)^T, \quad (4.46a)$$

$$\boldsymbol{\sigma}_s^i \approx \tilde{\boldsymbol{\sigma}}_s^i = \frac{1}{2} \sum_{j=1}^N \boldsymbol{\mathcal{C}} : \left[\nabla \boldsymbol{\varphi}_j \odot \hat{\mathbf{u}}_j + (\nabla \boldsymbol{\varphi}_j \odot \hat{\mathbf{u}}_j)^T \right]. \quad (4.46b)$$

Plugging (4.46a) and (4.46b) into (4.41), we obtain

$$\begin{aligned} & -\frac{1}{2} \sum_{i=1}^N \sum_{j=1}^N \int_{\Omega_n^i} (\nabla \boldsymbol{\varphi}_i \odot \hat{\mathbf{w}}_i) : \boldsymbol{\mathcal{C}} : \left[\nabla \boldsymbol{\varphi}_j \odot \hat{\mathbf{u}}_j + (\nabla \boldsymbol{\varphi}_j \odot \hat{\mathbf{u}}_j)^T \right] dx \\ & + \sum_{i=1}^N \int_{\Omega_n^i} (\nabla \boldsymbol{\varphi}_i \odot \hat{\mathbf{w}}_i) : \left(\alpha_B \mathbf{I} \sum_{\beta} S_{\beta,n}^i \rho_{\beta,n}^i \right) dx \\ & + \sum_{i=1}^N \int_{\Gamma_n^{N,x}} (\boldsymbol{\varphi}_i \circ \hat{\mathbf{w}}_i) \cdot \mathbf{t}_x^N d\Gamma \\ & + \sum_{i=1}^N \int_{\partial \Omega_n^i \cap \gamma_{n-1}^{ij,+}} (\boldsymbol{\varphi}_i \circ \hat{\mathbf{w}}_i) \cdot \left(\boldsymbol{\tau}^j + \mathbf{n} \sum_{\beta} S_{\beta,n-1}^j p_{\beta,n-1}^j \right) d\Gamma \\ & + \sum_{i=1}^N \int_{\partial \Omega_n^i \cap \gamma_{n-1}^{ij,-}} (\boldsymbol{\varphi}_i \circ \hat{\mathbf{w}}_i) \cdot \left(-\boldsymbol{\tau}^j + \mathbf{n} \sum_{\beta} S_{\beta,n-1}^j p_{\beta,n-1}^j \right) d\Gamma \\ & + \sum_{i=1}^N \int_{\Omega_n^i} (\boldsymbol{\varphi}_i \circ \hat{\mathbf{w}}_i) \cdot \mathbf{g} \left((1 - \phi_n^i) \rho_s + \phi_n^i \sum_{\beta} S_{\beta,n}^i \rho_{\beta,n}^i \right) dx = 0, \end{aligned} \quad (4.47)$$

which can be cast into a linear system of size $N \cdot n$, where N is the size of the basis and n is the dimension of the domain. Note that this requires a linearization due to a possibly non-linear dependency of pressures and saturations on the displacement. In this work, we apply the Newton-Raphson method to solve the non-linear system of equations (see Section 4.4). For the assembly of the linear system, the integrals in (4.47) need to be computed. On the basis of the discretization \mathcal{M}_n^i , the integrals are split into sums of integrals over the elements $E \in \mathcal{M}_n^i$, which are computed based on a quadrature rule. However, the integration requires evaluating the fluid phase saturations and pressures at the integration points, which will be discussed in Section 4.3. Note that in this work we consider piecewise linear and piecewise quadratic bases for the displacements. For both, the distributions of the degrees of freedom on a triangular mesh are illustrated

in Figure 4.4. Note that we use the abbreviations CG1 and CG2 to refer to continuous piecewise linear and piecewise quadratic finite elements.

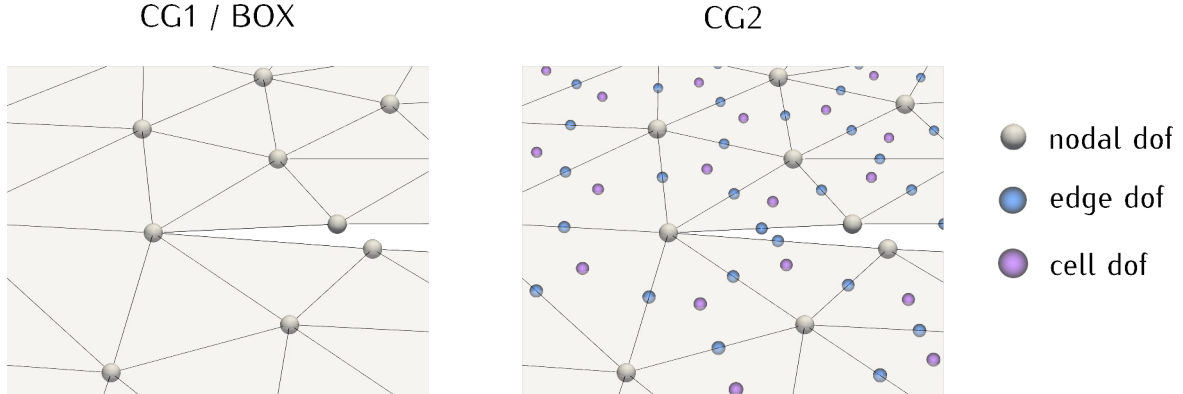


Figure 4.4 – Distribution of degrees of freedom. In both the BOX scheme and linear finite elements (CG1) the degrees of freedom are distributed among the grid vertices, however, at fractures, multiple degrees of freedom associated with the sides of the fractures are introduced. For quadratic finite elements (CG2), additional degrees of freedom are introduced at the cell and edge centers. Again, on fractures individual degrees of freedom are assigned to each side of the fracture. Note that the fracture opening is for illustrative purposes only, in the computational mesh the degrees of freedom on the two sides of the fracture overlap.

4.3 Evaluation of the coupling terms

In both the mixed-dimensional flow problem as well as the mixed-dimensional poromechanical problem, various processes lead to a coupling between the individual subdomains. For instance, in the full poromechanical problem considering two-phase flow, the flow equations for the bulk domain are coupled to the momentum balance equation for the bulk porous medium and vice versa, due to the dependency of the porosity on the displacement via (3.30), and the dependency of the body forces and the total stresses on the fluid pressures and saturations (see equations (3.42d) and (3.42c)). Apart from that, the flow equations for the bulk and the fracture domain are coupled due to transfer fluxes appearing as additional source term in the equations for the fracture domain. Furthermore, the contact conditions (3.43a) and (3.43b) depend on the bulk displacements, while the momentum balance equation of the porous medium depends on the Lagrange multiplier $\boldsymbol{\tau}$ for the contact tractions via (3.43d) and (3.43e). Finally, the flow equations in the fracture domain depend on the bulk displacement due to the relationship (3.47) for the hydraulic aperture, and the effective pressure in the

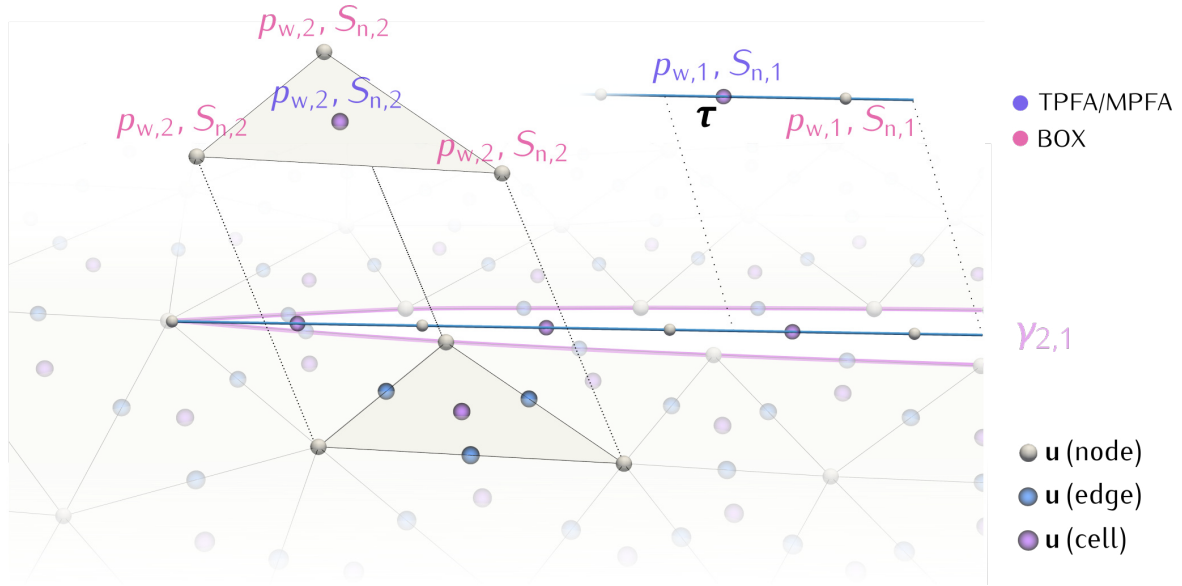


Figure 4.5 – Distribution of degrees of freedom for two-phase flow poroelastic fractured media. Depicted is a part of the bulk domain discretized with quadratic finite elements, where the degrees of freedom for the displacement are distributed over the cells, edges and nodes of the grid. Furthermore, the distribution of degrees of freedom for the flow equations of the bulk domain is depicted for an exemplary element. The degrees of freedom in the fracture as well as the contact tractions are illustrated along the line in the center of the open fracture. The blue variables refer to the case of a cell-centered scheme being used for the discretization of the flow equations, while the red variables are used with the BOX scheme.

fracture enters the momentum balance equation of the porous medium via the interface conditions (3.43d) and (3.43e).

In Section 4.1 we have seen that three different finite-volume schemes are considered for the discretization of the mixed-dimensional flow equations, namely the TPFA, MPFA and the BOX scheme. For the discretization of the mechanical equations, we consider the BOX as well as continuous piecewise linear or piecewise quadratic finite elements (see Section 4.2). The implementation allows for arbitrary combinations of schemes to be used for flow and mechanics, with the difference being the way how the coupling terms are evaluated.

Figure 4.5 illustrates how the degrees of freedom are distributed in this setting when using continuous, piecewise quadratic finite elements for the discretization of the momentum balance equation of the porous medium. On one of the depicted elements it is exemplarily shown how the degrees of freedom of the flow equations are distributed, i.e. along the vertices or the cells of the grid, depending on if a cell-centered or the BOX

scheme is used. The same holds for the lower-dimensional grid used for the fractures, which is conforming to the discretization of the interface in the bulk grid. Furthermore, we use piecewise constant Lagrange multipliers $\boldsymbol{\tau}$ for the contact traction on the same lower-dimensional grid used for the fractures, i.e. we locate the tractions $\boldsymbol{\tau}$ at the cell centers of the lower-dimensional grid. However, Wohlmuth [2011] show, that when linear finite elements are used for the mechanical deformations in contact problems, piecewise constant Lagrange multipliers on a conforming lower-dimensional grid lead to an unstable discretization. To overcome this problem, we use a coarser grid for the Lagrange multiplier when linear finite elements or the BOX scheme are used for the mechanics in the bulk domain. Although arbitrary grid choices are technically possible in the implementation, we choose the discretization of the Lagrange multiplier domain such that the discretization length is twice of that used for the discretization of flow in the fracture in two-dimensional settings. In three-dimensional settings in which triangular grids are used for the discretization of the fracture surfaces, we use a ratio of one third. An illustration for a two-dimensional case can be found in Section 5.3.1 in Figure 5.35.

Coupling fluxes The computation of the transfer fluxes between matrix and fracture has been discussed already in Section 4.1. For cell-centered schemes the position of the intermediate unknowns coincide with the locations of the degrees of freedom inside the fractures, and the fluxes can be computed without the need for interpolation. In the BOX scheme, however, the flux integration points lie in the centers of the sub-control volumes of the lower-dimensional discretization. Therefore, we first interpolate the primary variables to the integration point, then evaluate the secondary variables and finally compute the fluxes.

Porosity The effective porosity for both the flow equations and the momentum balance equation of the bulk domain is evaluated element-wise by computing $\nabla \cdot \mathbf{u}$ at the center of the elements and using equation (3.30).

Total stresses For the assembly of the total stress tensors at integration points within the bulk grid elements, the primary variables of the bulk flow equations are interpolated to the integration point and are then used to evaluate the secondary variables. With

those, the total stress is computed after (2.32). If a cell-centered scheme is used for the discretization of the flow equations, the interpolation is trivial as in this case all variables are constant per element. For the BOX scheme a linear interpolation is used (see Section 4.1.2). Please note also that the integration points are quadrature points if finite elements are used for the discretization of the mechanical equations, or the centers of the sub-control volume faces for which the discrete force is to be computed if the BOX scheme is employed (see Section 4.2.1).

Displacement jump During the assembly of the contact conditions (3.43a) and (3.43b), the jump in displacement has to be computed at integration points on the lower-dimensional grid elements of the discretization used for the Lagrange multiplier. To this end, at each integration point the displacements are evaluated within the two bulk grid elements adjacent to it and the displacement jump is computed after (3.33).

Hydraulic fracture aperture The hydraulic aperture is computed for each element of the lower-dimensional discretization by evaluating the displacement field in the two adjacent bulk grid elements at its center. With this, the normal displacement jump and the aperture are computed after (3.33a) and (3.47).

Internal tractions The contact tractions as well as the effective pressure in the fracture domain act as internal tractions on the bulk domain (see equations (3.43d) and (3.43e)). This traction is evaluated on an element-local basis by means of integration over those primary grid element faces that lie on internal boundaries. During the integration, the Lagrange multiplier is evaluated at each integration point, which is trivial as element-wise constant Lagrange multipliers are used. However, the effective pressure in an adjacent fracture might vary along the boundary if the BOX is used. Therefore, the primary variables of the flow equations in the fracture domain are interpolated at the integration point, and are then used to evaluate secondary variables on the basis of which the effective pressure is computed according to (3.43d). Note that this interpolation is again trivial if a cell-centered scheme is used for the discretization of the flow equations. If the BOX scheme is employed to discretize the mechanical equations, the internal boundary integral is evaluated by computing the traction at a single integration point per face (at the face center).

4.4 Solution strategy

For the temporal integration from a time t to the time $t + \Delta t$, we discretize the time derivatives in (3.23b) and (3.40b) with

$$\frac{\partial (|\epsilon_d^i| \phi_d^i \rho_\beta S_{\beta,d}^i)}{\partial t} = \frac{(|\epsilon_d^i| \phi_d^i \rho_\beta S_{\beta,d}^i)^{t+\Delta t} - (|\epsilon_d^i| \phi_d^i \rho_\beta S_{\beta,d}^i)^t}{\Delta t}, \quad (4.48)$$

where $(\cdot)^t$ is the known state at time t and $(\cdot)^{t+\Delta t}$ is the state for which it is solved. We employ an implicit time discretization scheme, i.e. all terms appearing in the problem formulations of Section 3.2.2 and Section 3.3.2 are evaluated on the time level $t + \Delta t$, except for the known state $(\cdot)^t$. Except for the case of incompressible single-phase flow, all equations are nonlinear, and we employ *Newton's method* as nonlinear solver. This means that in each Newton iteration, a linear system of the form

$$\mathbf{J} (\boldsymbol{\chi}^{k+1} - \boldsymbol{\chi}^k) = -\mathbf{r} \quad (4.49)$$

is solved. Here, $\mathbf{r} = \mathbf{r}(\boldsymbol{\chi}^k)$ is the residual of the nonlinear system of equations evaluated for the solution $\boldsymbol{\chi}^k$ in the k -th iteration and $\mathbf{J} = (\partial \mathbf{r} / \partial \boldsymbol{\chi})|_{\boldsymbol{\chi}=\boldsymbol{\chi}^k}$ is the corresponding Jacobian matrix. The new iterate $\boldsymbol{\chi}^{k+1}$ is obtained by solving the system (4.49) for the update $\Delta \boldsymbol{\chi}^k = \boldsymbol{\chi}^{k+1} - \boldsymbol{\chi}^k$.

Implementation in DuMu^x All schemes and models presented in this work have been implemented in the open-source simulator DuMu^x [Flemisch et al., 2011, Koch et al., 2018a], which is based on the modular C++ framework DUNE [Bastian et al., 2008a,b]. The latest DuMu^x release features a framework for multi-domain simulations, where each subdomain is represented by an individual DuMu^x model. This framework has been used in several works, for example, in the context of coupling free flow and porous medium flow [Weishaupt et al., 2019, Schneider et al., 2019], root-soil interaction [Koch et al., 2018b], biological tissue perfusion [Koch et al., 2019b] and well modeling [Koch et al., 2019a]. An overview over the framework, implementation concepts and several examples can be found in Koch et al. [2019]. For the assembly of the Jacobian matrix, DuMu^x provides a general multi-domain assembler implementation, in which the matrix entries are computed by means of numeric differentiation, and which assembles the

discrete systems in the form

$$\begin{bmatrix} \mathbf{A}_1 & \mathbf{C}_{12} & \cdots & \mathbf{C}_{1m} \\ \mathbf{C}_{21} & \mathbf{A}_2 & & \\ \vdots & & \ddots & \\ \mathbf{C}_{m1} & & & \mathbf{A}_m \end{bmatrix} \begin{bmatrix} \Delta\boldsymbol{\chi}_1 \\ \Delta\boldsymbol{\chi}_2 \\ \vdots \\ \Delta\boldsymbol{\chi}_m \end{bmatrix} = \begin{bmatrix} -\mathbf{r}_1 \\ -\mathbf{r}_2 \\ \vdots \\ -\mathbf{r}_m \end{bmatrix}. \quad (4.50)$$

Therein, m is the number of subdomains of the model and \mathbf{A}_i , $1 < i \leq m$, are the Jacobians of subdomain i . The coupling Jacobians $\mathbf{C}_{ij} = \partial\mathbf{r}_i/\partial\boldsymbol{\chi}_j$, $1 < i, j \leq m$, contain the derivatives of the residuals of subdomain i with respect to the degrees of freedom of subdomain j . As an example, the Jacobian matrix pattern for the mixed-dimensional poromechanical problem considering single-phase flow looks as follows:

$$\begin{bmatrix} \mathbf{A}_{\mathbf{p}_n} & \mathbf{C}_{\mathbf{p}_n}^{\mathbf{p}_{n-1}} & \mathbf{C}_{\mathbf{p}_n}^{\mathbf{U}} & \mathbf{0} \\ \mathbf{C}_{\mathbf{p}_{n-1}}^{\mathbf{p}_n} & \mathbf{A}_{\mathbf{p}_{n-1}} & \mathbf{C}_{\mathbf{p}_{n-1}}^{\mathbf{U}} & \mathbf{0} \\ \mathbf{C}_{\mathbf{U}}^{\mathbf{p}_n} & \mathbf{C}_{\mathbf{U}}^{\mathbf{p}_{n-1}} & \mathbf{A}_{\mathbf{U}} & \mathbf{C}_{\mathbf{U}}^{\mathbf{T}} \\ \mathbf{0} & \mathbf{0} & \mathbf{C}_{\mathbf{T}}^{\mathbf{U}} & \mathbf{A}_{\mathbf{T}} \end{bmatrix} \begin{bmatrix} \mathbf{p}_n \\ \mathbf{p}_{n-1} \\ \mathbf{U} \\ \mathbf{T} \end{bmatrix} = \begin{bmatrix} -\mathbf{r}_{\mathbf{p}_n} \\ -\mathbf{r}_{\mathbf{p}_{n-1}} \\ -\mathbf{r}_{\mathbf{U}} \\ -\mathbf{r}_{\mathbf{T}} \end{bmatrix}, \quad (4.51)$$

where we have collected the pressure degrees of freedom of the bulk and fracture domain in the vectors \mathbf{p}_n and \mathbf{p}_{n-1} , the degrees of freedom for the displacement in the bulk domain in \mathbf{U} and the Lagrange multipliers in \mathbf{T} . We have used these as subscripts to indicate the subdomain of which a residual is evaluated or differentiated, while for the derivatives the superscripts indicate with respect to which degrees of freedom they are evaluated. Note that $\mathbf{C}_{\mathbf{p}_n}^{\mathbf{p}_{n-1}} = (\mathbf{C}_{\mathbf{p}_{n-1}}^{\mathbf{p}_n})^T$, but the overall system matrix is non-symmetric.

The contact conditions (3.43a) and (3.43b) have kinks and jumps and are thus not differentiable for all values of the displacement jump. Specially tailored nonlinear solvers have been developed to solve the nonlinear complementary functions given in (3.38) and (3.39) (see e.g. Wohlmuth [2011], Berge et al. [2019]). However, for now we rely on the standard *Newton* solver available in DuMu^x together with the assembly routines based on numeric differentiation. Even though the cases presented in this document worked fine, there might be situations in which this leads to slow or even no convergence in the nonlinear solver. This is a current limitation of this approach and should be addressed in future investigations.

5 Numerical experiments

In this chapter we want to present several numerical examples with which we want to test and compare the different numerical schemes presented in Chapter 4. The focus of these investigations lies in comparing the schemes with respect to accuracy, where possible, as well as computational efficiency and the ability to reproduce expected phenomenological behavior. For the first set of test cases, in which mechanical deformations are not considered, we show additional solutions obtained with another discrete fracture model available in DuMu^x for comparison. This additional scheme was presented in Reichenberger et al. [2006], where we refer to for details on the method. At this point, we only want to mention that it is a conforming approach as well, in which the fractures are also modeled as lower-dimensional objects. Furthermore, the discretizations are also required to be conforming such that the bulk grid element faces coincide with the elements of the lower-dimensional discretization. The approach is based on the BOX method, but does not introduce additional degrees of freedom on the fractures as done in the BOX scheme presented in Section 4.1.2. Instead, pressure continuity across the fractures is assumed and transfer fluxes between fractures and matrix are not assembled. The fractures solely add storage capacity to the control volumes and provide additional connectivity between control volumes along grid faces that live on a fracture. For two-phase flow, the saturations in the matrix are reconstructed based on capillary pressure continuity between fractures and matrix. Detailed descriptions of the scheme can be found in the above-mentioned reference or in Tatomir [2013]. The presentations in both references are for two-phase flow, but the simplification to single-phase flow is straightforward. In the following, results obtained with this scheme are presented for comparison, where applicable, and we refer to the scheme with the alias BOX-CONT, in which the suffix CONT refers to the pressure being assumed continuous across the fractures. Finally, it should be mentioned that the grids for all examples shown in this chapter were created using the open-source mesh generator Gmsh [Geuzaine and Remacle, 2009].

5.1 Single-phase flow in rigid fractured porous media

The numerical examples shown in this section do not consider deformations of the solid skeleton, thus, in all examples the mixed-dimensional flow equations (3.23)-(3.27) are solved. Furthermore, a single fluid phase is considered, for which reason we omit subscripts related to the index of a phase throughout this section. For single-phase flow, we further note that $\kappa_r = 1.0$, which simplifies the problem formulation accordingly.

5.1.1 Test case 1: convergence test

In this test case we want to study the convergence behavior of the schemes for stationary and incompressible single-phase flow in the absence of gravity. For this setting, an analytical solution to the equi-dimensional problem in the case of a single fracture can be found in Hægland et al. [2009], which has been used in several works to study the convergence behavior of hybrid-dimensional schemes [Sandve et al., 2012, Ahmed et al., 2015]. It considers a rectangular domain $\Omega = (-0.5, 0.5) \times (-0.5, 0.5)$ with the subdomains $\Omega_f = (-0.5, 0.5) \times (-a/2, a/2)$ and $\Omega_b = \Omega \setminus \Omega_f$ for the fracture and the surrounding bulk porous matrix, respectively. The fluid properties are set to $\mu = 1 \text{ Pa}\cdot\text{s}$ and $\rho = 1 \text{ kg}/\text{m}^3$ and the permeabilities are defined as $\mathbf{K}_f = \mathbf{K}_1 = k \mathbf{I} \text{ m}^2$ and $\mathbf{K}_b = \mathbf{K}_2 = \mathbf{I} \text{ m}^2$. The analytical solution for the pressure distribution is given by

$$p(x, y) = \begin{cases} k \cos(x) \cosh(y) + (1 - k) \cos(x) \cosh(a/2) & (x, y) \in \Omega_b \\ \cos(x) \cosh(y) & (x, y) \in \Omega_f, \end{cases} \quad (5.1)$$

with the source term:

$$q(x, y) = \begin{cases} (1 - k) \cos(x) \cosh(a/2) & (x, y) \in \Omega_b \\ 0 & (x, y) \in \Omega_f. \end{cases} \quad (5.2)$$

Earlier studies reported second order convergence of pressure for both highly conductive ($k = 1 \cdot 10^4$) as well as low-permeable ($k = 1 \cdot 10^{-4}$) fractures as long as the discretization length h of the grid is significantly larger than the aperture, while convergence is lost when h approaches a [Sandve et al., 2012, Ahmed et al., 2015]. This

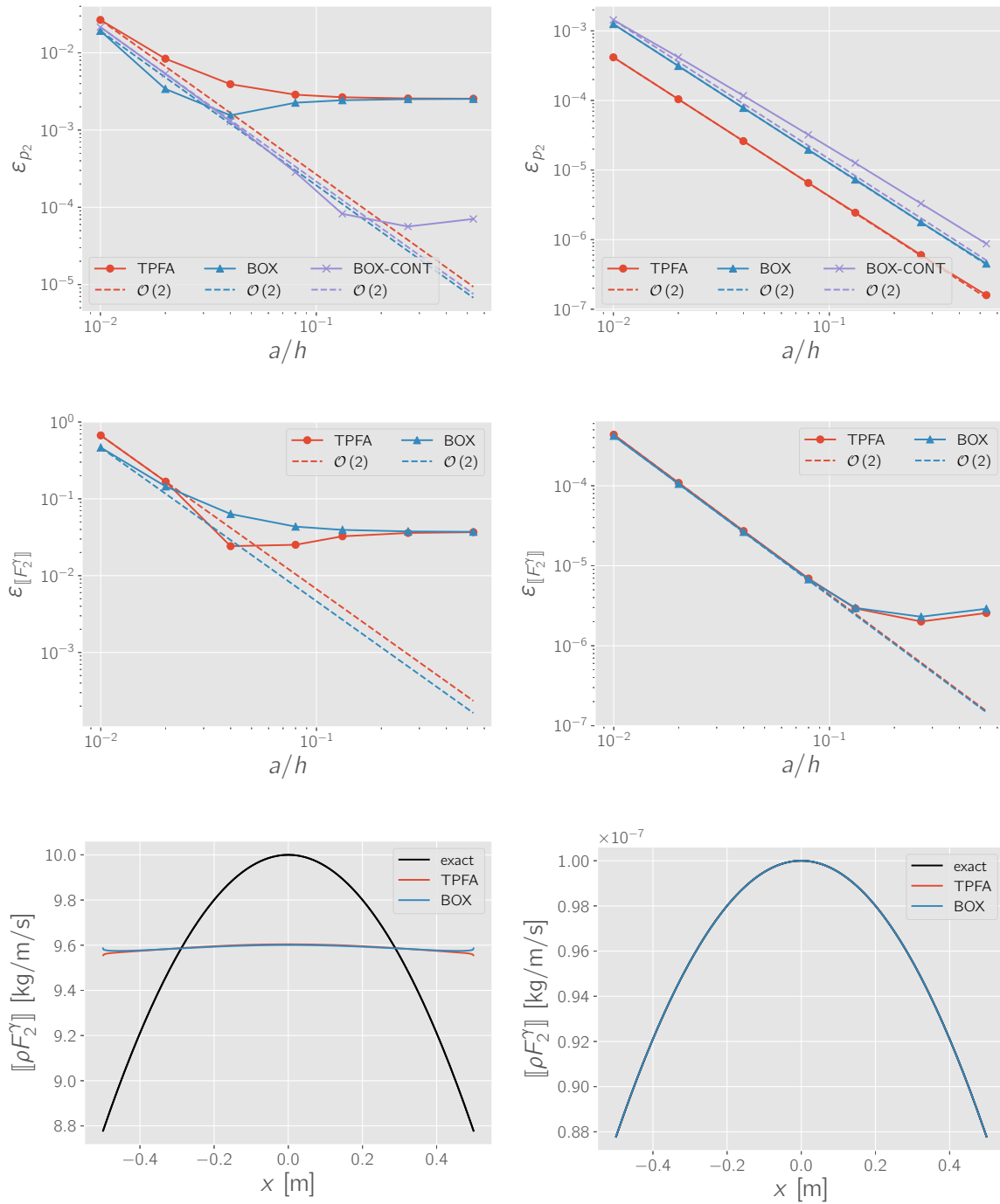


Figure 5.1 – Test case 1: convergence rates. Error in bulk pressure (top row) and the jump in fluxes (center row) versus the ratio of aperture to discretization length, where the aperture is $a = 1 \cdot 10^{-3}$ m. The bottom row shows the coupling source term plotted along the fracture for the finest grid. The left column shows the results obtained for the $k = 1 \cdot 10^4$ and the right column for $k = 1 \cdot 10^{-4}$.

is due to the fact that in a hybrid-dimensional discretization, a volume error is introduced as the volume of the fractures is effectively added to the domain. As long as the discretization length is small, this error does not seem to dominate, but becomes apparent in the convergence behavior of the pressure as the grid is refined further. We study the convergence behavior of the schemes on a series of refined grids $\mathcal{M}_{d,i}$, where $d \in \{1, 2\}$ again denotes the dimension of the grid and $i \in \{0, \dots, m\}$ is the refinement index. We use

$$\varepsilon_{p_d}^i = \sqrt{\frac{\sum_{E \in \mathcal{M}_{d,i}} (p_E - p_E^*)^2 |E|}{\sum_{E \in \mathcal{M}_{d,m}} (p_E^*)^2 |E|}}, \quad (5.3)$$

to measure the relative error in pressure, where p_E and p_E^* refer to the discrete and the exact solutions evaluated at the center of the element E . Furthermore, we use

$$\varepsilon_{\llbracket F_2^\gamma \rrbracket}^i = \sqrt{\frac{\sum_{E \in \mathcal{M}_{1,i}} (\llbracket F_2^\gamma \rrbracket_E - \llbracket F_2^\gamma \rrbracket_E^*)^2 |E|}{\sum_{E \in \mathcal{M}_{1,m}} (\llbracket F_2^\gamma \rrbracket_E^*)^2 |E|}}, \quad (5.4)$$

to measure the relative error in the transfer fluxes between fracture and matrix, where $\llbracket F_2^\gamma \rrbracket_E$ and $\llbracket F_2^\gamma \rrbracket_E^*$ are the discrete and the exact jump in fluxes across the fracture evaluated for the element E of the lower-dimensional grid $\mathcal{M}_{i,1}$. Recall that the jump in fluxes acts as a source term in the lower-dimensional domain, thus this measure gives an idea about the error made in the matrix-fracture transfer fluxes. We use Neumann boundary conditions on the lateral boundaries and Dirichlet boundary conditions on the top and bottom, both evaluated on the basis of the exact solution (5.1). Please note that here we do not consider the MPFA scheme, as the computations are carried out on a structured quadrilateral grid, in which case the scheme reduces to TPFA. For all schemes and refinements, the direct solver UMFPack was used to solve the resulting linear system [Davis, 2004].

With this test case we would like to quantify the errors introduced by the lower-dimensional description of the fracture. Previous studies showed that the error diminishes with decreasing aperture values (see e.g. [Sandve et al., 2012, Ahmed et al., 2015]). In this work, we set $a = 1 \cdot 10^{-3}$ m, for which the volume error is 0.1 % and which corresponds to the highest aperture value considered in the above mentioned references. Figure 5.1 shows the convergence behavior of the schemes for $k = \{1 \cdot 10^4, 1 \cdot 10^{-4}\}$ and $a = 1 \cdot 10^{-3}$ m. Therein, it can be seen from the right column that for the case of $k = 1 \cdot 10^{-4}$, all schemes and variables converge with second order at least up to

$a/h \approx 0.1$, while the lowest errors in pressure are observed for the TPFA scheme. Convergence of the coupling source term is lost for values of $a/h > 0.1$, with the irreducible relative error being in the order of $1 \cdot 10^{-6}$. As the values of the coupling source term are relatively small (see lower right plot in Figure 5.1), this does not seem to significantly affect the convergence of pressure. Note that this case, even though a low value for the fracture permeability was chosen, does not represent realistic situations of fractures acting as barriers, as the analytical solution does not exhibit a pressure jump across the fracture. For this reason we also observe convergence for the BOX-CONT scheme, which is not generally applicable in cases of blocking fractures.

In contrast to that, one can observe from the left column of Figure 5.2 that the irreducible error in the case of $k = 1 \cdot 10^4$ is much higher. Convergence is lost for all schemes in this case, while the BOX-CONT scheme shows a significantly smaller irreducible relative error in pressure in comparison with the TPFA and the BOX scheme. The irreducible error in the coupling source term is in the order of 3%. We note that for $k = 1 \cdot 10^4$ the bulk source term (5.2) in the matrix domain is significantly larger. As a result, the source term in the matrix is substantially overestimated due to the added volume that results from the hybrid-dimensional discretization. In addition to that, the boundary fluxes out of the fracture on the lateral sides are the dominating outfluxes in this case, which occur on the added volume of the fractures in the case of the TPFA and the BOX scheme. This latter effect does not play a role in the BOX-CONT scheme where no boundary fluxes on the fractures are computed. This could explain why the irreducible error in pressure is an order of magnitude lower than for the TPFA and the BOX scheme (see upper left plot in Figure 5.1). If the source term in the matrix domain within the elements adjacent to the fracture is rescaled to account for the volume of the overlapping fracture, convergence in pressure is maintained for all schemes and the considered refinements, while convergence of the source term seems to stagnate at an error of $\approx 1 \cdot 10^{-4}$ as the discretization length approaches the aperture (see Figure 5.2). Furthermore, the source term profile on the lower-dimensional fracture coincides very well with the analytical solution (see lower figure in Figure 5.2).

Summary The results shown in this section suggest that, for incompressible single-phase flow, the errors introduced by the lower-dimensional description of the fracture are comparatively small. As in previous studies (see e.g. [Sandve et al., 2012, Ahmed et al., 2015]), we observe that convergence is lost for the hybrid-dimensional schemes

as the discretization length approaches the aperture. Furthermore, for the case of $k = 1 \cdot 10^4$ significant irreducible errors were observed. However, the source term appeared to be the dominating source of error in this case, and, if scaled to account for the overlapping volume with the fracture, this error contribution could be ruled out and convergence was maintained up to $a/h \approx 1$. Apart from that, these issues related to the source term should not play an important role in most applications.

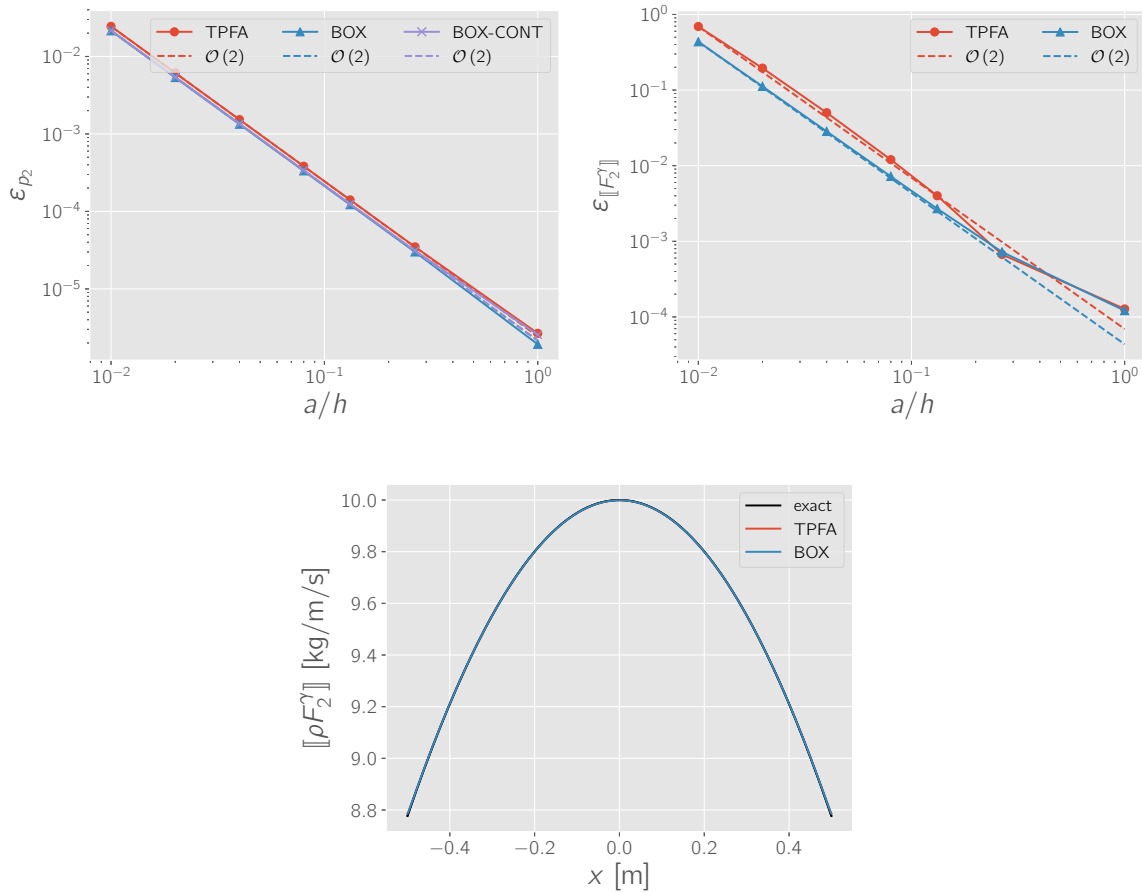


Figure 5.2 – Test case 1: scaling the source term. Error in matrix pressure (top left) and the jump in fluxes (top right) versus the ratio of aperture and discretization length, with $a = 1 \cdot 10^{-3}$ m and $k = 1 \cdot 10^4$, and where the source term in the matrix was scaled within the elements that are overlapping with the fracture to account for the reduced volume. The bottom figure shows the coupling source term plotted along the fracture for the finest grid.

5.1.2 Test case 2: anisotropic matrix permeability

This test case aims at investigating the performance of the hybrid-dimensional approaches in the context of full anisotropic permeability tensors in the matrix and situations in which a significant pressure jump occurs across blocking fractures. As in the previous test case (see Section 5.1.1), gravity is neglected and the fluid properties are set to $\mu = 1 \text{ Pa}\cdot\text{s}$ and $\rho = 1 \text{ kg/m}^3$. The domain is the same as in the previous test case, but we use no-flow boundary conditions on all sides except for an inlet and an outlet on the left and right boundaries, respectively. Zero pressure is applied at the outlet and unit pressure at the inlet. For an illustration of the setup see Figure 5.3. The permeabilities of the sub domains in the equi-dimensional and mixed-dimensional setting are given by

$$\mathbf{K}_b = \mathbf{K}_2 = \mathbf{R}(\Phi)^{-1} \begin{pmatrix} 1 & 0 \\ 0 & 1/5 \end{pmatrix} \mathbf{R}(\Phi), \quad \mathbf{K}_f = \mathbf{K}_1 = k \mathbf{I}. \quad (5.5)$$

Here, $\mathbf{R}(\Phi)$ is the two-dimensional rotation matrix with the rotation angle Φ . We consider a number of different fracture permeabilities, $k \in \{1 \cdot 10^{-4}, 1 \cdot 10^{-2}, 1 \cdot 10^2, 1 \cdot 10^4\}$, given in m^2 , as well as rotation angles $\Phi \in \{-\pi/4, 0, \pi/4\}$. For each combination, an equi-dimensional reference solution is computed using the standard MPFA scheme on an equi-dimensional, structured discretization of the domain consisting of 1 005 000

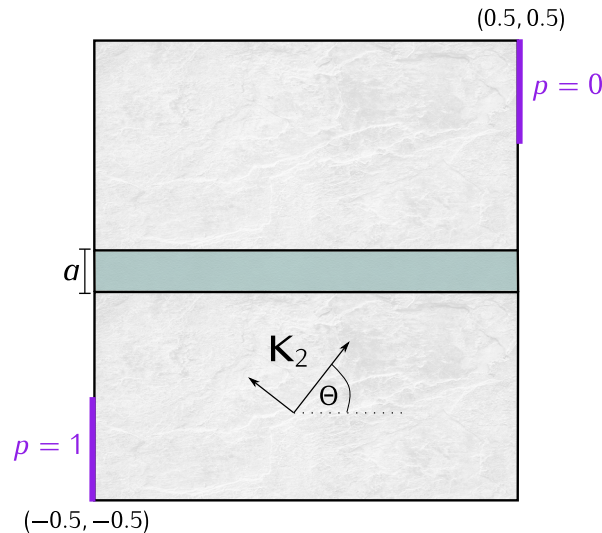


Figure 5.3 – Test case 2: domain and boundary conditions. The green region depicts the fracture, whereas the surrounding matrix domain is shown in gray.

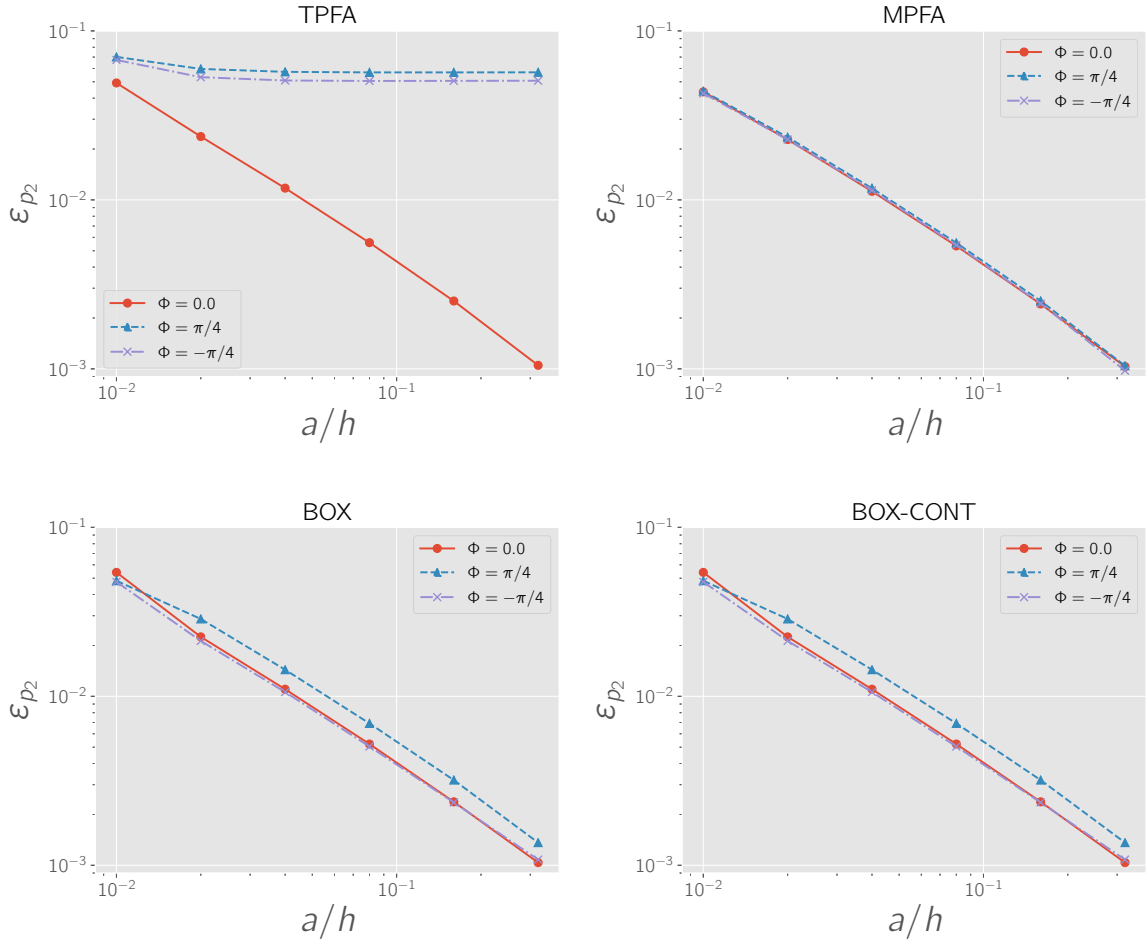


Figure 5.4 – Test case 2: convergence rates. Relative pressure errors obtained with the TPFA (top left), MPFA (top right), BOX (bottom left) and the BOX-CONT (bottom right) schemes for $k = 1 \cdot 10^4$ and different permeability angles Φ .

quadrilateral elements, where a discretization length of $h = a = 1 \cdot 10^{-3}$ m was used, and where the vertical discretization length was modified inside the fracture such that 5 elements discretize the width of the fracture. As in the previous test case, we apply the direct solver UMFPack [Davis, 2004] to solve the resulting linear system for all schemes and refinements, including the equi-dimensional reference solution. We compute numerical solutions using the hybrid-dimensional approaches on a series of grids $\mathcal{M}_{d,i}$, $i \in \{0, \dots, m\}$, where the coarsest discretization $\mathcal{M}_{n,0}$ of the matrix domain uses a discretization length of $h = 1/10$ m and the following refinements use $h_{i+1} = 0.5h_i$, up to the finest discretization with $h_5 = 1/320 = 3.125 \cdot 10^{-3}$ m. Thus, the finest discretization length corresponds to approximately three times the aperture and leads to

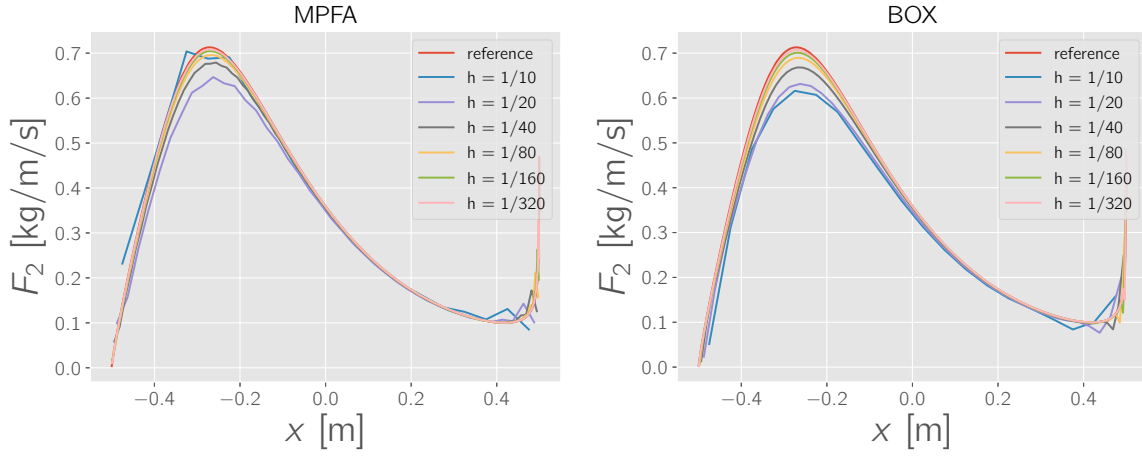


Figure 5.5 – Test case 2: transfer fluxes. Fluxes from matrix to fracture plotted along the lower interface computed with the MPFA (left) and the BOX (right) for the case of $k = 1 \cdot 10^4$ and $\Phi = \pi/4$.

a grid with 102 400 elements. In order to compute the relative error with respect to the reference solution, we perform an L2-projection of the pressure solution obtained for the matrix domain with the mixed-dimensional schemes onto the reference grid, from which the elements inside the fracture have been removed. Let us denote the reference discretization of the matrix domain with \mathcal{M}_{ref} and define the relative pressure error as follows:

$$\varepsilon_{p_2}^i = \sqrt{\frac{\sum_{E \in \mathcal{M}_{ref}} ([\Pi p_2^i]_E - p_E)^2 |E|}{\sum_{E \in \mathcal{M}_{ref}} (p_E)^2 |E|}}, \quad (5.6)$$

where $[\Pi p_2^i]_E$ is the projection Πp_2^i of the pressure solution obtained with a mixed-dimensional approach onto the reference grid, evaluated for the element E . Figure 5.4 shows the errors for all mixed-dimensional schemes, refinements and permeability angles for the case of $k = 1 \cdot 10^4$. First order convergence can be observed for all schemes, except for the TPFA scheme for $\Phi \neq 0$, as this scheme is inconsistent on grids that are not \mathbf{K} -orthogonal (see e.g. Edwards and Rogers [1998]). Furthermore, for all consistent configurations the relative error goes down to approximately one percent already with the second refinement, which corresponds to only 40×40 elements for the discretization of the matrix domain. The quality of the transfer fluxes between matrix and fracture are of particular interest as these are expected to be affected the most by the lower-dimensional description of the fracture. Figure 5.5 shows plots of the transfer fluxes from the matrix into the fracture along the lower interface for the case

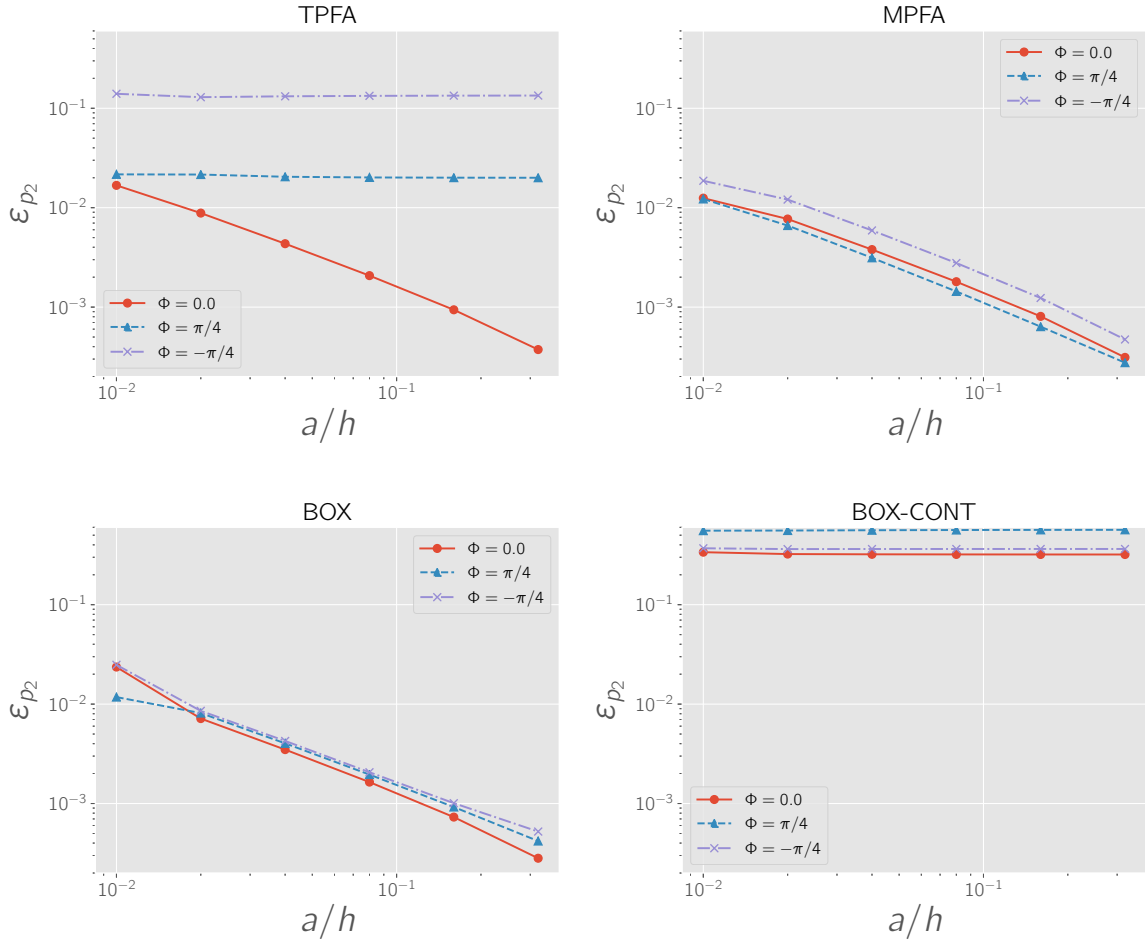


Figure 5.6 – Test case 2: convergence rates. Relative pressure errors obtained with the TPFA (top left), MPFA (top right), BOX (bottom left) and the BOX-CONT (bottom right) schemes for $k = 1 \cdot 10^{-4}$ and different permeability angles Φ .

of $\Phi = \pi/4$. We only show the results obtained with the MPFA and the BOX scheme at this point, as TPFA is inconsistent in this case and the BOX-CONT scheme does not allow for an evaluation of the transfer fluxes. From the reference profile it can be seen that the fluxes show a maximum at $x \approx -0.3$ and a minimum close to the right no-flow boundary, towards which they then show a steep increase again. This steep increase is rather poorly captured by the mixed-dimensional schemes on coarse grids, while for the finer discretizations the deviations diminish substantially. Apart from the coarsest grid, both schemes produce similar transfer flux profiles.

Figure 5.6 shows the errors in the case of a blocking fracture with $k = 1 \cdot 10^{-4}$. The MPFA and BOX scheme show first order convergence for all values of Φ , while the

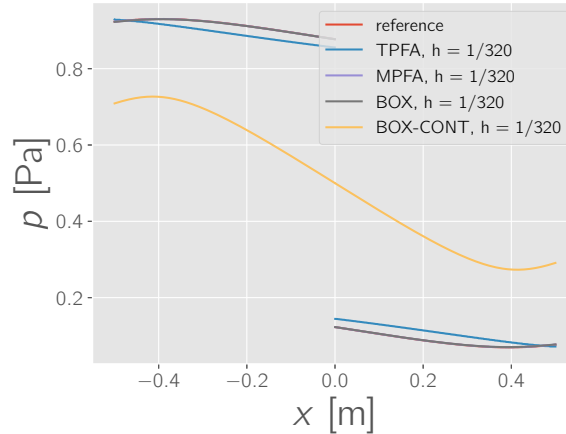


Figure 5.7 – Test case 2: pressure profiles. Matrix pressure plotted along the lines $(-0.5, -0.125) - (-a/2, -a/2)$ and $(a/2, a/2) - (0.5, 0.125)$ for the case of $k = 1 \cdot 10^{-4}$ and $\Phi = \pi/4$. Shown are the reference solution as well as the pressures obtained with the mixed-dimensional schemes on the finest grid. Note that the reference, the MPFA and the BOX solutions overlap.

TPFA scheme again does not converge for $\Phi \neq 0$ and the BOX-CONT scheme does not converge at all in this case. This is expected as the scheme assumes continuity of the pressure across the fracture, which generally does not hold in the case of blocking fractures. In fact, in this setup almost the entire pressure drop occurs across the fracture, which can be seen from the pressure plot depicted in Figure 5.7. It should be mentioned that, therein, the profiles obtained from the reference solution and the mixed-dimensional MPFA and BOX schemes overlap such that a visible distinction between the curves is impossible. On the other hand, the TPFA scheme deviates significantly from the reference solution due to its inconsistency in this case, and the BOX-CONT scheme produces a substantially different pressure profile due to the pressure continuity assumption across the fracture.

Summary We observed in this test case that both the hybrid-dimensional MPFA and BOX scheme converged to the reference solution for all tested values of k and Φ . The transfer fluxes between matrix and fracture were reproduced well, also in the case of anisotropic permeability tensors in the matrix. Apart from that, this test case shows that the BOX-CONT scheme, as expected, is not applicable to the case of low-permeable fractures, and that the TPFA scheme produces rather poor results if the grid is strongly non- \mathbf{K} -orthogonal. This is further illustrated in Figure 5.8, where the relative pressure

errors, obtained with the finest hybrid-dimensional grid, are plotted against different values of the fracture permeability k for all considered permeability angles Φ . While the relative pressure errors are below 1 % for the MPFA and the BOX scheme in all cases, it is in the order of 10 % for the TPFA scheme when $\Phi \neq 0$. For the BOX-CONT scheme, the errors increase towards lower fracture permeabilities and are in the order of 50 % for $k = 1 \cdot 10^{-4}$.

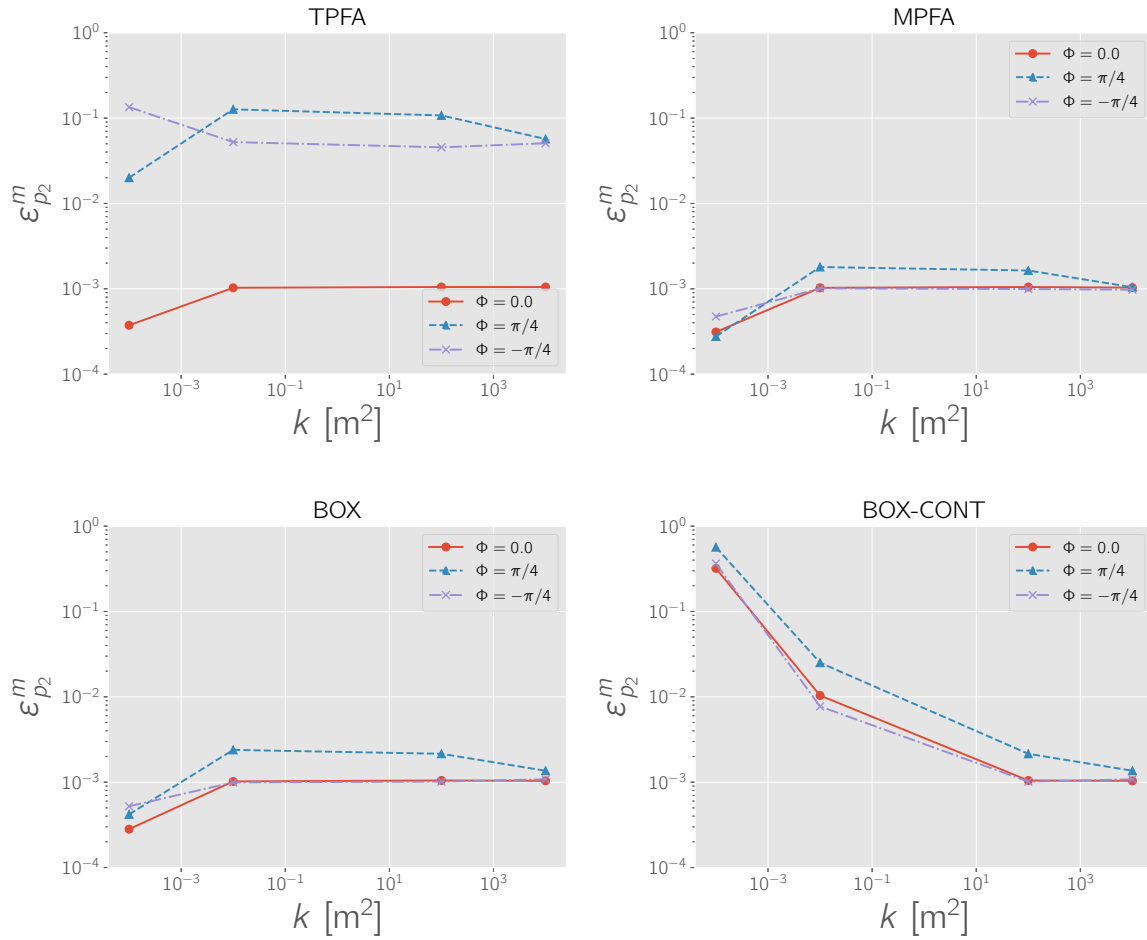


Figure 5.8 – Test case 2: pressure error vs permeability. Relative pressure errors on the finest grid plotted against different values of k and Φ .

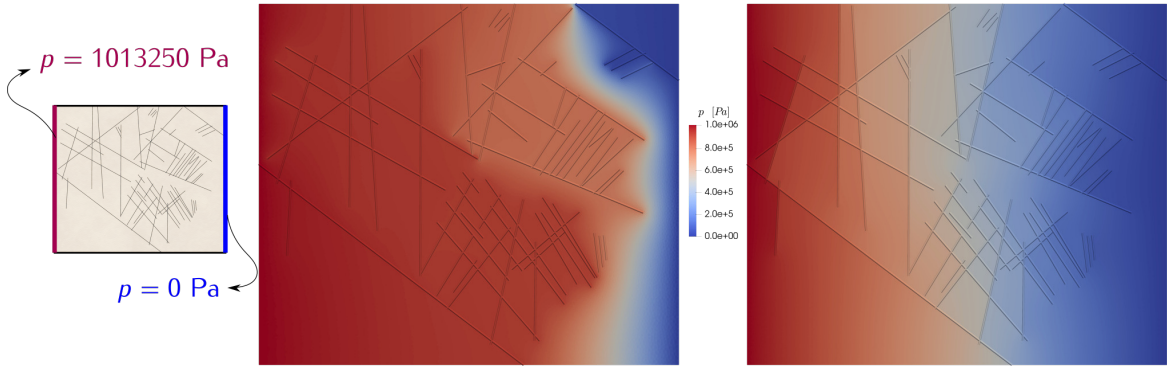


Figure 5.9 – Test case 3: domain, boundary conditions and pressure solutions. The left image illustrates the boundary conditions and the center and right images show the pressure solutions obtained with the MPFA scheme for $\mathbf{K}_f = \mathbf{K}_1 = 1 \cdot 10^{-8}$ and $\mathbf{K}_f = \mathbf{K}_1 = 1 \cdot 10^{-18}$, respectively. The lines represent the fracture network.

5.1.3 Test case 3: complex two-dimensional fracture network

This test case is taken from Flemisch et al. [2018] and considers a more realistic and complex network of fractures. As in the previous test cases, gravity is neglected, and we set $\mu = 1 \text{ Pa s}$ and $\rho = 1 \text{ kg/m}^3$ for the fluid properties. The domain has a size of $700 \text{ m} \times 600 \text{ m}$ and the permeabilities for the matrix and the fractures are set to $\mathbf{K}_m = \mathbf{K}_2 = \mathbf{I} \cdot 10^{-14} \text{ m}^2$ and $\mathbf{K}_f = \mathbf{K}_1 = \mathbf{I} \cdot 10^{-8} \text{ m}^2$, respectively. The fracture aperture is $a = 1 \cdot 10^{-2} \text{ m}$. In this work, we consider an additional case defining low-permeable fractures with $\mathbf{K}_f = \mathbf{K}_1 = \mathbf{I} \cdot 10^{-18} \text{ m}^2$. The fracture network as well as the domain and boundary conditions together with the pressure distributions computed with the MPFA scheme are depicted in Figure 5.9. Table 5.1 shows the number of degrees of freedom in both matrix and fracture as well as the number of non-zero entries in the system matrix for the different schemes on the grid used, which consists of 330 292 triangular elements for the matrix and 5870 one-dimensional elements for the fractures. Furthermore, the solver times using the direct solver libraries UMFPack [Davis, 2004] and SuperLU [Li, 2004], as well as the Dune implementations of the conjugate gradient (CG) and the biconjugate gradient stabilized method (BiCGSTAB) are listed. For the iterative solvers, we consider ILU0 preconditioning, and further test the BiCGSTAB solver also with preconditioning applied only to the diagonal blocks of the block-structured system matrix (see Section 4.4). Finally, the BiCGSTAB solver using the Algebraic Multigrid Method (AMG) as preconditioner on the diagonal blocks is also tested. Note that since the BOX-CONT scheme does not consider a separate

domain for the fractures, it does not lead to a block-structured system matrix and thus the variants applying preconditioning on the diagonal blocks cannot be tested for this scheme. The condition number estimates provided in Table 5.1 were computed using the SuperLU library.

As expected, the vertex-based schemes result in significantly fewer degrees of freedom on the chosen unstructured discretization of the domain when compared to the cell-centered schemes. Regarding the times required for the solution of the linear system, Table 5.1 shows that, at least for the direct solvers, solving the system is significantly more expensive with the MPFA scheme when compared to the remaining schemes. Moreover, it is remarkable that the direct solver UMFPack is much faster in solving the systems than any of the iterative solvers with the chosen preconditioners. In general, the number of iterations required to decrease the residual down to the threshold of $1 \cdot 10^{-16}$ are relatively high, and in some cases the iterative solvers do not converge within the maximum number of iterations (marked in Table 5.1 with "X"), which was set to 2000 here. While the solve step for TPFA and MPFA required a comparable amount of iterations when the AMG preconditioner was used, fewer iterations were needed for MPFA

Table 5.1 – Test case 3: matrix specifications, solver times and condition number estimates. The stop criterion for the iterative solvers was set to a residual threshold of $1 \cdot 10^{-16}$. For the iterative solvers, the numbers behind the slashes show the required number of iterations. All simulations were carried out on a single CPU with 2.1 GHz.

	TPFA	MPFA	BOX	BOX-CONT
#-dof matrix	330 292	330 292	171 597	165 698
#-dof fracture	5870	5870	5848	-
#-nnz	1 349 970	4 433 675	1 249 137	1 155 683
UMFPack	1.66 s	5.24 s	1.24 s	1.07 s
SuperLU	4.67 s	24.14 s	4.49 s	3.29 s
$\mathbf{K}_1 = \mathbf{I} \cdot 10^{-8} \text{ m}^2$				
Cond. num. est.	$2.59 \cdot 10^9$	$1.82 \cdot 10^9$	$1.42 \cdot 10^9$	$2.61 \cdot 10^9$
ILU0-CG	7.02 s /612	X	X	X
ILU0-BiCGSTAB	10.19 s /432.5	17.00 s /288.5	X	17.25 s /1038.5
BlockILU0-BiCGSTAB	11.49 s /463.5	18.39 s /304	X	
BlockAMG-BiCGSTAB	21.84 s /151	51.03 s /154	10.54 s /90.5	
$\mathbf{K}_1 = \mathbf{I} \cdot 10^{-18} \text{ m}^2$				
Cond. num. est.	$4.95 \cdot 10^7$	$4.35 \cdot 10^7$	$9.42 \cdot 10^7$	$(2.77 \cdot 10^6)$
ILU0-CG	16.14 s /1368	X	15.28 s /1651	(5.62 s /678)
ILU0-BiCGSTAB	21.52 s /930.5	28.36 s /478	9.75 s /517.5	(5.32 s /315.5)
BlockILU0-BiCGSTAB	23.42 s /979.5	28.68 s /497.5	9.82 s /526.5	
BlockAMG-BiCGSTAB	17.11 s /118	42.47 s /126.5	13.15 s /112.5	

than for TPFA with ILU0 preconditioning. Furthermore, although the condition number estimates are lower for the case of blocking fractures, more iterations were needed in this case for the cell-centered schemes when using ILU0 preconditioning, while in contrast to that, slightly fewer iterations were required when using the AMG preconditioner on the diagonal blocks. The iterative solvers generally seem to have problems solving the system arising from the BOX scheme for the case of highly-conductive fractures, where only the BiCGSTAB solver with AMG preconditioning converged. In the case of blocking fractures, however, all iterative solvers converged for the BOX scheme, requiring similar numbers of iterations as for the MPFA scheme (except for the CG solver). Note that the results for the blocking fractures and the BOX-CONT are shown in parentheses, as the scheme is generally not applicable in this case and the solution does not capture the phenomenology one would expect. This can be seen in Figure 5.10, where solution profiles along the lines $y = 500$ m and $x = 625$ m are shown. For comparison, the plots for the highly-conductive fractures furthermore show the pressure profile obtained with the *mortar-dfm* scheme from the benchmark study Flemisch et al. [2018], which is an approach based on mixed finite elements using mortars on the matrix fracture interfaces. Note that in the benchmark study Flemisch et al. [2018] a much coarser grid was used. Except for the BOX-CONT, which shows noticeable differences for the conductive fractures and substantial deviations for the blocking fractures, good agreement can be observed among the remaining schemes for both fracture permeabilities.

Summary This test case demonstrated the applicability of the considered schemes to incompressible single-phase flow on more complex two-dimensional geometries using both direct and iterative solvers, however, most of the latter had issues solving the system for the highly-conductive fractures using the BOX scheme. For all schemes and both fracture permeabilities the direct solvers were more efficient in solving the linear system, especially the direct solver UMFPack. It is difficult to draw a clear conclusion from the results for various reasons. First, larger numbers of iterations were required for the cell-centered schemes and the iterative solvers in the blocking fracture case even though the computed condition numbers were lower. Furthermore, for the BOX scheme the opposite was observed, as for the highly-conductive fracture case most of the iterative solvers did not converge, while all of them converged for blocking fractures. In contrast to that, when using AMG preconditioning on the diagonal blocks, the number of iterations are slightly lower for the blocking fracture case and the cell-

centered schemes, while again the opposite is the case for BOX. Regarding the solutions obtained with the different schemes, a good agreement between the results was observed, except for the BOX-CONT scheme, for which the computed pressure distributions showed noticeable deviations from those computed by the remaining schemes, especially for the case of blocking fractures.

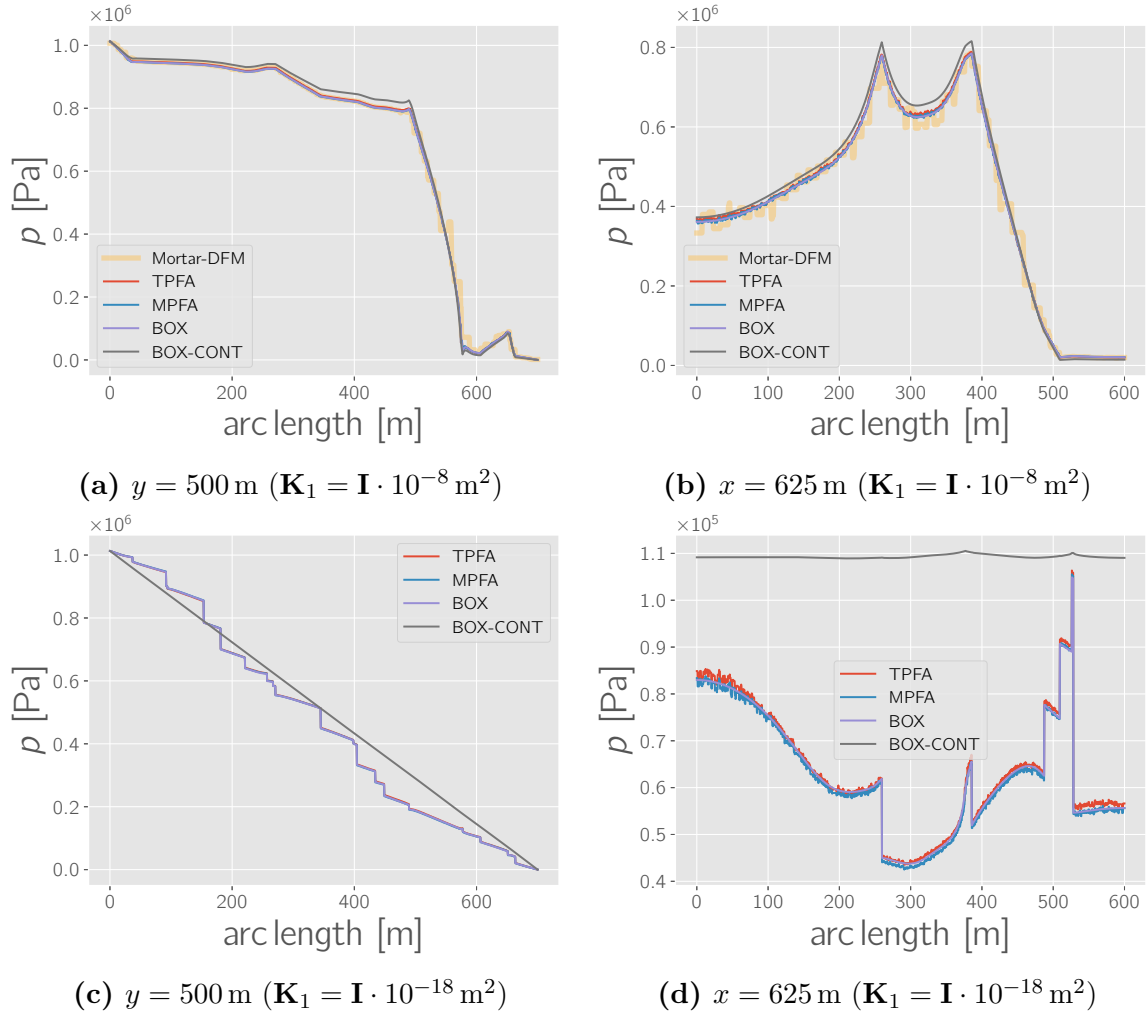


Figure 5.10 – Test case 3: pressure profiles. The plots were created along the lines $y = 500$ m and $x = 625$ m for the conductive fractures (upper row) and the blocking fracture case (bottom row).

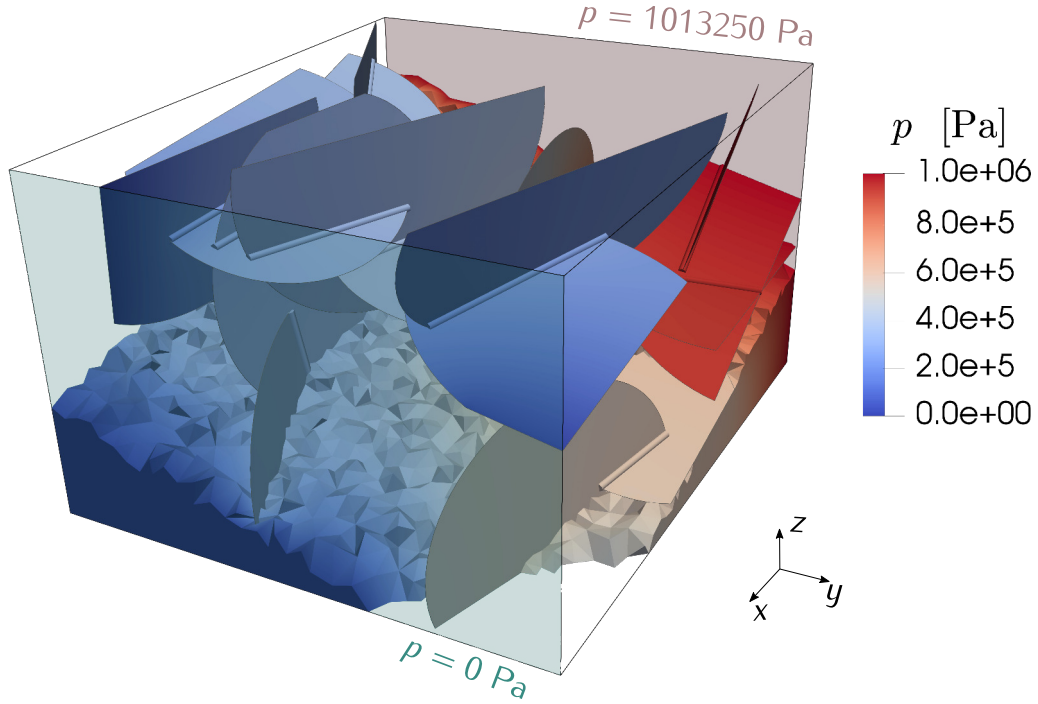


Figure 5.11 – Test case 4: domain, boundary conditions and pressure solution. The depicted pressure solution was computed with the hybrid-dimensional BOX scheme. The intersection lines are depicted as tubes for better visibility.

5.1.4 Test case 4: complex three-dimensional fracture network

This section is devoted to a three-dimensional extension of the test case presented in Section 5.1.3, and focuses on the applicability of the hybrid-dimensional schemes to complex three-dimensional settings. The domain outline, the fractures and their intersections are depicted in Figure 5.11 together with the pressure solution computed with the hybrid-dimensional BOX scheme. The size of the domain is given by $700 \text{ m} \times 600 \text{ m} \times 400 \text{ m}$ and the fracture network consists of 19 disk-shaped fractures, of which only parts of the elliptical disks are contained within the domain. As in the previous cases, gravity is not considered, and we use $\mu = 1 \text{ Pa s}$ and $\rho = 1 \text{ kg/m}^3$. The permeabilities are again given by $\mathbf{K}_m = \mathbf{K}_3 = \mathbf{I} \cdot 10^{-14} \text{ m}^2$ and $\mathbf{K}_f = \mathbf{K}_2 = \mathbf{I} \cdot 10^{-8} \text{ m}^2$ for the matrix and fractures, respectively, and the fracture aperture is set to $a = 0.01 \text{ m}$ and. The mesh consists of 224 346 tetrahedral elements for the matrix, 20 998 triangular elements for the fractures and 333 one-dimensional elements for the intersections of fractures. Simulations were carried out using the TPFA, MPFA, BOX, and the BOX-CONT

scheme. For the first three, solutions were computed for both the case of considering flow along intersections of fractures as well as for the case of using the continuity conditions (3.27). In the case of considering flow along intersections, the permeability and cross-sectional area of the intersections were set to $\mathbf{K}_{\text{is}} = \mathbf{K}_1 = \mathbf{I} \cdot 10^{-7} \text{ m}^2$ and $\epsilon_1 = 5 \cdot 10^{-4} \text{ m}^2$. We chose ϵ_1 such that it is in the order of a^2 , and assuming Hagen-Poiseuille type flow, this would lead to \mathbf{K}_1 being in the order of $1 \cdot 10^{-8} \text{ m}^2$. The (rather unphysically high) value for \mathbf{K}_1 was chosen to enforce permeability contrasts.

The number of degrees of freedom, the number of non-zero entries in the system matrix, linear solver times and condition number estimates are listed in Table 5.2. As in the two-dimensional test case of Section 5.1.3, the vertex-based schemes again lead to much fewer degrees of freedom and thus result in significantly smaller solver times. Moreover, it can be observed that in contrast to the two-dimensional case, the direct solvers are much less efficient than the iterative solvers. The lowest number of iterations and fastest solve steps for TPFA and BOX were observed with AMG preconditioning on the diagonal matrix blocks, although for MPFA a breakdown situation occurred. It is furthermore noteworthy that the condition number for MPFA is higher than for TPFA and more iterations were required for the solution of the system, which is also in contrast with the observations made on the two-dimensional setup.

If flow along the intersections of fractures is considered, only a minor number of unknowns, 333 for the cell-centered schemes and 358 for the BOX scheme, are added to the linear system (see Table 5.3). This seems to have a small impact on the condition numbers for MPFA and BOX, but for TPFA, the condition number increases by an order of magnitude. Furthermore, the iterative solvers with preconditioning applied only to the diagonal blocks need significantly more iterations than in the case of flow along the intersections being neglected, which also holds for MPFA and BOX.

Despite the large differences in performance, the results obtained by the different schemes are in good agreement, which can be seen from Figure 5.12, where the pressure profiles along two diagonals of the domain are shown. The pressure profiles agree very well among all schemes except for BOX-CONT, which predicts slightly lower pressures. Moreover, taking the flow along fracture intersections into account does not seem to have a visible effect on the pressure distribution in the matrix domain along the plotted lines, but significant local pressure differences can be seen for the pressure in the fracture, which is depicted in Figure 5.13. As expected from a phenomenological point of view, the largest differences in pressure are observed at the in- and outflow regions into or out of fracture intersections.

Table 5.2 – Test case 4.1: matrix specifications, solver times and condition number estimates. The stop criterion for the iterative solvers was set to a residual threshold of $1 \cdot 10^{-16}$. For the iterative solvers, the numbers behind the slashes show the required number of iterations. All simulations were carried out on a single CPU with 2.1 GHz.

	TPFA	MPFA	BOX	BOX-CONT
#-dof matrix	224 346	224 346	50 883	40 398
#-dof fracture	20 998	20 998	10 907	-
#-nnz	1 232 394	17 282 594	930 258	569 822
UMFPack	45.26 s	1054.36 s	8.60 s	4.25 s
SuperLU	452.15 s	5201.35 s	72.84 s	33.48 s
Cond. num. est.	$2.29 \cdot 10^7$	$5.96 \cdot 10^8$	$2.31 \cdot 10^7$	$9.60 \cdot 10^7$
ILU0-CG	5.25 s /445	X	X	1.79 s /464
ILU0-BiCGSTAB	7.79 s /322.5	133.73 s /467.5	3.13 s /180.5	1.20 s /151
BlockILU0-BiCGSTAB	8.31 s /327.5	115.09 s /442.5	2.51 s /177.5	
BlockAMG-BiCGSTAB	5.55 s /35	X	1.92 s /21	

Table 5.3 – Test case 4.2: matrix specifications, solver times and condition number estimates. The stop criterion for the iterative solvers was set to a residual threshold of $1 \cdot 10^{-16}$. For the iterative solvers, the numbers behind the slashes show the required number of iterations. All simulations were carried out on a single CPU with 2.1 GHz.

	TPFA	MPFA	BOX
#-dof matrix	224 346	224 346	50 883
#-dof fracture	20 998	20 998	11 939
#-dof intersection	333	333	358
#-nnz	1 232 031	17 296 050	945 319
UMFPack	44.14 s	1215.32 s	10.79 s
SuperLU	498.34 s	5646.01 s	88.01 s
Cond. num. est.	$4.72 \cdot 10^8$	$1.43 \cdot 10^8$	$3.05 \cdot 10^7$
ILU0-CG	5.40 s /459	X	X
ILU0-BiCGSTAB	8.06 s /336.5	141.31 s /523	4.05 s /235.5
BlockILU0-BiCGSTAB	19.81 s /733.5	272.88 s /1077.5	6.55 s /455.5
BlockAMG-BiCGSTAB	85.68 s /607.5	X	X

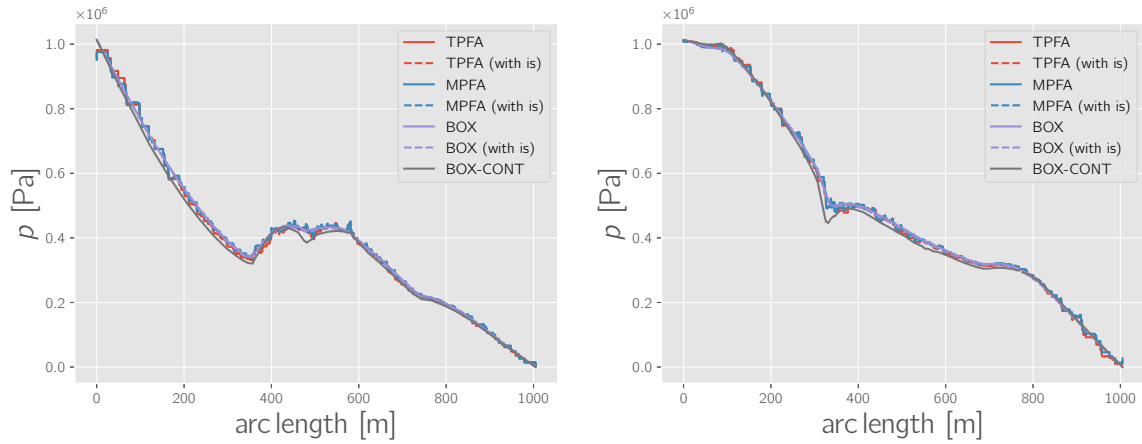


Figure 5.12 – Test case 4: pressure profiles. The plots to which it is referred to by “(with is)” in the legends depict the profiles for the cases taking into account flow along the intersections of fractures. The left image depicts the pressure along the line $(0\text{ m}, 0\text{ m}, 0\text{ m})-(700\text{ m}, 600\text{ m}, 400\text{ m})$ and the right image shows the plot along $(0\text{ m}, 600\text{ m}, 400\text{ m})-(700\text{ m}, 0\text{ m}, 0\text{ m})$.

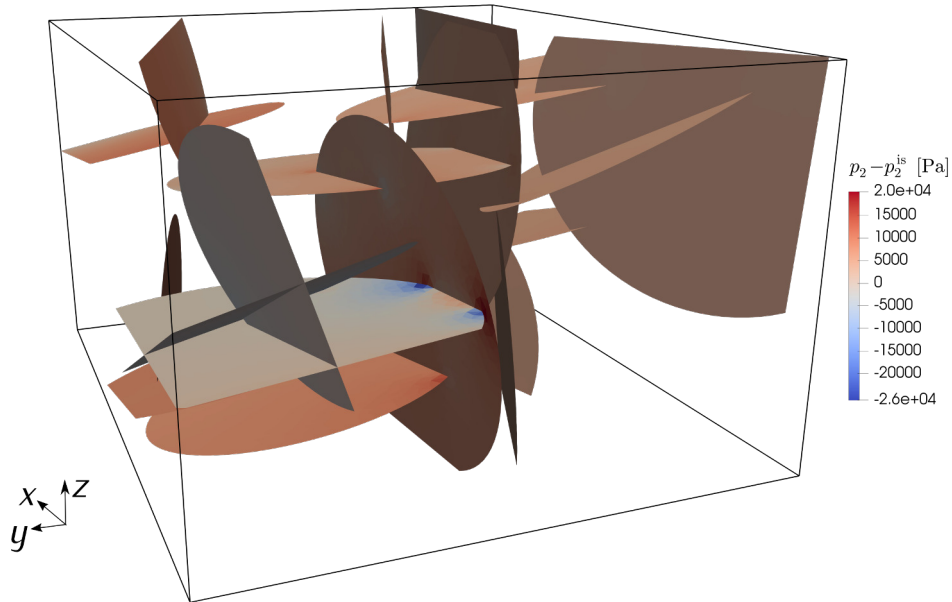


Figure 5.13 – Test case 4: influence of intersection flow on pressure. In the figure, p_2^{is} refers to the pressure in the fracture for the case of flow along intersections being considered, while p_2 is the pressure in the fracture when using the continuity conditions (3.27).

Summary The three-dimensional setup seemed to be better conditioned than the two-dimensional case, which could be due to the fact that in the latter all the fluid is forced to flow through the fractures as there is no flow paths from inlet to outlet without crossing a fracture. However, this is not undoubtedly reflected in the convergence behavior of the iterative solvers, from which it is difficult to draw a conclusion. Large differences in convergence of the BiCGSTAB solver for different preconditioners in the different cases could be observed, and none of them could be identified as the best option in all the cases. Further investigations are necessary to determine what preconditioning strategies are best suited for a specific situation, i.e. for conductive or blocking fractures and for cases considering fluid flow along the intersections of fractures.

5.1.5 Test case 5: determination of effective permeabilities

One application that the hybrid models could be used for is the determination of up-scaled properties of fractured rock, as it is done, for instance, in Matthai et al. [2007] using an equi-dimensional model. The first step in such procedures is the determination of the effective permeability of the medium, which is often done numerically by considering stationary single-phase flow, applying unit pressure differences on the domain and measuring the resulting fluxes. In experimental studies, similar procedures applied to core samples play an important role in characterizing rock specimens. For instance, knowledge about the permeability of the host rock is of particular importance for radioactive waste disposal applications, as very low permeabilities are required for the rock to act as a natural barrier. In the report "Abeitsbericht NAB 13-51" * published by the Swiss National Cooperative for the Disposal of Radioactive Waste (Nagra), the permeabilities of several specimens sampled at different depths of a clay formation are determined experimentally. They measured very low permeabilities in the order of $1 \cdot 10^{-22}$ - $1 \cdot 10^{-21}$ m² on cylindrical samples with 50 mm diameter and a height of 25 mm (see Figure 2-9 in the report). Figure 2-1 within the same report furthermore shows one of the samples immersed in synthetic pore water, in which conditions the sample has cracked open and reveals the orientation of bedding planes. The direction of coring was chosen orthogonal to bedding planes, for which reason predominantly horizontal and only a few inclined cracks are visible. In this test case we want to examine the possible influence of these bedding planes on the measured permeabilities,

*available for download at nagra.ch

assuming that they represent microscopic cracks that are present also in-situ. Please note that clays are generally very soft materials and therefore those cracks are likely to be completely closed in in-situ conditions. Thus, this test case is rather hypothetical. To this end, we create a set of 12 synthetic core samples with the dimensions used in the experiment, all of which are depicted in Figure 5.14, and which contain different artificial, randomly generated, embedded fracture networks. In the numerical experiments on these synthetic samples, we consider stationary and incompressible single-phase flow, zero gravity, and we use water as fluid phase with $\rho_{\text{H}_2\text{O}} = 1000 \text{ kg/m}^3$ and $\mu_{\text{H}_2\text{O}} = 1 \cdot 10^{-3} \text{ Pa}\cdot\text{s}$. We define the inlet boundary to be at the bottom of the domains and apply $p_{\text{H}_2\text{O}} = 2 \cdot 10^5 \text{ Pa}$, while on the top boundary, the outlet, $p_{\text{H}_2\text{O}} = 1 \cdot 10^5 \text{ Pa}$ is set. We then numerically measure the mass flux $Q_{\text{tot}} = Q_{\text{b}} + Q_{\text{f}}$ that leaves the domain through the outlet via the bulk porous medium and the fractures, and compute the effective permeability of the sample in vertical direction via

$$k_{\text{eff}} = \frac{Q_{\text{tot}} \Delta z \mu_{\text{H}_2\text{O}}}{A \Delta p \rho_{\text{H}_2\text{O}}}, \quad (5.7)$$

where $\Delta z = 25 \text{ mm}$ is the height of the sample, $A \approx \pi 0.025^2 \text{ m}^2$ is the inlet/outlet area (only approximately because we evaluate the area in the discrete setting) and $\Delta p = 1 \cdot 10^5 \text{ Pa}$ is the applied pressure difference. Note that $Q_{\text{f}} = 0$ if none of the fractures intersects with the outlet boundary. We set the matrix permeability to $\mathbf{K}_{\text{b}} = \mathbf{K}_3 = \mathbf{I} \cdot 10^{-21} \text{ m}^2$ such that it is in the order of magnitude of the experimental results. In all simulations, we use the cubic law (3.28) to define the tangential fracture permeability as a function of the hydraulic aperture, and use the conditions for open (or highly-conductive) fractures (3.26b) on the matrix-fracture interfaces.

Network characteristics All fracture networks contain three horizontal, non-intersecting fractures representing the bedding planes that are predominantly visible in the Nagra report mentioned above. These are generated such that they do not intersect each other nor the upper or lower domain boundaries. Throughout this section, we refer to networks that only consist of these three fractures as *type 1* networks. To each realization of type 1 networks, we then randomly create vertical fractures that possibly intersect each other as well as the horizontal fractures, but are also not allowed to intersect with the inlet or outlet boundary. These types of networks will be referred

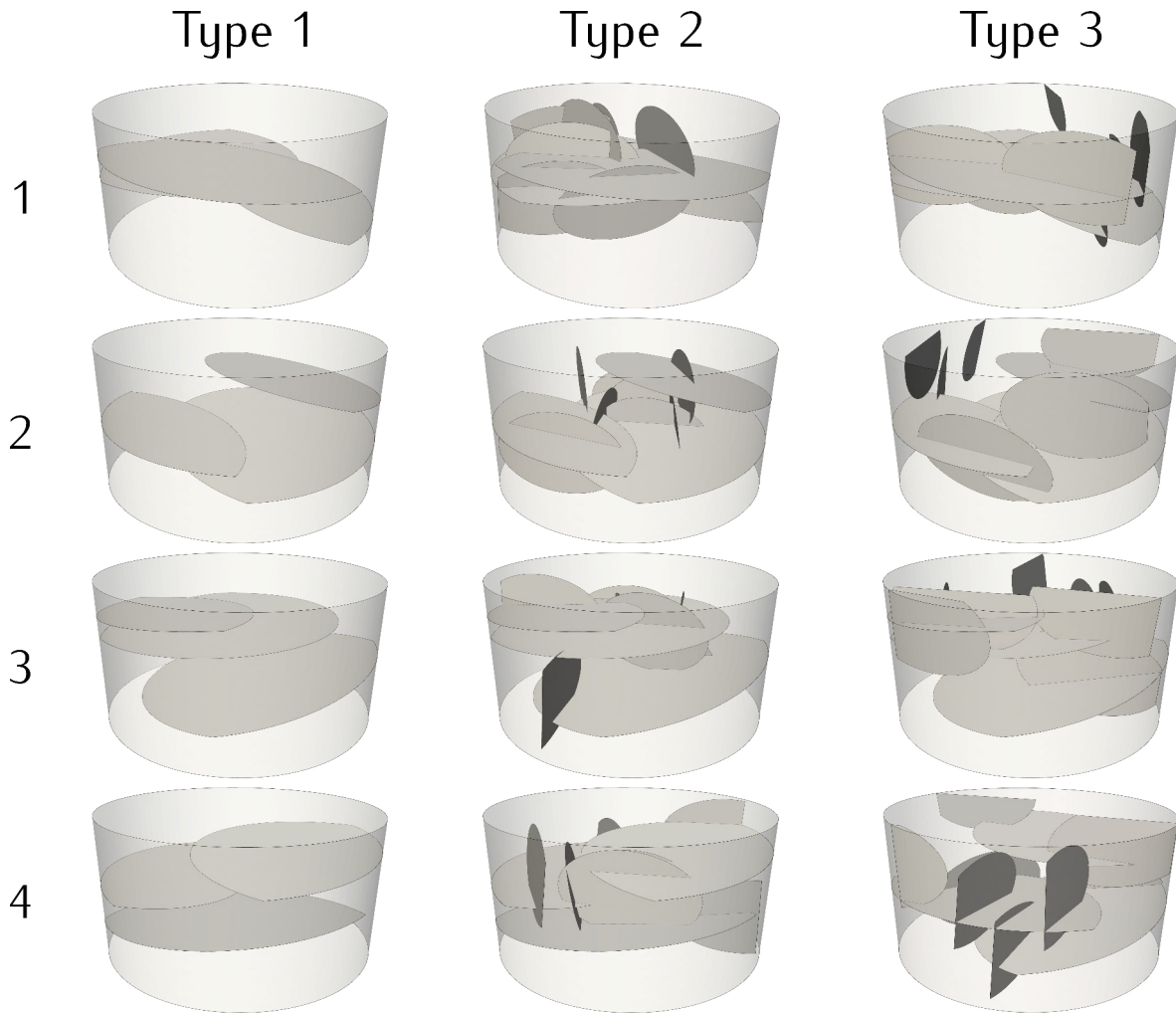


Figure 5.14 – Test case 5: artificial fracture networks. The networks are embedded in synthetic core samples with 50 mm diameter and 25 mm height.

to as *type 2* networks. Finally, *type 3* networks are created in the same manner as those of type 2, but at least one vertical fracture intersects with the outlet boundary. Four realizations of each type of networks were made, and we will use the notation \mathcal{F}_{ij} , $1 \leq i \leq 3$, $1 \leq j \leq 4$, to refer to the j -th realization of type i .

Discretization All grids contain about 70 000 tetrahedral elements and roughly 4000 to 6000 triangular elements, depending on the number of fractures. In a first investigation, we exemplarily pick network \mathcal{F}_{24} and compute the effective permeability using the TPFA, MPFA and BOX scheme, both considering and neglecting the fractures. In the latter case, i.e. neglecting the fractures, we should recover the matrix permeability when using a

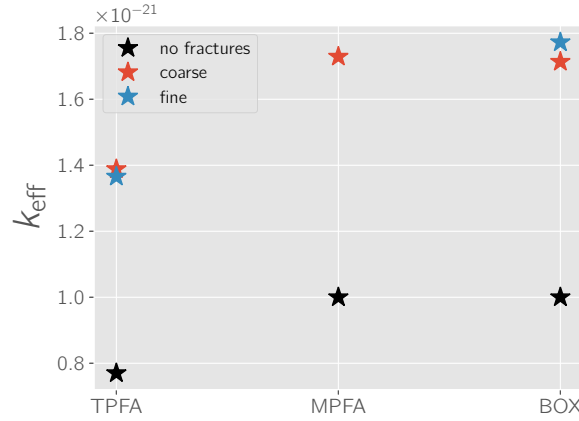


Figure 5.15 – Test case 5: effective permeabilities for network \mathcal{F}_{24} . The computations were done on grids consisting of 71 628 (labeled with "coarse" in the figure) and 573 024 elements (labeled with "fine" in the figure) and the aperture was set to $a = 1 \cdot 10^{-5}$ m.

consistent scheme. Both situations are computed on a grid containing 71 628 elements, as well as a refined grid consisting of 573 024 elements, with which we want to quantify the influence of the discretization on the numerically determined effective permeability. Here, the aperture is set to $a = 1 \cdot 10^{-5}$ m.

Figure 5.15 shows the results for the TPFA, MPFA and the BOX scheme. While both the MPFA and the BOX scheme do recover the prescribed bulk permeability in the case of not considering the fractures, significant deviations above 20% can be seen for TPFA due to its inconsistency on unstructured grids. With the fractures considered, the MPFA and the BOX scheme predict effective permeabilities in the same order which are roughly 60 to 70% higher than the permeability of the bulk medium. No substantial change in the numerically computed effective permeability could be seen when using the fine grid with the BOX scheme, while it was not possible to solve the large system with MPFA because the iterative solvers did not converge and the memory requirements for the direct solvers exceeded the available resources. On the basis of these observations we will perform the subsequently presented computations on the coarser grids with ≈ 70000 elements using the BOX scheme, which is both consistent and computationally more efficient.

Impact of the fracture aperture We now want to investigate how the effective permeability of the samples changes depending on the hydraulic fracture aperture. To this end, we consider 9 logarithmically spaced aperture values between $1 \cdot 10^{-8}$ m and $1 \cdot 10^{-4}$ m,

and for each of these apertures we numerically compute the effective permeabilities of all 12 networks using the BOX scheme. Figure 5.16a shows the results obtained for all synthetic samples, in which a clear segregation between the different types of fracture networks can be seen. For apertures of $1 \cdot 10^{-8}$ m, the effective permeability is equal to the one defined for the bulk porous medium, but as larger aperture values are reached, the effect of the increasing capacity of the fractures to conduct fluid becomes apparent. Figure 5.16a furthermore suggest a non-linear increase of k_{eff} with increasing apertures, which is expected due to the nonlinear relation (3.28) between the tangential fracture permeability and the aperture. Further increasing the apertures eventually leads to smaller increase in effective permeability until it reaches a maximum at $a \approx 1 \mu\text{m}$. In this situation, the flow is then limited by the ability of the medium to conduct fluid towards the fractures.

As expected phenomenologically, the horizontal and non-intersecting fractures do not add significant permeability to the samples in the direction of flow. In contrast to that, the permeabilities of the type 2 networks are between 1.5 and 2 times higher than that of the unfractured medium, while for the type 3 networks, factors of 3 can be observed. This difference is expected as in the networks of type 3, only the flow to the fractures is a limiting factor, whereas in the networks of type 2 also the flow towards the outlet must go through the bulk medium. A comparison of Figure 5.16a and Figure 5.16b furthermore shows that when a higher bulk permeability is considered, the permeability increase occurs at higher apertures. Recall that the fluxes in the fracture scale with a^3 due to the cubic law. From the Figures 5.16a and 5.16b we can see that a significant increase in permeability is observed for apertures values in the order of or greater as the cubic root of the bulk permeability, which marks the transition point above which the effective tangential permeability is greater than that of the surrounding medium. With these observations we note that the model is able to capture expected phenomena.

Regarding the maximum effective permeabilities for type 2 networks, the differences among the realizations of this type lie within a range of 12%, and the minimum and maximum values were observed for the networks \mathcal{F}_{21} and \mathcal{F}_{23} , respectively. Figure 5.17 shows the velocity distributions in the domain for these two networks and an aperture of $a = 3.16 \cdot 10^{-1}$ mm. It can be seen that the high velocities are concentrated at the bottom and the top of the domain, i.e. in regions where flow towards and away from the fractures occurs. Within the regions where fractures are present, comparatively small velocities can be seen as most of the flow goes through the fractures. For network \mathcal{F}_{23} , we note that a larger vertical extent is covered between the lowest and highest

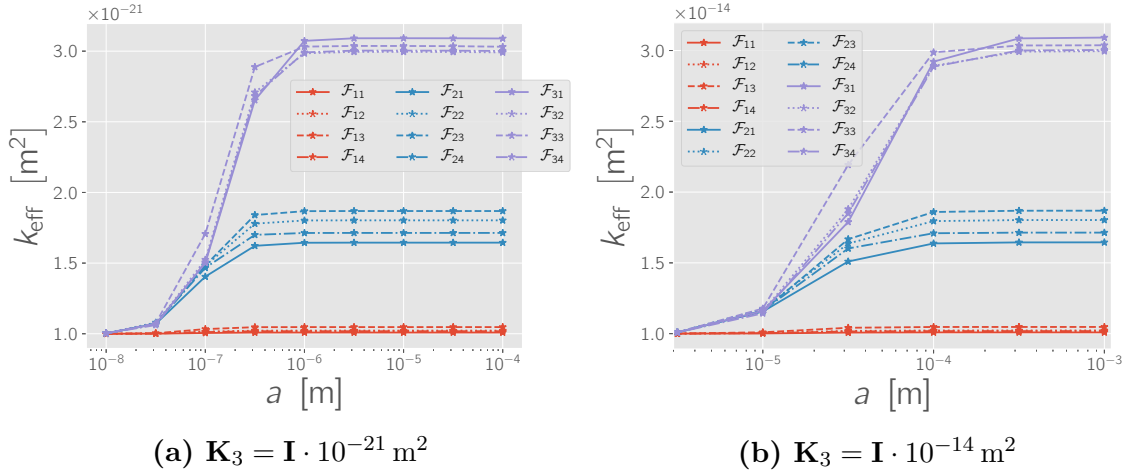


Figure 5.16 – Test case 5: numerically determined effective permeabilities. These are plotted against the considered values for the hydraulic aperture.

horizontal fractures, which leads to a shorter distance between the fracture network and the inlet and outlet boundaries. As almost the entire pressure drop occurs within the bulk medium, this in turn leads to higher flow velocities, which can also be seen from the pressure plots along the z -axis through the middle of the domain, given in Figure 5.18. Hence, with the bulk medium being the limiting factor for flow after the apertures have reached a critical value, the model suggests that the distance between the inlet and outlet boundaries and the fracture network has a significant impact on the effective permeability. We note that this is to be expected from a phenomenological point of view.

Summary Inspired by experimental results reported in the "Abeitsbericht NAB 13-51" published by Nagra, in this test case we numerically determined effective permeabilities of synthetic core samples. In a foregoing investigation, we compared the effective permeabilities determined by the TPFA, MPFA and the BOX scheme for a specific network and fracture aperture. Subsequently, we studied a set of 12 synthetic core samples using the BOX scheme, which is the most efficient scheme on the used tetrahedral grid. The results are in agreement with the expected phenomenological behavior, i.e. an increase in effective permeability with increasing apertures was observed, at least for those networks that exhibit vertical connectivity. A non-linear transition zone was observed between the effective permeability being equal to that of the bulk medium for very small apertures to a maximum value, which reflects the non-linear dependency of the

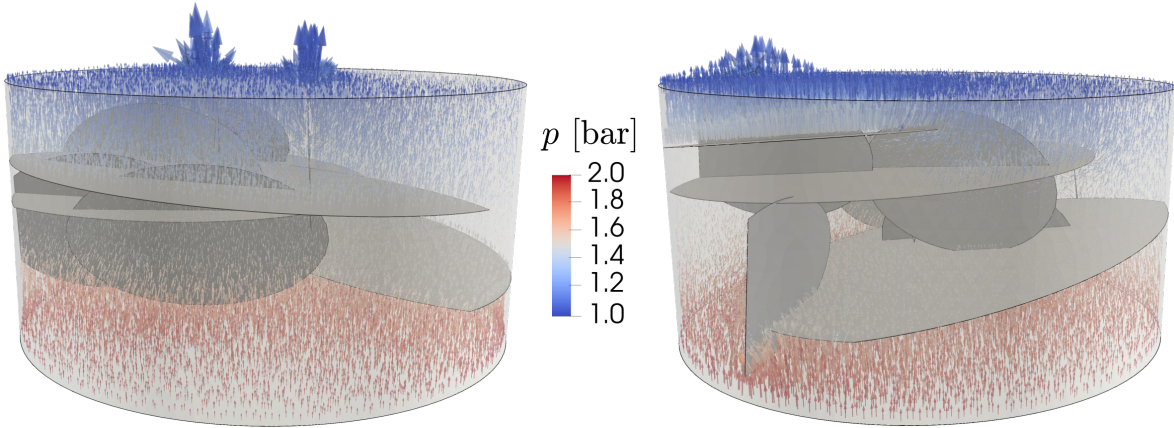


Figure 5.17 – Test case 5: velocity and pressure distributions. Depicted are the distributions for the networks \mathcal{F}_{21} (left) and \mathcal{F}_{23} (right) and an aperture of $a = 0.316$ mm. The arrows indicate the velocity and are colored with the pressure distribution.

tangential fracture permeability on the aperture by means of equation (3.28). Furthermore, the maximum value showed to be dependent on the network topology and was highest for networks that exhibit connections to the outlet boundary. Moreover, the impact of the fractures on the effective permeability became significant after the aperture reached values greater than the cubic root of the surrounding bulk permeability, which is in agreement with the fluxes in the fractures scaling with a^3 when using the cubic law.

Please note that we have neglected flow along the intersections of fractures in this case. In preliminary numerical simulations we did consider intersections of fractures, in which we assumed Hagen-Poiseuille type flow, i.e. the tangential permeabilities in the intersection regions were also defined proportional to a^2 . Using such a relation, after insertion into (3.23b) the tangential mass fluxes scale with a^4 and are thus at least three orders of magnitude smaller than the fluxes in the fractures for all aperture values considered here. Apart from that, we expect that the intersections possibly affect only the transition zone, as the minimum and maximum values of permeability for a specific network (of the types considered in this example) depend on the permeability of the bulk medium. Even though the effective permeabilities were not affected significantly by accounting for flow along intersections, this could have an effect on the actual flow pattern and become important when transport is considered. This will be addressed in Section 5.2.2.

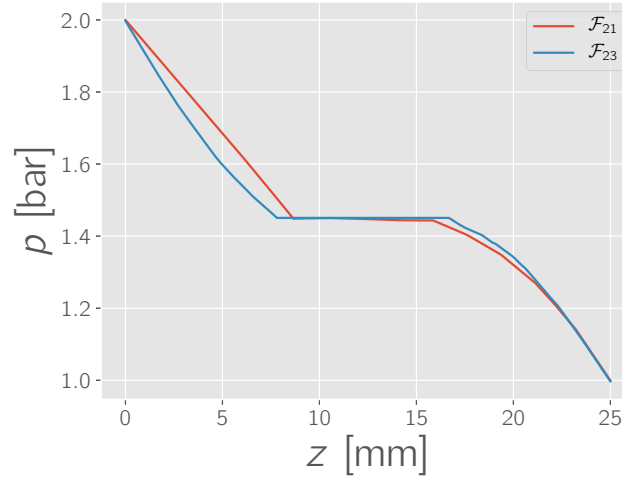


Figure 5.18 – Test case 5: pressure profiles. The plot shows the pressures in the bulk domain along the z -axis for the networks \mathcal{F}_{21} and \mathcal{F}_{23} .

5.1.6 Conclusions from the test cases

The investigations presented in Section 5.1.1 and 5.1.2 showed that the hybrid-dimensional schemes converge to equi-dimensional numerical or analytical reference solutions as long as the discretization length is larger than the aperture. Irreducible errors seemed to remain for $h < a$, however, the observations indicate that these are rather small. After excluding errors related to source terms, for all cases relative pressure errors $< 1\%$ were observed already for $h \approx 10a$. In Section 5.1.3 and 5.1.4, solver efficiencies were compared for the schemes on two- and three-dimensional setups involving complex fracture networks. As expected, the MPFA scheme is computationally much more expensive than the remaining schemes, especially on three-dimensional unstructured grids where the element stencils and interaction volumes become very large. The BOX and BOX-CONT schemes showed to be more efficient in terms of linear solver times as they lead to fewer degrees of freedom on unstructured discretizations. But, in some cases, the iterative solvers lacked convergence. Furthermore, as expected, the pressure solutions obtained with the BOX-CONT scheme did not capture relevant phenomena in the case of low-permeable fractures. In Section 5.1.5 the hybrid-dimensional schemes were applied to the task of determining effective permeabilities of synthetic core samples. Phenomenologically consistent results were observed, in which the effective permeabilities nonlinearly increase with the fracture aperture until reaching a maximum value, which seemed to be characteristic for a certain type of network topology.

5.2 Two-phase flow in rigid fractured porous media

In this section we want to test the hybrid-dimensional schemes on problems involving two-phase flow. In all examples, the mixed-dimensional flow equations (3.23)-(3.27) are solved, in which we use the van-Genuchten-Mualem relationship to relate capillary pressures and relative permeabilities to the saturations (see Section 2.1), and use a regularization for water saturations above 99% and below 1% (for details we refer to the DuMu^x documentation [Flemisch et al., 2011, Koch et al., 2018a]). In Section 5.2.1, a simple two-dimensional geometry is considered for which an equi-dimensional reference solution can be computed. The test case presented in Section 5.2.2 considers a more complex, three-dimensional geometry that was designed to mimic a gas injection scenario into a cylindrical core sample.

5.2.1 Test case 6: crossing fractures

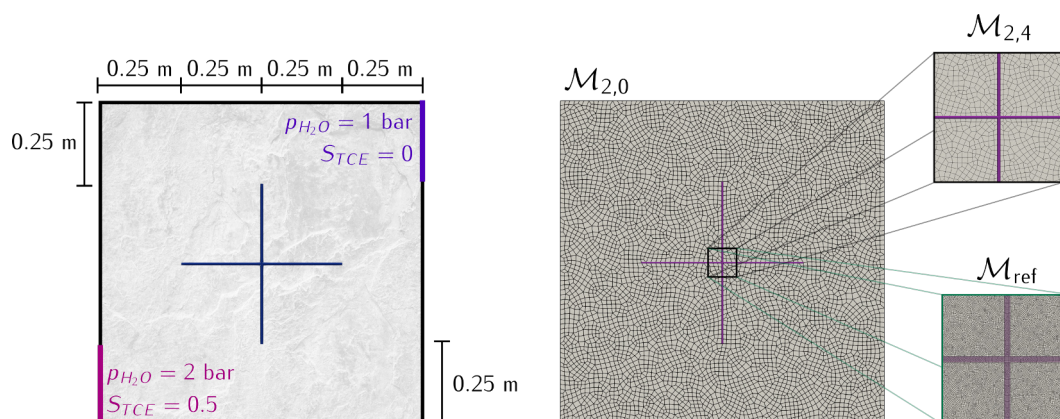


Figure 5.19 – Test case 6: domain, boundary conditions and grids. The left image shows the boundary conditions, while on the right a snapshot of the coarsest hybrid-dimensional grid is shown. Furthermore, a close-up on the intersection region is provided, in which both the finest hybrid-dimensional and the reference grid are depicted.

In this test case, we consider a unit square domain, $\Omega = (-0.5, -0.5) \times (0.5, 0.5)$, with two fractures intersecting at an angle of 90° in its center. The domain is initially fully saturated with water, the wetting phase, and an inflow of the non-wetting phase, liquid Trichloroethene (TCE), is enforced through the inlet boundary located on the lower left side of the domain boundary, where an elevated water pressure and a saturation of $S_{TCE} = 0.5$ is prescribed. Both the domain and the boundary conditions are illustrated

in Figure 5.19. Gravitational forces are neglected, and the fluid densities and viscosities are given by $\rho_{\text{H}_2\text{O}} = 1000 \text{ kg/m}^3$, $\rho_{\text{TCE}} = 1460 \text{ kg/m}^3$, $\mu_{\text{H}_2\text{O}} = 1 \cdot 10^{-3} \text{ Pa s}$ and $\mu_{\text{TCE}} = 5.7 \cdot 10^{-4} \text{ Pa s}$, respectively. The final simulation time is set to $t_{\text{end}} = 1 \cdot 10^4 \text{ s}$ with an initial and maximum time step size of $\Delta t = 0.1 \text{ s}$ and $\Delta t_{\text{max}} = 250 \text{ s}$. The time step size is adjusted depending on the convergence behavior of the nonlinear solver as described in Appendix B.

The schemes were tested for both highly-conductive as well as low-permeable fractures, and for both cases an equi-dimensional reference solution was computed with the MPFA scheme on a locally refined, quadrilateral grid with approximately 4 elements discretizing the aperture of $a = 1 \cdot 10^{-3} \text{ m}$ of the fracture. Numerical solutions were then computed for the hybrid-dimensional schemes on a series of grids $\mathcal{M}_{d,i}, i \in \{0, \dots, m\}$ with $m = 4$, which were refined locally around the fracture. Figure 5.19 shows the grid used for the bulk domain in the coarsest hybrid-dimensional discretization $\mathcal{M}_{2,0}$, as well as a close-up on the discretizations of the fracture intersection regions within the finest hybrid-dimensional mesh $\mathcal{M}_{2,4}$ as well as the equi-dimensional reference grid. It can be seen that the finest hybrid-dimensional discretization is still significantly coarser than the reference grid, which contains 611 086 elements and was constructed defining a characteristic length of $h_f = a/4 = 2.5 \cdot 10^{-4} \text{ m}$ within the fractures and $h_b = 5 \cdot 10^{-2} \text{ m}$ on the boundaries. The latter characteristic length is used by the coarsest hybrid-dimensional grid within the entire domain, while the finest hybrid-dimensional grid is refined towards the fracture such that $h_f = a = 1 \cdot 10^{-3} \text{ m}$ in the region close to the fractures. An overview over the number of cells used for the different grids can be found in Table 5.4. The permeability and porosity of the matrix

Table 5.4 – Test case 6: grid specifications. Number of cells used in the reference grid and the hybrid-dimensional grids on different refinement levels.

Grid	#-cells ($d = 2$)	#-cells ($d = 1$)	h_f/a
$\mathcal{M}_{d,0}$	5880	68	15.0
$\mathcal{M}_{d,1}$	8172	100	10.0
$\mathcal{M}_{d,2}$	16 198	200	5.0
$\mathcal{M}_{d,3}$	26 526	500	0.5
$\mathcal{M}_{d,4}$	100 458	1000	1.0
\mathcal{M}_{ref}	611 086	-	0.25

were set to $\mathbf{K}_b = \mathbf{K}_2 = \mathbf{I} \cdot 10^{-13} \text{ m}^2$ and $\phi_b = \phi_2 = 0.2$ and the parameters for the van Genuchten-Mualem model (see Section 2.1) were chosen as $\alpha_b^{\text{VG}} = \alpha_2^{\text{VG}} = 1 \cdot 10^{-3} \text{ 1/Pa}$ and $n_b^{\text{VG}} = n_2^{\text{VG}} = 3$.

Highly-conductive fractures In a first test we want to consider fractures that are highly permeable in comparison to the surrounding porous matrix, and use $\mathbf{K}_f = \mathbf{K}_1 = \mathbf{I} \cdot 10^{-9} \text{ m}^2$ and $\phi_f = \phi_1 = 0.5$ as well as $\alpha_f^{\text{VG}} = \alpha_1^{\text{VG}} = 1 \cdot 10^{-2} \text{ m}^2$ and $n_f^{\text{VG}} = n_1^{\text{VG}} = 2$. This causes rapid transport of TCE along the fractures as soon as it reaches them, which can be seen in Figure 5.20, where the saturation distribution at the final simulation time is depicted for both the reference and the hybrid-dimensional MPFA scheme together with the distributions of the errors in saturation for the different hybrid-dimensional schemes. From the saturation distributions one can observe that the hybrid-dimensional and the equi-dimensional results agree rather well, with the errors predominantly being located in the two TCE plumes leaving the fractures towards the outlet. Moreover, it can be seen that the largest errors occur for the BOX-CONT scheme, especially in the matrix regions adjacent to the highly saturated parts of the fractures. This is related to the interface condition the scheme uses to reconstruct the saturation in the matrix based on the saturation inside the fracture.

Figure 5.21 shows plots of the saturation in the matrix through the domain for all hybrid-dimensional schemes and grid refinements. While the saturation distribution upstream to the fractures is in good agreement with the reference, the TPFA, MPFA, and BOX scheme significantly overestimate the saturation in the downstream region of the fractures with the coarse grids, where the reference predicts fully water-saturated conditions. However, these deviations decrease upon refinement and might be related to numerical diffusion which is much larger on the coarser grids. This is not only due to the poorer spatial, but also the poorer temporal resolution. The very small elements inside the fracture in the reference grid require smaller time steps, and a total of 408 time steps was necessary to compute the reference solution. For comparison, only 142 and 184 time steps were necessary with the MPFA and the BOX scheme on the finest grid, while on refinement level 3 these numbers reduce to 92 and 117, respectively. Nevertheless, despite the substantial differences in computational cost, a rather good agreement between the reference and the hybrid-dimensional MPFA solution can be seen already on the third refinement level. Since for the BOX-CONT transfer fluxes between fracture and matrix are not constructed, the influence of numerical diffusion on the

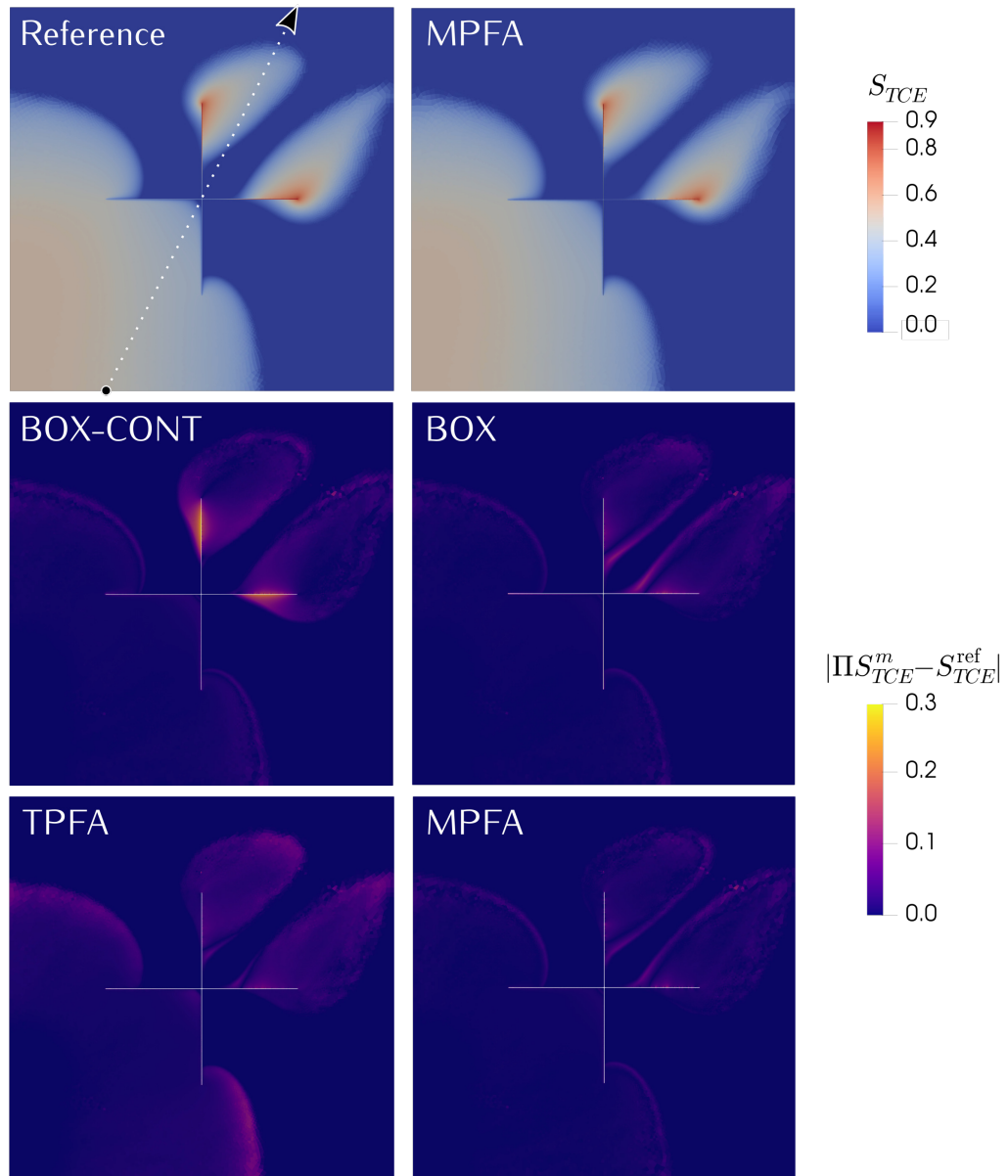


Figure 5.20 – Test case 6.1: saturation distributions. The saturation in the reference and the hybrid-dimensional MPFA solution on the finest grid are shown in the upper row. The center and bottom row show the saturation error distributions for the different mixed-dimensional schemes at the final simulation time. These depict the absolute difference between the reference saturation S_{TCE}^{ref} and the L2-projection of the saturation distribution on finest hybrid-dimensional grid ΠS_{TCE}^m . The dashed white line depicts the line along which the plots in Figure 5.21 were generated.

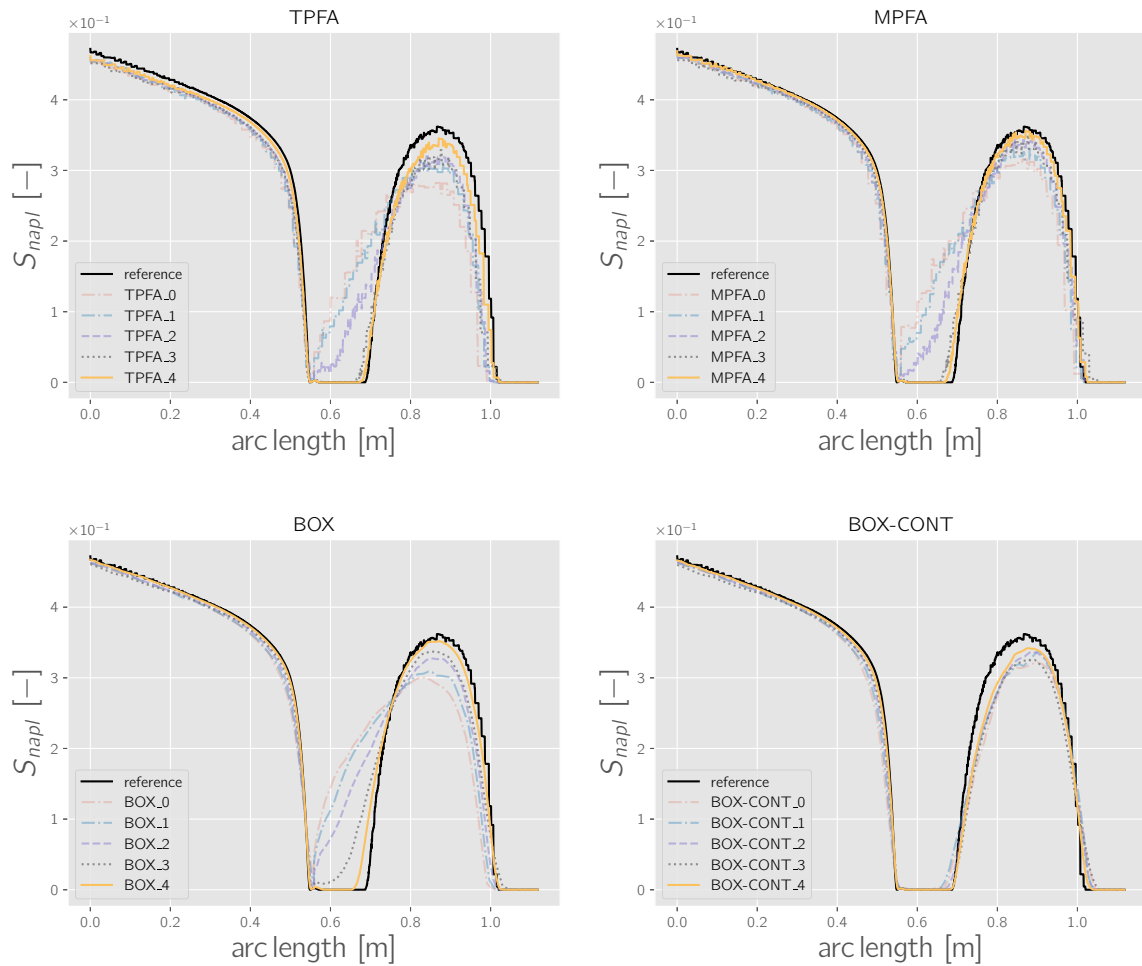


Figure 5.21 – Test case 6.1: saturation plots. The plots show the saturation along the line $(-0.25, -0.5) - (0.25, 0.5)$ for the case of highly permeable fractures. See Figure 5.20 for an illustration of the line along which the plots were generated. The integer sub-scripts indicate the refinement levels of the hybrid-dimensional grids.

saturations in the near region downstream of the fractures seems to be less prominent. This is again due to the interface condition which produces very low saturations in the matrix if the saturation in the fracture is small. The drawback of this approach has been discussed earlier.

Low-conductive fractures Let us now change the fracture properties such that they act as both hydraulic and capillary barriers, and set $\mathbf{K}_f = \mathbf{K}_1 = \mathbf{I} \cdot 10^{-16} \text{ m}^2$, $\phi_f = \phi_1 = 0.05$, $\alpha_f^{\text{VG}} = \alpha_1^{\text{VG}} = 1 \cdot 10^{-4} \text{ m}^2$ and $n_f^{\text{VG}} = n_1^{\text{VG}} = 2$. In this case, flow occurs predominantly around the fractures, and both hydraulic and capillary effects cause the TCE to accumulate before the fractures, which can be seen from the reference saturation distribution shown in Figure 5.22. The pooling regions and the regions of the TCE saturation front are those where the highest deviations between the reference and the hybrid-dimensional schemes, apart from the BOX-CONT scheme, occur. The deviations at the saturation front might be influenced by the fact that the reference grid is still significantly finer and numerical diffusion caused by both spatial and temporal resolution differences could play an important role. On the other hand, the deviations in the regions where TCE accumulates are influenced by the fact that the matrix-fracture interfaces are at different locations, as in the hybrid-dimensional discretizations the interface is geometrically located at the center of the two-dimensional fracture. However, the hybrid-dimensional schemes produce much thinner and much less pronounced pooling regions which can be seen in the plots shown in Figure 5.23. With increasing refinement the saturation distributions obtained by the hybrid-dimensional MPFA and BOX schemes do approach the reference in regions further away from the fractures, but still show noticeable differences close to the fracture even for the finest grid. In the reference solution a very steep increase in saturation towards the fractures can be seen on the upstream side, while on the downstream side, TCE can be quickly transported away from the fractures and the saturations are comparatively small. Both the steep increase on the upstream as well as the low saturations on the downstream sides close to the fractures are captured rather poorly by the hybrid-dimensional schemes. As can be seen in Figure 5.23, an additional simulation has been performed with the TPFA scheme on a grid that uses the same discretization length around the fracture as the reference and which consists of 519 160 two-dimensional and 4000 one-dimensional elements. However, this did not lead to a significant improvement of the issues mentioned above. We have seen in the Sections 5.1.1 and 5.1.2 that the hybrid-dimensional

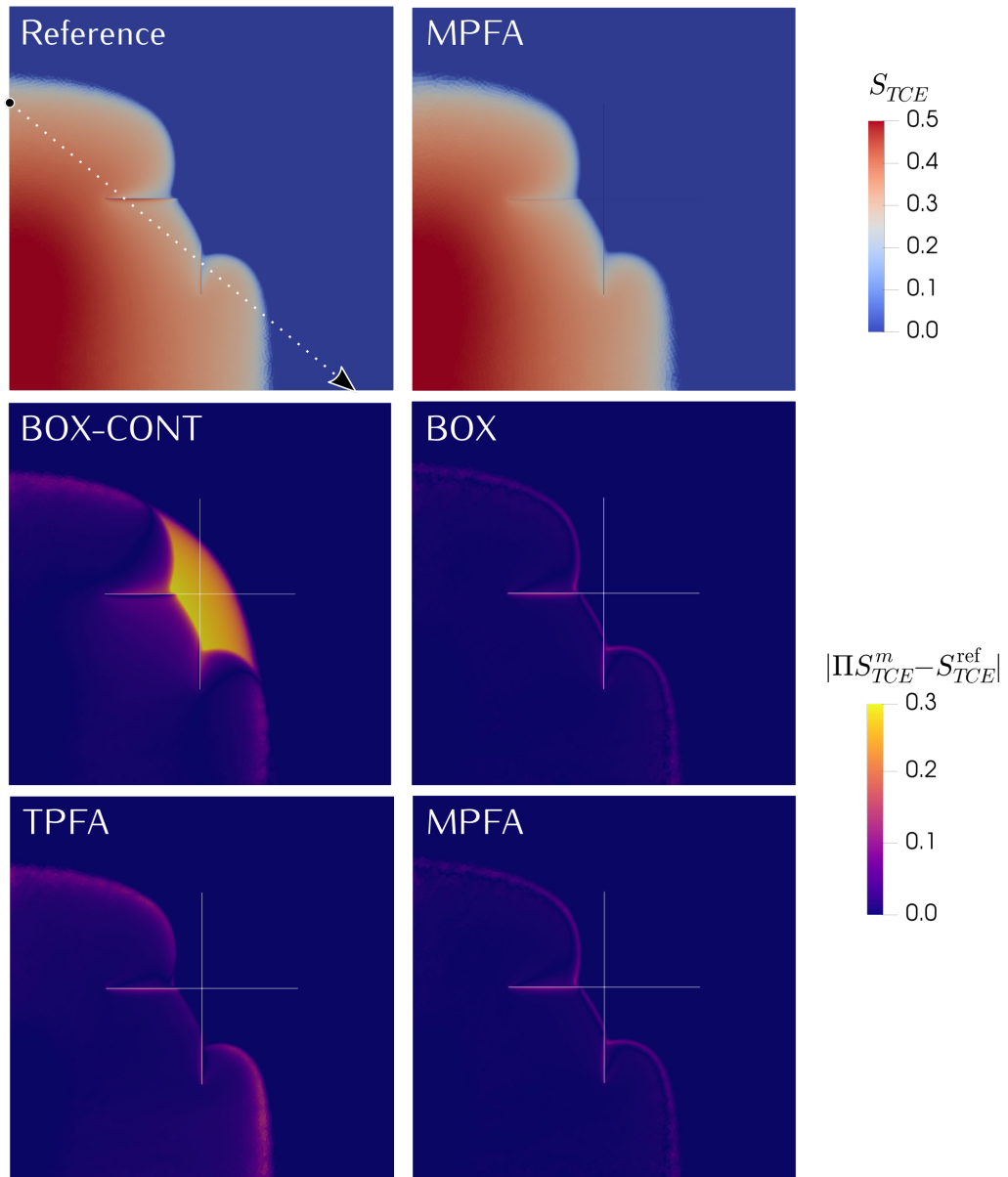


Figure 5.22 – Test case 6.2: saturation distributions. The saturation in the reference and the hybrid-dimensional MPFA solution on the finest grid are shown in the upper row. The center and bottom row show the saturation error distributions for the different mixed-dimensional schemes. These depict the absolute difference between the reference saturation S_{TCE}^{ref} and the L2-projection of the saturation distribution on finest hybrid-dimensional grid onto the reference grid ΠS_{TCE}^m . The dashed white line depicts the line along which the plots in Figure 5.23 were generated.

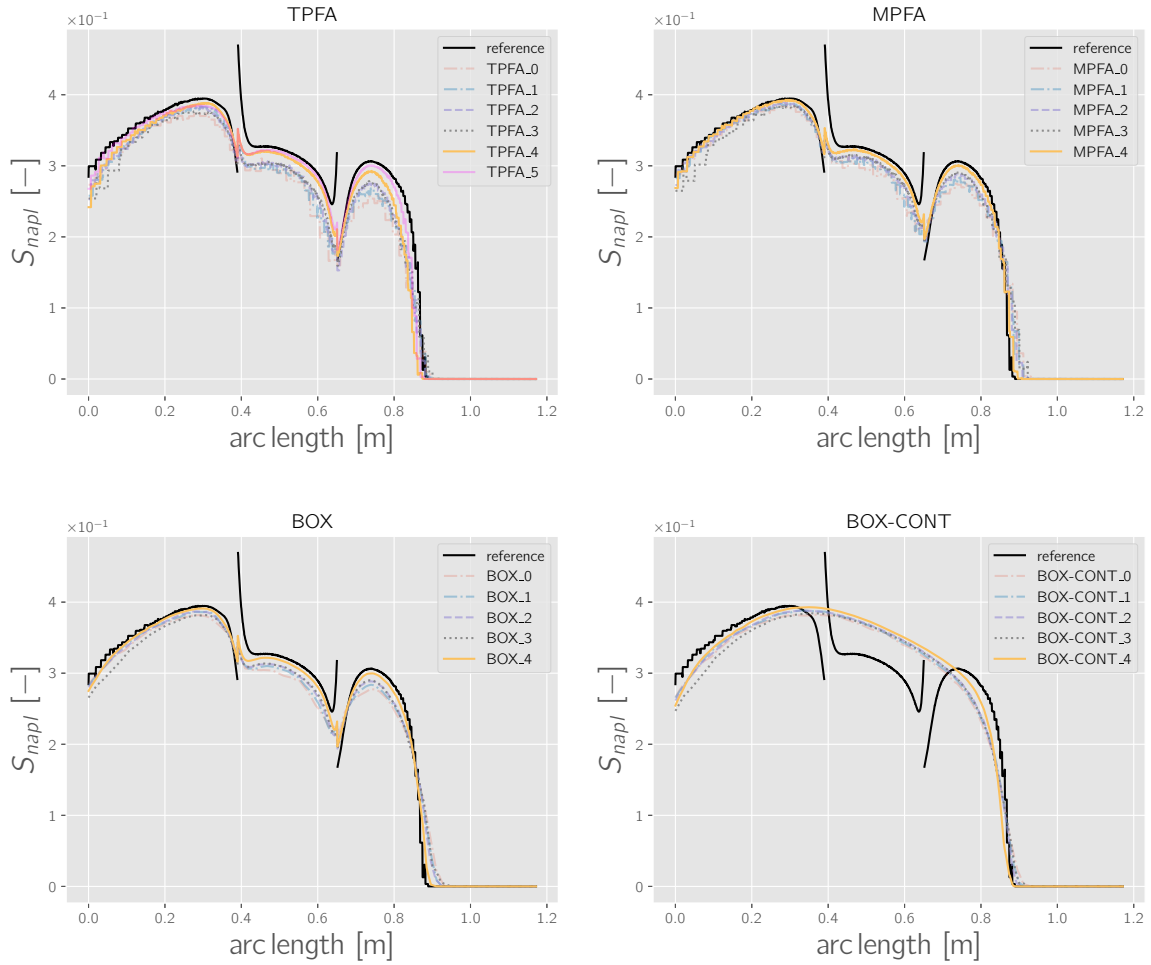


Figure 5.23 – Test case 6.2: saturation plots. The plots show the saturation along the line $(-0.5, 0.25) - (0.4, -0.5)$ for the case of low permeable fractures. See Figure 5.22 for an illustration of the line along which the plots were generated. The integer sub-scripts indicate the refinement levels of the hybrid-dimensional grids.

schemes capture the transfer fluxes between matrix and fracture rather well when compared to analytical or equi-dimensional reference solutions. In the context of two-phase flow, however, both the mobility and the capillary pressure add nonlinearities to the flux terms. In this case of blocking fractures, a saturation profile develops across the fracture due to the slow transport within the fracture and the fast transport away from it on the downstream side. We suppose that the origin of the above-mentioned deviations lies in the lower-dimensional description of the fractures, in which the saturations represent cross-section averaged values. As a consequence, using the averaged value together with the upwind scheme that is applied in this work, the mobility for

the transport out of the fracture is overestimated, while the capillary pressure inside the fracture is underestimated at the interface on the upstream side. This means that both the transport into the fracture as well as out of it are overestimated, which could explain the smaller saturation jumps as in the reference.

Figure 5.24 shows again the saturation profile obtained with the MPFA scheme on the finest grid as well as the reference solution, but, it additionally depicts the saturation profile obtained from an equi-dimensional discretization (using MPFA) which considers only one element for the discretization of the fracture width. This grid was constructed such that the discretization length matches the one used in the finest hybrid-dimensional discretization. As expected, the equi-dimensional discretization with only one cell discretizing the width of the fracture agrees very well with the hybrid-dimensional discretization. Note that this equi-dimensional discretization, in contrast to the hybrid-dimensional discretizations, does not introduce a volume error. The good agreement between the two solutions indicates that this source of error does not play an important role in this case, but that the error is dominated by the poor approximation of the transfer fluxes. However, despite the deviations very close to the fracture, the hybrid-dimensional models qualitatively capture the expected phenomena, except for the BOX-CONT scheme, for which substantial deviations can be observed.

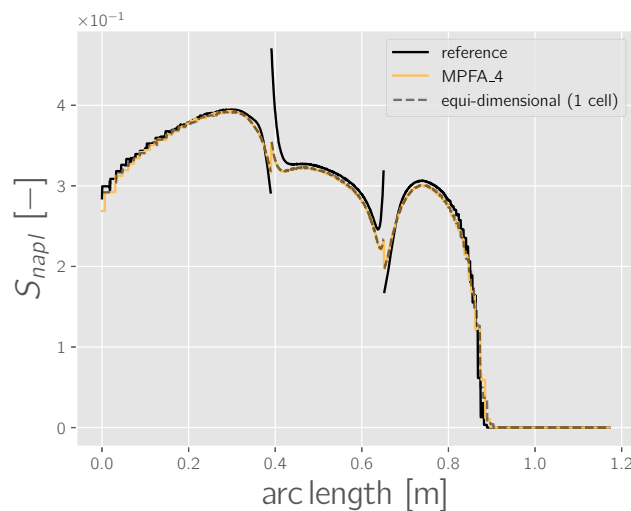


Figure 5.24 – Test case 6.2: saturation plots. The saturation obtained with the hybrid-dimensional MPFA scheme on the finest grid ($\mathcal{M}_{2,4}$), the reference saturation and the saturation obtained from an equi-dimensional discretization with only one cell discretizing the width of the fracture, plotted along the line $(-0.5, 0.25) - (0.4, -0.5)$ for the case of low permeable fractures. See Figure 5.22 for an illustration of the line along which the plots were generated.

Summary In this test case the quality of the results obtained with the hybrid-dimensional schemes in the context of two-phase flow were analyzed by comparison against equi-dimensional reference solutions. Both highly-conductive as well as blocking fractures were considered, where for the first case a rather good agreement among the solutions was observed. Furthermore, the errors diminished with each refinement step. In the case of blocking fractures, it could be seen that the lower-dimensional description of the fractures leads to larger errors, in particular in the close vicinity of the fractures where step saturation gradients were observed in the equi-dimensional reference solution and which could not be properly captured by the hybrid-dimensional schemes. A comparison with an equi-dimensional solution with only one grid cell discretizing the width of the fractures showed that this effect is caused by the fact that the saturation and mobility profiles along the width of the fractures are not properly captured. Future work could be aimed at investigating if the modified transmission conditions at matrix-fracture interfaces, recently presented in Aghili et al. [2019], Brenner et al. [2018], lead to better results for low-conductive fractures. It should be mentioned that these conditions require a local Newton solver for the assembly of each discrete flux. However, in the rest of the domain the shape of the saturation front was captured rather well by all schemes except the BOX-CONT scheme, which failed to capture the relevant phenomena. We note that the comparisons shown in this test case are of rather qualitative nature and do not claim to be rigorous. A more rigorous comparison would require, for instance, a more elaborate evaluation of the time step sizes to be used on each refinement level.

5.2.2 Test case 7: two-phase flow in a synthetic core sample

Experiments conducted on core samples of a target formation in order to characterize the in-situ rock are important in many geotechnical engineering applications. One example was already mentioned in Section 5.1.5, which was devoted to the determination of effective permeabilities. However, in many applications two-phase flow processes might be of importance, and experiments considering the displacement of a fluid phase by another fluid phase could help in understanding the two-phase flow mechanisms occurring in a specific type of rock. In this example, we want to apply the hybrid-dimensional schemes to a gas injection scenario into a synthetic core sample of fractured rock, for which we consider a cylindrical geometry with a diameter of 10 cm

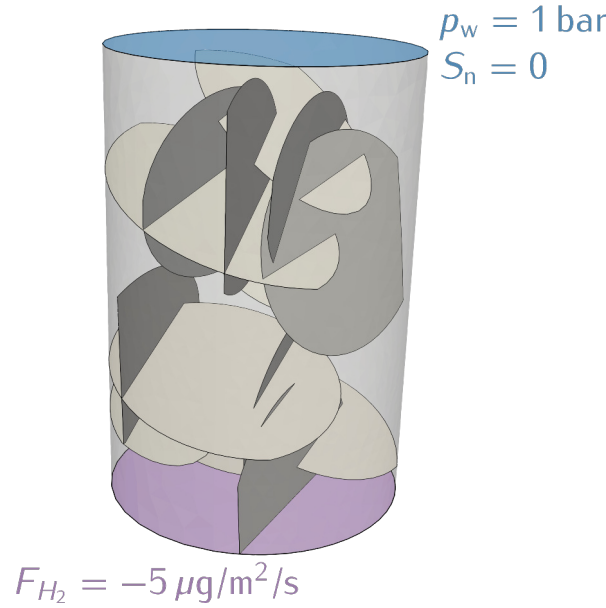


Figure 5.25 – Test case 7: domain, fracture network and boundary conditions. On the top of the domain, both pressure and saturation are fixed, while an injection of hydrogen on the bottom boundary is realized via a Neumann boundary condition. Note that the injection occurs into both the bulk medium and the fracture intersecting with the bottom boundary.

and a height of 15 cm. A random fracture network, shown in Figure 5.25 together with the boundary conditions, is embedded into the domain.

We consider an injection of hydrogen across the bottom boundary into an initially fully water-saturated medium at a constant pressure of $p_{H_2O} = 1 \text{ bar}$. The DuMu^x implementations of water and hydrogen are used, which are based on Wagner and Kretzschmar [2008], Reid et al. [1987] and for which further details can be found in the DuMu^x documentation [Flemisch et al., 2011, Koch et al., 2018a]. We define water to be the wetting phase in this setting and set the permeability and porosity of the bulk medium to $\mathbf{K}_3 = \mathbf{I} \cdot 10^{-14} \text{ m}^2$ and $\phi_3 = 0.1$, respectively, while $\alpha_3^{\text{VG}} = 1 \cdot 10^{-4} \text{ 1/Pa}$ and $n_3^{\text{VG}} = 3.0$ are used for the parameters of the van-Genuchten-Mualem relationship (see Section 2.1). For the fractures and intersections of fractures we will distinguish between cases of conductive and blocking fractures again in the sequel. The fracture aperture and cross-section area of intersections of fractures are set to $a = 5 \cdot 10^{-4} \text{ m}$ and $\epsilon_1 = 1 \cdot 10^{-6} \text{ m}^2$.

Table 5.5 – Test case 7.1: parameter choices. Permeability, porosity and the van-Genuchten-Mualem model in the subdomains for the case of highly-conductive fractures.

	\mathbf{K}_d [m ²]	ϕ_d [-]	α_d^{VG} [1/Pa]	n_d^{VG} [-]
Ω_3	$\mathbf{I} \cdot 10^{-14}$	0.1	$1 \cdot 10^{-4}$	3.0
Ω_2	$\mathbf{I} \cdot 10^{-10}$	0.5	$1 \cdot 10^{-3}$	2.5
Ω_1	$\{\mathbf{I} \cdot 10^{-8}, \mathbf{I} \cdot 10^{-18}\}$	$\{0.7, 0.01\}$	$\{5 \cdot 10^{-2}, 1 \cdot 10^{-5}\}$	2.5

Highly-conductive fractures Let us consider fractures that act as conduits for flow. We associate higher permeabilities with higher porosities and lower capillary pressures, and on the basis of these considerations we choose the parameters given in Table 5.5. In a first setting, let us neglect flow along fracture intersections and investigate the influence of the fractures with and without considering gravitational acceleration. Figure 5.26 shows the velocity and saturation distribution in the domain after 20 s of hydrogen injection, in which a very strong influence of the fractures on the flow field can be observed. While in the case of no fractures (see Figure 5.26b) hydrogen has only invaded about half of the domain, the presence of fractures cause hydrogen to already be produced at the outlet at this point in time. This is confirmed by the temporal evolution of the hydrogen mass contained within the domain shown in Figure 5.27 together with the curves of production at the outlet. In the case of the fractures being neglected, production of hydrogen at the outlet begins at later simulation times (see Figure 5.27b). The figure furthermore shows that TPFA predicts noticeably different production curves when compared to MPFA, while the deviations between BOX and MPFA are smaller. However, it should be taken into account that by specifying Dirichlet boundary conditions on the top boundary, the uppermost strip of sub-control volume faces on the lateral boundaries also allow for outflow in the BOX scheme, which is due to the fact that they are connected to Dirichlet boundary vertices. This leads to an increased outflow area which explains the earlier onset of production. Please note that we do not show results for the hybrid-dimensional MPFA scheme here, because some of the optimization capabilities in DuMu^x are not yet available for the MPFA implementation of the hybrid-dimensional model, which makes it computationally very expensive on unstructured grids in three dimensions.

Another interesting observation is that if the presence of fractures is neglected, gravity has a very small influence on the production curves (see Figure 5.27b), while noticeably more hydrogen is produced under the influence of gravitational forces when fractures

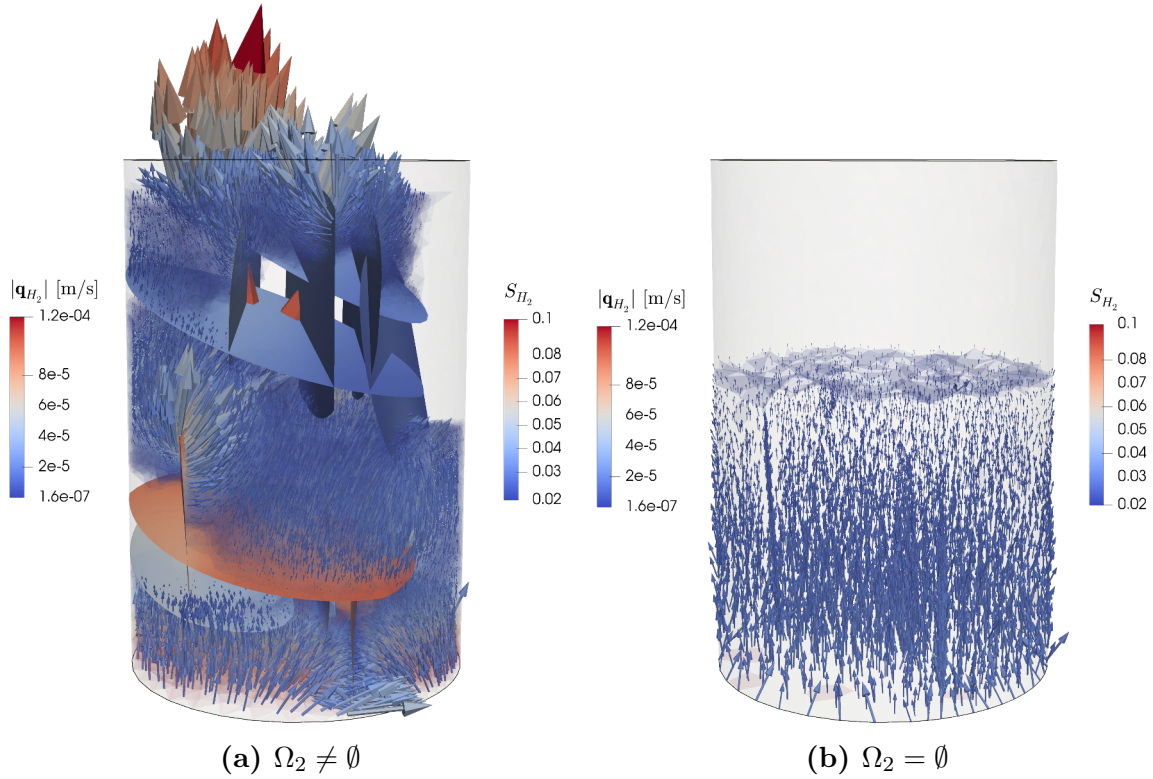


Figure 5.26 – Test case 7.1: saturation and velocity distributions. These are shown after 20s of injection for the case of fractures being considered (a) and neglected (b). Gravitational acceleration was not taken into account in the depicted results. The arrows show the velocities and are colored with the magnitude. The shaded volumes depict regions in which hydrogen saturations are above 1% and are colored with the hydrogen saturation, which is depicted on the fractures as well.

are present. This effect is particularly pronounced in the initial production rates, which seem to increase faster when gravity is considered. Let us relate the driving forces due to injection and buoyancy with the dimensionless number:

$$B = \frac{\Delta p/H}{\Delta \rho g}, \quad (5.8)$$

where Δp is the pressure difference applied to the core sample of height $H = 0.015$ m. We see that for high pressure gradients or low density differences $\Delta \rho$, the system is controlled by the injection. The density difference $\Delta \rho$ between water and hydrogen is in the order of ≈ 1000 kg/m³ (the gas density is below 1 kg/m³ in all simulations). However, the pressure gradients depend on the effective permeability of the medium. We have seen in Section 5.1.5 that almost the entire pressure drop occurs within the

matrix, while the pressure drop over highly-permeable fracture networks is very small. This means that inside the fracture the flow field might be dominated by buoyancy.

Figures 5.28a and 5.28b show plots of the pressure along the z -axis from the bottom to the top boundary. As expected, the pressure difference is higher in the case of an unfractured medium and the pressure drop along the regions where fractures are present is very small. The pressure difference across the sample is $> 2 \cdot 10^5$ Pa in both cases and thus it is $B > 1360$, i.e. the injection is the dominating driving force in the matrix. However, the plots shown in Figure 5.28 show that this is not necessarily the case inside the fractures, where the pressure gradients are very small. Figure 5.29 depicts the differences in saturation and velocity in the fracture domain between the cases of considering and neglecting gravity. One can clearly see that when gravity is considered, higher saturations are observed in the top regions of fractures, indicating faster vertical transport driven by buoyancy and accumulation at the top of the fractures. This could explain the deviations observed in the production curves.

It should be mentioned that the production curves are computed by subtracting the contained mass of hydrogen from the injected mass. By doing so, the BOX-CONT scheme predicts produced hydrogen directly from the beginning of the injection, when hydro-

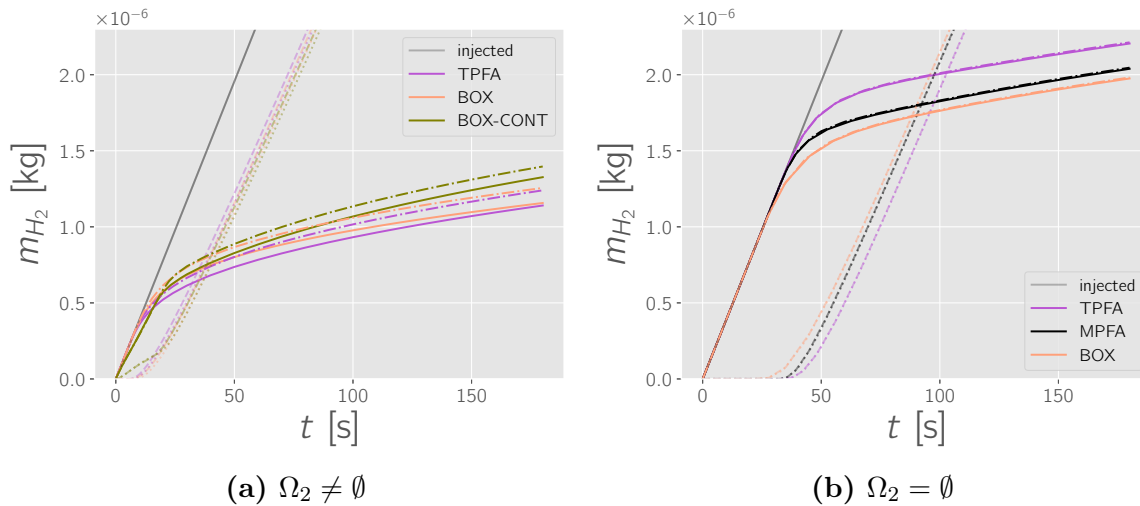


Figure 5.27 – Test case 7.1: production curves. Temporal evolution of the mass of hydrogen contained in the domain and hydrogen production curves. Figure (a) shows the case of the fractures being taken into account, while in (b) only the bulk medium is considered. The solid lines are for the case of gravity being taken into account, while the corresponding dash-dotted lines with the same color are the results for neglected gravity. The opaque dashed and dotted lines are the corresponding production curves for the case of considered and neglected gravity, respectively.

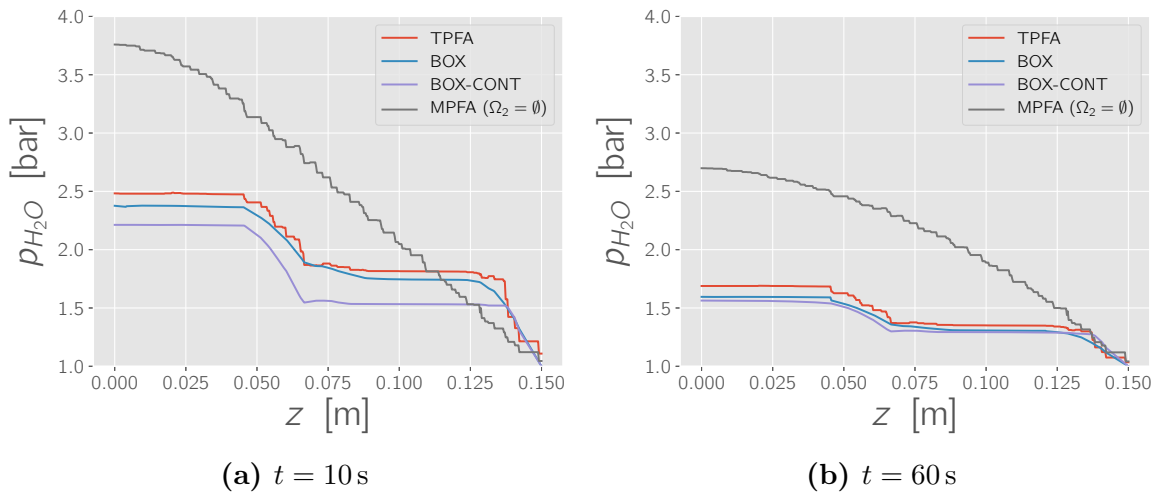


Figure 5.28 – Test case 7.1: pressure plots. Water pressure plotted along the z -axis from the bottom to the top of the domain for two different points in time. For comparison, the pressure profile for the case of neglecting the fractures is shown ($\Omega_2 = \emptyset$). Flow along intersections has not been taken into account in any of the results shown here.

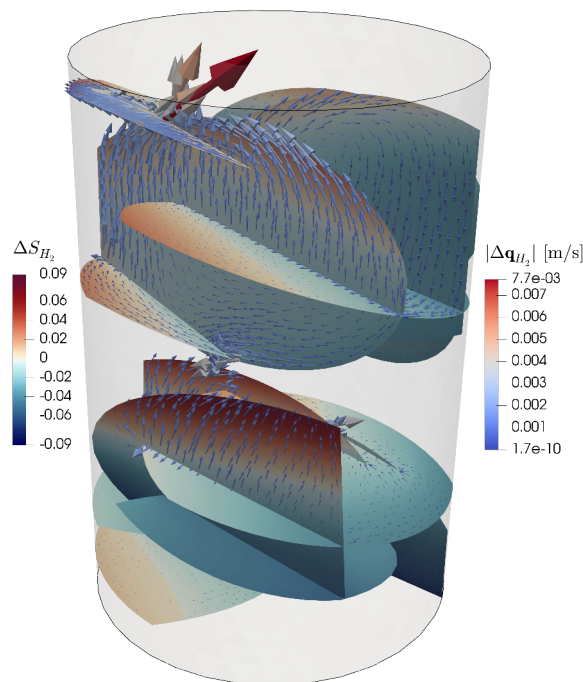


Figure 5.29 – Test case 7.1: influence of gravity on saturation and velocity. The figure shows the difference in hydrogen saturation and velocity in Ω_2 at $t = 40\text{ s}$ between the cases of considering and neglecting gravity. The arrows illustrate the velocity difference and are colored with the magnitude. The results shown here were obtained with the BOX scheme.

gen is still far away from the outlet boundary (see Figure 5.27). This is due to the fact that the scheme is not mass conservative due to the interface condition it uses for the saturations at matrix-fracture interfaces. This is a significant drawback of the scheme. We want to dedicate the remainder of this paragraph to investigate the influence of flow along fracture intersections. To this end, we perform additional simulations taking into account flow in intersections of fractures, for which we use the BOX scheme and the parameters listed in Table 5.5. Moreover, gravitational acceleration is neglected. Figure 5.30a shows the temporal evolution of hydrogen mass in the domain and associated production curves, where the curves for neglected gravity from Figure 5.27 are depicted again for comparison. It can be seen that the production rate at the outlet is slightly increased when flow along highly-permeable intersections is considered. The intersections have a quite significant impact on the flow field, which is illustrated in Figure 5.31. Due to the lower capillary pressures, the saturations in the intersections are generally higher than in the adjacent fractures, and they seem to influence quite substantially the saturation distribution and the locations of preferential flow paths within the fracture domain. In contrast to that, Figure 5.30b suggests that the pressure distributions in the bulk medium are almost identical for both cases.

In the rather hypothetical case of blocking fracture intersections, the onset of hydrogen production occurs significantly later. This effect is also visible in the pressure plots in Figure 5.30b, where in this case one can see that the pressure build-up at the inlet is higher and a pressure drop across the fractured regions is noticeable. This is in agreement with the expected behavior, and it shows that in such configuration the resistance to flow through the fracture network is no longer negligible for the overall resistance of the core sample.

Blocking fractures Let us now assume fractures that are less conductive than the bulk medium. Therefore, we define them to exhibit lower permeabilities and porosities and assume that higher capillary pressures prevail inside the fractures in comparison to the surrounding medium. We again consider two sub-cases related to the properties of the fracture intersections, which include both low-permeable intersections as well as such that are more permeable than the bulk medium. As in the previous paragraph, the latter situation might not represent a realistic scenario but is included here again to investigate the possible influences of the intersection properties. The parameter choices for both configurations are given in Table 5.6.

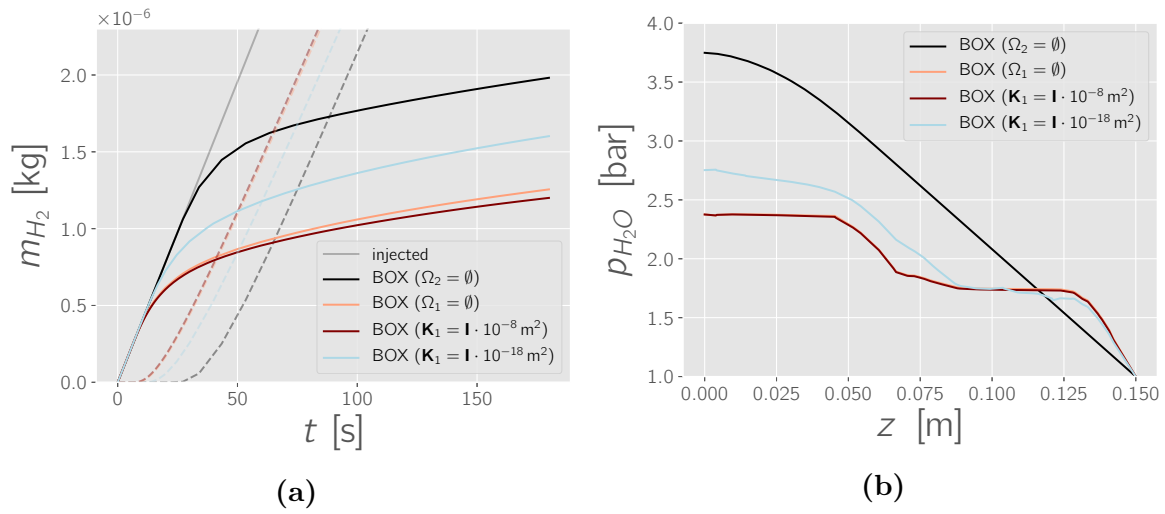


Figure 5.30 – Test case 7.1: influence of intersection flow on hydrogen production and water pressure. Hydrogen mass and produced mass over time for the case of considering flow along intersections of fractures in the absence of gravity (a). For comparison, the curves neglecting the fractures ($\Omega_2 = \emptyset$) and fracture intersections ($\Omega_1 = \emptyset$) from Figure 5.27 are depicted again. In (b), the pressure is plotted from bottom to top along the z -axis through the domain.

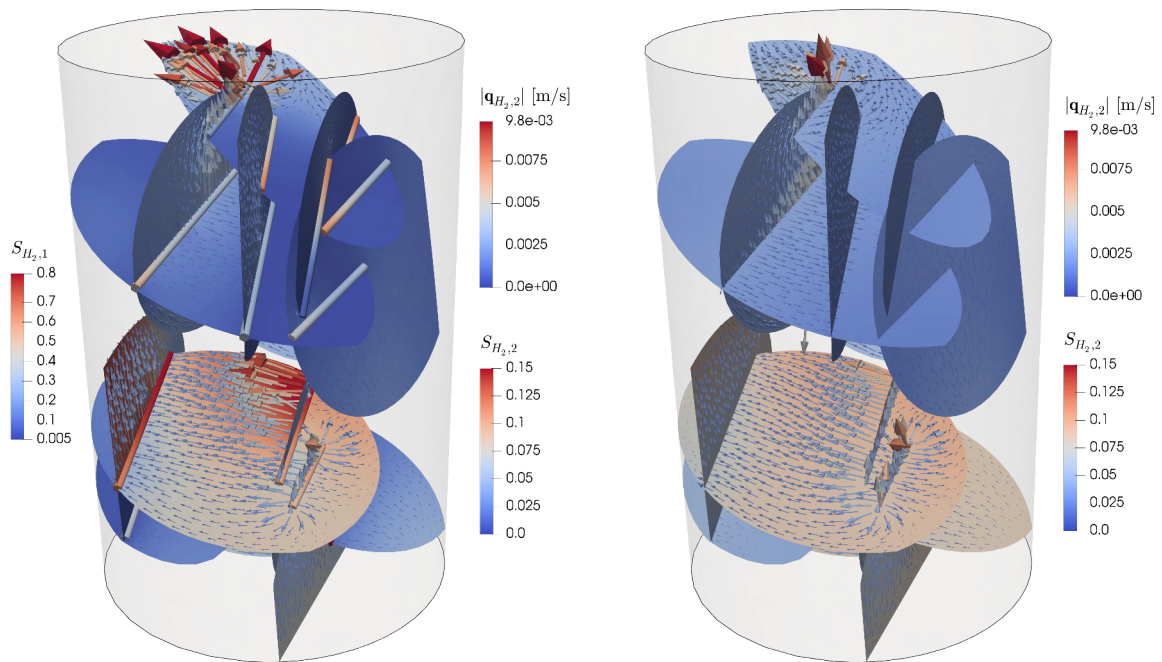


Figure 5.31 – Test case 7.1: influence of intersection flow on hydrogen saturation and velocity. Shown are the hydrogen saturation and velocity distributions in Ω_2 and Ω_1 at $t = 20$ s for flow along intersections ($\mathbf{K}_1 = \mathbf{I} \cdot 10^{-8} \text{ m}^2$) taken into account (left) and neglected (right). Gravitational acceleration was not considered in the results shown here.

Table 5.6 – Parameters for test case 7.2. Permeability, porosity and the van-Genuchten-Mualem model in the subdomains for the case of blocking fractures.

	\mathbf{K}_d [m ²]	ϕ_d [-]	α_d^{VG} [1/Pa]	n_d^{VG} [-]
Ω_3	$\mathbf{I} \cdot 10^{-14}$	0.1	$1 \cdot 10^{-4}$	3.0
Ω_2	$\mathbf{I} \cdot 10^{-16}$	0.05	$5 \cdot 10^{-5}$	2.5
Ω_1	$\{\mathbf{I} \cdot 10^{-18}, \mathbf{I} \cdot 10^{-12}\}$	$\{0.01, 0.5\}$	$\{1 \cdot 10^{-5}, 5 \cdot 10^{-4}\}$	2.5

Figure 5.32a depicts the production curves for the case of neglecting flow along fracture intersections, and shows that the presence of the low-conductive fractures leads to a somewhat delayed onset of production. Furthermore, as one would expect, gravitational acceleration has a minor effect on the production rates. Following the ideas presented in the discussion of the previous paragraph, we argue that in the case of blocking fractures, gravity has a small influence on the flow field as the pressure drop across the fractures is significant. This can be seen in Figure 5.32b, which furthermore shows that the pressure build-up is higher for blocking fractures when compared to the bulk medium only, thus the overall resistance to flow is significantly higher than in the case of the unfractured sample. This is confirmed visually in Figure 5.33, which depicts a snapshot of the saturation and velocity distributions in the bulk medium and the fractures after 20 s of injection. For comparison, this is shown side by side with the distributions for the unfractured medium from Figure 5.26b (but with a different color bar). As in the case of conductive fractures, a strong influence of the fractures on the flow pattern can be observed, in which flow now occurs predominantly around the fractures. Both the saturation and velocity distributions as well as the production curves show to be physically meaningful results, in which the expected phenomena are captured qualitatively. A quantitative assessment using experimental results could be subject of future investigations.

Please note that we also investigated the influence of the fracture intersections on the results. However, only very small differences could be observed, for which reason we do not present any visualization of these results at this point. Since no direct mass transfer between the bulk medium and the intersections is considered in the model, it is not surprising that the intersections had little to no influence even in the case of high intersection permeabilities ($\mathbf{K}_1 = \mathbf{I} \cdot 10^{-12} \text{ m}^2$), as the flow through the fracture network is limited by the low fracture permeabilities.

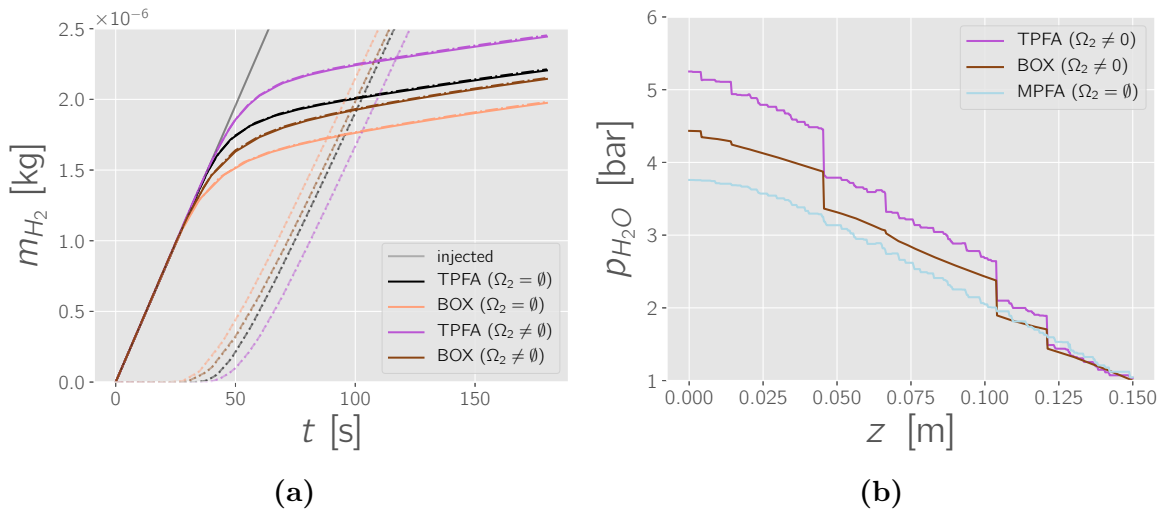


Figure 5.32 – Test case 7.2: production curves. Temporal evolution of the mass of hydrogen contained in the domain and hydrogen production curves (a), where the solid lines are for the case considering gravity and the dash-dotted lines with the same color are the results without gravity. The opaque dashed and dotted lines are the corresponding production curves for considered and neglected gravity, respectively. In (b), the pressure is plotted from bottom to top along the z -axis through the domain.

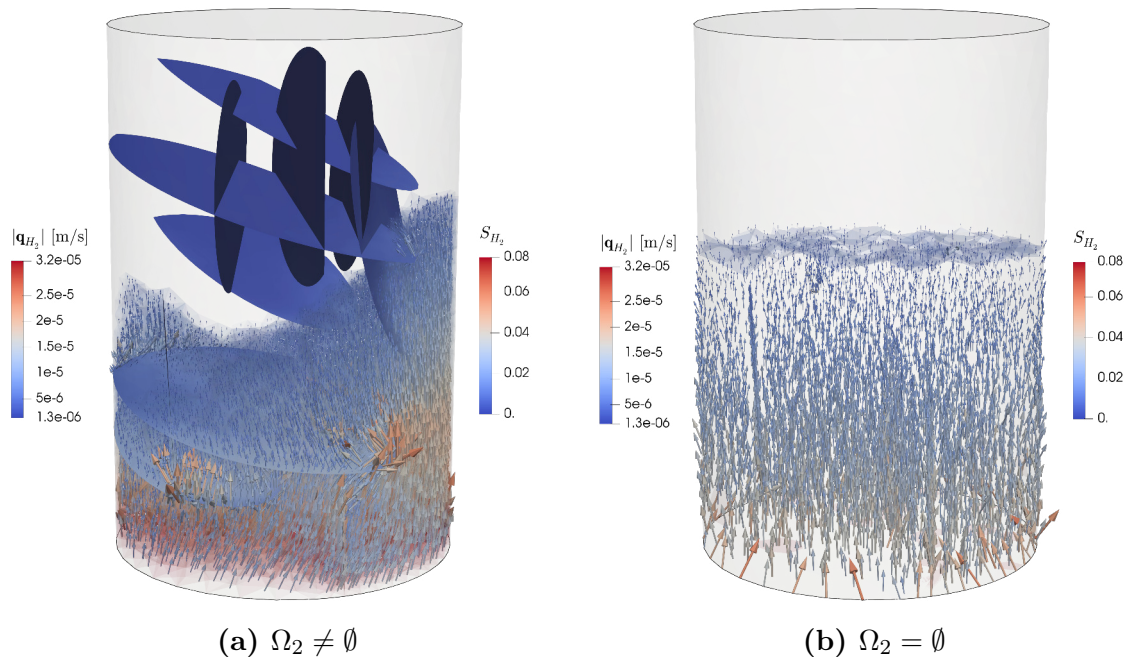


Figure 5.33 – Test case 7.2: saturation and velocity distributions. These are shown after 20s of injection considering blocking (a) and no fractures (b). The arrows show the velocities and are colored with the magnitude. The shaded volumes depict regions in which hydrogen saturations are above 1% and are colored with saturation.

Summary In this example the hybrid-dimensional models have been applied to a hydrogen injection scenario into a three-dimensional synthetic core sample containing a number of fractures. A rather strong influence of the fractures on the flow field could be observed, where it was furthermore shown that the presence of highly-permeable fractures can lead to gravity becoming an influential factor in an otherwise fully injection-controlled regime. Moreover, it was observed that the intersections of fractures can significantly influence the local flow field with a noticeable impact also on the hydrogen production at the outlet. For blocking fractures, the influence of both flow along intersections as well as gravitational acceleration was rather small. The first can be explained with the fact that in case of blocking fractures most of the flow occurs within the bulk medium and not through the fractures, such that the hydraulic properties of fracture intersections have little importance for the flow field. The latter can be explained with the injection-dominated flow regime due to the high pressure gradients across the domain.

5.2.3 Conclusions from the test cases

In the comparisons against an equi-dimensional reference solution presented in Section 5.2.1 it was seen that, in the case of highly-conductive fractures, the hybrid-dimensional schemes were able to capture the most relevant phenomena associated with two-phase flow already for fairly coarse discretizations containing only approximately 5% of the elements of the reference grid. The rapid transport of the non-wetting phase through the fractures and infiltration back into the matrix at the downstream fracture tips was reproduced rather well. In the case of blocking fractures, the schemes qualitatively captured the transport phenomena, including the pooling of the non-wetting phase before the fractures and rapid transport away from them on the downstream side. However, the saturations of the non-wetting phase in the pooling region very close to the fractures could not be quantitatively reproduced. In Section 5.2.2, a gas injection scenario into a synthetic fractured core sample was simulated, which was used to investigate the influence of gravity and flow along fracture intersections on the experimental results. One interesting observation was that in cases in which gravity plays a minor role for unfractured media, it can become an influential factor if conductive fractures are present. Moreover, taking into account flow along intersections of fractures can have a

significant impact on the local flow field with noticeable effects on the gas production at the outlet.

5.3 *Single-phase flow in deformable fractured poroelastic media*

Up until now all examples have considered undeformable, rigid solid matrices. In the subsequent test cases, the deformation of the solid matrix and its feedback on the flow processes are taken into account. To this end, we solve the mixed-dimensional system consisting of the equations (3.40) - (3.45). As in Section 5.1, in the example presented in Section 5.3.2 and 5.3.3 we consider a single fluid phase and note that $\kappa_r = 1$. For simplicity, gravitational forces are neglected in all examples. In Section 5.3.1, we do not consider the presence of a fluid phase but solve a purely mechanical problem with a single fracture for which an analytical solution exists. Subsequently, poromechanical simulations are carried out on two- and three-dimensional geometries in Section 5.3.2. In all simulations considering fluid flow, the hydraulic aperture of the fractures is related to the displacement jump via equation (3.47). Recall that therein, ϱ_0 denotes the initial gap between the fracture surfaces and a_0 is the aperture in case of contact. For the tangential fracture permeability we use the cubic law (3.28). Thus, when the fracture surfaces are in contact, i.e. $\varrho = 0$, an irreducible tangential permeability of $k_{n-1}^{\parallel} = a_0^2/12$ remains. In all two-dimensional examples, the plane strain state is considered. Unless denoted otherwise, the parameter c of the complementary functions (3.38) and (3.39) is set to $c = 1 \text{ GPa/m}$.

5.3.1 *Test case 8: convergence study*

The investigations presented in this Section are devoted to testing the convergence behavior of the mechanical models on a setup for which an analytical solution exists. To this end, we consider a single-phasic solid material and only solve the mechanical equations (3.42), (3.43) and (3.45) from the mixed-dimensional system presented in Section 3.3. Therein, all coupling terms related to the presence of fluid phases are set to zero. The analytical solution was derived in Phan et al. [2003] for an unbounded domain with a single fracture of length L that is inclined with respect to laterally exerted compressive stresses at an angle Θ . An illustration is given in Figure 5.34. The

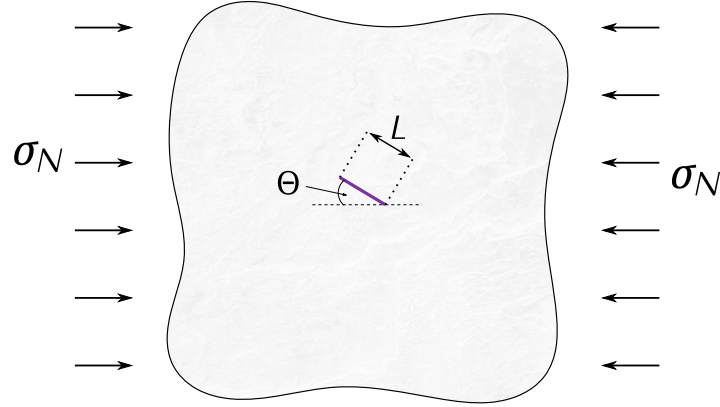


Figure 5.34 – Test case 8: single fracture under compression in an unbounded domain. Illustration of the conceptual domain for which the analytical solution (5.9) was derived.

analytical expressions for the normal and tangential tractions on the fracture surface as well as the tangential displacement jump are given by

$$t^\perp = \sigma_N \sin^2 \Theta, \quad (5.9a)$$

$$t^\parallel = \sigma_N \sin \Theta (\cos \Theta - F \sin \Theta), \quad (5.9b)$$

$$\llbracket u \rrbracket^\parallel = \frac{4(1-\nu)t^\parallel}{E} \sqrt{\left(\frac{L}{2}\right)^2 - \left(\zeta - \frac{L}{2}\right)^2}, \quad (5.9c)$$

where $0 \leq \zeta \leq L$ is the local coordinate on the fracture, $\sigma_N < 0$ is the exerted compressive stress (see Figure 5.34) and E and ν refer to Young's modulus and Poisson's ratio of the material. For the numerical computations we consider $\nu = 0.25$, $E = 2 \cdot 10^{10}$ Pa, $L = 10$ m, $\Theta = 20^\circ$, $F = 0.5$ and use a comparatively large domain with a size of $500 \text{ m} \times 500 \text{ m}$ in order to minimize the influence of external boundary conditions on the solution at the fracture surface. Zero-displacement Dirichlet boundary conditions are set on the degree of freedom on the lower-left corner of the domain, while on the lateral boundaries the stress σ_N is applied. Homogeneous Neumann boundary conditions are used on the top and bottom boundaries. As discussed in Section 4.3, if a linear scheme is applied to the discretization of the mechanical equations in the bulk medium, the grid used for the Lagrange multiplier τ is chosen coarser in comparison to the grid in the surrounding bulk medium. This is illustrated in Figure 5.35, where the coarsest grids used in the convergence study are shown. The coarsest discretization considers only two elements for the Lagrange multiplier and the grids of the bulk medium are

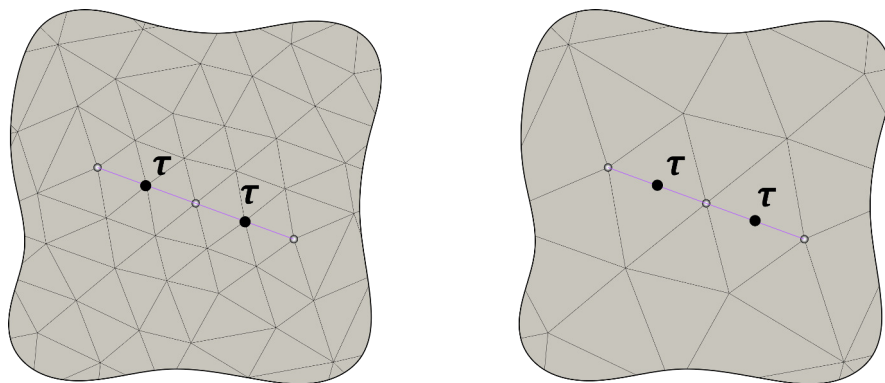


Figure 5.35 – Test case 8: discretization of the contact region. Close-up on the discretization of the bulk medium and the fracture for the coarsest grid used in the convergence study. If a linear scheme is used for the mechanical equations, the discretization used for the Lagrange multiplier is coarser than the bulk discretization (left). For quadratic finite elements used in the bulk medium, a conforming discretization can be chosen (right).

locally refined around the fracture to match the desired ratio illustrated in Figure 5.35. The conforming grid for the bulk medium used in conjunction with quadratic finite elements for the mechanics consists of 696 elements, while the refined grid used with linear schemes contains 2784 elements. We consider 3 refinement steps such that the final bulk grids consist of 44 544 (conforming) and 178 176 (refined) elements, respectively, and 16 lower-dimensional elements discretize the fracture. Let us denote with \mathcal{M}_τ the mesh used for the Lagrange multiplier, and define the error of the tangential displacement jump with respect to the analytical solution by

$$\varepsilon_{[[u]]^\perp} = \sqrt{\sum_{E \in \mathcal{M}_\tau} \left([[u]]_E^\parallel - [[u]]_E^{\parallel,*} \right)^2 |E|}, \quad (5.10)$$

where $[[u]]_E^{\parallel,*}$ and $[[u]]_E^\parallel$ refer to the analytical solution (5.9c) and the discrete solution evaluated at the center of the element E , respectively.

Figure 5.36 shows the errors plotted against the grid refinement. For CG2 on the conforming grid a rate of 0.92 was measured, while 0.88 was observed for all other schemes. Figure 5.37 shows plots of the tangential displacement jump and the normal traction, where the latter is shown normalized against the constant analytical solution (5.9a). The results were obtained on a separate discretization using 32 elements on the fracture and 46 076 and 182 836 elements in the bulk medium in the conforming and refined configurations, respectively. Figure 5.37a shows that the tangential displacement jump is captured quite well. Note that BOX and CG1 give identical results, while

the solutions for CG2, both on the conforming and the refined grid configurations, are slightly closer to the analytical solution. Figure 5.37b shows that oscillations in the normal component of the Lagrange multiplier in the order of up to 10% can be observed in the regions close to the fracture tips. These seem to be more prominent for the linear schemes and show to be lowest for CG2 on the refined grid. Such oscillations are a well-known numerical problem due to the stress singularity at fracture tips, and similar results were reported e.g. in Berge et al. [2019], Garipov et al. [2016].

Summary Convergence of the schemes for a purely mechanical problem involving frictional contact on a single fracture was investigated. All schemes converged with rates in the order of ≈ 0.9 and the lowest errors were observed for quadratic finite elements being used in the bulk domain. The convergence rates might be influenced by the fact that the analytical solution was derived for an unbounded domain. Oscillations in the normal tractions close to the fracture tips were noticed, which is a known phenomenon caused by the stress singularity at fracture tips and which has been reported for various numerical schemes in the literature [Berge et al., 2019, Garipov et al., 2016]. The maximum observed oscillations were in the order of 10% for the linear schemes and were located very close to the fracture tips. The oscillations showed to quickly decline with

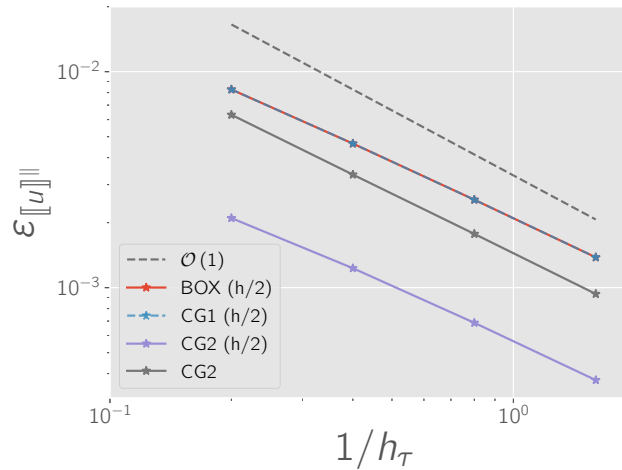


Figure 5.36 – Test case 8: convergence rates. The rates are shown for $\|u\|$, obtained for the BOX scheme as well as CG1 and CG2. For the linear schemes, the bulk grid is refined such that its discretization of the fracture is twice as fine as the grid used for the Lagrange multiplier. This grid configuration has been tested for CG2 as well and is indicated in the legend with " $h/2$ ".

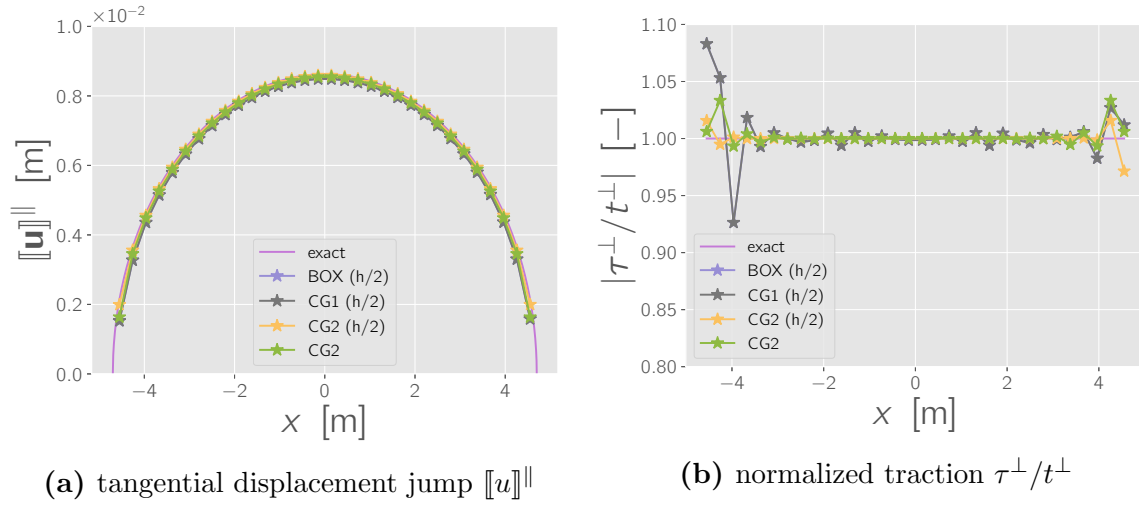


Figure 5.37 – Test case 8: tangential displacement jump and normal traction. Plots of $[[u]]^{\parallel}$ and τ^{\perp} , normalized with the analytical solution (5.9a) for the normal traction t^{\perp} , obtained with the different schemes against the analytical solution. Those computations that were performed on bulk grids that were refined with respect to the grid used for the Lagrange multiplier are denoted in the legends with “(h/2)”.

increasing distance from the tips, however, for the linear schemes visible oscillations in the order of $< 1\%$ were observed over the entire fracture. Apart from this issue, the analytical solution was captured rather well, especially in terms of the tangential displacement jump.

5.3.2 Test case 9: closing fractures

In the results presented in the previous sections we have observed a strong influence of highly-conductive fractures on the flow field. For example, in Section 5.1.5, a significant increase in effective permeabilities could be seen due to the presence of open fractures. But, depending on their orientation with respect to the in- and outlets, the fractures might close and no longer provide preferential flow paths. In this section, we want to investigate this effect on two- and three-dimensional domains, while comparing the different numerical schemes both in terms of the results as well as computational cost. In all simulations, we use $\rho = 1000 \text{ kg/m}^3$ and $\mu = 1 \cdot 10^{-3} \text{ Pa s}$ for the fluid properties, and $\nu = 0.25$ for Poisson’s ratio of the solid matrix. The Biot coefficient is set to $\alpha_B = 1.0$ and the permeability of the bulk medium is $\mathbf{K}_b = \mathbf{I} \cdot 10^{-14} \text{ m}^2$.

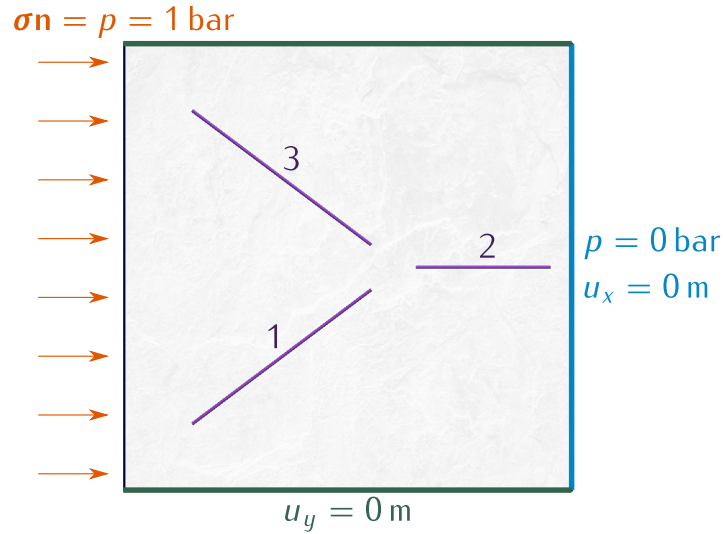


Figure 5.38 – Test case 9: domain and boundary conditions. For those boundary conditions that are not illustrated here, we set no-flow or no-stress. The three fractures are identified by the integer numbers depicted in the figure.

Two-dimensional domain We consider the unit square domain $\Omega = (0, 0) \times (1, 1)$ with three fully immersed and non-intersecting fractures. Fluid injection occurs on the left boundary at a pressure of $p = 1$ bar, while zero pressure is prescribed on the right boundary. On the latter, the horizontal displacement is further set to zero and the vertical displacement is zero on the top and bottom boundaries. For a graphical illustration of the boundary conditions, see Figure 5.38.

In the sequel, we perform computations for varying values of Young’s modulus E , the hydraulic fracture aperture a_0 in case of contact and the initial gap ϱ_0 , as given in Table 5.7, to investigate the influence of these parameters on the flow field and the effective permeabilities of the medium. Furthermore, we compare the results of the different numerical schemes as well as the involved computational cost. The latter is measured in terms of the number of iterations required to solve the nonlinear system of equations, where the convergence criterion is defined by a residual threshold of $1 \cdot 10^{-6}$. Moreover, we measure the average CPU time required to solve the linear system in each iteration using the direct solver UMFPack [Davis, 2004]. We use a grid consisting of 100 712 triangular elements with 256 one-dimensional segments discretizing the fractures. As in the previous section, we consider a coarser discretization for the Lagrange multiplier, using 128 elements, in order to achieve a mesh ratio as depicted in Figure 5.35. For quadratic finite elements being used in the mechanical domain, we again consider a conforming grid configuration as well.

Table 5.7 – Test case 9: parameter choices.

	ϱ_0 [m]	a_0 [m]	E [Pa]
case 9.1	0	$1 \cdot 10^{-7}$	$1 \cdot 10^9$
case 9.2	0	$1 \cdot 10^{-4}$	$1 \cdot 10^9$
case 9.3	$1 \cdot 10^{-4}$	$1 \cdot 10^{-7}$	$1 \cdot 10^9$
case 9.4	$1 \cdot 10^{-4}$	$1 \cdot 10^{-4}$	$1 \cdot 10^9$
case 9.5	$1 \cdot 10^{-4}$	$1 \cdot 10^{-7}$	$1 \cdot 10^8$

Table 5.8 shows the effective permeabilities computed by the different scheme combinations and parameter choices listed in Table 5.7. For case 9.1, i.e. for an initial gap of zero and a rather small hydraulic aperture in case of contact, it can be seen that all scheme combinations, except for those involving TPFA, recover the permeability of the bulk medium as the effective permeability. A deviation of 5 % is observed when TPFA is used. This indicates that the influence of the fractures on the hydraulic behavior of the domain is negligible for such small hydraulic apertures. Furthermore, the choice of mechanical boundary conditions does not lead to an opening of any of the fractures, such that the results simply reveal the consistency of the schemes used for the flow equations, while no significant feedback of the mechanical deformation on the flow pattern is observable. This can be seen in the left image of Figure 5.39, where the pressure and velocity distributions are shown for this case. Apart from this, only minor deviations in mechanical quantities could be observed when comparing the results of the different scheme combinations. As an example, Figure 5.40 shows the tangential displacement jump along fracture 1 and the normal traction along fracture 2 for two combinations of schemes. With the fractures providing very little space for fluid migration, a linear pressure profile develops in the domain (see right image in Figure 5.39), which in turn explains the linearly increasing normal traction that can be seen on fracture 2. Moreover, tangential slip occurs along the entire length of fracture 1. However, when a hydraulic fracture aperture of $a_0 = 1 \cdot 10^{-4}$ m is chosen for the fracture surfaces being in contact (case 9.2), a significant increase in the order of 36 % can be observed for the effective permeability (see Table 5.8). In this case, flow occurs predominantly through the fractures and the pressure distribution is significantly influenced by them, which can be seen from the right image in Figure 5.39. In particular, regions of inflow into the fractures and outflow back into the bulk medium develop, which implicate corresponding pressure gradients. These pressure gradients in turn affect the mechanics and

Table 5.8 – Test case 9: effective permeabilities. Shown are the effective permeabilities computed with different combinations of numerical schemes and the different parameter values for ϱ_0 , a_0 and E as shown in Table 5.7. The permeability values in the table are given in $\text{m}^2 \cdot 1 \cdot 10^{-14}$.

scheme (\mathbf{u})	scheme (p)	\mathcal{M}_τ	k_{eff} (9.1)	k_{eff} (9.2)	k_{eff} (9.3)	k_{eff} (9.4)	k_{eff} (9.5)
BOX	MPFA	coarsened	1.00	1.36	1.35	1.38	1.01
BOX	TPFA	coarsened	0.95	1.30	1.29	1.31	0.96
CG1	BOX	coarsened	1.00	1.36	1.35	1.38	1.01
CG1	MPFA	coarsened	1.00	1.36	1.35	1.38	1.01
CG1	TPFA	coarsened	0.95	1.30	1.29	1.31	0.96
CG2	BOX	coarsened	1.00	1.36	1.35	1.38	1.01
CG2	MPFA	coarsened	1.00	1.36	1.35	1.38	1.01
CG2	TPFA	coarsened	0.95	1.30	1.29	1.31	0.96
CG2	BOX	conforming	1.00	1.36	1.35	1.38	1.01
CG2	MPFA	conforming	1.00	1.36	1.35	1.38	1.01
CG2	TPFA	conforming	0.95	1.30	1.29	1.31	0.96

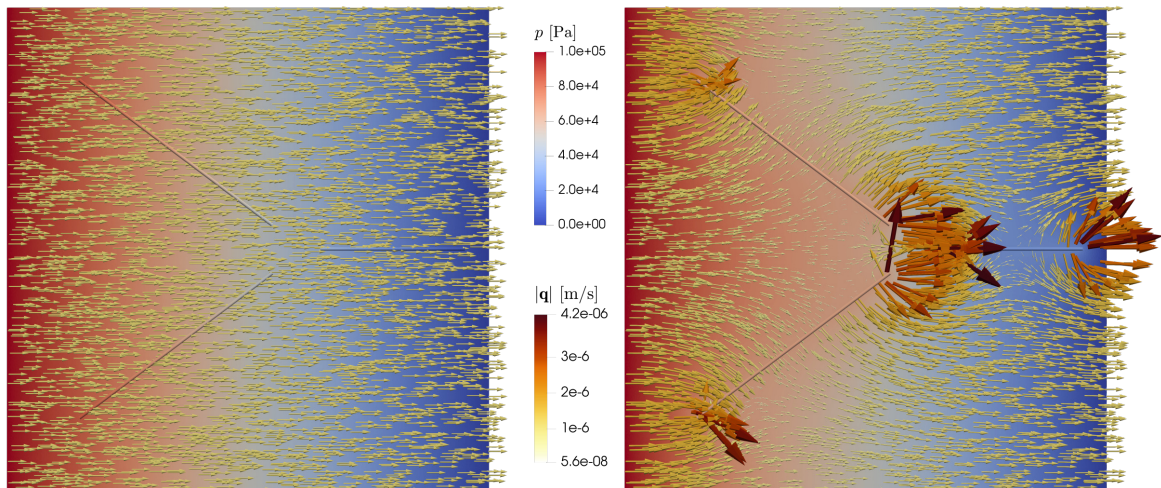


Figure 5.39 – Test case 9.1/9.2: pressure and velocity distributions. The left and right images show the results for test cases 9.1 and 9.2, respectively. Both solutions were obtained with CG2 for the discretization of the displacement and MPFA for pressure.

lead to higher contact tractions in regions of inflow, while lower tractions are seen in the regions of outflow. This is illustrated by the plots of the tangential contact traction along fracture 1 shown in the image on the right of Figure 5.41. The contact tractions for case 9.1 are depicted as well in order to visualize the effect of the changes in the pressure distribution on the contact mechanics. Increased contact tractions are observed in the inflow region of the fracture, in particular in terms of the normal traction, which is indicated by the friction bound being significantly higher. This high friction bound causes the left region of the fracture to be in a sticking state, i.e. no tangential slip is observed, as can be seen from the left image of Figure 5.41. In contrast to that, the smaller contact forces in the outflow regions lead to a comparatively larger tangential slip when compared to case 9.1 (see Figure 5.40).

By comparing the results of case 9.1 and 9.2 we have seen that, as expected from the investigations of the previous sections, the parameter a_0 has a large influence on the resulting flow field. Furthermore, we have seen that the models are capable of capturing the mechanical response to these changes in the flow field. Until now, the fractures were initially closed, and in the subsequent cases 9.3, 9.4 and 9.5 we want to consider fractures that are initially open with $\varrho_0 = 1 \cdot 10^{-4}$ m. The effective permeabilities shown in Table 5.8 suggest that there is little difference in the flow field between the cases 9.2 and 9.3, while in case 9.5 the fractures seem to have a more prominent impact on the effective permeabilities. In contrast to that, when considering a softer material, as done in case 9.5, the impact of the fractures on the overall conductivity of the domain becomes negligible. The differences can be explained on the basis of the plots of the

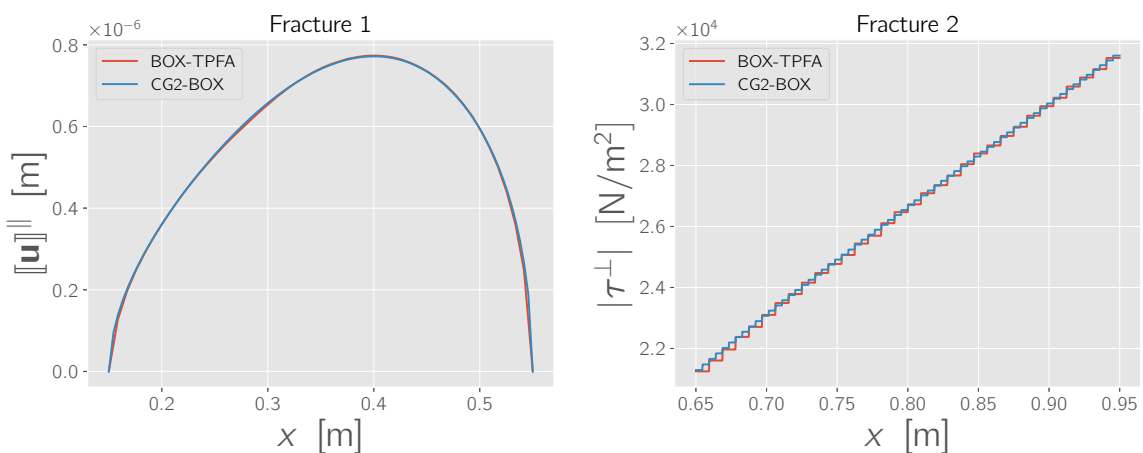


Figure 5.40 – Test case 9.1: tangential slip and normal traction. For fracture 1, the tangential slip is shown (left), while the normal traction is plotted along fracture 2 (right).

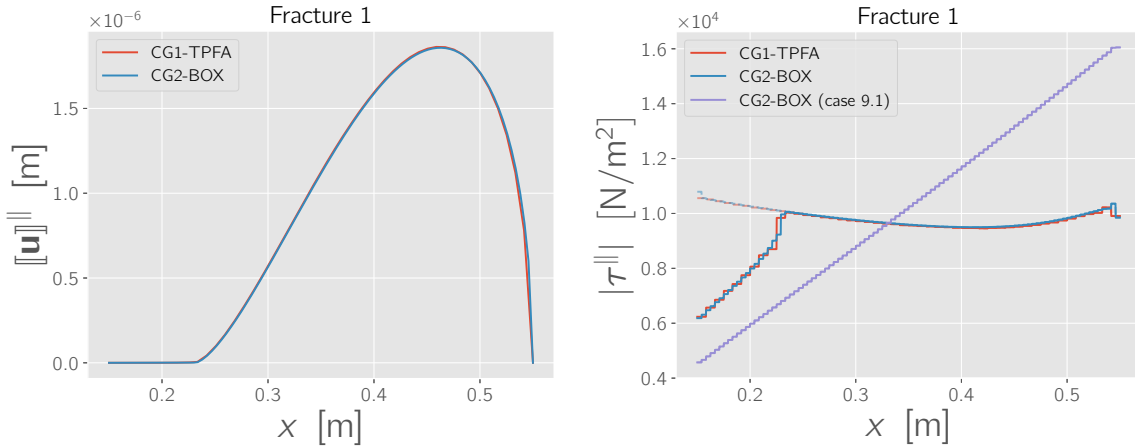


Figure 5.41 – Test case 9.2: tangential slip and tangential traction. The tangential slip (left) and the tangential traction (right) are shown for fracture 1. In the latter, the opaque dashed lines depict the friction bound $F\tau^{\perp}$. For comparison, the tractions of case 9.1 are shown as well, for which the tangential tractions coincide with the friction bound along the entire fracture.

gap along fracture 1 given in Figure 5.42. We observe that the gap profiles obtained in case 9.3 and 9.4 are nearly identical. However, case 9.4 considers a larger value for a_0 and thus, the hydraulic aperture, modeled after (3.47), is larger. This explains the higher conductivity of the overall domain as listed in Table 5.8. Moreover, it can be seen in Figure 5.42 that when considering the soft material of case 9.5, the fractures close and do no longer provide preferential flow paths for the fluid to migrate through.

We could not observe significant deviations in the results obtained with the different combinations of schemes listed in Table 5.8. However, the computational cost varies strongly, which can be seen in Table 5.9. The most efficient combination is the use of linear finite elements for the displacement and the BOX scheme for pressure, while the computationally most expensive combination is CG2 for the displacement and MPFA for pressure. While the authors are not aware of any works coupling finite elements for the displacement with MPFA for flow, Garipov et al. [2016] use both linear and quadratic finite elements coupled to TPFA. In the context of two-phase flow in poroelastic and unfractured porous media, linear finite elements have been successfully coupled to the BOX scheme in Darcis [2013], Beck [2018], however, these works do not consider fractures.

Three-dimensional domain Let us now consider a cylindrical domain with the same geometry as the synthetic core sample in Section 5.2.2, i.e. a radius of 5 cm and a

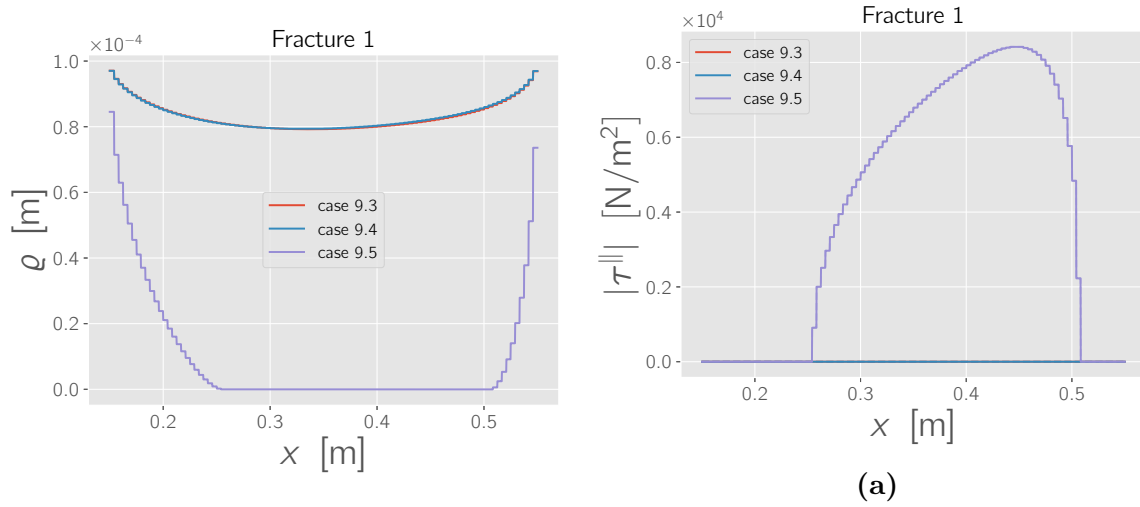


Figure 5.42 – Test case 9.3/9.4/9.5: gap and tangential traction. The gap (left) and the tangential traction (right) are shown for fracture 1 and the cases 9.3, 9.4 and 9.5. The depicted results were obtained using CG2 for the displacement and MPFA for pressure on a discretization that was fully conforming to the grid used for the Lagrange multiplier. Note that the entire part of the fracture which is in contact has slipped and therefore the tangential traction shown in the right plot is equal to the friction bound.

height of 15 cm. However, in this case we consider a single elliptical fracture that is fully immersed in the domain. An inlet pressure of 1 bar is applied on the bottom, while zero pressure is set at the outlet on the top boundary. On the latter, we furthermore fix the vertical displacement to $u_z = 0$ m and on the outer rim of the top boundary we additionally fix the horizontal displacements to $u_x = u_y = 0$ m. No-flow boundary conditions and a confining stress of 1 bar are used on the lateral boundaries. The fracture is initially closed, i.e. $\rho_0 = 0$ m, and we consider hydraulic fracture apertures in the case of contact of $a_0 \in \{1 \cdot 10^{-7} \text{ m}, 1 \cdot 10^{-4} \text{ m}\}$. Since only minor differences between the results of the different schemes were observed on the two-dimensional setting, here we use the BOX scheme for the discretization of the flow equations and CG1 for the mechanical equations, as this combination is the computationally most efficient on unstructured discretizations.

The contact traction and pressure on the fracture, as well as regions with the largest velocities in the bulk medium, are depicted in Figure 5.43. The results show that a similar behavior as in the two-dimensional setting can be observed, i.e. the contact tractions seem to linearly increase for $a_0 = 1 \cdot 10^{-7}$ m, while a more or less constant profile develops for $a_0 = 1 \cdot 10^{-4}$ m. The latter can again be explained by the significant influence of the fracture on the flow field and the pressure distribution as discussed

Table 5.9 – Test case 9.1: computational cost. Number of degrees of freedom, number of nonlinear solver iterations and average linear solver time for various combinations of schemes.

scheme (\mathbf{u})	scheme (p)	\mathcal{M}_τ	#-dof	#-iterations	average solve time [s]
BOX	MPFA	coarsened	202 706	17	5.2
BOX	TPFA	coarsened	202 706	16	3.6
CG1	BOX	coarsened	152 738	16	1.7
CG1	MPFA	coarsened	202 706	17	5.2
CG1	TPFA	coarsened	202 706	15	3.9
CG2	BOX	coarsened	657 066	15	7.0
CG2	MPFA	coarsened	707 034	15	16.0
CG2	TPFA	coarsened	707 034	15	9.2
CG2	BOX	conforming	657 322	22	7.2
CG2	MPFA	conforming	707 290	23	16.1
CG2	TPFA	conforming	707 290	21	9.3

earlier for the two-dimensional setting.

In both cases, the fracture is sticking, i.e. the tangential displacement jump is zero. In order to force a slip across the fracture, we repeat the simulation with $\varrho_0 = 0$ m and $a_0 = 1 \cdot 10^{-7}$ m using an unrealistically small friction coefficient of $F = 0.001$. A close-up on the fracture, showing the tangential slip as well as the tangential tractions, is given in Figure 5.44. It can be seen that the model correctly predicts the slip direction parallel to the tangential tractions and in opposite direction. The largest tractions are observed in the top part of the fracture, where the normal tractions and therefore the friction bound is largest (see Figure 5.43). Furthermore, the largest slip is observed in the interior of the fracture, slightly above its center where the tractions are larger, while it comes to rest towards the fracture tip.

Summary Various combinations of numerical schemes have been applied to a two-dimensional test case considering fluid injection into a poroelastic domain containing three fractures. The effective permeabilities of the overall domain have been computed for different values of Young’s modulus, initial mechanical fracture apertures and hydraulic fracture apertures in case of contact. All of these parameters have been shown to have a large impact on the effective permeabilities as they influence the hydraulic fracture aperture and with this the ability of the fractures to conduct fluid. A permeability increase in the order of 36% was observed for hydraulic fracture apertures of $a = 0.1$ mm. However, it was seen that depending on the stiffness of the material, the

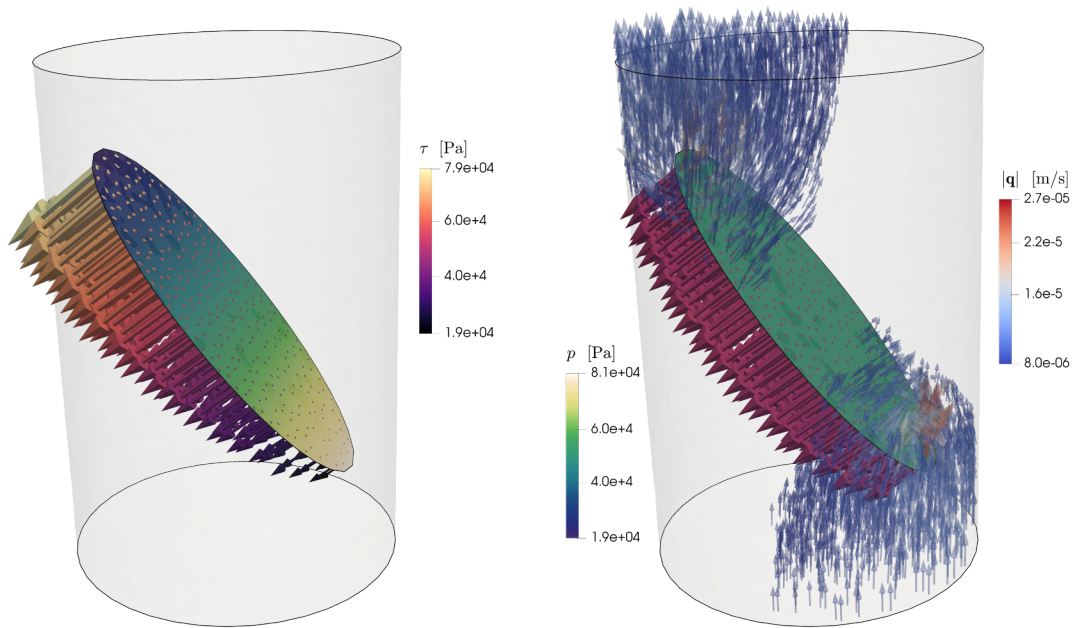


Figure 5.43 – Test case 9.6: three-dimensional results. Pressure and contact traction on the fracture for $a_0 = 1 \cdot 10^{-7}$ m (left) and $a_0 = 1 \cdot 10^{-4}$ m (right). Furthermore, the velocities above $8 \cdot 10^{-6}$ m/s are illustrated with the opaque arrows and indicate the influence of the fracture on the flow field.

mechanical displacements induced by the injection can cause open fractures to close, in which case their influence on the flow field might diminish. Please note that this can also occur for more stiff materials when higher injection pressures are applied. Thus, the effective permeability of fractured porous media is not only a function of the initial fracture aperture, but also of the stiffness of the material, the irregularity of the fracture surfaces (expressed by means of a_0) as well as the applied pressure difference. Moreover, the orientation of the fractures with respect to the direction of flow might also be of importance, in particular in cases where the fractures close.

Furthermore, all combinations of schemes that the implementation in DuMu^x allows for were successfully applied to this test case, and only minor deviations in the results were observed when using different schemes. Despite the small deviations, the computational cost varies substantially among the different schemes, which was investigated in terms of number of iterations of the nonlinear solver as well as the average linear solver time. Major differences were observed in the latter, while the number of nonlinear iterations were similar for most schemes.

We have furthermore presented results for a three-dimensional domain, which showed to be in agreement with the two-dimensional results from a phenomenological perspec-

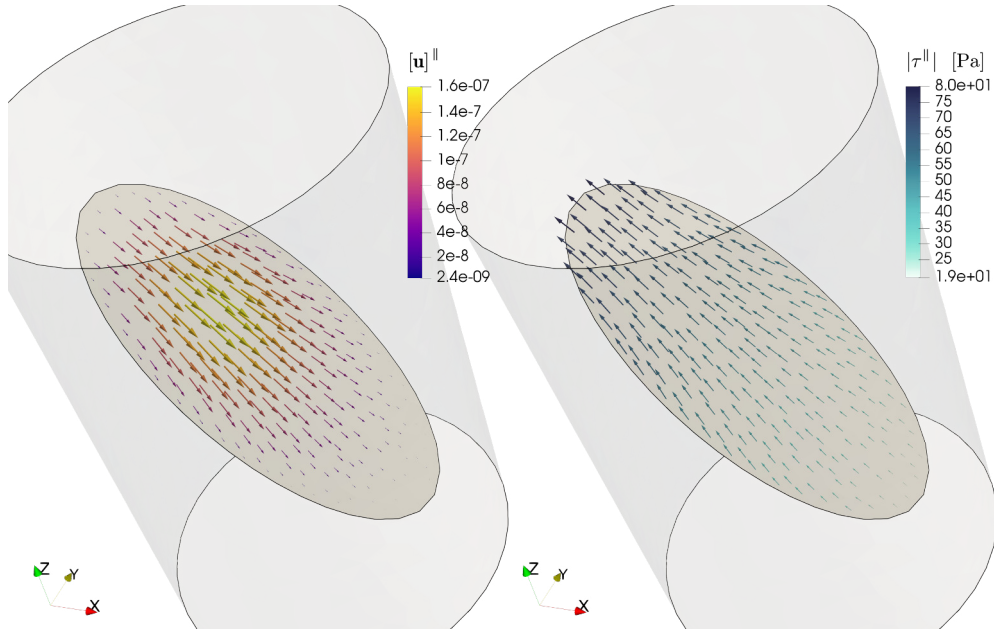


Figure 5.44 – Test case 9.7: three-dimensional results for low friction. Tangential slip (left image) and tangential traction (right image) for the case of $\varrho_0 = 0$ m, $a_0 = 1 \cdot 10^{-7}$ m and $F = 0.001$.

tive. Additional complexity in the model arises in three dimensions when slip occurs across the fractures, as the slip direction has to be found by the non-linear solver. In the results shown here, a slip was forced by choosing a very small friction coefficient of $F = 0.001$. Physically meaningful results were obtained, in which the slip direction is parallel to the tangential tractions and in opposite direction. Moreover, the maximum slip was observed in the center regions of the fracture while it came to rest towards the fracture tip.

5.3.3 Test case 10: consolidation

In the previous sections, transient effects were neglected and stationary pressure distributions and deformations were computed. However, poroelastic media are characterized by a transient response to external forces. An illustrative example is the consolidation problem, which can be found in standard textbooks as e.g. Jaeger et al. [2007]. It considers a fluid-saturated medium, to which a normal traction is applied on the top boundary. This causes an instantaneous pressure increase in the domain, followed by a slow drainage of the fluid out of the domain until the pressure is relaxed back to its

initial state. During this drainage process, the domain undergoes vertical deformation. In this section, we want to use such a setting on fractured porous media. To this end, we consider a two-dimensional square domain with a size of $100\text{ m} \times 100\text{ m}$ containing three fractures. The permeability and the initial porosity of the bulk medium are set to $\mathbf{K}_2 = \mathbf{I} \cdot 10^{-12}\text{ m}^2$ and $\phi_2 = 0.15$, respectively. The fractures are initially mechanically closed, i.e. $\varrho_0 = 0\text{ m}$, and the irreducible hydraulic aperture in case of contact is set to $a_0 = 1 \cdot 10^{-6}\text{ m}$. Young's modulus and Poisson's ratio of the solid are set to $E = 6\text{ GPa}$ and $\nu = 0.25$, the Biot coefficient is $\alpha_B = 1.0$. We use no-flow boundary conditions on all sides except the top boundary, on which the pressure is fixed to its initial value of $p = 0$. The displacement is fixed to $\mathbf{u} = \mathbf{0}\text{ m}$ on the bottom boundary, while on the lateral boundaries only the x-component is fixed to $u_x = 0\text{ m}$. On the top boundary, a compressive normal traction of $\mathbf{t} = [0, -4\text{ MPa}]^T$ is applied. As mentioned earlier, we consider an incompressible fluid with $\rho = 1000\text{ kg/m}^3$ and $\mu = 1 \cdot 10^{-3}\text{ Pa s}$, and thus, the transient behavior is fully governed by the dependency of the porosity on the displacement as given by equation (3.30).

Figure 5.45 shows the displacement field in the bulk medium together with the slip on the fractures and the contact tractions for both frictional and frictionless contact at the final simulation time of $t = 4900\text{ s}$. If friction is considered, the maximum slip occurs above the kink on the left fracture and is in the order of 0.5 mm . This slip causes a small dip in the subsidence profile as can be seen in Figure 5.46a. While a constant subsidence of the top boundary can be seen when the fractures are neglected, the slip occurring on the fracture surfaces leads to locally higher subsidence. In the rather hypothetical case of frictionless contact, this effect is much more pronounced and two main dips associated with the left and the middle fractures can be seen in the subsidence profiles (see Figure 5.46b). Moreover, a small region of the left fracture below the kink opens, where the contact tractions are zero, and right above the kink a maximum in the contact traction develops. This maximum traction seems to be a numerical artifact rather than physical behavior and might be caused by the rather large slip in this case of no friction. However, if friction is considered no issues at the fracture kink can be observed. At the final simulation time, the pressure has almost entirely relaxed back to its initial value. This can also be seen in the temporal evolution of the average subsidence shown in Figure 5.47, which shows that the major displacements occur in the first 2000 s . Note that the curves for CG1-BOX and CG2-BOX with $F = 0.5$ are very close together and can hardly be distinguished in the plot. Moreover, the curve for CG2-MPFA with $F = 0.5$ is only slightly below the one for neglected frac-

tures ($\Omega_1 = \emptyset$). It is noteworthy that slight differences in the transient behavior can be observed between MPFA and BOX used for the discretization of the flow equations. This could again be related to the Dirichlet boundary conditions on the top boundary, which allow for outflow across the uppermost lateral sub-control volume faces when the BOX scheme is used. This would also explain the faster subsidence, which is driven by the outflow of fluid. However, the deviations are rather small.

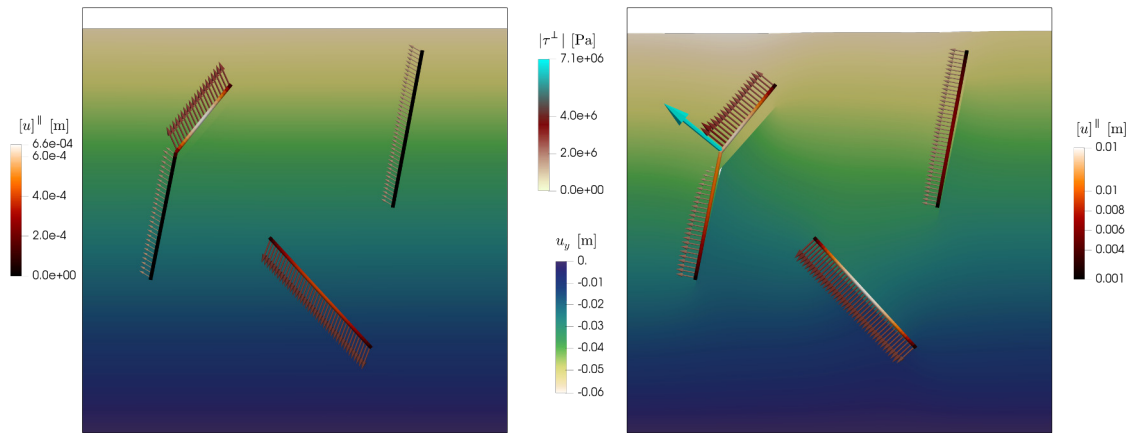


Figure 5.45 – Test case 10: displacement, slip and contact tractions. The left figure depicts the results for the case of frictional contact, while the right figure shows the results for $F = 0$, i.e. no friction. Both show the state at the final simulation time $t = 4900$ s. The fractures are depicted in the undeformed state at their original locations, while the domain is warped with the displacement field. The black outline illustrates the domain boundary in the undeformed state. The depicted results were obtained using CG2 for the discretization of the mechanical equations and the MPFA for the discretization of the flow equations.

Summary In this test case we have applied the models to the problem of consolidation of a fractured porous medium, and have compared the results to those of an unfractured medium. The models were able to capture the transient behavior of a poroelastic medium subject to compression. Moreover, from a phenomenological perspective, physically meaningful results were obtained for the fractured medium, in which the slip occurring on the fractures causes an increase in subsidence when compared to the unfractured medium.

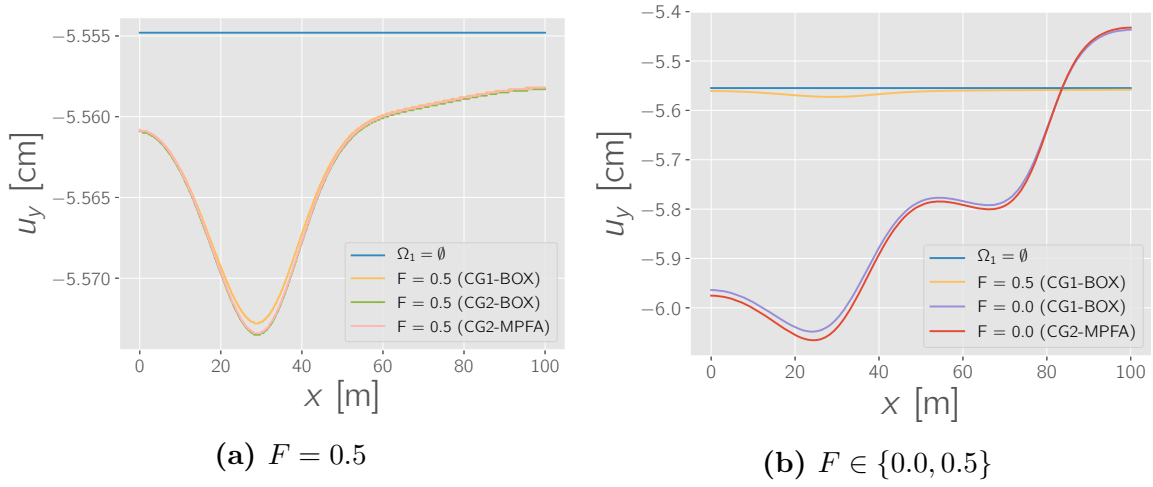


Figure 5.46 – Test case 10: subsidence profiles. Shown are the subsidence profiles, i.e. the vertical displacement u_y plotted along the x -coordinate, at the time $t = 4900$ s. The left image shows the results for frictional contact, while in the right image those for frictionless contact are added. Shown are the results obtained with various combinations of numerical schemes.

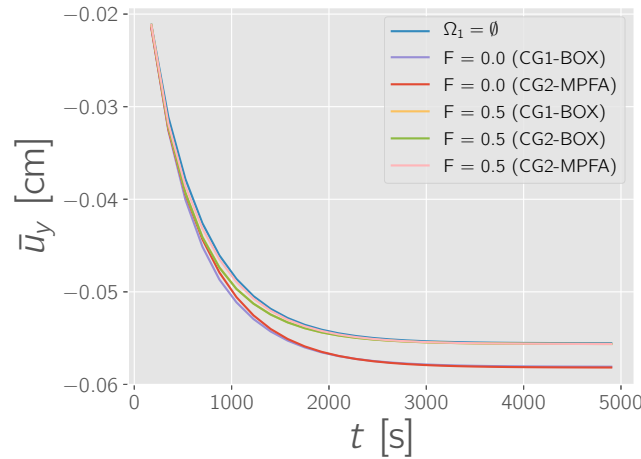


Figure 5.47 – Test case 10: subsidence over time. Shown is the temporal evolution of the subsidence for frictional and frictionless contact and the different combinations of schemes used. Each data point represents the average value of the vertical displacement u_y along the top boundary.

5.3.4 Conclusions from the test cases

The examples presented in this section showed the applicability of the models to two- and three-dimensional problems involving closing fractures, where both sticking and sliding fractures have been considered. Phenomenologically meaningful results have been obtained in investigations on the effective permeability of a domain undergoing mechanical deformations, where the magnitude of the deformations was controlled by adjusting the stiffness of the material. In the case of closing fractures, the effective permeability of the domain was almost the same as that of the unfractured medium, while for a stiffer material, an increase in the order of 35 % was observed. This illustrates the potentially strong influence of the mechanical deformations on the hydraulic properties of fractured rock. Moreover, it should be taken into account that changing the pressure difference applied to the domain could lead to similar observations. Thus, while in the case of rigid porous media the effective permeability showed to be dependent on the fracture network topology as well as aperture distributions and the permeability of the bulk medium, in poroelastic media the applied pressure difference, the stiffness of the bulk material and the hydraulic fracture aperture in case of contact become influential parameters as well. Finally, the consolidation problem featured in the last example showed that the models are also capable of capturing the transient effects caused by the sliding of the fracture surfaces.

5.4 Two-phase flow in deformable fractured poroelastic media

The results presented in the previous section mostly focused on stationary problems, except for the consolidation problem. However, as all fractures were initially in full contact in this case, flow along the fractures did not have a major impact. In the examples of this section we want to investigate the influence of closing and dilating fractures on the transient flow fields in the context of two-phase flow. To this end, we will consider a two- and a three-dimensional example in the following subsections. While the first example features dynamically closing and re-opening fractures, the three-dimensional example shown in Section 5.4.2 describes a situation in which dilation occurs primarily. As in the examples for single-phase flow, gravity is neglected in both test cases and in the two-dimensional test case the plain strain state is considered.

5.4.1 Test case 11: dynamically closing and re-opening fractures

In Section 5.3.2 we have investigated the effect of closing fractures in the context of single-phase flow. In particular, it was seen that the effective permeability increase caused by the presence of conductive fractures might vanish if the material is soft and if the fractures are oriented such that they close under the compressive forces of fluid injection. In this test case we reuse the geometric setting and boundary conditions from Section 5.3.2, but set the initial gap to $\varrho_0 = 2 \cdot 10^{-4}$ m and consider two-phase flow using liquid water and liquid TCE for the fluid phases. As in the other examples considering these fluids, we have $\rho_{\text{H}_2\text{O}} = 1000$ kg/m³, $\mu_{\text{H}_2\text{O}} = 1 \cdot 10^{-3}$ Pa s, $\rho_{\text{TCE}} = 1460$ kg/m³ and $\mu_{\text{TCE}} = 5.7 \cdot 10^{-4}$ Pa s. For an illustration of the domain and the boundary conditions we refer to Figure 5.38, however, we additionally set $S_{\text{TCE}} = 0.5$ on the left and $S_{\text{TCE}} = 0.0$ on the right boundary.

The final simulation time is set to $t_{\text{end}} = 36\,000$ s and we use an initial and maximum time step size of 20 s and 1600 s, respectively. As in the single-phase case, we use $\mathbf{K}_2 = \mathbf{I} \cdot 10^{-14}$ m² and $\phi_{2,0} = 0.15$ for the permeability and initial porosity of the bulk medium. The porosity is again modeled depending on the deformation after equation (3.30). The parameters for the van-Genuchten-Mualem model for the capillary pressure and relative permeability-saturation relationships are set to $\alpha_2^{\text{VG}} = 1 \cdot 10^{-4}$ Pa s and $n_2^{\text{VG}} = 3$ for the bulk medium and $\alpha_1^{\text{VG}} = 2 \cdot 10^{-1}$ 1/Pa and $n_1^{\text{VG}} = 2.5$ for the fractures. Note that the latter are independent of the aperture in this case for the sake of simplicity. Investigations considering aperture-dependent parameters capillary pressure-saturation relationships are presented in Section 5.4.2. Regarding the material properties of the bulk medium, we use $\nu = 0.25$ and $E \in \{0.1, 1\}$, where the latter are given in GPa. The grid used in this example consists of 25 240 triangular and 128 line elements for the discretization of the bulk medium and the fractures, respectively. Furthermore, a grid with 64 line elements are used for the Lagrange multiplier. We use CG1 for the discretization of the mechanical equations and the BOX scheme for the flow equations, as this combination has shown to be the most efficient.

Figure 5.48 depicts the TCE saturation and velocity distributions at three different time levels for the case of $E = 1 \cdot 10^9$ GPa, which show a strong influence of the fractures on the flow field. TCE is rapidly transported along the two inclined fractures, infiltrates back into the matrix and enters the right horizontal fracture to be transported quickly towards the outlet. The smallest observed aperture in this configuration was $1.76 \cdot 10^{-4}$ m, which corresponds to a decrease of 11 %. This corresponds to a maximum

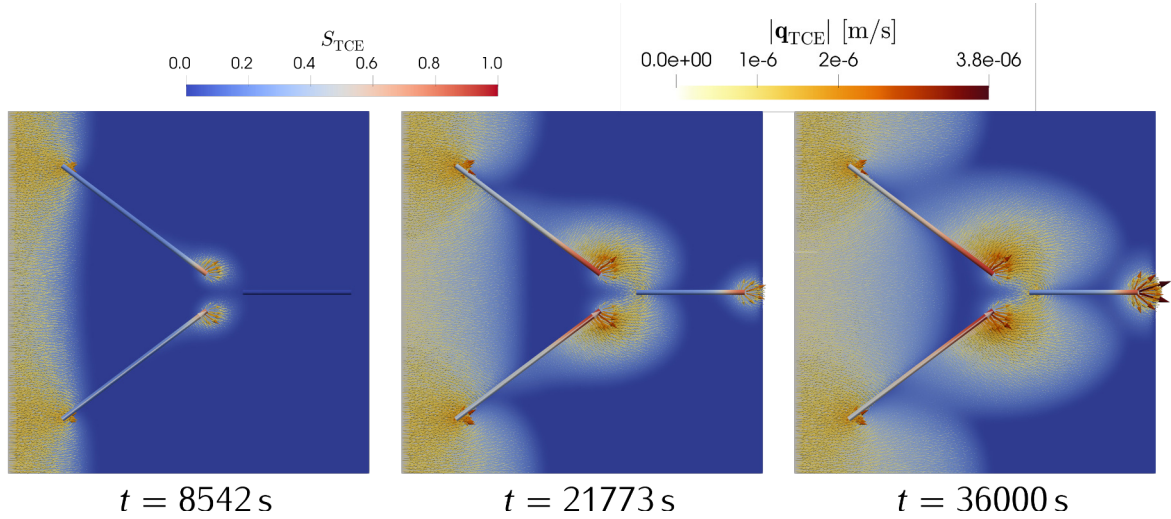


Figure 5.48 – Test case 11: TCE saturation and velocity for $E = 1$ GPa. The pictures show the TCE saturation and velocities in the domain at different time levels, which are indicated below the images.

decrease in tangential permeability of approximately 14%, for which the fractures are still orders of magnitude more permeable than the surrounding matrix.

However, in the case of the softer material with $E = 0.1$ GPa, the inclined fractures partly close within the first 1500 s, which leads to an accumulation of TCE in the left parts of the inclined fractures before the contact regions. This is illustrated in Figure 5.49, where the saturation and velocity distributions in the domain are depicted at three different time levels together with plots of the gap, the effective pressure and the contact tractions along one of the inclined fractures. The normal tractions that develop in the contact region are in the order of 0.1 bar, which is a bit lower than what was observed in the single phase case (see e.g. the friction bound shown in Figure 5.42a). It can be seen that the entire contact region is sliding, as the tangential tractions and the friction bound are equal. However, the effective pressures rise with time as more TCE enters the domain and the left regions of the fractures. Over time, the contact region becomes smaller until eventually contact is lost. The second row of Figure 5.49 shows the state at the time step when the fracture surfaces loose contact. It can be seen that the effective pressure in the contact region has risen such that its increase surpasses the normal contact tractions and pushes open the fracture walls. Until the state at the final simulation time, shown in the bottom row of the figure, the pressure keeps rising and the fracture continues to open.

These effects are also reflected in the temporal evolution of the mass of TCE contained

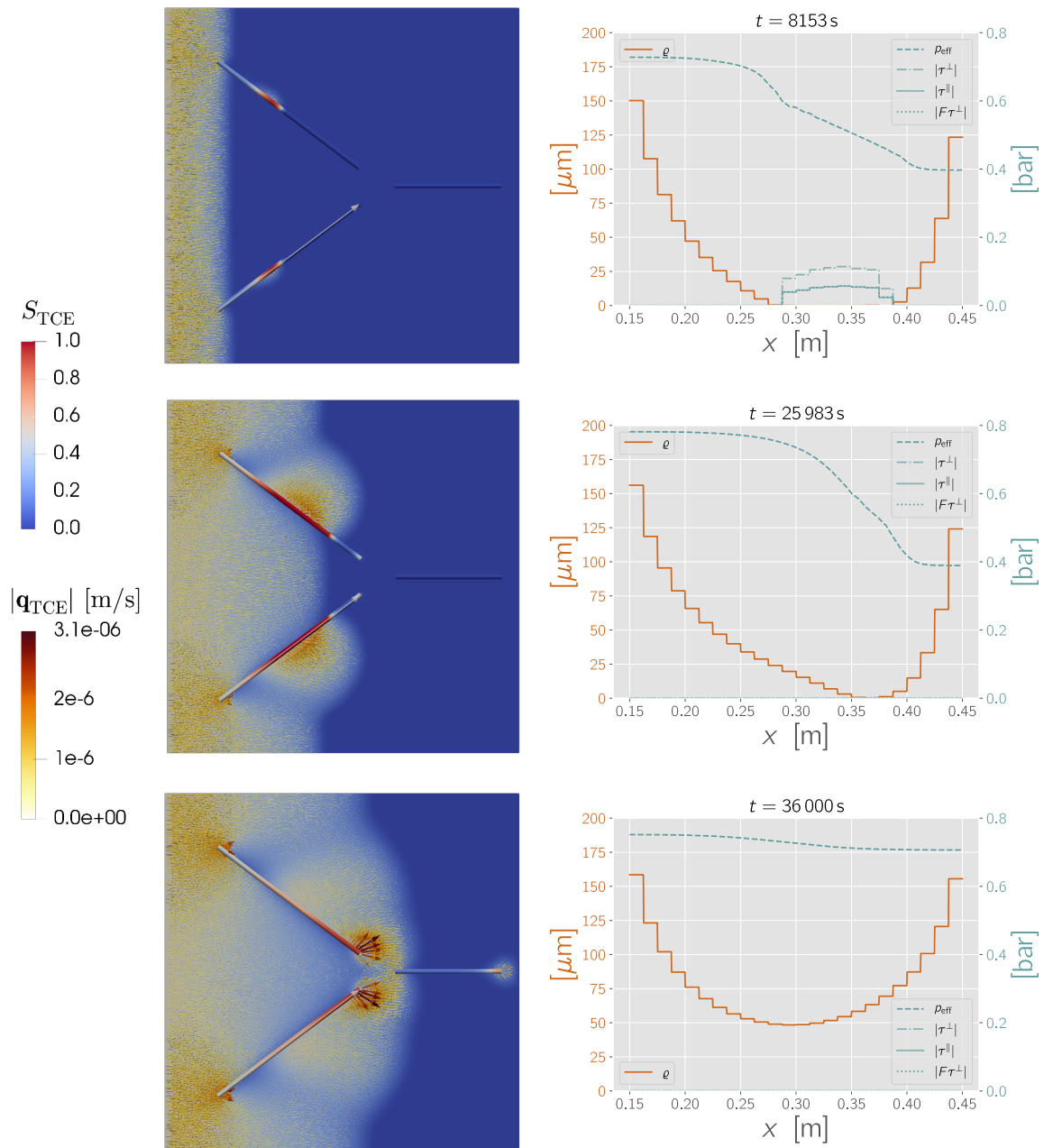


Figure 5.49 – Test case 11: TCE saturation, velocity and contact tractions for $E = 0.1$ GPa. The pictures in the left column show the TCE saturation and velocities in the domain at different time levels. In the right column, plots of the gap, the contact tractions and the effective pressure on one of the fractures are shown. The large white arrows above the lower fracture in the left pictures illustrate the line along which the plots are taken. The time levels associated with each row is given in the titles of the plots on the right.

in the subdomains shown in Figure 5.50. For the soft material, a slower increase of mass is observed within the fractures until $t \approx 250\,000$ s, i.e. until the fractures open again. After that, a more rapid increase can be seen as the opening regions fill up with TCE. Another kink can be observed at $t \approx 32\,000$ s, which is when the right fracture is infiltrated. The overall mass of TCE contained within the fractures is below 1% of that in the bulk medium. Nevertheless, noticeably less TCE is observed in the bulk domain in the case of the soft material, as the overall resistivity of the medium is larger in this case (see effective permeabilities in Section 5.3.2).

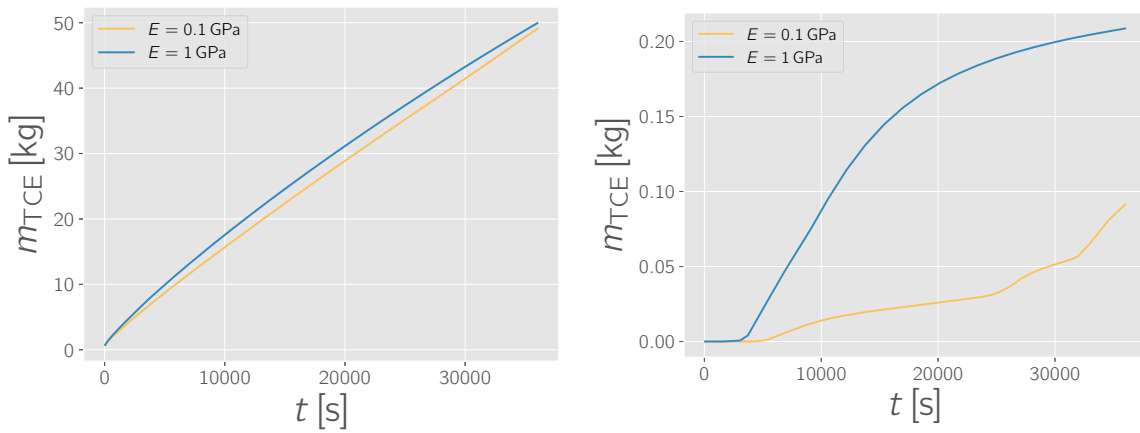


Figure 5.50 – Test case 11: mass of TCE over time. The left and right plots show the mass of TCE contained in the bulk medium and the fractures, respectively.

Summary In this test case the geometry as well as the pressure, stress and displacement boundary conditions from the single-phase case presented in Section 5.3.2 were reused, but a two-phase flow scenario with TCE entering the domain through the inlet was considered. It was seen that the infiltration of TCE into the domain can have significant effects on the displacement field and in particular on the fracture aperture. In the initial phase of the numerical experiment, regions of contact, which were similar to the single-phase case, develop on the fractures for the softer material. However, as the pressure conditions changed over time with the infiltration of TCE, the fracture surfaces lost contact causing a redistribution of the flow field.

5.4.2 Test case 12: dilating fractures

Let us now address the issue of fractures that open due to the mechanical deformation of the bulk medium. To this end, consider again a synthetic core sample with a diameter of 10 cm and a height of 15 cm as in the examples shown in the Sections 5.2.2 and 5.3.2. Two non-intersecting fractures are contained in this sample, of which one extends to the bottom boundary and one to the lateral boundary. Initially, the domain is fully saturated with liquid water, for which we have $\rho_{\text{H}_2\text{O}} = 1000 \text{ kg/m}^3$ and $\mu_{\text{H}_2\text{O}} = 1 \cdot 10^{-3} \text{ Pa}\cdot\text{s}$. We consider the injection of liquid Trichloroethene (TCE) with $\rho_{\text{TCE}} = 1460 \text{ kg/m}^3$ and $\mu_{\text{TCE}} = 5.7 \cdot 10^{-4} \text{ Pa}\cdot\text{s}$ at an injection rate of $7.5 \text{ g}/(\text{sm}^2)$ across the entire bottom boundary. The pressure build-up at the inlet is furthermore used as normal stress boundary condition for the mechanical problem. On the top boundary we prescribe $p_{\text{H}_2\text{O}} = 0 \text{ bar}$ and $S_{\text{TCE}} = 0$, while no-flow boundary conditions are used on the lateral boundary. The vertical displacement is fixed on the top boundary to $u_z = 0 \text{ m}$, and on the outer rim of the top boundary we additionally fix $u_x = u_y = 0 \text{ m}$. On the lateral boundary, no-stress conditions are applied.

The permeability and initial porosity of the matrix are given by $\mathbf{K}_3 = \mathbf{I} \cdot 10^{-14} \text{ m}^2$ and $\phi_{3,0} = 0.15$, while the porosity is again modeled depending on the deformation after equation (3.30). We use $\nu = 0.25$ and consider different Young's moduli $E \in \{0.25, 50\}$, here given in GPa, in order to investigate the influence of the magnitude of the fracture dilation on the flow field. The initial gap is set to $\varrho_0 = 1 \cdot 10^{-5} \text{ m}$ and the hydraulic aperture in case of contact is $a_0 = 1 \cdot 10^{-7} \text{ m}$.

For the parameters of the van-Genuchten-Mualem model for capillary pressure and relative permeability-saturation relationships, we use $\alpha_3^{\text{VG}} = 1 \cdot 10^{-4} \text{ 1/Pa}$ and $n_3^{\text{VG}} = 3$ in the bulk medium and $n_2^{\text{VG}} = 2.5$ in the fractures. Following the ideas presented in Walton et al. [2017], we linearly scale the capillary pressures in the fractures with the aperture. We define a reference state at a hydraulic aperture of $a_{\text{ref}} = 1 \cdot 10^{-7} \text{ m}$ for which we set $\alpha_{2,\text{ref}}^{\text{VG}} = 1 \cdot 10^{-4} \text{ 1/Pa}$, i.e. for such small apertures the capillary pressure-saturation relationship is equal to the one in the matrix. For any aperture a , the capillary pressure-saturation relationship is then obtained by scaling $\alpha_{2,\text{ref}}^{\text{VG}}$ with the aperture ratio, i.e.:

$$\alpha_2^{\text{VG}} = \alpha_{2,\text{ref}}^{\text{VG}} \frac{a}{a_{\text{ref}}}. \quad (5.11)$$

The grid used in this example consists of 43 672 tetrahedral and 880 triangular elements for the discretization of the bulk medium and the fractures, respectively. Furthermore,

a triangular grid with 220 elements is used for the Lagrange multiplier, although in this case the fracture surfaces do not come into contact. We use an initial time step size of $\Delta t = 1$ s, which is increased according to the convergence of the nonlinear solver up to a maximum value of $\Delta t = 100$ s. The final simulation time is set to $t_{\text{end}} = 3000$ s. As in the previous test case, we use CG1 for the discretization of the mechanical equations and the BOX scheme for the flow equations, as this combination is the computationally most efficient.

Figure 5.52 shows the evolution of deformation and the maximum velocities of TCE at three different points in time for the soft material with $E = 0.25$ GPa. Furthermore, it depicts the difference in TCE saturation between the model runs considering the high and low Young's moduli. It can be seen that saturation differences up to 38 % occur as a result of the aperture differences between the two realizations. In the case of the soft material ($E = 0.25$ GPa), the maximum observed aperture is $a = 8.43 \cdot 10^{-5}$ m which corresponds to an increase of 843 %. For the stiff material, maximum aperture changes of approximately 5 % occur. The influence of this dilation is also visible in integral measures as the temporal evolution of the mass of TCE contained in the domain as well as TCE production curves. These are shown in Figure 5.51a, where a slightly earlier onset of production of TCE at the outlet can be observed in the case of the soft material. This effect is caused by the increased tangential permeability of the fractures due to the dilation. The storage capacity of the fractures is negligibly small

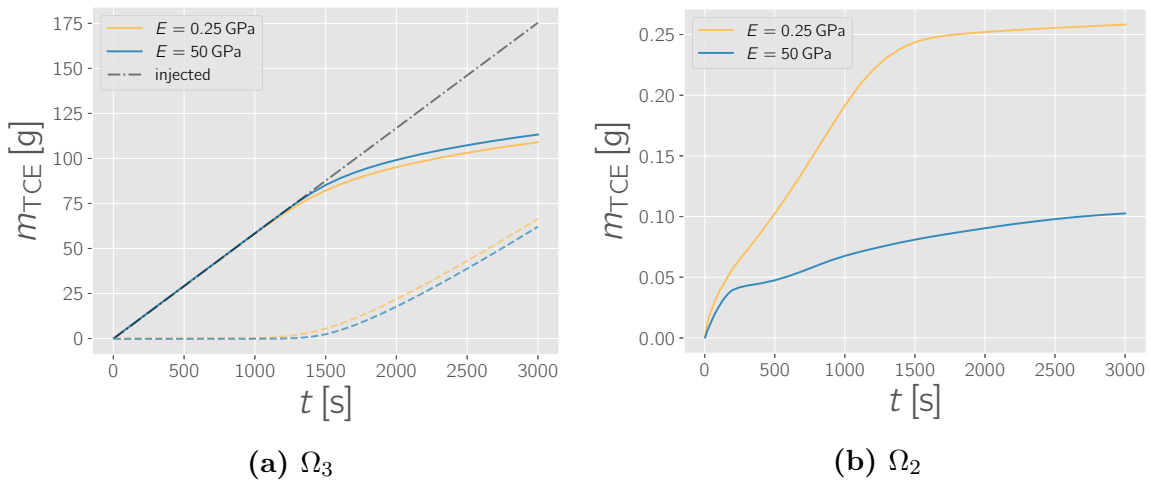


Figure 5.51 – Test case 12: mass of TCE over time. The plots show the mass of TCE contained in the bulk medium (left) and the fractures (right) over time. The dashed lines in the left plot show the corresponding TCE production curves.

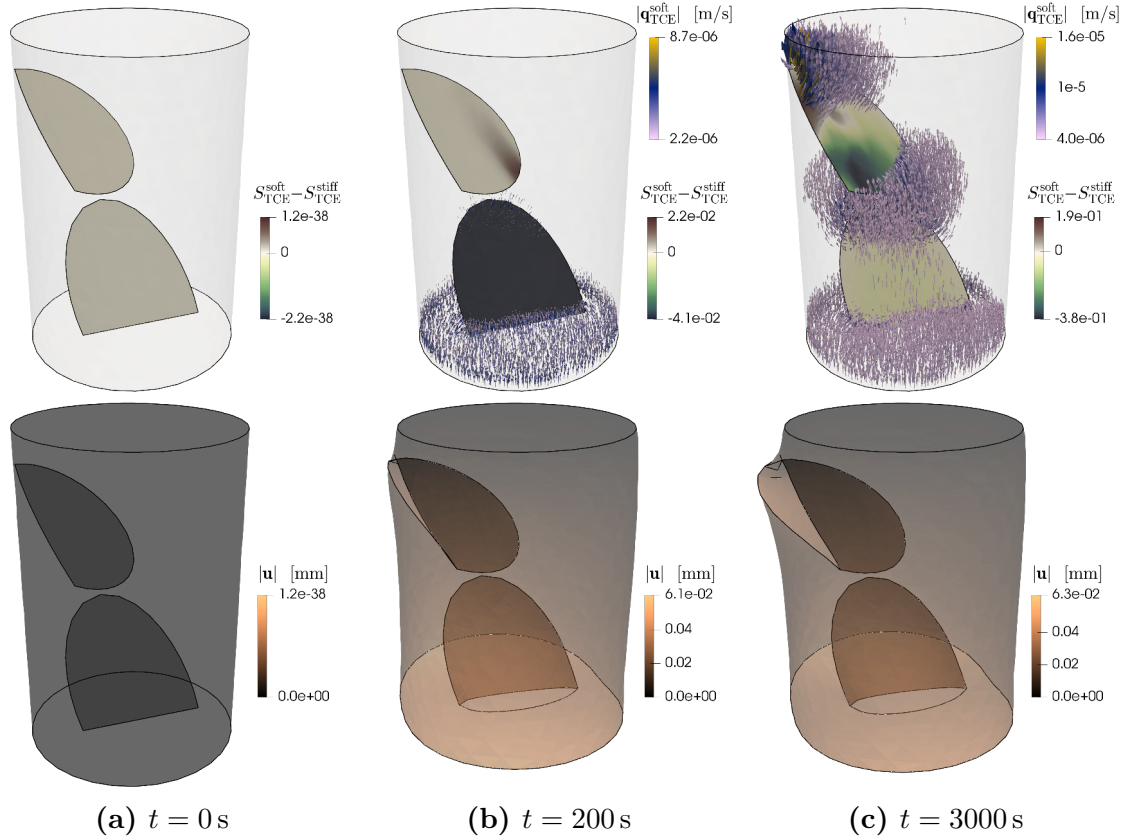


Figure 5.52 – Test case 12: saturation, velocity and deformation. The upper row shows the largest 80% of the TCE velocities obtained for $E = 0.25$ GPa, indicated by the arrows colored with the velocity magnitude. Moreover, on the fractures the difference in TCE saturation between the model runs using $E = 0.25$ GPa (soft) and $E = 50$ GPa (stiff) is depicted. The bottom row shows the deformation of the domain for the case of $E = 0.25$ GPa, where the displacements are exaggerated by a factor of 400. Each column shows the results for a certain time level which is given below the respective deformation distribution.

in comparison to the overall mass in the domain, which can be seen by comparing the Figures 5.51a and 5.51b. The latter shows the mass of TCE contained in the fractures, of which more than twice as much is contained in the fractures of the soft material at the final simulation time (see Figure 5.51b).

Figure 5.52 furthermore suggests that the aperture of the upper fracture further increases after the infiltration of non-wetting phase. The actual temporal evolution of the volume of the fractures is depicted in Figure 5.53, which shows that the volume of the upper fracture slightly increases initially, followed by a decrease in volume until ≈ 500 s and a subsequent increase with the infiltration of TCE into it at later times. The volume changes of the union of both fractures shows rather large variations between

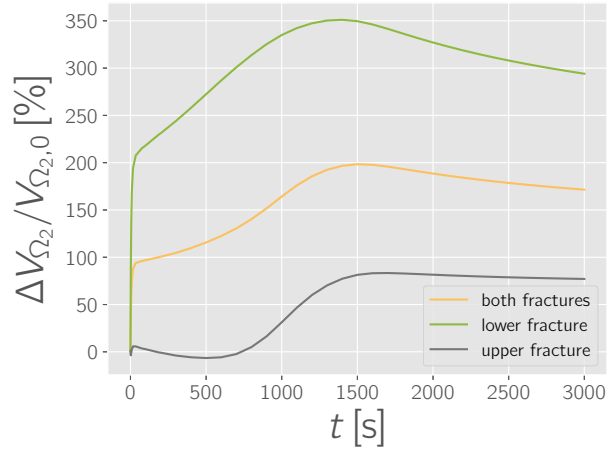


Figure 5.53 – Test case 12: fracture volume change over time. The plots show the relative difference in volume of the fractures with respect to the initial volume, plotted over time.

100 % and 200 % over the simulation time, which illustrates the transient nature of the feedback between flow and mechanics. This effect might have a much more pronounced impact on the production at the outlet in cases with a higher fracture density or in the case of intersecting fracture networks.

Summary In this test case, numerical results for two-phase flow through a fractured poroelastic core sample were shown, where an injection of TCE was imposed on the entire bottom boundary of the sample. For a soft material, significant fracture aperture changes up to 843 % were observed, which resulted in significantly different saturation distributions on the fractures when compared to a more stiff material. Fracture dilation had a major effect on the temporal evolution the mass of TCE contained in the fractures, while noticeable differences were also observed in the temporal evolution of the production of TCE at the outlet. However, a substantial effect on the production curves was not observed, which might be related to the unconnected nature and the small density of the fracture network in this test case. But, the effect could be much more pronounced for other fracture networks, which is suggested by the rather large volume changes observed in the fractures.

5.4.3 *Conclusions from the test cases*

The examples illustrated the complex interactions between flow and mechanics involved in two-phase flow. Cases featuring dilating fractures as well as dynamically closing and re-opening fractures were studied and physically meaningful results were observed. The mechanical deformations of the fracture surfaces showed to have a significant impact on the flow field inside and around the fractures, which produce noticeable effects on integral measures such as the overall mass contained in the domain and non-wetting phase production curves. The models showed to be able to capture the complex flow patterns that arise in such configurations in both two- and three-dimensional setups.

6 *Summary and Outlook*

In this work, several numerical approaches to the modeling of single- and two-phase flow in rigid fractured porous media as well as deformable fractured poroelastic media have been presented. Hybrid-dimensional formulations were derived, in which the fractures are modeled as entities of codimension 1 and fracture intersections as entities of codimension 2. The flow processes along these entities are described by means of cross section-integrated balance equations, in which the interaction with the next higher-dimensional domain is incorporated via source terms. These are composed of the transfer fluxes between the domains of codimension one, for which coupling conditions are formulated on the basis of pressure and flux continuity across the interfaces. The flow model has been extended to the case of deformable poroelastic bulk media, in which open fractures are contained and where flow along intersections is not considered. Different numerical approaches to the solution of the mixed-dimensional flow model have been presented, which comprise cell-centered finite volume schemes, using both two-point flux approximation (TPFA) and multi-point flux approximation (MPFA) techniques, as well as an approach based on the vertex-centered BOX scheme. For the discretization of the mechanical equations, we have considered the BOX scheme and the standard galerkin finite element method and have introduced Lagrange multipliers on the fractures that represent the tractions that arise if the fracture surfaces come into contact. The implementation allows the combination of any of the schemes derived for the mixed-dimensional flow equations with the mechanical solver, except for using the BOX scheme for both flow and mechanics.

In Chapter 2, the basic concepts, ideas and constitutive equations, on the basis of which flow and deformations in porous media are described, were introduced. Moreover, the derivations of the conservation equations underlying the presented models were outlined. In Chapter 3, we have presented the derivations of the mixed-dimensional flow model as well as the mixed-dimensional model considering both flow in fractures and mechanical deformations of the bulk medium. In the scope of the derivation of the

latter, we also outlined the conditions used on fracture surfaces that are in mechanical contact. The presentation of the numerical schemes used to solve the mixed-dimensional model equations was the focus of Chapter 4. We have started with the introduction of the TPFA, MPFA and the BOX scheme used for the mixed-dimensional flow model. Subsequently, we have outlined the solution of the mechanical equations using both the BOX as well as the standard galerkin finite element method, before we then described how the coupling terms between flow and mechanics are evaluated. At the end of the chapter, further details on the solution strategy were provided. In Chapter 5, we have presented the results to a number of test cases, each of which was designed to test either accuracy, efficiency or the capability to reproduce specific expected physical phenomena.

The chapter was started with two convergence tests for incompressible single-phase flow in porous media with a single fracture, considering both isotropic and anisotropic permeability tensors in the bulk medium. Good convergence was observed until the elements used in the bulk medium became smaller than the aperture of the fracture, which is in agreement with the observations presented in e.g. Martin et al. [2005], Sandve et al. [2012], Ahmed et al. [2015]. Moreover, no convergence was observed when TPFA was used in conjunction with anisotropic permeability tensors in the bulk medium, which was to be expected as the scheme is not consistent in this case. We furthermore applied the schemes to a benchmark case taken from Flemisch et al. [2018], for which a good agreement with the results reported in the original study were observed. We then performed numerical single-phase flow experiments on synthetic core samples devoted to determining the effective permeabilities of the samples. Physically meaningful results were obtained, in which we observed a nonlinear dependency of the effective permeabilities on the hydraulic aperture of the fractures. This dependency arises from the nonlinear relationship between the tangential fracture permeability and the hydraulic aperture.

Subsequently, we presented two test cases related to two-phase flow, where in the first one the results of the mixed-dimensional schemes were compared to an equi-dimensional reference solution for a case with two intersecting fractures. Good agreement between the results was observed for highly-conductive fractures, whereas larger deviations appeared in the case of blocking fractures. However, these were concentrated on the very close vicinity of the fractures, in which the pooling of the non-wetting phase before the impermeable fractures was not fully captured quantitatively. The deviations diminished with increasing distance to the fractures and the models showed to be able

to capture the overall flow field qualitatively. In the second test case we presented numerical results to gas injection scenarios into a synthetic core sample containing an arbitrary fracture network. We investigated the influence of gravity and the flow along intersections on the experimental results and found that in experimental conditions in which gravity has a minor impact on the temporal production profile of gas at the outlet, it can become a significant factor if conductive fractures are present. Moreover, considering flow along intersections can have a significant effect on the local flow field with noticeable impact on the production of gas at the outlet.

In the remainder of the chapter, we have tested the different numerical schemes for cases involving deformable poroelastic bulk media. Convergence was tested numerically for a purely mechanical test case considering a single fracture in frictional contact. Subsequently, we have applied the schemes to a two-dimensional domain with three fractures, for which the effective permeability was determined numerically using different values for the hydraulic fracture aperture in case of contact as well as initial gaps and material stiffnesses of the bulk medium. Physically meaningful results and dependencies of the effective permeability on the above-mentioned parameters were observed, which showed that the mechanical deformations can substantially alter the effective hydraulic properties of the domain depending on the stiffness of the material. Phenomenologically similar results were also obtained for a three-dimensional domain with a single fracture. We then considered a consolidation problem, in which the transient response of a fractured poroelastic medium to an instantaneous external force was investigated. The results were compared to the case of an unfractured medium, which revealed physically meaningful subsidence profiles with larger subsidence above sliding fractures. Finally, two- and three-dimensional test cases involving two-phase flow were presented, which focused on the phenomena of closing and dilating fractures. The numerical results featured dynamically closing and re-opening fractures causing substantial redistributions of the surrounding flow fields. These effects caused noticeable differences also in integral measures such as the temporal evolution of the production of the non-wetting phase at the outlet, which shows that taking deformation into account could be of importance e.g. in the interpretation of experimental results.

6.1 Outlook

The current implementation suffers from two major limitations. First, the code is not yet parallelized which makes it inefficient to use for large-scale simulations. Secondly, as mentioned in Section 4.4, we currently use the default Newton solver implemented in DuMu^x as nonlinear solver for the contact mechanical problem. However, the nonlinear complementary functions used to fulfill the inequalities involved in the contact conditions exhibit kinks and jumps are not generally differentiable. The current choice of nonlinear solver together with numeric differentiation showed to work in most cases, however, the number of iterations required to solve the system of equations is probably higher than if a specifically tailored nonlinear solver was used. Moreover, convergence is not guaranteed. In Wohlmuth [2011], Berge et al. [2019], semi-smooth Newton solvers are used to solve the problem of frictional contact. The approach involves the identification of the state of contact (sticking, sliding or no contact) at the degrees of freedom in the contact region and in each iteration. However, it is unclear how to define the state of contact at a nodal degree of freedom that is located at the intersection of two fractures, where the state could be different in each of them. Berge et al. [2019] use a cell-centered finite volume scheme for the discretization of the mechanical equations in which no displacement unknowns are located at intersections of fractures, however, the numerical examples presented therein do not consider intersecting fractures. Due to this unclarity, the results presented in this work are also restricted to media containing non-intersecting fractures.

Another issue is that in all results shown here, we have assumed fracture propagation not to occur. In future studies, this should be evaluated on the basis of propagation criteria to ensure that physically meaningful results are interpreted, or, the fractures could be growing dynamically. The latter would require remeshing techniques including mass conservative mappings to the updated geometries and grids.

Regarding the cell-centered approaches presented in this work, it was seen that the TPFA scheme, as it is well-known, is inconsistent on grids that are not \mathbf{K} -orthogonal. On the other hand, the MPFA scheme considered in this work is computationally very expensive on unstructured discretizations, in particular on tetrahedral grids. Future research could be targeted at using more recently developed nonlinear finite volume schemes [Schneider, 2018], which have been shown to be both consistent and efficient as they usually maintain small stencil sizes.

A Effective Porosity

Equation (3.30) for the effective porosity can be derived from the mass balance of the solid matrix (2.45) using the following two relationships *:

$$\begin{aligned}\operatorname{tr}(\boldsymbol{\epsilon}_s) &= \nabla \cdot \mathbf{u} = \det \mathbf{F}_s - 1, \\ \nabla \cdot \mathbf{v}_s &= \frac{(\det \mathbf{F}_s)}{\det \mathbf{F}_s}.\end{aligned}\tag{A.1}$$

Let us first rearrange (2.45) to:

$$\frac{\partial \phi}{\partial t} + \nabla \phi \mathbf{v}_s = (1 - \phi) \nabla \cdot \mathbf{v}_s,\tag{A.2}$$

where we identify the material time derivative $\dot{\phi} = \frac{\partial \phi}{\partial t} + \nabla \phi^T \mathbf{v}_s$. Further inserting the relationships state above, we end up with:

$$\frac{\dot{\phi}}{(1 - \phi)} = \frac{(\det \mathbf{F}_s)}{\det \mathbf{F}_s}.\tag{A.3}$$

*These relationships were taken from the lecture notes of the lecture "Einführung in die Kontinuumsmechanik von Mehrphasenmaterialien" given at the Institute for Mechanics of the University of Stuttgart in 2013

Let us now integrate the above equation from a reference time t_0 to the time t :

$$\begin{aligned}
\int_{t_0}^t \frac{\dot{\phi}}{(1-\phi)} dt &= \int_{t_0}^t \frac{(\dot{\det \mathbf{F}_s})}{\det \mathbf{F}_s} dt \\
\rightarrow [-\ln(1-\phi)]_{t_0}^t &= [\ln(\det \mathbf{F}_s)]_{t_0}^t \\
\rightarrow -\ln(1-\phi) + \ln(1-\phi_0) &= \ln(\det \mathbf{F}_s) - \ln(\det \mathbf{F}_{s,0}) \quad (\text{A.4}) \\
\rightarrow \frac{1-\phi_0}{1-\phi} &= \det(\mathbf{F}_s), \\
\rightarrow \frac{1-\phi_0}{1-\phi} &= \nabla \cdot \mathbf{u} + 1,
\end{aligned}$$

where we have introduced the porosity ϕ_0 at the time t_0 and have used $\mathbf{F}_{s,0} = \mathbf{I}$ and therefore $\det(\mathbf{F}_{s,0}) = 1$ and $\ln(\det \mathbf{F}_{s,0}) = 0$. Rearrangement of the last equation of (A.4) leads to the expression for the effective porosity at a time t as a function of the displacement and the initial (or reference) porosity ϕ_0 :

$$\phi_{\text{eff}} = \frac{\phi_0 + \nabla \cdot \mathbf{u}}{1 + \nabla \cdot \mathbf{u}}. \quad (\text{A.5})$$

B Time step control

In this work, the time step sizes in transient nonlinear problems is adjusted depending on the convergence of the Newton solver. Let us consider the n -th time step in a simulation, for which N iterations of the nonlinear solver were necessary to fulfill the convergence criterion. The time step size Δt^{n+1} is then computed the following way:

$$\Delta t^{n+1} = \begin{cases} \Delta t^n \left(\frac{1}{1 + \frac{N - N_{\text{target}}}{N_{\text{target}}}} \right), & \text{for } N_{\text{max}} > N > N_{\text{target}}, \\ \Delta t^n \left(1 + \frac{N_{\text{target}} - N}{1.2 N_{\text{target}}} \right), & \text{for } N \leq N_{\text{target}}, \end{cases} \quad (\text{B.1})$$

where N_{target} defines the desired number of Newton iterations and N_{max} is maximum number of iterations. If in a time step $N = N_{\text{max}}$ is reached, the time step size is reduced by a factor of 0.5 and time integration is retried. This procedure is repeated until a successful time integration or if a maximum number of retries is reached.

Bibliography

- I. Aavatsmark. An introduction to multipoint flux approximations for quadrilateral grids. *Computational Geosciences*, 6(3):405–432, 2002. ISSN 1573-1499. doi:10.1023/A:1021291114475.
- I. Aavatsmark, G. Eigestad, B. Mallison, and J. Nordbotten. A compact multipoint flux approximation method with improved robustness. *Numerical Methods for Partial Differential Equations*, 24(5):1329–1360, 2008. ISSN 1098-2426. doi:10.1002/num.20320.
- L. Agélas, D. A. Di Pietro, and J. Droniou. The g method for heterogeneous anisotropic diffusion on general meshes. *ESAIM: Mathematical Modelling and Numerical Analysis*, 44(4):597–625, 2010. doi:10.1051/m2an/2010021.
- J. Aghili, K. Brenner, J. Hennicker, R. Masson, and L. Trenty. Two-phase Discrete Fracture Matrix models with linear and nonlinear transmission conditions. *GEM - International Journal on Geomathematics*, Jan. 2019. doi:10.1007/s13137-019-0118-6.
- R. Ahmed, M. Edwards, S. Lamine, B. Huisman, and M. Pal. Control-volume distributed multi-point flux approximation coupled with a lower-dimensional fracture model. *Journal of Computational Physics*, 284:462 – 489, 2015. ISSN 0021-9991. doi:10.1016/j.jcp.2014.12.047.
- R. Ahmed, M. G. Edwards, S. Lamine, B. A. Huisman, and M. Pal. Cvd-mpfa full pressure support, coupled unstructured discrete fracture–matrix darcy-flux approximations. *Journal of Computational Physics*, 349:265 – 299, 2017. ISSN 0021-9991. doi:10.1016/j.jcp.2017.07.041.
- N. Andrianov and H. M. Nick. Modeling of waterflood efficiency using outcrop-based fractured models. *Journal of Petroleum Science and Engineering*, 183:106350, 2019. ISSN 0920-4105. doi:10.1016/j.petrol.2019.106350.

- P. F. Antonietti, L. Formaggia, A. Scotti, M. Verani, and N. Verzott. Mimetic finite difference approximation of flows in fractured porous media. *ESAIM: Mathematical Modelling and Numerical Analysis*, 50(3):809–832, 2016.
- P. Bastian, M. Blatt, A. Dedner, C. Engwer, R. Klöfkorn, R. Kornhuber, M. Ohlberger, and O. Sander. A generic grid interface for parallel and adaptive scientific computing. part II: Implementation and tests in DUNE. *Computing*, 82(2):121–138, 2008a. ISSN 1436-5057. doi:10.1007/s00607-008-0004-9.
- P. Bastian, M. Blatt, A. Dedner, C. Engwer, R. Klöfkorn, M. Ohlberger, and O. Sander. A Generic Grid Interface for Parallel and Adaptive Scientific Computing. Part I: Abstract Framework. *Computing*, 82(2–3):103–119, 2008b. doi:10.1007/s00607-008-0003-x.
- J. Bear. *Dynamics of fluids in porous media*. Courier Corporation, 2013.
- M. Beck. *Conceptual approaches for the analysis of coupled hydraulic and geomechanical processes*. PhD thesis, Universitätsbibliothek der Universität Stuttgart, Holzgartenstr. 16, 70174 Stuttgart, 2018.
- R. L. Berge, I. Berre, E. Keilegavlen, J. M. Nordbotten, and B. Wohlmuth. Finite volume discretization for poroelastic media with fractures modeled by contact mechanics. *arXiv e-prints*, art. arXiv:1905.03346, 2019.
- I. Berre, W. Boon, B. Flemisch, A. Fumagalli, D. Gläser, E. Keilegavlen, A. Scotti, I. Stefansson, and A. Tatomir. Call for participation: Verification benchmarks for single-phase flow in three-dimensional fractured porous media, 2018.
- M. A. Biot. General theory of three-dimensional consolidation. *Journal of applied physics*, 12(2):155–164, 1941.
- W. M. Boon, J. M. Nordbotten, and I. Yotov. Robust discretization of flow in fractured porous media. *SIAM Journal on Numerical Analysis*, 56(4):2203–2233, 2018. doi:10.1137/17M1139102.
- K. Brenner, M. Groza, C. Guichard, and R. Masson. Vertex approximate gradient scheme for hybrid dimensional two-phase darcy flows in fractured porous media. In J. Fuhrmann, M. Ohlberger, and C. Rohde, editors, *Finite Volumes for Complex*

-
- Applications VII-Elliptic, Parabolic and Hyperbolic Problems*, pages 507–515, Cham, 2014. Springer International Publishing.
- K. Brenner, J. Hennicker, R. Masson, and P. Samier. Hybrid-dimensional modelling of two-phase flow through fractured porous media with enhanced matrix fracture transmission conditions. *Journal of Computational Physics*, Mar. 2018. doi:10.1016/j.jcp.2017.12.003.
- R. H. Brooks and A. T. Corey. Hydraulic properties of porous media and their relation to drainage design. *Transactions of the ASAE*, 7(1):26–0028, 1964.
- P. C. Carman. Fluid flow through granular beds. *Transactions, Institution of Chemical Engineers*, 15:150–166, 1937.
- M. Darcis. *Coupling models of different complexity for the simulation of CO2 storage in deep saline aquifers*. PhD thesis, Universitätsbibliothek der Universität Stuttgart, Holzgartenstr. 16, 70174 Stuttgart, 2013.
- T. A. Davis. Algorithm 832: Umfpack v4.3—an unsymmetric-pattern multifrontal method. *ACM Trans. Math. Softw.*, 30(2):196–199, 2004. ISSN 0098-3500. doi:10.1145/992200.992206.
- M. G. Edwards and C. F. Rogers. Finite volume discretization with imposed flux continuity for the general tensor pressure equation. *Computational Geosciences*, 2(4):259–290, Dec 1998. ISSN 1573-1499. doi:10.1023/A:1011510505406.
- W. Ehlers. *Foundations of multiphasic and porous materials*, pages 3–86. Springer Berlin Heidelberg, Berlin, Heidelberg, 2002. ISBN 978-3-662-04999-0. doi:10.1007/978-3-662-04999-0_1.
- B. Flemisch, M. Darcis, K. Erbertseder, B. Faigle, A. Lauser, K. Mosthaf, S. Müthing, P. Nuske, A. Tatomir, M. Wolff, and R. Helmig. Dumux: Dune for multi-Phase, Component, Scale, Physics, ... flow and transport in porous media. *Advances in Water Resources*, 34:1102–1112, 2011. doi:10.1016/j.advwatres.2011.03.007.
- B. Flemisch, I. Berre, W. Boon, A. Fumagalli, N. Schwenck, A. Scotti, I. Stefansson, and A. Tatomir. Benchmarks for single-phase flow in fractured porous media. *Advances in Water Resources*, 111:239 – 258, 2018. ISSN 0309-1708. doi:10.1016/j.advwatres.2017.10.036.

- M. Fourar, S. Bories, R. Lenormand, and P. Persoff. Two-phase flow in smooth and rough fractures: Measurement and correlation by porous-medium and pipe flow models. *Water Resources Research*, 29:3699–3708, 11 1993. doi:10.1029/93WR01529.
- N. Frih, V. Martin, J. E. Roberts, and A. Saâda. Modeling fractures as interfaces with nonmatching grids. *Computational Geosciences*, 16(4):1043–1060, 2012.
- H. A. Friis and M. G. Edwards. A family of mpfa finite-volume schemes with full pressure support for the general tensor pressure equation on cell-centered triangular grids. *Journal of Computational Physics*, 230(1):205 – 231, 2011. ISSN 0021-9991. doi:10.1016/j.jcp.2010.09.012.
- A. Fumagalli and A. Scotti. A numerical method for two-phase flow in fractured porous media with non-matching grids. *Advances in Water Resources*, 62:454 – 464, 2013. ISSN 0309-1708. doi:10.1016/j.advwatres.2013.04.001.
- T. Garipov, M. Karimi-Fard, and H. Tchelepi. Discrete fracture model for coupled flow and geomechanics. *Computational Geosciences*, 20(1):149–160, 2016. doi:10.1007/s10596-015-9554-z.
- C. Geuzaine and J.-F. Remacle. Gmsh: A 3-d finite element mesh generator with built-in pre- and post-processing facilities. *International Journal for Numerical Methods in Engineering*, 79(11):1309–1331, 2009. ISSN 1097-0207. doi:10.1002/nme.2579.
- D. Gläser, R. Helmig, B. Flemisch, and H. Class. A discrete fracture model for two-phase flow in fractured porous media. *Advances in Water Resources*, 110:335 – 348, 2017. ISSN 0309-1708. doi:doi.org/10.1016/j.advwatres.2017.10.031.
- D. Gläser, B. Flemisch, R. Helmig, and H. Class. A hybrid-dimensional discrete fracture model for non-isothermal two-phase flow in fractured porous media. *GEM-International Journal on Geomathematics*, 10(1):5, 2019.
- A. Grillo, D. Logashenko, S. Stichel, and G. Wittum. Forchheimer’s correction in modelling flow and transport in fractured porous media. *Computing and Visualization in Science*, 15, 08 2013. doi:10.1007/s00791-013-0208-1.
- K. Häberle. *Fluid-phase transitions in a multiphasic model of CO₂ sequestration into deep aquifers: a fully coupled analysis of transport phenomena and solid deforma-*

-
- tion. PhD thesis, Universitätsbibliothek der Universität Stuttgart, Holzgartenstr. 16, 70174 Stuttgart, 2017.
- H. Hægland, A. Assteerawatt, H. K. Dahle, G. T. Eigestad, and R. Helmig. Comparison of cell-and vertex-centered discretization methods for flow in a two-dimensional discrete-fracture-matrix system. *Advances in Water resources*, 32(12):1740–1755, 2009. doi:10.1016/j.advwatres.2009.09.006.
- R. Helmig. *Multiphase flow and transport processes in the subsurface: a contribution to the modeling of hydrosystems*. Springer-Verlag, 1997.
- R. Huber and R. Helmig. Multiphase flow in heterogeneous porous media: A classical finite element method versus an implicit pressure-explicit saturation-based mixed finite element-finite volume approach. *International Journal for Numerical Methods in Fluids*, 29(8):899–920, 1999.
- R. G. Hughes and M. J. Blunt. Network modeling of multiphase flow in fractures. *Advances in Water Resources*, 24(3-4):409–421, 2001.
- S. Hüeber and B. Wohlmuth. A primal-dual active set strategy for non-linear multibody contact problems. *Computer Methods in Applied Mechanics and Engineering*, 194(27):3147 – 3166, 2005. ISSN 0045-7825. doi:10.1016/j.cma.2004.08.006.
- J. Jaeger, N. Cook, and R. Zimmerman. *Fundamentals of Rock Mechanics*. Wiley, 2007. ISBN 9780632057597.
- J. Jaffré, M. Mnejja, and J. Roberts. A discrete fracture model for two-phase flow with matrix-fracture interaction. *Procedia Computer Science*, 4:967 – 973, 2011. ISSN 1877-0509. doi:doi.org/10.1016/j.procs.2011.04.102.
- M. Karimi-Fard and A. Firoozabadi. Numerical simulation of water injection in fractured media using the discrete-fracture model and the galerkin method. *SPE Reservoir Evaluation and Engineering*, 6:117–126, 04 2003. doi:10.2118/83633-PA.
- M. Karimi-Fard, L. Durlofsky, and K. Aziz. An efficient discrete-fracture model applicable for general-purpose reservoir simulators. *SPE Journal*, 9:227–236, 2004.
- H. Kazemi, L. Merrill Jr, K. Porterfield, P. Zeman, et al. Numerical simulation of water-oil flow in naturally fractured reservoirs. *Society of Petroleum Engineers Journal*, 16(06):317–326, 1976. doi:10.2118/5719-PA.

- E. Keilegavlen, A. Fumagalli, R. Berge, I. Stefansson, and I. Berre. Porepy: An open source simulation tool for flow and transport in deformable fractured rocks. Technical report, arXiv:1712.00460 [cs.CE], 2017.
- T. Koch, D. Gläser, K. Weishaupt, S. Ackermann, M. Beck, B. Becker, S. Burbulla, H. Class, E. Coltman, T. Fetzner, B. Flemisch, C. Grüninger, K. Heck, J. Hommel, T. Kurz, M. Lipp, F. Mohammadi, M. Schneider, G. Seitz, S. Scholz, and F. Weinhardt. Dumux 3.0.0. Dec. 2018a. doi:10.5281/zenodo.2479595.
- T. Koch, K. Heck, N. Schröder, H. Class, and R. Helmig. A new simulation framework for soil-root interaction, evaporation, root growth, and solute transport. *Vadose Zone Journal*, 17, 2018b. doi:10.2136/vzj2017.12.0210. 1.
- T. Koch, D. Gläser, K. Weishaupt, S. Ackermann, M. Beck, B. Becker, S. Burbulla, H. Class, E. Coltman, S. Emmert, T. Fetzner, C. Grüninger, K. Heck, J. Hommel, T. Kurz, M. Lipp, F. Mohammadi, S. Scherrer, M. Schneider, G. Seitz, L. Stadler, M. Utz, F. Weinhardt, and B. Flemisch. Dumu^x 3 – an open-source simulator for solving flow and transport problems in porous media with a focus on model coupling. *arXiv e-prints*, art. arXiv:1909.05052, 2019.
- T. Koch, R. Helmig, and M. Schneider. A new and consistent well model for one-phase flow in anisotropic porous media using a distributed source model. *arXiv e-prints*, art. arXiv:1907.12653, 2019a.
- T. Koch, M. Schneider, R. Helmig, and P. Jenny. Modeling tissue perfusion in terms of 1d-3d embedded mixed-dimension coupled problems with distributed sources. *arXiv e-prints*, art. arXiv:1905.03346, 2019b.
- M. Köppel. Flow modelling of coupled fracture-matrix porous media systems with a two mesh concept. Master’s thesis, Pomdapi INRIA Rocquencourt, 2013.
- M. Köppel, V. Martin, J. Jaffré, and J. E. Roberts. A lagrange multiplier method for a discrete fracture model for flow in porous media. *Computational Geosciences*, pages 1–15, 2018.
- M. Köppel, V. Martin, and J. E. Roberts. A stabilized lagrange multiplier finite-element method for flow in porous media with fractures. *GEM-International Journal on Geomathematics*, 10(1):7, 2019.

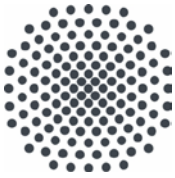
-
- M. Kozeny. Uber kapillare leitung des wassers im boden. *Sitzber. Akad. Wiss. Wein, Math-naturw*, 136:Abt. II a, P. 277, 1927.
- C. Le Potier. A nonlinear finite volume scheme satisfying maximum and minimum principles for diffusion operators. *International Journal on Finite Volumes*, pages 1–20, Dec. 2009.
- X. S. Li. Superlu: Sparse direct solver and preconditioner. In *13th DOE ACTS Collection Workshop*, 2004.
- L. Luckner, M. T. Van Genuchten, and D. Nielsen. A consistent set of parametric models for the two-phase flow of immiscible fluids in the subsurface. *Water Resources Research*, 25(10):2187–2193, 1989. doi:10.1029/WR025i010p02187.
- V. Martin, J. Jaffré, and J. E. Roberts. Modeling fractures and barriers as interfaces for flow in porous media. *SIAM Journal on Scientific Computing*, 26(5):1667–1691, 2005. doi:10.1137/S1064827503429363.
- S. K. Matthai, A. Mezentsev, and M. Belayneh. Finite element - node-centered finite-volume two-phase-flow experiments with fractured rock represented by unstructured hybrid-element meshes. *Society of Petroleum Engineers*, 2007. doi:10.2118/93341-PA.
- R. D. McFarland and H. Murphy. Extracting energy from hydraulically-fractured geothermal reservoirs. Technical report, Los Alamos Scientific Lab., N. Mex.(USA), 1976.
- C. A. Mendoza. *Capillary Pressure and Relative Transmissivity Relationships Describing Two-Phase Flow Through Rough-Walled Fractures in Geologic Materials*. PhD thesis, University of Waterloo, Waterloo, Ontario, Canada, 1992.
- J. Monteagudo, A. Rodriguez, H. Florez, et al. Simulation of flow in discrete deformable fractured porous media. In *SPE reservoir simulation symposium, The Woodlands, TX*, 2011. doi:10.2118/141267-MS.
- Y. Mualem. A new model for predicting the hydraulic conductivity of unsaturated porous media. *Water Resources Research*, 12(3):513–522, 1976. ISSN 1944-7973. doi:10.1029/WR012i003p00513.

- National Research Council and others. *Rock fractures and fluid flow: contemporary understanding and applications*. The National Academies Press, 1996. doi:10.17226/2309.
- M. Nejati, A. Paluszny, and R. W. Zimmerman. A finite element framework for modeling internal frictional contact in three-dimensional fractured media using unstructured tetrahedral meshes. *Computer Methods in Applied Mechanics and Engineering*, 306:123 – 150, 2016. ISSN 0045-7825. doi:10.1016/j.cma.2016.03.028.
- J. M. Nordbotten, W. M. Boon, A. Fumagalli, and E. Keilegavlen. Unified approach to discretization of flow in fractured porous media. *Computational Geosciences*, 23(2):225–237, 2019.
- G. Penuela, F. Civan, R. Hughes, M. Wiggins, et al. Time-dependent shape factors for interporosity flow in naturally fractured gas-condensate reservoirs. In *SPE Gas Technology Symposium*. Society of Petroleum Engineers, 2002.
- P. Persoff and K. Pruess. Two-phase flow visualization and relative permeability measurement in natural rough-walled rock fractures. *Water Resources Research*, 31(5):1175–1186, 1995. doi:10.1029/95WR00171.
- A.-V. Phan, J. A. L. Napier, L. J. Gray, and T. Kaplan. Symmetric-galerkin bem simulation of fracture with frictional contact. *International Journal for Numerical Methods in Engineering*, 57(6):835–851, 2003. doi:10.1002/nme.707.
- K. Pruess. *Brief Guide to the MINC-method for Modeling Flow and Transport in Fractured Media*. United States. Department of Energy, 1992.
- K. Pruess and Y. W. Tsang. On two-phase relative permeability and capillary pressure of rough-walled rock fractures. *Water Resources Research*, 26(9):1915–1926, 1990. doi:10.1029/WR026i009p01915.
- K. Pruess, J. Wang, and Y. Tsang. On thermohydrologic conditions near high-level nuclear wastes emplaced in partially saturated fractured tuff: 2. effective continuum approximation. *Water Resources Research*, 26(6):1249–1261, 1990.
- L. J. Pyrak-Nolte, D. Helgeson, G. M. Haley, J. W. Morris, et al. Immiscible fluid flow in a fracture. In *The 33th US Symposium on Rock Mechanics (USRMS)*. American Rock Mechanics Association, 1992.

-
- J. Qian, X. Zhou, H. Zhan, H. Dong, and L. Ma. Numerical simulation and evaluation of groundwater resources in a fractured chalk aquifer: a case study in zinder well field, niger. *Environmental earth sciences*, 72(8):3053–3065, 2014.
- V. Reichenberger, H. Jakobs, P. Bastian, and R. Helmig. A mixed-dimensional finite volume method for two-phase flow in fractured porous media. *Advances in Water Resources*, 29(7):1020–1036, 2006.
- R. Reid, J. Prausnitz, and B. Poling. *The properties of gases and liquids*. McGraw-Hill Inc., 1987.
- E. Romm. *Fluid flow in fractured rocks*. Moscow: Nedra Publishing House, 1966. [Translated from Russian].
- P. Royer, J.-L. Auriault, J. Lewandowska, and C. Serres. Continuum modelling of contaminant transport in fractured porous media. *Transport in Porous Media*, 49(3): 333–359, Dec 2002. ISSN 1573-1634. doi:10.1023/A:1016272700063.
- T. Sandve, I. Berre, and J. Nordbotten. An efficient multi-point flux approximation method for discrete fracture–matrix simulations. *Journal of Computational Physics*, 231(9):3784 – 3800, 2012. ISSN 0021-9991. doi:10.1016/j.jcp.2012.01.023.
- M. Schneider. *Nonlinear finite volume schemes for complex flow processes and challenging grids*. PhD thesis, Universitätsbibliothek der Universität Stuttgart, Holzgartenstr. 16, 70174 Stuttgart, 2018.
- M. Schneider, B. Flemisch, and R. Helmig. Monotone nonlinear finite-volume method for nonisothermal two-phase two-component flow in porous media. *International Journal for Numerical Methods in Fluids*, 84, 12 2016. doi:10.1002/flid.4352.
- M. Schneider, K. Weishaupt, D. Gläser, W. M. Boon, and R. Helmig. Coupling staggered-grid and MPFA finite volume methods for free flow/porous-medium flow problems. *arXiv preprint arXiv:1902.02568*, 2019.
- N. Schwenck. *An XFEM-based model for fluid flow in fractured porous media*. PhD thesis, Universitätsbibliothek der Universität Stuttgart, Holzgartenstr. 16, 70174 Stuttgart, 2015.

- P. Schädle, P. Zulian, D. Vogler, S. R. Bhopalam, M. G. Nestola, A. Ebigbo, R. Krause, and M. O. Saar. 3d non-conforming mesh model for flow in fractured porous media using lagrange multipliers. *Computers & Geosciences*, 132:42 – 55, 2019. ISSN 0098-3004. doi:10.1016/j.cageo.2019.06.014.
- A. R. Shaik, S. S. Rahman, N. H. Tran, and T. Tran. Numerical simulation of fluid-rock coupling heat transfer in naturally fractured geothermal system. *Applied Thermal Engineering*, 31(10):1600 – 1606, 2011. ISSN 1359-4311. doi:10.1016/j.applthermaleng.2011.01.038.
- B. K. Sovacool. Cornucopia or curse? reviewing the costs and benefits of shale gas hydraulic fracturing (fracking). *Renewable and Sustainable Energy Reviews*, 37:249 – 264, 2014. ISSN 1364-0321. doi:10.1016/j.rser.2014.04.068.
- A.-B. Tatomir. *From discrete to continuum concepts of flow in fractured porous media*. PhD thesis, Universitätsbibliothek der Universität Stuttgart, Holzgartenstr. 16, 70174 Stuttgart, 2013.
- M. Tene, M. S. A. Kobaisi, and H. Hajibeygi. Algebraic multiscale method for flow in heterogeneous porous media with embedded discrete fractures (fams). *Journal of Computational Physics*, 321:819 – 845, 2016. ISSN 0021-9991. doi:10.1016/j.jcp.2016.06.012.
- M. Tene, S. B. Bosma, M. S. A. Kobaisi, and H. Hajibeygi. Projection-based embedded discrete fracture model (pedfm). *Advances in Water Resources*, 105:205 – 216, 2017. ISSN 0309-1708. doi:10.1016/j.advwatres.2017.05.009.
- K. Terzaghi et al. *Erdbaumechanik auf bodenphysikalischer grundlage*. 1925.
- F. Torabi, A. Q. Firouz, A. Kavousi, and K. Asghari. Comparative evaluation of immiscible, near miscible and miscible co2 huff-n-puff to enhance oil recovery from a single matrix–fracture system (experimental and simulation studies). *Fuel*, 93: 443–453, 2012.
- E. Ucar, I. Berre, and E. Keilegavlen. Three-dimensional numerical modeling of shear stimulation of fractured reservoirs. *Journal of Geophysical Research: Solid Earth*, 123(5):3891–3908, 2018.

-
- M. Van Genuchten. A closed-form equation for predicting the hydraulic conductivity of unsaturated soils¹. *Soil Science Society of America Journal*, 44, 09 1980.
- W. Wagner and H.-J. Kretzschmar. *IAPWS Industrial Formulation 1997 for the Thermodynamic Properties of Water and Steam*. In: *International Steam Tables.*, pages 7–150. Springer Berlin Heidelberg, Berlin, Heidelberg, 2008. ISBN 978-3-540-74234-0.
- K. M. Walton, A. J. A. Unger, M. A. Ioannidis, and B. L. Parker. Impact of eliminating fracture intersection nodes in multiphase compositional flow simulation. *Water Resources Research*, 53(4):2917–2939, 2017. doi:10.1002/2016WR020088.
- J. Warren and P. Root. The behavior of naturally fractured reservoirs. *Society of Petroleum Engineers Journal*, 3(03):245–255, 1963.
- K. Weishaupt, V. Joekar-Niasar, and R. Helmig. An efficient coupling of free flow and porous media flow using the pore-network modeling approach. *Journal of Computational Physics: X*, 1:100011, Jan. 2019. doi:10.1016/j.jcpx.2019.100011.
- B. Wohlmuth. Variationally consistent discretization schemes and numerical algorithms for contact problems. *Acta Numerica*, 20:569–734, 2011. doi:10.1017/S0962492911000079.
- R. W. Zimmerman and G. S. Bodvarsson. Hydraulic conductivity of rock fractures. *Transport in porous media*, 23(1):1–30, 1996.
- R. W. Zimmerman, G. Chen, T. Hadgu, and G. S. Bodvarsson. A numerical dual-porosity model with semianalytical treatment of fracture/matrix flow. *Water resources research*, 29(7):2127–2137, 1993.
- R. W. Zimmerman, T. Hadgu, and G. S. Bodvarsson. A new lumped-parameter model for flow in unsaturated dual-porosity media. *Advances in Water Resources*, 19(5): 317–327, 1996.



Institut für Wasser- und Umweltsystemmodellierung Universität Stuttgart

Pfaffenwaldring 61
70569 Stuttgart (Vaihingen)
Telefon (0711) 685 - 60156
Telefax (0711) 685 - 51073
E-Mail: iws@iws.uni-stuttgart.de
<http://www.iws.uni-stuttgart.de>

Direktoren

Prof. Dr. rer. nat. Dr.-Ing. András Bárdossy
Prof. Dr.-Ing. Rainer Helmig
Prof. Dr.-Ing. Wolfgang Nowak
Prof. Dr.-Ing. Silke Wieprecht

Vorstand (Stand 1.5.2019)

Prof. Dr. rer. nat. Dr.-Ing. A. Bárdossy
Prof. Dr.-Ing. R. Helmig
Prof. Dr.-Ing. W. Nowak
Prof. Dr.-Ing. S. Wieprecht
Prof. Dr. J.A. Sander Huisman
Jürgen Braun, PhD
apl. Prof. Dr.-Ing. H. Class
PD Dr.-Ing. Claus Haslauer
Stefan Haun, PhD
PD Dr.-Ing. habil. Sergey Oladyskkin
Dr. rer. nat. J. Seidel
Dr.-Ing. K. Terheiden

Emeriti

Prof. Dr.-Ing. habil. Dr.-Ing. E.h. Jürgen Giesecke
Prof. Dr.h.c. Dr.-Ing. E.h. Helmut Kobus, PhD

Lehrstuhl für Wasserbau und Wassermengenwirtschaft

Leiterin: Prof. Dr.-Ing. Silke Wieprecht
Stellv.: Dr.-Ing. Kristina Terheiden
Versuchsanstalt für Wasserbau
Leiter: Stefan Haun, PhD

Lehrstuhl für Hydromechanik und Hydrosystemmodellierung

Leiter: Prof. Dr.-Ing. Rainer Helmig
Stellv.: apl. Prof. Dr.-Ing. Holger Class

Lehrstuhl für Hydrologie und Geohydrologie

Leiter: Prof. Dr. rer. nat. Dr.-Ing. András Bárdossy
Stellv.: Dr. rer. nat. Jochen Seidel
Hydrogeophysik der Vadosen Zone
(mit Forschungszentrum Jülich)
Leiter: Prof. Dr. J.A. Sander Huisman

Lehrstuhl für Stochastische Simulation und Sicherheitsforschung für Hydrosysteme

Leiter: Prof. Dr.-Ing. Wolfgang Nowak
Stellv.: PD Dr.-Ing. habil. Sergey Oladyskkin

VEGAS, Versuchseinrichtung zur Grundwasser- und Altlastensanierung

Leiter: Jürgen Braun, PhD
PD Dr.-Ing. Claus Haslauer

Verzeichnis der Mitteilungshefte

- 1 Röhnisch, Arthur: *Die Bemühungen um eine Wasserbauliche Versuchsanstalt an der Technischen Hochschule Stuttgart*, und Fattah Abouleid, Abdel: *Beitrag zur Berechnung einer in lockeren Sand gerammten, zweifach verankerten Spundwand*, 1963
- 2 Marotz, Günter: *Beitrag zur Frage der Standfestigkeit von dichten Asphaltbelägen im Großwasserbau*, 1964
- 3 Gurr, Siegfried: *Beitrag zur Berechnung zusammengesetzter ebener Flächentragwerke unter besonderer Berücksichtigung ebener Stauwände, mit Hilfe von Randwert- und Lastwertmatrizen*, 1965
- 4 Plica, Peter: *Ein Beitrag zur Anwendung von Schalenkonstruktionen im Stahlwasserbau*, und Petrikat, Kurt: *Möglichkeiten und Grenzen des wasserbaulichen Versuchswesens*, 1966

- 5 Plate, Erich: *Beitrag zur Bestimmung der Windgeschwindigkeitsverteilung in der durch eine Wand gestörten bodennahen Luftschicht*, und
Röhnisch, Arthur; Marotz, Günter: *Neue Baustoffe und Bauausführungen für den Schutz der Böschungen und der Sohle von Kanälen, Flüssen und Häfen; Gestehungskosten und jeweilige Vorteile*, sowie
Unny, T.E.: *Schwingungsuntersuchungen am Kegelstrahlschieber*, 1967
- 6 Seiler, Erich: *Die Ermittlung des Anlagenwertes der bundeseigenen Binnenschiffahrtsstraßen und Talsperren und des Anteils der Binnenschifffahrt an diesem Wert*, 1967
- 7 *Sonderheft anlässlich des 65. Geburtstages von Prof. Arthur Röhnisch mit Beiträgen von*
Benk, Dieter; Breitling, J.; Gurr, Siegfried; Haberhauer, Robert; Honekamp, Hermann; Kuz, Klaus Dieter; Marotz, Günter; Mayer-Vorfelder, Hans-Jörg; Miller, Rudolf; Plate, Erich J.; Radomski, Helge; Schwarz, Helmut; Vollmer, Ernst; Wildenhahn, Eberhard; 1967
- 8 Jumikis, Alfred: *Beitrag zur experimentellen Untersuchung des Wassernachschubs in einem gefrierenden Boden und die Beurteilung der Ergebnisse*, 1968
- 9 Marotz, Günter: *Technische Grundlagen einer Wasserspeicherung im natürlichen Untergrund*, 1968
- 10 Radomski, Helge: *Untersuchungen über den Einfluß der Querschnittsform wellenförmiger Spundwände auf die statischen und rammtechnischen Eigenschaften*, 1968
- 11 Schwarz, Helmut: *Die Grenztragfähigkeit des Baugrundes bei Einwirkung vertikal gezogener Ankerplatten als zweidimensionales Bruchproblem*, 1969
- 12 Erbel, Klaus: *Ein Beitrag zur Untersuchung der Metamorphose von Mittelgebirgsschneedecken unter besonderer Berücksichtigung eines Verfahrens zur Bestimmung der thermischen Schneequalität*, 1969
- 13 Westhaus, Karl-Heinz: *Der Strukturwandel in der Binnenschifffahrt und sein Einfluß auf den Ausbau der Binnenschiffskanäle*, 1969
- 14 Mayer-Vorfelder, Hans-Jörg: *Ein Beitrag zur Berechnung des Erdwiderstandes unter Ansatz der logarithmischen Spirale als Gleitflächenfunktion*, 1970
- 15 Schulz, Manfred: *Berechnung des räumlichen Erddruckes auf die Wandung kreiszylindrischer Körper*, 1970
- 16 Mobasser, Manoutschehr: *Die Rippenstützmauer. Konstruktion und Grenzen ihrer Standicherheit*, 1970
- 17 Benk, Dieter: *Ein Beitrag zum Betrieb und zur Bemessung von Hochwasserrückhaltebecken*, 1970
- 18 Gàl, Attila: *Bestimmung der mitschwingenden Wassermasse bei überströmten Fischbauchklappen mit kreiszylindrischem Staublech*, 1971, vergriffen
- 19 Kuz, Klaus Dieter: *Ein Beitrag zur Frage des Einsetzens von Kavitationserscheinungen in einer Düsenströmung bei Berücksichtigung der im Wasser gelösten Gase*, 1971, vergriffen
- 20 Schaak, Hartmut: *Verteilleitungen von Wasserkraftanlagen*, 1971
- 21 *Sonderheft zur Eröffnung der neuen Versuchsanstalt des Instituts für Wasserbau der Universität Stuttgart mit Beiträgen von*
Brombach, Hansjörg; Dirksen, Wolfram; Gàl, Attila; Gerlach, Reinhard; Giesecke, Jürgen; Holthoff, Franz-Josef; Kuz, Klaus Dieter; Marotz, Günter; Minor, Hans-Erwin; Petrikat, Kurt; Röhnisch, Arthur; Rueff, Helge; Schwarz, Helmut; Vollmer, Ernst; Wildenhahn, Eberhard; 1972
- 22 Wang, Chung-su: *Ein Beitrag zur Berechnung der Schwingungen an Kegelstrahlschiebern*, 1972
- 23 Mayer-Vorfelder, Hans-Jörg: *Erdwiderstandsbeiwerte nach dem Ohde-Variationsverfahren*, 1972
- 24 Minor, Hans-Erwin: *Beitrag zur Bestimmung der Schwingungsanfachungsfunktionen überströmter Stauklappen*, 1972, vergriffen
- 25 Brombach, Hansjörg: *Untersuchung strömungsmechanischer Elemente (Fluidik) und die Möglichkeit der Anwendung von Wirbelkammerelementen im Wasserbau*, 1972, vergriffen
- 26 Wildenhahn, Eberhard: *Beitrag zur Berechnung von Horizontalfilterbrunnen*, 1972

- 27 Steinlein, Helmut: *Die Eliminierung der Schwebstoffe aus Flußwasser zum Zweck der unterirdischen Wasserspeicherung, gezeigt am Beispiel der Iller*, 1972
- 28 Holthoff, Franz Josef: *Die Überwindung großer Hubhöhen in der Binnenschifffahrt durch Schwimmerhebwerke*, 1973
- 29 Röder, Karl: *Einwirkungen aus Baugrundbewegungen auf trog- und kastenförmige Konstruktionen des Wasser- und Tunnelbaues*, 1973
- 30 Kretschmer, Heinz: *Die Bemessung von Bogenstaumauern in Abhängigkeit von der Talform*, 1973
- 31 Honekamp, Hermann: *Beitrag zur Berechnung der Montage von Unterwasserpipelines*, 1973
- 32 Giesecke, Jürgen: *Die Wirbelkammertriode als neuartiges Steuerorgan im Wasserbau*, und Brombach, Hansjörg: *Entwicklung, Bauformen, Wirkungsweise und Steuereigenschaften von Wirbelkammerverstärkern*, 1974
- 33 Rueff, Helge: *Untersuchung der schwingungserregenden Kräfte an zwei hintereinander angeordneten Tiefschützen unter besonderer Berücksichtigung von Kavitation*, 1974
- 34 Röhnisch, Arthur: *Einpreßversuche mit Zementmörtel für Spannbeton - Vergleich der Ergebnisse von Modellversuchen mit Ausführungen in Hüllwellrohren*, 1975
- 35 *Sonderheft anlässlich des 65. Geburtstages von Prof. Dr.-Ing. Kurt Petrikat mit Beiträgen von:* Brombach, Hansjörg; Erbel, Klaus; Flinspach, Dieter; Fischer jr., Richard; Gál, Attila; Gerlach, Reinhard; Giesecke, Jürgen; Haberhauer, Robert; Hafner Edzard; Hausenblas, Bernhard; Horlacher, Hans-Burkhard; Hutarew, Andreas; Knoll, Manfred; Krummet, Ralph; Marotz, Günter; Merkle, Theodor; Miller, Christoph; Minor, Hans-Erwin; Neumayer, Hans; Rao, Syamala; Rath, Paul; Rueff, Helge; Ruppert, Jürgen; Schwarz, Wolfgang; Topal-Gökceli, Mehmet; Vollmer, Ernst; Wang, Chung-su; Weber, Hans-Georg; 1975
- 36 Berger, Jochum: *Beitrag zur Berechnung des Spannungszustandes in rotationssymmetrisch belasteten Kugelschalen veränderlicher Wandstärke unter Gas- und Flüssigkeitsdruck durch Integration schwach singulärer Differentialgleichungen*, 1975
- 37 Dirksen, Wolfram: *Berechnung instationärer Abflußvorgänge in gestauten Gerinnen mittels Differenzenverfahren und die Anwendung auf Hochwasserrückhaltebecken*, 1976
- 38 Horlacher, Hans-Burkhard: *Berechnung instationärer Temperatur- und Wärmespannungsfelder in langen mehrschichtigen Hohlzylindern*, 1976
- 39 Hafner, Edzard: *Untersuchung der hydrodynamischen Kräfte auf Baukörper im Tiefwasserbereich des Meeres*, 1977, ISBN 3-921694-39-6
- 40 Ruppert, Jürgen: *Über den Axialwirbelkammerverstärker für den Einsatz im Wasserbau*, 1977, ISBN 3-921694-40-X
- 41 Hutarew, Andreas: *Beitrag zur Beeinflussbarkeit des Sauerstoffgehalts in Fließgewässern an Abstürzen und Wehren*, 1977, ISBN 3-921694-41-8, vergriffen
- 42 Miller, Christoph: *Ein Beitrag zur Bestimmung der schwingungserregenden Kräfte an unterströmten Wehren*, 1977, ISBN 3-921694-42-6
- 43 Schwarz, Wolfgang: *Druckstoßberechnung unter Berücksichtigung der Radial- und Längsverschiebungen der Rohrwandung*, 1978, ISBN 3-921694-43-4
- 44 Kinzelbach, Wolfgang: *Numerische Untersuchungen über den optimalen Einsatz variabler Kühlsysteme einer Kraftwerkskette am Beispiel Oberrhein*, 1978, ISBN 3-921694-44-2
- 45 Barczewski, Baldur: *Neue Meßmethoden für Wasser-Luftgemische und deren Anwendung auf zweiphasige Auftriebsstrahlen*, 1979, ISBN 3-921694-45-0
- 46 Neumayer, Hans: *Untersuchung der Strömungsvorgänge in radialen Wirbelkammerverstärkern*, 1979, ISBN 3-921694-46-9
- 47 Elalfy, Youssef-Elhassan: *Untersuchung der Strömungsvorgänge in Wirbelkammerdioden und -drosseln*, 1979, ISBN 3-921694-47-7
- 48 Brombach, Hansjörg: *Automatisierung der Bewirtschaftung von Wasserspeichern*, 1981, ISBN 3-921694-48-5
- 49 Geldner, Peter: *Deterministische und stochastische Methoden zur Bestimmung der Selbstdichtung von Gewässern*, 1981, ISBN 3-921694-49-3, vergriffen

- 50 Mehlhorn, Hans: *Temperaturveränderungen im Grundwasser durch Brauchwassereinleitungen*, 1982, ISBN 3-921694-50-7, vergriffen
- 51 Hafner, Edzard: *Rohrleitungen und Behälter im Meer*, 1983, ISBN 3-921694-51-5
- 52 Rinnert, Bernd: *Hydrodynamische Dispersion in porösen Medien: Einfluß von Dichteunterschieden auf die Vertikalvermischung in horizontaler Strömung*, 1983, ISBN 3-921694-52-3, vergriffen
- 53 Lindner, Wulf: *Steuerung von Grundwasserentnahmen unter Einhaltung ökologischer Kriterien*, 1983, ISBN 3-921694-53-1, vergriffen
- 54 Herr, Michael; Herzer, Jörg; Kinzelbach, Wolfgang; Kobus, Helmut; Rinnert, Bernd: *Methoden zur rechnerischen Erfassung und hydraulischen Sanierung von Grundwasserkontaminationen*, 1983, ISBN 3-921694-54-X
- 55 Schmitt, Paul: *Wege zur Automatisierung der Niederschlagsermittlung*, 1984, ISBN 3-921694-55-8, vergriffen
- 56 Müller, Peter: *Transport und selektive Sedimentation von Schwebstoffen bei gestautem Abfluß*, 1985, ISBN 3-921694-56-6
- 57 El-Qawasmeh, Fuad: *Möglichkeiten und Grenzen der Tropfbewässerung unter besonderer Berücksichtigung der Verstopfungsanfälligkeit der Tropfelemente*, 1985, ISBN 3-921694-57-4, vergriffen
- 58 Kirchenbaur, Klaus: *Mikroprozessorgesteuerte Erfassung instationärer Druckfelder am Beispiel seegangsbelasteter Baukörper*, 1985, ISBN 3-921694-58-2
- 59 Kobus, Helmut (Hrsg.): *Modellierung des großräumigen Wärme- und Schadstofftransports im Grundwasser*, Tätigkeitsbericht 1984/85 (DFG-Forschergruppe an den Universitäten Hohenheim, Karlsruhe und Stuttgart), 1985, ISBN 3-921694-59-0, vergriffen
- 60 Spitz, Karlheinz: *Dispersion in porösen Medien: Einfluß von Inhomogenitäten und Dichteunterschieden*, 1985, ISBN 3-921694-60-4, vergriffen
- 61 Kobus, Helmut: *An Introduction to Air-Water Flows in Hydraulics*, 1985, ISBN 3-921694-61-2
- 62 Kaleris, Vassilios: *Erfassung des Austausches von Oberflächen- und Grundwasser in horizontalebene Grundwassermodellen*, 1986, ISBN 3-921694-62-0
- 63 Herr, Michael: *Grundlagen der hydraulischen Sanierung verunreinigter Porengrundwasserleiter*, 1987, ISBN 3-921694-63-9
- 64 Marx, Walter: *Berechnung von Temperatur und Spannung in Massenbeton infolge Hydratation*, 1987, ISBN 3-921694-64-7
- 65 Koschitzky, Hans-Peter: *Dimensionierungskonzept für Sohlbelüfter in Schußbrinnen zur Vermeidung von Kavitationsschäden*, 1987, ISBN 3-921694-65-5
- 66 Kobus, Helmut (Hrsg.): *Modellierung des großräumigen Wärme- und Schadstofftransports im Grundwasser*, Tätigkeitsbericht 1986/87 (DFG-Forschergruppe an den Universitäten Hohenheim, Karlsruhe und Stuttgart) 1987, ISBN 3-921694-66-3
- 67 Söll, Thomas: *Berechnungsverfahren zur Abschätzung anthropogener Temperaturanomalien im Grundwasser*, 1988, ISBN 3-921694-67-1
- 68 Dittrich, Andreas; Westrich, Bernd: *Bodenseeufererosion, Bestandsaufnahme und Bewertung*, 1988, ISBN 3-921694-68-X, vergriffen
- 69 Huwe, Bernd; van der Ploeg, Rienk R.: *Modelle zur Simulation des Stickstoffhaushaltes von Standorten mit unterschiedlicher landwirtschaftlicher Nutzung*, 1988, ISBN 3-921694-69-8, vergriffen
- 70 Stephan, Karl: *Integration elliptischer Funktionen*, 1988, ISBN 3-921694-70-1
- 71 Kobus, Helmut; Zilliox, Lothaire (Hrsg.): *Nitratbelastung des Grundwassers, Auswirkungen der Landwirtschaft auf die Grundwasser- und Rohwasserbeschaffenheit und Maßnahmen zum Schutz des Grundwassers*. Vorträge des deutsch-französischen Kolloquiums am 6. Oktober 1988, Universitäten Stuttgart und Louis Pasteur Strasbourg (Vorträge in deutsch oder französisch, Kurzfassungen zweisprachig), 1988, ISBN 3-921694-71-X

- 72 Soyeaux, Renald: *Unterströmung von Stauanlagen auf klüftigem Untergrund unter Berücksichtigung laminarer und turbulenter Fließzustände*, 1991, ISBN 3-921694-72-8
- 73 Kohane, Roberto: *Berechnungsmethoden für Hochwasserabfluß in Fließgewässern mit überströmten Vorländern*, 1991, ISBN 3-921694-73-6
- 74 Hassinger, Reinhard: *Beitrag zur Hydraulik und Bemessung von Blocksteinrampen in flexibler Bauweise*, 1991, ISBN 3-921694-74-4, vergriffen
- 75 Schäfer, Gerhard: *Einfluß von Schichtenstrukturen und lokalen Einlagerungen auf die Längsdispersion in Porengrundwasserleitern*, 1991, ISBN 3-921694-75-2
- 76 Giesecke, Jürgen: *Vorträge, Wasserwirtschaft in stark besiedelten Regionen; Umweltforschung mit Schwerpunkt Wasserwirtschaft*, 1991, ISBN 3-921694-76-0
- 77 Huwe, Bernd: *Deterministische und stochastische Ansätze zur Modellierung des Stickstoffhaushalts landwirtschaftlich genutzter Flächen auf unterschiedlichem Skalenniveau*, 1992, ISBN 3-921694-77-9, vergriffen
- 78 Rommel, Michael: *Verwendung von Kluftdaten zur realitätsnahen Generierung von Kluftnetzen mit anschließender laminar-turbulenter Strömungsberechnung*, 1993, ISBN 3-92 1694-78-7
- 79 Marschall, Paul: *Die Ermittlung lokaler Stofffrachten im Grundwasser mit Hilfe von Einbohrloch-Meßverfahren*, 1993, ISBN 3-921694-79-5, vergriffen
- 80 Ptak, Thomas: *Stofftransport in heterogenen Porenaquiferen: Felduntersuchungen und stochastische Modellierung*, 1993, ISBN 3-921694-80-9, vergriffen
- 81 Haakh, Frieder: *Transientes Strömungsverhalten in Wirbelkammern*, 1993, ISBN 3-921694-81-7
- 82 Kobus, Helmut; Cirpka, Olaf; Barczewski, Baldur; Koschitzky, Hans-Peter: *Versuchseinrichtung zur Grundwasser- und Altlastensanierung VEGAS, Konzeption und Programmrahmen*, 1993, ISBN 3-921694-82-5
- 83 Zang, Weidong: *Optimaler Echtzeit-Betrieb eines Speichers mit aktueller Abflußregenerierung*, 1994, ISBN 3-921694-83-3, vergriffen
- 84 Franke, Hans-Jörg: *Stochastische Modellierung eines flächenhaften Stoffeintrages und Transports in Grundwasser am Beispiel der Pflanzenschutzmittelproblematik*, 1995, ISBN 3-921694-84-1
- 85 Lang, Ulrich: *Simulation regionaler Strömungs- und Transportvorgänge in Karstaquiferen mit Hilfe des Doppelkontinuum-Ansatzes: Methodenentwicklung und Parameteridentifikation*, 1995, ISBN 3-921694-85-X, vergriffen
- 86 Helmig, Rainer: *Einführung in die Numerischen Methoden der Hydromechanik*, 1996, ISBN 3-921694-86-8, vergriffen
- 87 Cirpka, Olaf: *CONTRACT: A Numerical Tool for Contaminant Transport and Chemical Transformations - Theory and Program Documentation -*, 1996, ISBN 3-921694-87-6
- 88 Haberlandt, Uwe: *Stochastische Synthese und Regionalisierung des Niederschlages für Schmutzfrachtberechnungen*, 1996, ISBN 3-921694-88-4
- 89 Croisé, Jean: *Extraktion von flüchtigen Chemikalien aus natürlichen Lockergesteinen mittels erzwungener Luftströmung*, 1996, ISBN 3-921694-89-2, vergriffen
- 90 Jorde, Klaus: *Ökologisch begründete, dynamische Mindestwasserregelungen bei Ausleitungskraftwerken*, 1997, ISBN 3-921694-90-6, vergriffen
- 91 Helmig, Rainer: *Gekoppelte Strömungs- und Transportprozesse im Untergrund - Ein Beitrag zur Hydrosystemmodellierung-*, 1998, ISBN 3-921694-91-4, vergriffen
- 92 Emmert, Martin: *Numerische Modellierung nichtisothermer Gas-Wasser Systeme in porösen Medien*, 1997, ISBN 3-921694-92-2
- 93 Kern, Ulrich: *Transport von Schweb- und Schadstoffen in staugeregelten Fließgewässern am Beispiel des Neckars*, 1997, ISBN 3-921694-93-0, vergriffen
- 94 Förster, Georg: *Druckstoßdämpfung durch große Luftblasen in Hochpunkten von Rohrleitungen* 1997, ISBN 3-921694-94-9

- 95 Cirpka, Olaf: *Numerische Methoden zur Simulation des reaktiven Mehrkomponententransports im Grundwasser*, 1997, ISBN 3-921694-95-7, vergriffen
- 96 Färber, Arne: *Wärmetransport in der ungesättigten Bodenzone: Entwicklung einer thermischen In-situ-Sanierungstechnologie*, 1997, ISBN 3-921694-96-5
- 97 Betz, Christoph: *Wasserdampfdistillation von Schadstoffen im porösen Medium: Entwicklung einer thermischen In-situ-Sanierungstechnologie*, 1998, SBN 3-921694-97-3
- 98 Xu, Yichun: *Numerical Modeling of Suspended Sediment Transport in Rivers*, 1998, ISBN 3-921694-98-1, vergriffen
- 99 Wüst, Wolfgang: *Geochemische Untersuchungen zur Sanierung CKW-kontaminierter Aquifere mit Fe(0)-Reaktionswänden*, 2000, ISBN 3-933761-02-2
- 100 Sheta, Hussam: *Simulation von Mehrphasenvorgängen in porösen Medien unter Einbeziehung von Hysterese-Effekten*, 2000, ISBN 3-933761-03-4
- 101 Ayros, Edwin: *Regionalisierung extremer Abflüsse auf der Grundlage statistischer Verfahren*, 2000, ISBN 3-933761-04-2, vergriffen
- 102 Huber, Ralf: *Compositional Multiphase Flow and Transport in Heterogeneous Porous Media*, 2000, ISBN 3-933761-05-0
- 103 Braun, Christopherus: *Ein Upscaling-Verfahren für Mehrphasenströmungen in porösen Medien*, 2000, ISBN 3-933761-06-9
- 104 Hofmann, Bernd: *Entwicklung eines rechnergestützten Managementsystems zur Beurteilung von Grundwasserschadensfällen*, 2000, ISBN 3-933761-07-7
- 105 Class, Holger: *Theorie und numerische Modellierung nichtisothermer Mehrphasenprozesse in NAPL-kontaminierten porösen Medien*, 2001, ISBN 3-933761-08-5
- 106 Schmidt, Reinhard: *Wasserdampf- und Heißblutinjektion zur thermischen Sanierung kontaminierter Standorte*, 2001, ISBN 3-933761-09-3
- 107 Josef, Reinhold: *Schadstoffextraktion mit hydraulischen Sanierungsverfahren unter Anwendung von grenzflächenaktiven Stoffen*, 2001, ISBN 3-933761-10-7
- 108 Schneider, Matthias: *Habitat- und Abflussmodellierung für Fließgewässer mit unscharfen Berechnungsansätzen*, 2001, ISBN 3-933761-11-5
- 109 Rathgeb, Andreas: *Hydrodynamische Bemessungsgrundlagen für Lockerdeckwerke an überströmbaren Erddämmen*, 2001, ISBN 3-933761-12-3
- 110 Lang, Stefan: *Parallele numerische Simulation instationärer Probleme mit adaptiven Methoden auf unstrukturierten Gittern*, 2001, ISBN 3-933761-13-1
- 111 Appt, Jochen; Stumpp Simone: *Die Bodensee-Messkampagne 2001, IWS/CWR Lake Constance Measurement Program 2001*, 2002, ISBN 3-933761-14-X
- 112 Heimerl, Stephan: *Systematische Beurteilung von Wasserkraftprojekten*, 2002, ISBN 3-933761-15-8, vergriffen
- 113 Iqbal, Amin: *On the Management and Salinity Control of Drip Irrigation*, 2002, ISBN 3-933761-16-6
- 114 Silberhorn-Hemminger, Annette: *Modellierung von Kluftaquifersystemen: Geostatistische Analyse und deterministisch-stochastische Kluftgenerierung*, 2002, ISBN 3-933761-17-4
- 115 Winkler, Angela: *Prozesse des Wärme- und Stofftransports bei der In-situ-Sanierung mit festen Wärmequellen*, 2003, ISBN 3-933761-18-2
- 116 Marx, Walter: *Wasserkraft, Bewässerung, Umwelt - Planungs- und Bewertungsschwerpunkte der Wasserbewirtschaftung*, 2003, ISBN 3-933761-19-0
- 117 Hinkelmann, Reinhard: *Efficient Numerical Methods and Information-Processing Techniques in Environment Water*, 2003, ISBN 3-933761-20-4
- 118 Samaniego-Eguiguren, Luis Eduardo: *Hydrological Consequences of Land Use / Land Cover and Climatic Changes in Mesoscale Catchments*, 2003, ISBN 3-933761-21-2
- 119 Neunhäuserer, Lina: *Diskretisierungsansätze zur Modellierung von Strömungs- und Transportprozessen in geklüftet-porösen Medien*, 2003, ISBN 3-933761-22-0
- 120 Paul, Maren: *Simulation of Two-Phase Flow in Heterogeneous Poros Media with Adaptive Methods*, 2003, ISBN 3-933761-23-9

- 121 Ehret, Uwe: *Rainfall and Flood Nowcasting in Small Catchments using Weather Radar*, 2003, ISBN 3-933761-24-7
- 122 Haag, Ingo: *Der Sauerstoffhaushalt staugeregelter Flüsse am Beispiel des Neckars - Analysen, Experimente, Simulationen -*, 2003, ISBN 3-933761-25-5
- 123 Appt, Jochen: *Analysis of Basin-Scale Internal Waves in Upper Lake Constance*, 2003, ISBN 3-933761-26-3
- 124 Hrsg.: Schrenk, Volker; Batereau, Katrin; Barczewski, Baldur; Weber, Karolin und Koschitzky, Hans-Peter: *Symposium Ressource Fläche und VEGAS - Statuskolloquium 2003, 30. September und 1. Oktober 2003*, 2003, ISBN 3-933761-27-1
- 125 Omar Khalil Ouda: *Optimisation of Agricultural Water Use: A Decision Support System for the Gaza Strip*, 2003, ISBN 3-933761-28-0
- 126 Batereau, Katrin: *Sensorbasierte Bodenluftmessung zur Vor-Ort-Erkundung von Schadensherden im Untergrund*, 2004, ISBN 3-933761-29-8
- 127 Witt, Oliver: *Erosionsstabilität von Gewässersedimenten mit Auswirkung auf den Stofftransport bei Hochwasser am Beispiel ausgewählter Stauhaltungen des Oberrheins*, 2004, ISBN 3-933761-30-1
- 128 Jakobs, Hartmut: *Simulation nicht-isothermer Gas-Wasser-Prozesse in komplexen Kluft-Matrix-Systemen*, 2004, ISBN 3-933761-31-X
- 129 Li, Chen-Chien: *Deterministisch-stochastisches Berechnungskonzept zur Beurteilung der Auswirkungen erosiver Hochwasserereignisse in Flusstauhaltungen*, 2004, ISBN 3-933761-32-8
- 130 Reichenberger, Volker; Helmig, Rainer; Jakobs, Hartmut; Bastian, Peter; Niessner, Jennifer: *Complex Gas-Water Processes in Discrete Fracture-Matrix Systems: Up-scaling, Mass-Conservative Discretization and Efficient Multilevel Solution*, 2004, ISBN 3-933761-33-6
- 131 Hrsg.: Barczewski, Baldur; Koschitzky, Hans-Peter; Weber, Karolin; Wege, Ralf: *VEGAS - Statuskolloquium 2004*, Tagungsband zur Veranstaltung am 05. Oktober 2004 an der Universität Stuttgart, Campus Stuttgart-Vaihingen, 2004, ISBN 3-933761-34-4
- 132 Asie, Kemal Jabir: *Finite Volume Models for Multiphase Multicomponent Flow through Porous Media*. 2005, ISBN 3-933761-35-2
- 133 Jacoub, George: *Development of a 2-D Numerical Module for Particulate Contaminant Transport in Flood Retention Reservoirs and Impounded Rivers*, 2004, ISBN 3-933761-36-0
- 134 Nowak, Wolfgang: *Geostatistical Methods for the Identification of Flow and Transport Parameters in the Subsurface*, 2005, ISBN 3-933761-37-9
- 135 Süß, Mia: *Analysis of the influence of structures and boundaries on flow and transport processes in fractured porous media*, 2005, ISBN 3-933761-38-7
- 136 Jose, Surabhin Chackiath: *Experimental Investigations on Longitudinal Dispersive Mixing in Heterogeneous Aquifers*, 2005, ISBN: 3-933761-39-5
- 137 Filiz, Fulya: *Linking Large-Scale Meteorological Conditions to Floods in Mesoscale Catchments*, 2005, ISBN 3-933761-40-9
- 138 Qin, Minghao: *Wirklichkeitsnahe und recheneffiziente Ermittlung von Temperatur und Spannungen bei großen RCC-Staumauern*, 2005, ISBN 3-933761-41-7
- 139 Kobayashi, Kenichiro: *Optimization Methods for Multiphase Systems in the Subsurface - Application to Methane Migration in Coal Mining Areas*, 2005, ISBN 3-933761-42-5
- 140 Rahman, Md. Arifur: *Experimental Investigations on Transverse Dispersive Mixing in Heterogeneous Porous Media*, 2005, ISBN 3-933761-43-3
- 141 Schrenk, Volker: *Ökobilanzen zur Bewertung von Altlastensanierungsmaßnahmen*, 2005, ISBN 3-933761-44-1
- 142 Hundecha, Hirpa Yeshewatesfa: *Regionalization of Parameters of a Conceptual Rainfall-Runoff Model*, 2005, ISBN: 3-933761-45-X
- 143 Wege, Ralf: *Untersuchungs- und Überwachungsmethoden für die Beurteilung natürlicher Selbstreinigungsprozesse im Grundwasser*, 2005, ISBN 3-933761-46-8

- 144 Breiting, Thomas: *Techniken und Methoden der Hydroinformatik - Modellierung von komplexen Hydrosystemen im Untergrund*, 2006, ISBN 3-933761-47-6
- 145 Hrsg.: Braun, Jürgen; Koschitzky, Hans-Peter; Müller, Martin: *Ressource Untergrund: 10 Jahre VEGAS: Forschung und Technologieentwicklung zum Schutz von Grundwasser und Boden*, Tagungsband zur Veranstaltung am 28. und 29. September 2005 an der Universität Stuttgart, Campus Stuttgart-Vaihingen, 2005, ISBN 3-933761-48-4
- 146 Rojanschi, Vlad: *Abflusskonzentration in mesoskaligen Einzugsgebieten unter Berücksichtigung des Sickerraumes*, 2006, ISBN 3-933761-49-2
- 147 Winkler, Nina Simone: *Optimierung der Steuerung von Hochwasserrückhaltebeckensystemen*, 2006, ISBN 3-933761-50-6
- 148 Wolf, Jens: *Räumlich differenzierte Modellierung der Grundwasserströmung alluvialer Aquifere für mesoskalige Einzugsgebiete*, 2006, ISBN: 3-933761-51-4
- 149 Kohler, Beate: *Externe Effekte der Laufwasserkraftnutzung*, 2006, ISBN 3-933761-52-2
- 150 Hrsg.: Braun, Jürgen; Koschitzky, Hans-Peter; Stuhmann, Matthias: *VEGAS-Statuskolloquium 2006*, Tagungsband zur Veranstaltung am 28. September 2006 an der Universität Stuttgart, Campus Stuttgart-Vaihingen, 2006, ISBN 3-933761-53-0
- 151 Niessner, Jennifer: *Multi-Scale Modeling of Multi-Phase - Multi-Component Processes in Heterogeneous Porous Media*, 2006, ISBN 3-933761-54-9
- 152 Fischer, Markus: *Beanspruchung eingerdeter Rohrleitungen infolge Austrocknung bindiger Böden*, 2006, ISBN 3-933761-55-7
- 153 Schneck, Alexander: *Optimierung der Grundwasserbewirtschaftung unter Berücksichtigung der Belange der Wasserversorgung, der Landwirtschaft und des Naturschutzes*, 2006, ISBN 3-933761-56-5
- 154 Das, Tapash: *The Impact of Spatial Variability of Precipitation on the Predictive Uncertainty of Hydrological Models*, 2006, ISBN 3-33761-57-3
- 155 Bielinski, Andreas: *Numerical Simulation of CO₂ sequestration in geological formations*, 2007, ISBN 3-933761-58-1
- 156 Mödinger, Jens: *Entwicklung eines Bewertungs- und Entscheidungsunterstützungssystems für eine nachhaltige regionale Grundwasserbewirtschaftung*, 2006, ISBN 3-933761-60-3
- 157 Manthey, Sabine: *Two-phase flow processes with dynamic effects in porous media - parameter estimation and simulation*, 2007, ISBN 3-933761-61-1
- 158 Pozos Estrada, Oscar: *Investigation on the Effects of Entrained Air in Pipelines*, 2007, ISBN 3-933761-62-X
- 159 Ochs, Steffen Oliver: *Steam injection into saturated porous media – process analysis including experimental and numerical investigations*, 2007, ISBN 3-933761-63-8
- 160 Marx, Andreas: *Einsatz gekoppelter Modelle und Wetterradar zur Abschätzung von Niederschlagsintensitäten und zur Abflussvorhersage*, 2007, ISBN 3-933761-64-6
- 161 Hartmann, Gabriele Maria: *Investigation of Evapotranspiration Concepts in Hydrological Modelling for Climate Change Impact Assessment*, 2007, ISBN 3-933761-65-4
- 162 Kebede Gurmessa, Tesfaye: *Numerical Investigation on Flow and Transport Characteristics to Improve Long-Term Simulation of Reservoir Sedimentation*, 2007, ISBN 3-933761-66-2
- 163 Trifković, Aleksandar: *Multi-objective and Risk-based Modelling Methodology for Planning, Design and Operation of Water Supply Systems*, 2007, ISBN 3-933761-67-0
- 164 Götzinger, Jens: *Distributed Conceptual Hydrological Modelling - Simulation of Climate, Land Use Change Impact and Uncertainty Analysis*, 2007, ISBN 3-933761-68-9
- 165 Hrsg.: Braun, Jürgen; Koschitzky, Hans-Peter; Stuhmann, Matthias: *VEGAS – Kolloquium 2007*, Tagungsband zur Veranstaltung am 26. September 2007 an der Universität Stuttgart, Campus Stuttgart-Vaihingen, 2007, ISBN 3-933761-69-7
- 166 Freeman, Beau: *Modernization Criteria Assessment for Water Resources Planning; Klamath Irrigation Project, U.S.*, 2008, ISBN 3-933761-70-0

- 167 Dreher, Thomas: *Selektive Sedimentation von Feinstschwebstoffen in Wechselwirkung mit wandnahen turbulenten Strömungsbedingungen*, 2008, ISBN 3-933761-71-9
- 168 Yang, Wei: *Discrete-Continuous Downscaling Model for Generating Daily Precipitation Time Series*, 2008, ISBN 3-933761-72-7
- 169 Kopecki, Ianina: *Calculational Approach to FST-Hemispheres for Multiparametrical Benthos Habitat Modelling*, 2008, ISBN 3-933761-73-5
- 170 Brommundt, Jürgen: *Stochastische Generierung räumlich zusammenhängender Niederschlagszeitreihen*, 2008, ISBN 3-933761-74-3
- 171 Papafotiou, Alexandros: *Numerical Investigations of the Role of Hysteresis in Heterogeneous Two-Phase Flow Systems*, 2008, ISBN 3-933761-75-1
- 172 He, Yi: *Application of a Non-Parametric Classification Scheme to Catchment Hydrology*, 2008, ISBN 978-3-933761-76-7
- 173 Wagner, Sven: *Water Balance in a Poorly Gauged Basin in West Africa Using Atmospheric Modelling and Remote Sensing Information*, 2008, ISBN 978-3-933761-77-4
- 174 Hrsg.: Braun, Jürgen; Koschitzky, Hans-Peter; Stuhmann, Matthias; Schrenk, Volker: *VEGAS-Kolloquium 2008 Ressource Fläche III*, Tagungsband zur Veranstaltung am 01. Oktober 2008 an der Universität Stuttgart, Campus Stuttgart-Vaihingen, 2008, ISBN 978-3-933761-78-1
- 175 Patil, Sachin: *Regionalization of an Event Based Nash Cascade Model for Flood Predictions in Ungauged Basins*, 2008, ISBN 978-3-933761-79-8
- 176 Assteerawatt, Anongnart: *Flow and Transport Modelling of Fractured Aquifers based on a Geostatistical Approach*, 2008, ISBN 978-3-933761-80-4
- 177 Karnahl, Joachim Alexander: *2D numerische Modellierung von multifraktionalem Schwebstoff- und Schadstofftransport in Flüssen*, 2008, ISBN 978-3-933761-81-1
- 178 Hiester, Uwe: *Technologieentwicklung zur In-situ-Sanierung der ungesättigten Bodenzone mit festen Wärmequellen*, 2009, ISBN 978-3-933761-82-8
- 179 Laux, Patrick: *Statistical Modeling of Precipitation for Agricultural Planning in the Volta Basin of West Africa*, 2009, ISBN 978-3-933761-83-5
- 180 Ehsan, Saqib: *Evaluation of Life Safety Risks Related to Severe Flooding*, 2009, ISBN 978-3-933761-84-2
- 181 Prohaska, Sandra: *Development and Application of a 1D Multi-Strip Fine Sediment Transport Model for Regulated Rivers*, 2009, ISBN 978-3-933761-85-9
- 182 Kopp, Andreas: *Evaluation of CO₂ Injection Processes in Geological Formations for Site Screening*, 2009, ISBN 978-3-933761-86-6
- 183 Ebigbo, Anozie: *Modelling of biofilm growth and its influence on CO₂ and water (two-phase) flow in porous media*, 2009, ISBN 978-3-933761-87-3
- 184 Freiboth, Sandra: *A phenomenological model for the numerical simulation of multiphase multicomponent processes considering structural alterations of porous media*, 2009, ISBN 978-3-933761-88-0
- 185 Zöllner, Frank: *Implementierung und Anwendung netzfreier Methoden im Konstruktiven Wasserbau und in der Hydromechanik*, 2009, ISBN 978-3-933761-89-7
- 186 Vasin, Milos: *Influence of the soil structure and property contrast on flow and transport in the unsaturated zone*, 2010, ISBN 978-3-933761-90-3
- 187 Li, Jing: *Application of Copulas as a New Geostatistical Tool*, 2010, ISBN 978-3-933761-91-0
- 188 AghaKouchak, Amir: *Simulation of Remotely Sensed Rainfall Fields Using Copulas*, 2010, ISBN 978-3-933761-92-7
- 189 Thapa, Pawan Kumar: *Physically-based spatially distributed rainfall runoff modelling for soil erosion estimation*, 2010, ISBN 978-3-933761-93-4
- 190 Wurms, Sven: *Numerische Modellierung der Sedimentationsprozesse in Retentionsanlagen zur Steuerung von Stoffströmen bei extremen Hochwasserabflussereignissen*, 2011, ISBN 978-3-933761-94-1

- 191 Merkel, Uwe: *Unsicherheitsanalyse hydraulischer Einwirkungen auf Hochwasserschutzdeiche und Steigerung der Leistungsfähigkeit durch adaptive Strömungsmodellierung*, 2011, ISBN 978-3-933761-95-8
- 192 Fritz, Jochen: *A Decoupled Model for Compositional Non-Isothermal Multiphase Flow in Porous Media and Multiphysics Approaches for Two-Phase Flow*, 2010, ISBN 978-3-933761-96-5
- 193 Weber, Karolin (Hrsg.): *12. Treffen junger WissenschaftlerInnen an Wasserbauinstituten*, 2010, ISBN 978-3-933761-97-2
- 194 Blifernicht, Jan-Geert: *Probability Forecasts of Daily Areal Precipitation for Small River Basins*, 2011, ISBN 978-3-933761-98-9
- 195 Hrsg.: Koschitzky, Hans-Peter; Braun, Jürgen: *VEGAS-Kolloquium 2010 In-situ-Sanierung - Stand und Entwicklung Nano und ISCO -*, Tagungsband zur Veranstaltung am 07. Oktober 2010 an der Universität Stuttgart, Campus Stuttgart-Vaihingen, 2010, ISBN 978-3-933761-99-6
- 196 Gafurov, Abror: *Water Balance Modeling Using Remote Sensing Information - Focus on Central Asia*, 2010, ISBN 978-3-942036-00-9
- 197 Mackenberg, Sylvia: *Die Quellstärke in der Sickerwasserprognose: Möglichkeiten und Grenzen von Labor- und Freilanduntersuchungen*, 2010, ISBN 978-3-942036-01-6
- 198 Singh, Shailesh Kumar: *Robust Parameter Estimation in Gauged and Ungauged Basins*, 2010, ISBN 978-3-942036-02-3
- 199 Doğan, Mehmet Onur: *Coupling of porous media flow with pipe flow*, 2011, ISBN 978-3-942036-03-0
- 200 Liu, Min: *Study of Topographic Effects on Hydrological Patterns and the Implication on Hydrological Modeling and Data Interpolation*, 2011, ISBN 978-3-942036-04-7
- 201 Geleta, Habtamu Itefa: *Watershed Sediment Yield Modeling for Data Scarce Areas*, 2011, ISBN 978-3-942036-05-4
- 202 Franke, Jörg: *Einfluss der Überwachung auf die Versagenswahrscheinlichkeit von Staustufen*, 2011, ISBN 978-3-942036-06-1
- 203 Bakimchandra, Oinam: *Integrated Fuzzy-GIS approach for assessing regional soil erosion risks*, 2011, ISBN 978-3-942036-07-8
- 204 Alam, Muhammad Mahboob: *Statistical Downscaling of Extremes of Precipitation in Mesoscale Catchments from Different RCMs and Their Effects on Local Hydrology*, 2011, ISBN 978-3-942036-08-5
- 205 Hrsg.: Koschitzky, Hans-Peter; Braun, Jürgen: *VEGAS-Kolloquium 2011 Flache Geothermie - Perspektiven und Risiken*, Tagungsband zur Veranstaltung am 06. Oktober 2011 an der Universität Stuttgart, Campus Stuttgart-Vaihingen, 2011, ISBN 978-3-933761-09-2
- 206 Haslauer, Claus: *Analysis of Real-World Spatial Dependence of Subsurface Hydraulic Properties Using Copulas with a Focus on Solute Transport Behaviour*, 2011, ISBN 978-3-942036-10-8
- 207 Dung, Nguyen Viet: *Multi-objective automatic calibration of hydrodynamic models – development of the concept and an application in the Mekong Delta*, 2011, ISBN 978-3-942036-11-5
- 208 Hung, Nguyen Nghia: *Sediment dynamics in the floodplain of the Mekong Delta, Vietnam*, 2011, ISBN 978-3-942036-12-2
- 209 Kuhlmann, Anna: *Influence of soil structure and root water uptake on flow in the unsaturated zone*, 2012, ISBN 978-3-942036-13-9
- 210 Tuhtan, Jeffrey Andrew: *Including the Second Law Inequality in Aquatic Ecodynamics: A Modeling Approach for Alpine Rivers Impacted by Hydropeaking*, 2012, ISBN 978-3-942036-14-6
- 211 Tolossa, Habtamu: *Sediment Transport Computation Using a Data-Driven Adaptive Neuro-Fuzzy Modelling Approach*, 2012, ISBN 978-3-942036-15-3
- 212 Tatomir, Alexandru-Bodgan: *From Discrete to Continuum Concepts of Flow in Fractured Porous Media*, 2012, ISBN 978-3-942036-16-0

- 213 Erbertseder, Karin: *A Multi-Scale Model for Describing Cancer-Therapeutic Transport in the Human Lung*, 2012, ISBN 978-3-942036-17-7
- 214 Noack, Markus: *Modelling Approach for Interstitial Sediment Dynamics and Reproduction of Gravel Spawning Fish*, 2012, ISBN 978-3-942036-18-4
- 215 De Boer, Cjestrir Volkert: *Transport of Nano Sized Zero Valent Iron Colloids during Injection into the Subsurface*, 2012, ISBN 978-3-942036-19-1
- 216 Pfaff, Thomas: *Processing and Analysis of Weather Radar Data for Use in Hydrology*, 2013, ISBN 978-3-942036-20-7
- 217 Lebreuz, Hans-Henning: *Addressing the Input Uncertainty for Hydrological Modeling by a New Geostatistical Method*, 2013, ISBN 978-3-942036-21-4
- 218 Darcis, Melanie Yvonne: *Coupling Models of Different Complexity for the Simulation of CO₂ Storage in Deep Saline Aquifers*, 2013, ISBN 978-3-942036-22-1
- 219 Beck, Ferdinand: *Generation of Spatially Correlated Synthetic Rainfall Time Series in High Temporal Resolution - A Data Driven Approach*, 2013, ISBN 978-3-942036-23-8
- 220 Guthke, Philipp: *Non-multi-Gaussian spatial structures: Process-driven natural genesis, manifestation, modeling approaches, and influences on dependent processes*, 2013, ISBN 978-3-942036-24-5
- 221 Walter, Lena: *Uncertainty studies and risk assessment for CO₂ storage in geological formations*, 2013, ISBN 978-3-942036-25-2
- 222 Wolff, Markus: *Multi-scale modeling of two-phase flow in porous media including capillary pressure effects*, 2013, ISBN 978-3-942036-26-9
- 223 Mosthaf, Klaus Roland: *Modeling and analysis of coupled porous-medium and free flow with application to evaporation processes*, 2014, ISBN 978-3-942036-27-6
- 224 Leube, Philipp Christoph: *Methods for Physically-Based Model Reduction in Time: Analysis, Comparison of Methods and Application*, 2013, ISBN 978-3-942036-28-3
- 225 Rodríguez Fernández, Jhan Ignacio: *High Order Interactions among environmental variables: Diagnostics and initial steps towards modeling*, 2013, ISBN 978-3-942036-29-0
- 226 Eder, Maria Magdalena: *Climate Sensitivity of a Large Lake*, 2013, ISBN 978-3-942036-30-6
- 227 Greiner, Philipp: *Alkoholinjektion zur In-situ-Sanierung von CKW Schadensherden in Grundwasserleitern: Charakterisierung der relevanten Prozesse auf unterschiedlichen Skalen*, 2014, ISBN 978-3-942036-31-3
- 228 Lauser, Andreas: *Theory and Numerical Applications of Compositional Multi-Phase Flow in Porous Media*, 2014, ISBN 978-3-942036-32-0
- 229 Enzenhöfer, Rainer: *Risk Quantification and Management in Water Production and Supply Systems*, 2014, ISBN 978-3-942036-33-7
- 230 Faigle, Benjamin: *Adaptive modelling of compositional multi-phase flow with capillary pressure*, 2014, ISBN 978-3-942036-34-4
- 231 Oladyshkin, Sergey: *Efficient modeling of environmental systems in the face of complexity and uncertainty*, 2014, ISBN 978-3-942036-35-1
- 232 Sugimoto, Takayuki: *Copula based Stochastic Analysis of Discharge Time Series*, 2014, ISBN 978-3-942036-36-8
- 233 Koch, Jonas: *Simulation, Identification and Characterization of Contaminant Source Architectures in the Subsurface*, 2014, ISBN 978-3-942036-37-5
- 234 Zhang, Jin: *Investigations on Urban River Regulation and Ecological Rehabilitation Measures, Case of Shenzhen in China*, 2014, ISBN 978-3-942036-38-2
- 235 Siebel, Rüdiger: *Experimentelle Untersuchungen zur hydrodynamischen Belastung und Standsicherheit von Deckwerken an überströmbaren Erddämmen*, 2014, ISBN 978-3-942036-39-9
- 236 Baber, Katherina: *Coupling free flow and flow in porous media in biological and technical applications: From a simple to a complex interface description*, 2014, ISBN 978-3-942036-40-5

- 237 Nuske, Klaus Philipp: *Beyond Local Equilibrium — Relaxing local equilibrium assumptions in multiphase flow in porous media*, 2014, ISBN 978-3-942036-41-2
- 238 Geiges, Andreas: *Efficient concepts for optimal experimental design in nonlinear environmental systems*, 2014, ISBN 978-3-942036-42-9
- 239 Schwenck, Nicolas: *An XFEM-Based Model for Fluid Flow in Fractured Porous Media*, 2014, ISBN 978-3-942036-43-6
- 240 Chamorro Chávez, Alejandro: *Stochastic and hydrological modelling for climate change prediction in the Lima region, Peru*, 2015, ISBN 978-3-942036-44-3
- 241 Yulizar: *Investigation of Changes in Hydro-Meteorological Time Series Using a Depth-Based Approach*, 2015, ISBN 978-3-942036-45-0
- 242 Kretschmer, Nicole: *Impacts of the existing water allocation scheme on the Limarí watershed – Chile, an integrative approach*, 2015, ISBN 978-3-942036-46-7
- 243 Kramer, Matthias: *Luftbedarf von Freistrahlturbinen im Gegendruckbetrieb*, 2015, ISBN 978-3-942036-47-4
- 244 Hommel, Johannes: *Modeling biogeochemical and mass transport processes in the sub-surface: Investigation of microbially induced calcite precipitation*, 2016, ISBN 978-3-942036-48-1
- 245 Germer, Kai: *Wasserinfiltration in die ungesättigte Zone eines makroporösen Hanges und deren Einfluss auf die Hangstabilität*, 2016, ISBN 978-3-942036-49-8
- 246 Hörning, Sebastian: *Process-oriented modeling of spatial random fields using copulas*, 2016, ISBN 978-3-942036-50-4
- 247 Jambhekar, Vishal: *Numerical modeling and analysis of evaporative salinization in a coupled free-flow porous-media system*, 2016, ISBN 978-3-942036-51-1
- 248 Huang, Yingchun: *Study on the spatial and temporal transferability of conceptual hydrological models*, 2016, ISBN 978-3-942036-52-8
- 249 Kleinknecht, Simon Matthias: *Migration and retention of a heavy NAPL vapor and remediation of the unsaturated zone*, 2016, ISBN 978-3-942036-53-5
- 250 Kwakye, Stephen Oppong: *Study on the effects of climate change on the hydrology of the West African sub-region*, 2016, ISBN 978-3-942036-54-2
- 251 Kissinger, Alexander: *Basin-Scale Site Screening and Investigation of Possible Impacts of CO₂ Storage on Subsurface Hydrosystems*, 2016, ISBN 978-3-942036-55-9
- 252 Müller, Thomas: *Generation of a Realistic Temporal Structure of Synthetic Precipitation Time Series for Sewer Applications*, 2017, ISBN 978-3-942036-56-6
- 253 Grüninger, Christoph: *Numerical Coupling of Navier-Stokes and Darcy Flow for Soil-Water Evaporation*, 2017, ISBN 978-3-942036-57-3
- 254 Suroso: *Asymmetric Dependence Based Spatial Copula Models: Empirical Investigations and Consequences on Precipitation Fields*, 2017, ISBN 978-3-942036-58-0
- 255 Müller, Thomas; Mosthaf, Tobias; Gunzenhauser, Sarah; Seidel, Jochen; Bárdossy, András: *Grundlagenbericht Niederschlags-Simulator (NiedSim3)*, 2017, ISBN 978-3-942036-59-7
- 256 Mosthaf, Tobias: *New Concepts for Regionalizing Temporal Distributions of Precipitation and for its Application in Spatial Rainfall Simulation*, 2017, ISBN 978-3-942036-60-3
- 257 Fenrich, Eva Katrin: *Entwicklung eines ökologisch-ökonomischen Vernetzungsmodells für Wasserkraftanlagen und Mehrzweckspeicher*, 2018, ISBN 978-3-942036-61-0
- 258 Schmidt, Holger: *Microbial stabilization of lotic fine sediments*, 2018, ISBN 978-3-942036-62-7
- 259 Fetzer, Thomas: *Coupled Free and Porous-Medium Flow Processes Affected by Turbulence and Roughness – Models, Concepts and Analysis*, 2018, ISBN 978-3-942036-63-4
- 260 Schröder, Hans Christoph: *Large-scale High Head Pico Hydropower Potential Assessment*, 2018, ISBN 978-3-942036-64-1
- 261 Bode, Felix: *Early-Warning Monitoring Systems for Improved Drinking Water Resource Protection*, 2018, ISBN 978-3-942036-65-8

- 262 Gebler, Tobias: *Statistische Auswertung von simulierten Talsperrenüberwachungsdaten zur Identifikation von Schadensprozessen an Gewichtsstaumauern*, 2018, ISBN 978-3-942036-66-5
- 263 Harten, Matthias von: *Analyse des Zuppinger-Wasserrades – Hydraulische Optimierungen unter Berücksichtigung ökologischer Aspekte*, 2018, ISBN 978-3-942036-67-2
- 264 Yan, Jieru: *Nonlinear estimation of short time precipitation using weather radar and surface observations*, 2018, ISBN 978-3-942036-68-9
- 265 Beck, Martin: *Conceptual approaches for the analysis of coupled hydraulic and geomechanical processes*, 2019, ISBN 978-3-942036-69-6
- 266 Haas, Jannik: *Optimal planning of hydropower and energy storage technologies for fully renewable power systems*, 2019, ISBN 978-3-942036-70-2
- 267 Schneider, Martin: *Nonlinear Finite Volume Schemes for Complex Flow Processes and Challenging Grids*, 2019, ISBN 978-3-942036-71-9
- 268 Most, Sebastian Christopher: *Analysis and Simulation of Anomalous Transport in Porous Media*, 2019, ISBN 978-3-942036-72-6
- 269 Buchta, Rocco: *Entwicklung eines Ziel- und Bewertungssystems zur Schaffung nachhaltiger naturnaher Strukturen in großen sandgeprägten Flüssen des norddeutschen Tieflandes*, 2019, ISBN 978-3-942036-73-3
- 270 Thom, Moritz: *Towards a Better Understanding of the Biostabilization Mechanisms of Sediment Beds*, 2019, ISBN 978-3-942036-74-0
- 271 Stolz, Daniel: *Die Nullspannungstemperatur in Gewichtsstaumauern unter Berücksichtigung der Festigkeitsentwicklung des Betons*, 2019, ISBN 978-3-942036-75-7
- 272 Rodriguez Pretelin, Abelardo: *Integrating transient flow conditions into groundwater well protection*, 2020, ISBN: 978-3-942036-76-4
- 273 Weishaupt, Kilian: *Model Concepts for Coupling Free Flow with Porous Medium Flow at the Pore-Network Scale: From Single-Phase Flow to Compositional Non-Isothermal Two-Phase Flow*, 2020, ISBN: 978-3-942036-77-1
- 274 Koch, Timo: *Mixed-dimension models for flow and transport processes in porous media with embedded tubular network systems*, 2020, ISBN: 978-3-942036-78-8
- 275 Gläser, Dennis: *Discrete fracture modeling of multi-phase flow and deformation in fractured poroelastic media*, 2020, ISBN: 978-3-942036-79-5

Die Mitteilungshefte ab der Nr. 134 (Jg. 2005) stehen als pdf-Datei über die Homepage des Instituts: www.iws.uni-stuttgart.de zur Verfügung.